Autonomous Landing of a Fixed-Wing Unmanned Aircraft With Partial Wing and Stabiliser Losses

by

Gideon L. Hugo

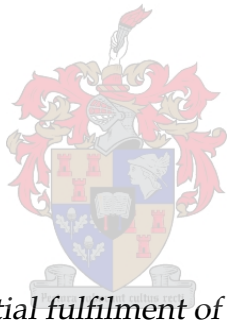

Thesis presented in partial fulfilment of the requirements for the degree of Master in Engineering in the Faculty of Engineering at Stellenbosch University

Supervisor: Dr. Jacobus A.A. Engelbrecht

March 2017

Declaration

By submitting this thesis electronically, I declare that the entirety of the work contained therein is my own, original work, that I am the sole author thereof (save to the extent explicitly otherwise stated), that reproduction and publication thereof by Stellenbosch University will not infringe any third party rights and that I have not previously in its entirety or in part submitted it for obtaining any qualification.

Date: ..... March 2017 .....

Abstract

This thesis presents the design, implementation and verification of an autonomous landing system for a fixed-wing unmanned aerial vehicle that is able to land the aircraft after suffering partial wing loss and partial losses of the horizontal and vertical stabilisers. A fault-tolerant flight control system is designed, which ensures that the inner-loop controllers remain stable and within acceptable transient response specifications when the aircraft suffers partial wing, horizontal stabiliser, and vertical stabiliser losses. The design approach is to find controller gains that provide the best performance for the undamaged aircraft, while still providing at least the minimum acceptable performance over all damage cases. An algorithm calculates the controller gains, if such gains exist, with different combinations of natural frequencies and damping ratios for all damage cases until both the desired closed-loop performance and robustness are obtained. Autonomous landing is accomplished using a state machine that guides the aircraft through the landing phases. The flight control laws, waypoint navigation, and autonomous landing system were verified in simulation and with practical flight tests. Landing accuracies within a 1.5 m radius circle are accomplished in simulation for an aircraft with 20% wing loss, 70% horizontal stabiliser loss, and 20% vertical stabiliser loss.

Uittreksel

Hierdie tesis beskryf die ontwerp, implementering en verifiëring van 'n outonome landingstelsel vir 'n vastevlerk-onbemande vliegtuig wat in staat is om die vliegtuig te land nadat dit gedeeltelike vlerkverlies en gedeeltelike verlies van die horisontale en vertikale stabiliseerders ervaar het. 'n Fout-tolerante vlugbeheerstelsel is ontwerp wat verseker dat die binnelusbeheerders stabiel en binne aanvaarbare oorgansverskynsel-spesifikasies bly wanneer die vliegtuig hierdie verliese ervaar. Die ontwerps benadering is om beheerder-aanwinste te vind wat die beste oorgangsverskynsels vir die onbeskadigde vliegtuig haal, terwyl die aanwinste nog ten minste die minimum aanvaarbare oorgangsverskynsels oor al die verlies gevalle haal. 'n Iteratiewe algoritme bereken die beheerder-aanwinste, indien sodanige aanwinste bestaan, met verskillende kombinasies van natuurlike frekwensies en dempings verhoudings vir alle skadegevalle tot beide die gewenste geslotelusgedrag en robuustheid verkry word. Die outonome landing word uitgevoer met behulp van 'n toestandsmasjien wat die vliegtuig deur die landingsfases neem. Die vlugbeheerwette en landingstelsel word deur simulasie geverifieer, asook deur praktiese vlugtoetse. 'n Landingsakkuraatheid binne 'n sirkel van 1.5 m radius word in simulasie behaal vir 'n vliegtuig met 20 % vlerkverlies, 70 % horisontale stabiliseerderverlies, en 20 % vertikale stabiliseerderverlies.

Acknowledgements

I would like to express my sincere gratitude to the following people and organisations for their contributions towards this dissertation,

- Dr. Jacobus A.A. Engelbrecht for his support, guidance and advice throughout the course of this project. Your friendship is very much valued.
- My family for all the support and the loving environment that has allowed me to achieve all that I have today.
- All the ESL research students for the friendly, highly enjoyable research environment they have played a part in creating.
- The UAV research funding partners, in particular Armscor for their financial support.

Contents

List of Figures

List of Tables

Abbreviations and Acronyms

AC	Aerodynamic Centre
AVL	Athena Vortex Lattice
CAN	Controller area network
CM	Centre of mass
DCM	Direction cosine matrix
DGPS	Differential Global Positioning System
EoM	Equations of motion
ESL	Electronic Systems Laboratory
FDI	Fault detection and isolation
GPS	Global Positioning System
GCS	Ground control station
HIL	Hardware-in-the-loop
IMU	Inertial measurement unit
LQR	Linear quadratic regulator
LSA	Lateral specific acceleration
MIMO	Multi-input, multi-output
NED	North-East-Down reference frame
NMP	Non-minimum phase
NP	Neutral point
NSA	Normal specific acceleration
OBC	On-board computer
RC	Radio control
6DoF	Six degrees of freedom
UAV	Unmanned aerial vehicle

Greek Letters

α	Angle of attack
β	Angle of sideslip
δ_a	Aileron perturbation from trim condition

δ_A	Aileron total deflection
δ_e	Elevator perturbation from trim condition
δ_E	Elevator total deflection
δ_r	Rudder perturbation from trim condition
δ_R	Rudder total deflection
ΔT	Throttle perturbation from trim condition
ΔT_c	Throttle command perturbation from trim condition
Δx	Centre of mass shift in the X_B-axis
Δy	Centre of mass shift in the Y_B-axis
Δz	Centre of mass shift in the Z_B-axis
ϵ	Downwash angle
ϕ	Roll angle perturbation
λ	Eigenvalue
θ	Pitch angle perturbation
ρ	Air density
$\bar{\rho}$	Vector from arbitrary point A to the centre of mass
τ_T	Engine time constant
η	Dynamic pressure ratio
ω_n	Natural frequency
ψ	Yaw angle perturbation
ζ	Damping ratio
Φ	Roll angle
Θ	Pitch angle
Ψ	Yaw angle

Small Letters

b	Wing span
c	Mean aerodynamic chord
e	Oswald efficiency factor
g	Gravitational acceleration
h	Altitude perturbation
$\dot{h}$	Climb rate perturbation
l_H	Horizontal stabiliser moment arm
l_V	Vertical stabiliser moment arm
l_{WF}	Wing-fuselage moment arm
m	Mass
p	Roll rate perturbation

q	Pitch rate perturbation
$\bar{q}$	Dynamic pressure
r	Yaw rate perturbation
s	Semi-span
u	Axial velocity perturbation
v	Lateral velocity perturbation
w	Normal velocity perturbation
y	Cross track error
$\dot{y}$	Cross track error

Capital Letters

A	Aspect ratio
C_D	Aerodynamic drag coefficient
C_l	Aerodynamic roll moment coefficient
C_L	Aerodynamic lift coefficient
C_m	Aerodynamic pitching moment coefficient
C_n	Aerodynamic yaw moment coefficient
C_x	Aerodynamic axial force coefficient
C_y	Aerodynamic side force coefficient
C_z	Aerodynamic normal force coefficient
I	Moment of inertia
I_{xx}	Moment of inertia about the roll axis
I_{yy}	Moment of inertia about the pitch axis
I_{zz}	Moment of inertia about the yaw axis
I_{xy}	Roll and pitch product of inertia
I_{xz}	Roll and yaw product of inertia
I_{zy}	Pitch and yaw product of inertia
L	Roll moment
M	Pitch moment
N	Yaw moment
P	Roll rate
Q	Pitch rate
R	Yaw rate
S	Reference wing area
T	Engine thrust magnitude
T_c	Engine thrust command
U	Axial velocity

V	Side velocity
$\bar{V}$	Airspeed
W	Normal velocity
X	Axial force
Y	Side force
Z	Normal force

Constants

$g =$	9.81 m/s^2
$\rho =$	1.225 kg/m^3

Subscripts

0	Zero angle of attack
ac	Aerodynamic centre
A	Referenced to the arbitrary fixed point A
B	Body reference frame
cm	Referenced to the centre of mass
H	Horizontal stabiliser
np	Referenced to the neutral point
V	Vertical stabiliser
W	Wind reference frame
WF	Wing-fuselage
S	Stability reference frame

Superscripts

A	Aerodynamic
G	Gravitational
T	Thrust or transpose

CHAPTER 1

Introduction

This chapter begins by providing the background and motivation for the research presented in this thesis. A brief survey of previous research performed at Stellenbosch University on similar topics, as well as how the research presented in this thesis builds on it, is given. After considering prior work, the research objectives for this project are defined. A description of the unmanned aircraft system that served as the platform for the research is given, as well as an overview of the project execution. The chapter concludes with an outline of how the thesis is structured.

1.1 Background

Unmanned aerial vehicles (UAVs) are becoming more popular for military as well as commercial use. Removing the human aspect from the machine results in a system that can operate in more harsh environments and for longer periods. A few examples of the ever-expanding applications of UAVs are notably combat missions, search and rescue, disaster management, surveying and also as delivery systems. A UAV is typically adapted for a specific application, which allows it to perform at its best for the given mission. Each application introduces new uncertainties and complications that need to be considered in the development process. A fully autonomous UAV is capable of performing autonomous take-off, navigation and landings, which all form part of the typical aircraft phases or tasks seen in Figure 1.1. Of all these tasks, landing the aircraft is the most difficult. Landing typically entails aligning the aircraft with the runway, reducing the aircraft's airspeed (which is kept well above stall speed) and following a glide path at a certain sink rate until touchdown. For a UAV to successfully perform a fully autonomous landing, strict longitudinal and lateral-directional control are required to ensure that the aircraft follows the desired glide path and stays within the runway bounds while approaching the touchdown point. A significant amount of research continues to go into the development of UAVs and how they can reliably integrated into military and civil airspace. Human safety is one of the most important factors that needs to be considered before sending a UAV into missions.

A UAV sent into civil airspace must be capable of operating under various conditions without endangering humans or their property. Even though legislation still prohibit delivery UAVs due to numerous safety reasons, companies such as Amazon and Google are actively researching and developing UAVs as a medium for delivering goods. UAVs used for military applications encounter different uncertainties and complications on the battlefield. They operate under dangerous environments and are constantly at risk of suffering physical damage or being destroyed by enemy fire. Regardless of the application, the goal remains the same: to reliably reach the target/destination and then return home safely even in dangerous and unknown circumstances. It will therefore be beneficial if a UAV can operate normally even after suffering damage. When a

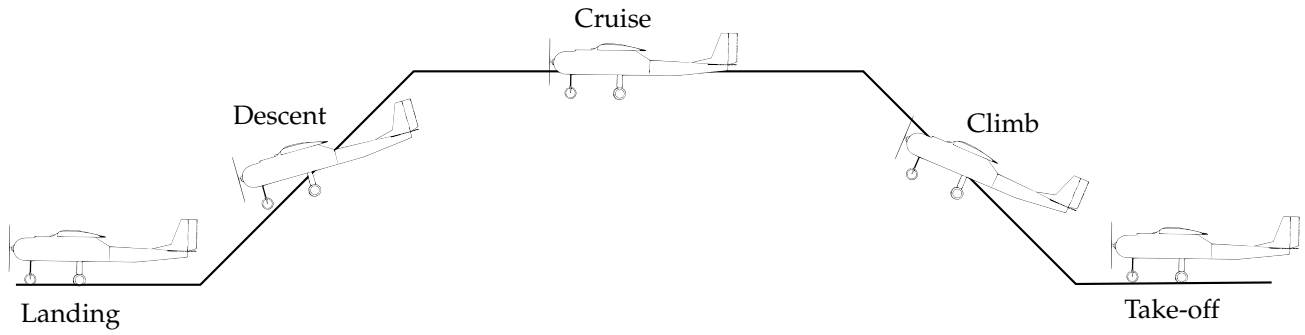

Figure 1.1: The flight phases of a typical flight mission

UAV experiences a malfunction, be it a result of physical damage or harsh environmental impacts, the UAV must have the ability to isolate the fault and try to recover from it if possible. This leads to a whole new research field, namely fault-tolerant control systems. A fault-tolerant control system is capable of controlling a system with adequate performance even if several faults or failures occur within the system [1]. Faults that can occur include physical damage, such as partial wing or stabiliser losses, and actuator or sensor failures.

The autonomous landing of a fixed-wing unmanned aircraft with structural damage, in particular partial wing loss and stabiliser losses, is presented in this thesis. The aircraft stability with partial wing loss and stabiliser losses are investigated. Based on the aircraft stability and dynamics the most prominent fault-tolerant flight control system for this particular application is selected. The fault-tolerant flight control system ensures stability and acceptable transient response specifications when the aircraft suffers partial wing, horizontal stabiliser, and vertical stabiliser losses, which enables the aircraft to perform successful autonomous landing.

1.2 Previous Research at Stellenbosch University

The topic of fault-tolerant control has grown in popularity in the literature over the last three decades [1]. This is due to the demand for safety, reliability, maintainability, and survivability in technical systems [1]. Standard feedback control systems do not have the ability to control a complex system or aircraft with severe plant deviations with satisfactory performance. In order to increase the safety and reliability of aircraft systems, fault-tolerant flight control systems are introduced.

Stellenbosch University already has a well established UAV research program with several successful projects completed. These projects range from autonomous take-off and landing (ATOL) to fault-tolerant control, and collision detection and avoidance. The work presented in this thesis builds on previous research projects done at Stellenbosch University which focussed on damaged aircraft and fault-tolerant flight control. Though no work has been done on autonomous landings of damaged unmanned aircraft, this previous research at Stellenbosch University acts as the framework for the research performed for this thesis.

The research into autonomous fixed-wing aircraft began when Peddle presented his study on *Autonomous Flight of a Model Aircraft* in 2005 [2]. In his research, the successful development of a conventional flight autopilot for a model aircraft was presented. A mathematical model for the aircraft was obtained as a function of the aircraft's physical properties. Control systems were

developed for conventional flight. A navigator was developed to enable the use of a path planner for waypoint navigation.

Following the success of Peddle's study, several research projects on autonomous take-off and landing of fixed-wing aircraft were conducted. Roos presented his thesis on the *Autonomous Take-Off and Landing of a Fixed-Wing UAV* [3]. In his thesis, the successful design and practical demonstration of flight and runway controllers required for the autonomous take-off and landing of a fixed-wing aircraft were presented. A nonlinear runway model and wind gust model were developed. The conventional flight controllers developed by Peddle were extended and improved to remove the single trim condition constraint. A de-crab controller was also designed, which allowed for cross wind landings. A landing state machine was designed to enable the UAV to execute the different stages of landing. Runway guidance controllers were also designed for taxiing the UAV on the runway. All of the controllers were successfully demonstrated with simulations and practical flight tests. The GPS position measurement used in his project was normal GPS accuracy, which limited the accuracy with which the aircraft could be landed, and meant that successful landing on a narrow runway or under severe wind conditions could not be guaranteed.

After Roos, achieving reliable and accurate landings became the new primary research objective at Stellenbosch University. Visser presented his thesis on *The Precision Landing of a UAV* in 2008 [4]. Visser made use of an infrared camera to obtain precision position measurements for the UAV when close to the runway. A monocular vision algorithm that used markers situated on the runway was developed to supply accurate position measurements upon the final approach of the landing.

After Visser, the focus changed from using a combination of sensors to determine the UAVs position upon approach to using a high-precision GPS. Smit presented his thesis on the *Autonomous Landing of a Fixed-Wing UAV Using DGPS* [5]. In his thesis, a high-precision differential GPS was used as an aid to landing a fixed-wing aircraft on a stationary platform. This study formed part of the ongoing research at Stellenbosch University to autonomously land a fixed-wing aircraft on a moving platform in adverse wind conditions. The practical results that were obtained verified that the aircraft was able to land within a circle with a radius of 7.5 m (with the target landing point at the centre of the circle).

In parallel with the ATOL research, a number of fault-tolerant control research projects for fixed-wing aircraft have been conducted. Blaaw presented his thesis on *Flight Control System for a Variable Stability Blended-Wing-Body UAV* [6]. In his thesis, the analysis, design, simulation and practical implementation of a novel control system for a variable stability blended-wing-body UAV was presented. The aircraft had a moveable centre of mass that allowed it to operate in an aerodynamically optimised minimum drag configuration during cruise flight. The primary purpose of the flight control system was to regain nominal static stability for all centre of mass positions. Blaaw showed that acceleration based control methodology developed by Peddle [7] can be used with minor modification to elegantly solve the variable stability control problem. Blaaw concluded with flight test results that the fixed-gain flight control system was capable of controlling the variable stability aircraft at centre of mass locations where a human pilot could not.

An alternative flight control system design approach was followed to solve the variable stability problem when Basson presented his thesis on *Fault-tolerant Adaptive Control of an UAV* in 2011 [8]. In his thesis, the development of an adaptive longitudinal control system for a UAV was

presented. The usefulness of fault-tolerant adaptive control was demonstrated by introducing a shift in the centre of mass (in the forward or backward direction), which was known to have a dramatic effect on the stability of a fixed-wing aircraft. Practical flight tests showed that the adaptive control system could re-stabilise an unstable aircraft without any knowledge of the change in the aircraft's dynamics. The research projects presented by Blaaw and Basson are of significant importance since the aircraft's centre of mass will shift when it suffers damage in this project.

Beeton presented his thesis on *Fault-tolerant Flight Control of a UAV with Asymmetrical Damage to its Primary Lifting Surfaces* [9]. In his thesis, the design, analysis, implementation and verification of a fault-tolerant flight control system were presented. A passive fixed-gain fault-tolerant approach was followed. A robust controller was implemented that was tolerant against the structural damage that causes asymmetrical flight dynamics. The goal was to keep flight stability after damage has occurred to the aircraft without any knowledge of the damage or when it occurred. The robustness and performance of the autopilot were verified with simulations and practical flight tests. A successful practical flight test was demonstrated with 20% semi-span wing loss. Beeton found that the partial wing loss damage case only had a significant effect on the trim of the aircraft, and no significant effect on its dynamics. The logical next step is therefore to design a fixed-gain (non-adaptive) flight control system that is robust to partial stabiliser loss. The horizontal stabiliser loss and vertical stabiliser loss damage cases are chosen because it results in significant changes to both the trim and the dynamics of the aircraft. The flight control laws will therefore have to be able to find the new trim and also be robust to the changes in the aircraft dynamics. Furthermore, Beeton stated in his recommendations that the safety pilot struggled to land the aircraft when it suffered from partial wing loss. This was mainly due to higher landing speeds and pilot induced oscillations in the roll dynamics when approaching the touchdown point.

By considering the abovementioned research, it is clear that the current research project builds on several research projects completed at Stellenbosch University and that further research is required to successfully complete this project. The direct line of the previous Stellenbosch University research leading to this project is as follows:

- Blaauw designed a fixed-gain flight control system with gain scheduling for a variable stability UAV (the flight control laws had explicit knowledge of the CM location).
- Basson designed an adaptive flight control system for a variable stability UAV (the flight control laws did not have explicitly knowledge of the CM location).
- Beeton designed a fixed-gain (non-adaptive) flight control system that was robust to partial wing loss. However, partial wing loss only had a significant effect on the trim of the aircraft, and no significant effect on its dynamics. Furthermore, the safety pilot found it difficult to land the aircraft when the aircraft suffered from partial wing loss.
- Smit designed a flight control system that was able to land a fixed-wing aircraft (a conventional undamaged aircraft) accurately on a stationary platform using a high-precision GPS. Practical flight test results showed that the flight control system was able to land the aircraft sufficiently accurate.

A research gap therefore exists to design a fixed-gain or adaptive flight control system that is robust to partial stabiliser loss. This damage case is chosen because it results in significant

changes to both the trim and the dynamics of the aircraft. Another research gap exists to design a flight control system capable of landing a fixed-wing aircraft that has suffered partial wing loss. Furthermore, the flight control system must find the new trim and be able to autonomously land the aircraft when it suffered partial wing loss. The flight control laws will therefore have to be able to find the new trim and also be robust to the changes in the aircraft dynamics when the aircraft suffers from partial wing loss and partial stabiliser losses.

1.3 Research Objectives

The primary research objective of this research project is to design and implement a fault-tolerant flight control system with the capability to land a fixed-wing unmanned aircraft that has suffered partial wing loss and partial stabiliser losses. The objective must be verified with high-fidelity simulations and practical flight tests. Achieving this objective will require an accurate aircraft model that includes the effects of partial wing loss and partial stabiliser losses. Obtaining an accurate aircraft model is key in investigating the stability of the aircraft as a function of the damage it has suffered. Valid flight equilibriums must be established to determine if the aircraft can be flown with the amount of damage it has suffered. The flight control system cannot be expected to successfully control an aircraft without an existing, valid flight equilibrium. A stability analysis must be conducted to see how the stability of the aircraft changes as a function of partial wing loss and partial stabiliser losses. When the behaviour of the damaged aircraft is fully understood, a fault-tolerant flight control system can be designed which is capable of landing an unmanned aircraft autonomously.

A secondary objective is to ensure that the autonomous landings for the undamaged aircraft are sufficiently accurate. Hence the performance of the undamaged aircraft must not be degraded to such an extent that the performance becomes unacceptable. Achieving this objective will require the trade-off between performance and robustness to be optimised.

1.4 Contributions

This research project made the following contributions:

- A dynamic nonlinear aircraft model was developed that accounted for partial wing loss, partial horizontal stabiliser loss, and partial vertical stabiliser loss. The model was validated by supplying the aircraft with elevator and rudder doublets during practical flight tests. The changes in the natural frequency and damping ratio of the short period mode and Dutch roll mode were observed during the doublets to verify that the changes correspond to that of the model.

- A fault-tolerant flight control system architecture was developed that is robust to 20% wing tip loss (semi-span), 70% horizontal stabiliser tip loss (semi-span), and 20% vertical stabiliser tip loss (span) while retaining the desired performance required of auto-landings. By utilising the prior knowledge of the aircraft dynamics for all the modelled damage cases, robust inner-loop controller gains were obtained using an algorithm. The robustness of the flight control system was verified during practical flight tests.

1.5 Project Overview

In this section, a brief overview of the project execution is provided. The test aircraft and the avionics are described to give the reader a better understanding of the aircraft and test setup used throughout this thesis, as the basis for the modelling, stability analysis, and control system design.

1.5.1 Overview

This research project uses the following methodology: first an aircraft model that accounts for partial wing loss and stabiliser losses is developed. The model is then used to do a stability analysis of the aircraft as a function of the percentage of wing loss, the percentage of horizontal stabiliser loss, and the percentage of vertical stabiliser loss respectively. Following the stability analysis, a fault-tolerant flight control system to autonomously land the unmanned aircraft that suffered partial wing loss, partial horizontal stabiliser loss, and partial vertical stabiliser loss is developed. A landing strategy and landing state machine are then developed to guide the unmanned aircraft to the touchdown point and then to standstill. The flight control system is thoroughly tested with a high-fidelity simulation environment and with practical flight tests. If the flight control system does not perform as required, changes are made and the flight control system is tested again.

1.5.2 Test Aircraft and Avionics

The test aircraft that is used for the practical flight tests is a Phoenix Trainer 60 aircraft, as seen in Figure 1.2. This is the standard aircraft used at Stellenbosch University and multiple projects have been completed on it [5], [9], [10]. The aircraft is a trainer aircraft and therefore has good

Figure 1.2: Test aircraft: Phoenix trainer 60 modified to represent partial wing loss, partial horizontal stabiliser loss, and partial vertical stabiliser loss

handling qualities, making it easier to control for research purposes. Table 1.1 provides some of the aircraft's specifications. A more detailed description of the test aircraft is given in Appendix B for the readers perusal.

Table 1.1: Test aircraft specifications

Parameter	Value	Unit
Wing span	1.918	m
Mass (Total)	7.71	kg
Max thrust	48	N

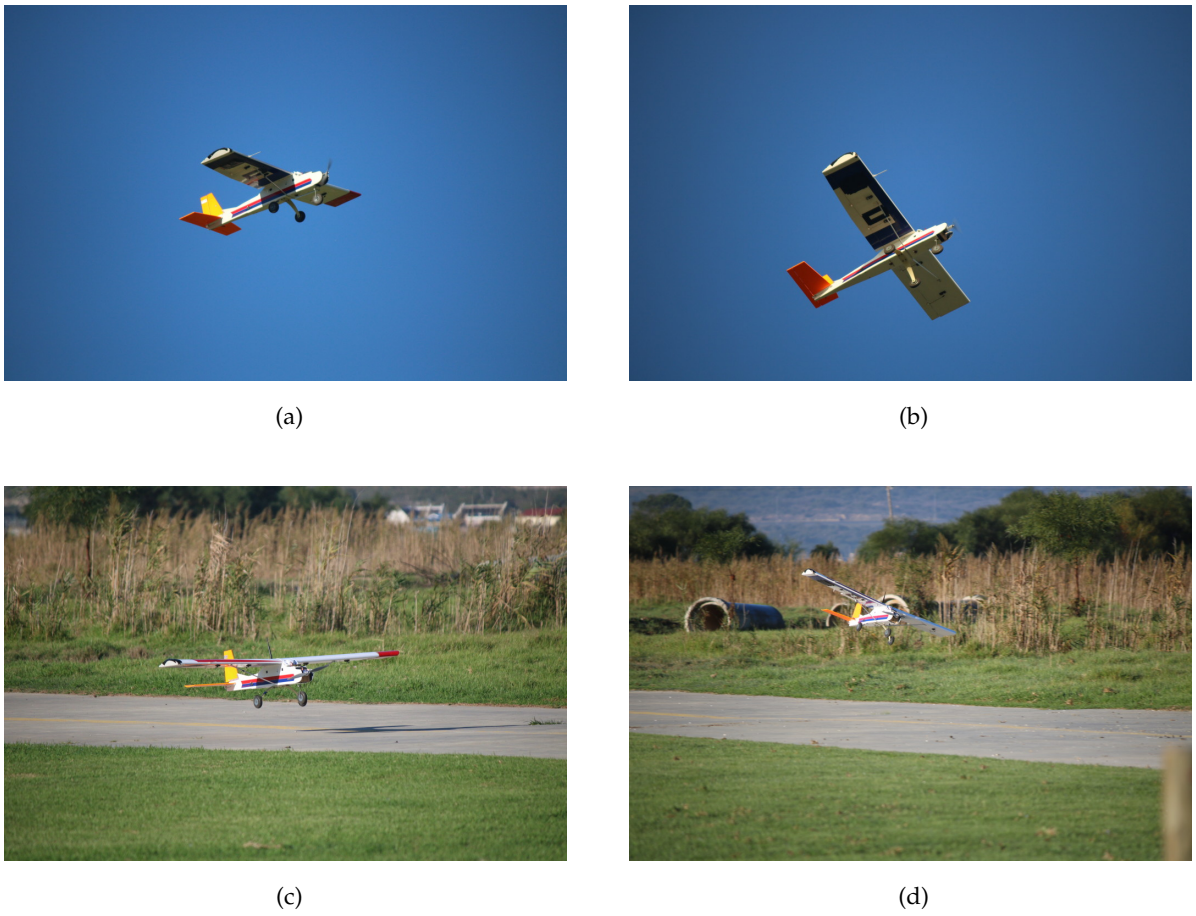

(a) (b)

(c) (d)

Figure 1.3: Photos of test aircraft during flight tests: (a) and (b) shows the undamaged and damaged aircraft in flight and (c) and (d) shows the undamaged and damaged aircraft attempting to land. In all of the above images, the safety pilot is in control of the aircraft

Figure 1.4 shows the flight test setup in diagram form. The principal moments of inertia and centre of mass location are stated as determined by Smit through several tests [5]. The mass stated in Table 1.1 is the total aircraft mass, which includes the airframe (with the tip loss modifications), the avionics, the actuators and the masses of the batteries. Due to all the modifications done to the aircraft, the mass increased significantly and turned out to be higher than desired. The aircraft would therefore have to fly at a higher cruise and touchdown airspeed than initially desired. The safety pilot performed an RC flight, whereby he recommended a suitable cruise airspeed for the particular aircraft. The aircraft is modified to represent partial wing tip loss, partial horizontal stabiliser tip loss, and vertical stabiliser tip loss (see Figure 1.3). Each of the aforementioned tips is attached to the airframe with a spring-loaded release mechanism that can be triggered from the RC remote. The wing is modified with a 20% semi-span tip loss, the horizontal stabiliser with

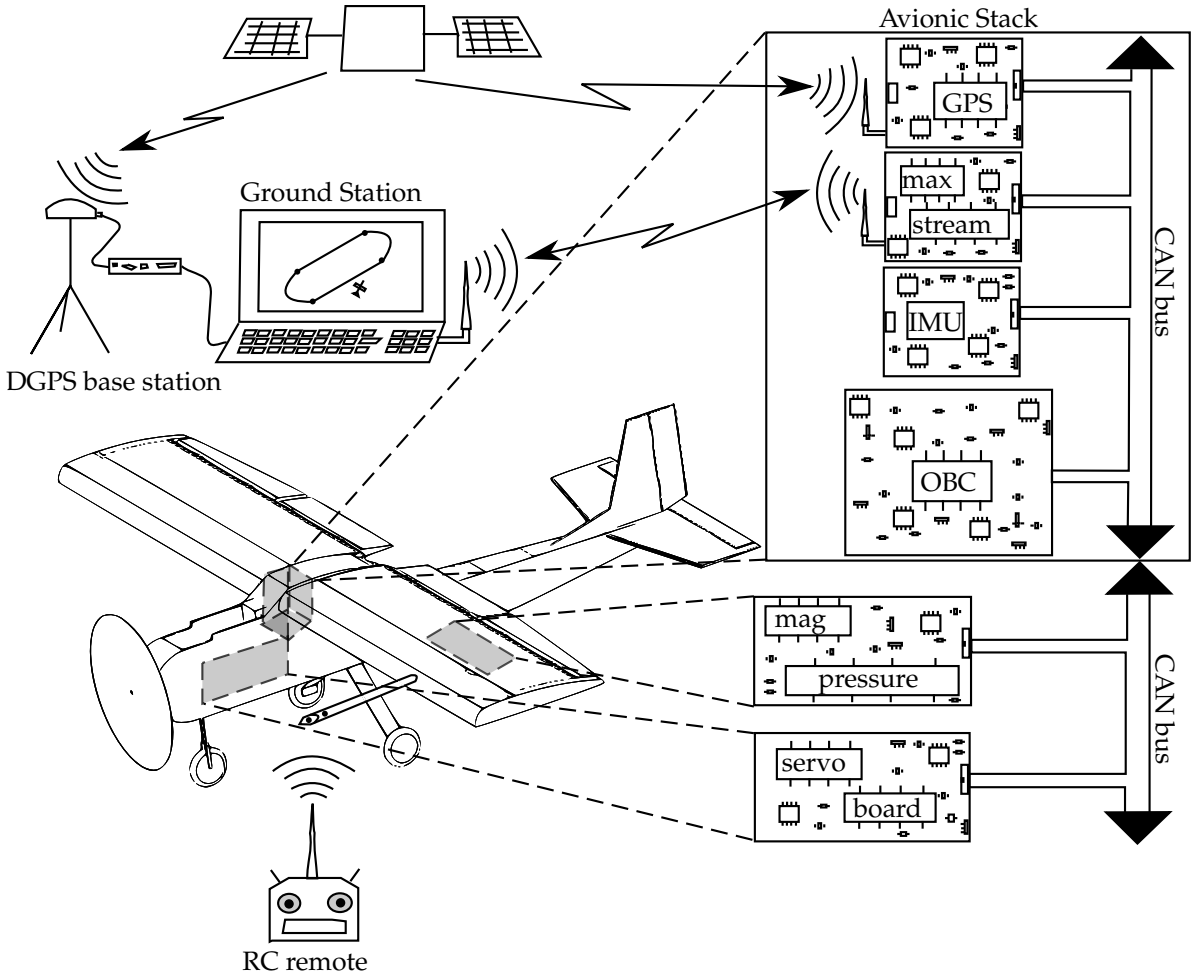

Figure 1.4: Block diagram of the practical flight test setup

a 70% semi-span tip loss and the vertical stabiliser with a 20% span tip loss. The wing release mechanism was developed by Beeton [9] and the stabiliser release mechanisms by Maggot [11]. The aircraft is equipped with in-house designed avionics which have been refined over the years.

The avionics consists of an on-board computer, a DGPS receiver, a six-degree-of-freedom (6DoF) IMU, a wireless transmitter and receiver, a magnetometer, an air pressure sensor and a servo board. All of the aforementioned components communicate with the on-board computer via a CAN bus. The aircraft communicates with a ground control station (GCS) through a wireless communication link. Telemetry data is sent down to the GCS at a fixed rate, which allows the GCS operator to monitor the aircraft's states and modes at all times. The GCS consists of a computer running the GCS software, a wireless RF link to communicate with the aircraft, and the DGPS base station unit. During flight tests the GCS operator can send control commands to the aircraft. Different controllers can be armed and disarmed depending on the requirements of the test. Furthermore, real time kinematic (RTK) correction packets are sent to the aircraft for DGPS purposes.

A DGPS is used to obtain an accurate position of the aircraft, which is required for accurate automatic landings. Previous projects have been conducted at Stellenbosch University, where computer vision techniques and ultrasonic sensors were used to obtain a better estimate of the aircraft's position relative to the runway for landing purposes [4]. With DGPS, this is not necessary

due to the high position accuracies that can be obtained. Through a conversion (standard GPS output to inertial reference frame), the DGPS supplies the on-board computer with the aircraft's inertial North-East-Down position (NED) and ground speed ($\dot{N}\dot{E}\dot{D}$). The 6DoF IMU supplies the aircraft with body reference frame angular rates ($P_B Q_B R_B$) and accelerations ($\dot{U}_B \dot{V}_B \dot{W}_B$), and a magnetometer supplies the aircraft with the magnetic field vector also in the body reference frame. A kinematic state estimator estimates the aircraft's attitude, ground speed and position by propagating a kinematic dynamic model based on the IMU measurements, and correcting the propagated states using the DGPS and magnetometer. The kinematic state estimator is an extended Kalman filter with states,

$$\hat{\mathbf{x}} = \begin{bmatrix} \hat{N} & \hat{E} & \hat{D} & \hat{\dot{N}} & \hat{\dot{E}} & \hat{\dot{D}} & \hat{\Phi} & \hat{\Theta} & \hat{\Psi} \end{bmatrix}^T \tag{1.5.1}$$

where $\hat{N}$, $\hat{E}$, $\hat{D}$ and $\hat{\dot{N}}$, $\hat{\dot{E}}$, $\hat{\dot{D}}$ are the position and ground velocity estimates of the aircraft in the inertial reference frame and $\hat{\Phi}$, $\hat{\Theta}$, $\hat{\Psi}$ are the attitude estimates of the aircraft. A pressure sensor, which is used to measure both the pitot and static pressure, is used to obtain the dynamic pressure and thus the airspeed $\bar{V}$ of the aircraft.

Initially, before the autopilot is armed, the aircraft is controlled by a safety pilot via the RC remote. The RC remote transmits to an RC receiver, which is connected to the servo board on the aircraft. All of the control surfaces are controlled with servo motors that are commanded by the servo board. When operating in autopilot mode, the control commands are sent from the on-board computer via the CAN bus to the servo board, which in turn commands the servo motors to the desired positions. The safety pilot has the authority to take control of the aircraft, bypassing the autopilot when he deems it necessary.

The aircraft avionics hardware have been refined over the years and are used mostly unchanged. For more detailed information about the avionics, see [4], [5], [9], [8], and [10]. The sensors were all recalibrated and modifications were made to permit for the tip loss modifications. An additional battery voltage sensor was developed and integrated with the existing avionics to measure the motor battery voltage. Previously the flight durations were timed (with a watch) to determine when the motor battery's voltage level is low and the aircraft should be landed. Additional missing features were added to the ground control station. A notable feature that was added was an active map interface where waypoints can be added and the location of the aircraft can be viewed.

1.6 Thesis Outline

This thesis is partitioned into nine chapters, as shown in Figure 1.5. Chapter 1 provided an introduction to the thesis. In Chapter 2, a brief literature review will be presented. This includes research done outside of Stellenbosch University in order to obtain a wider perspective and greater knowledge of the research field.

In Chapter 3, a mathematical aircraft model that accounts for partial wing loss and stabiliser losses is developed. This model is required for stability analysis, control system design and nonlinear simulations. Applicable aircraft notations and definitions required for the modelling of the aircraft dynamics are described, and the 6DoF equations of motion model is developed that allows for a shift in the centre of mass. The forces and moments acting on the aircraft for a number of damage cases are modelled and investigated.

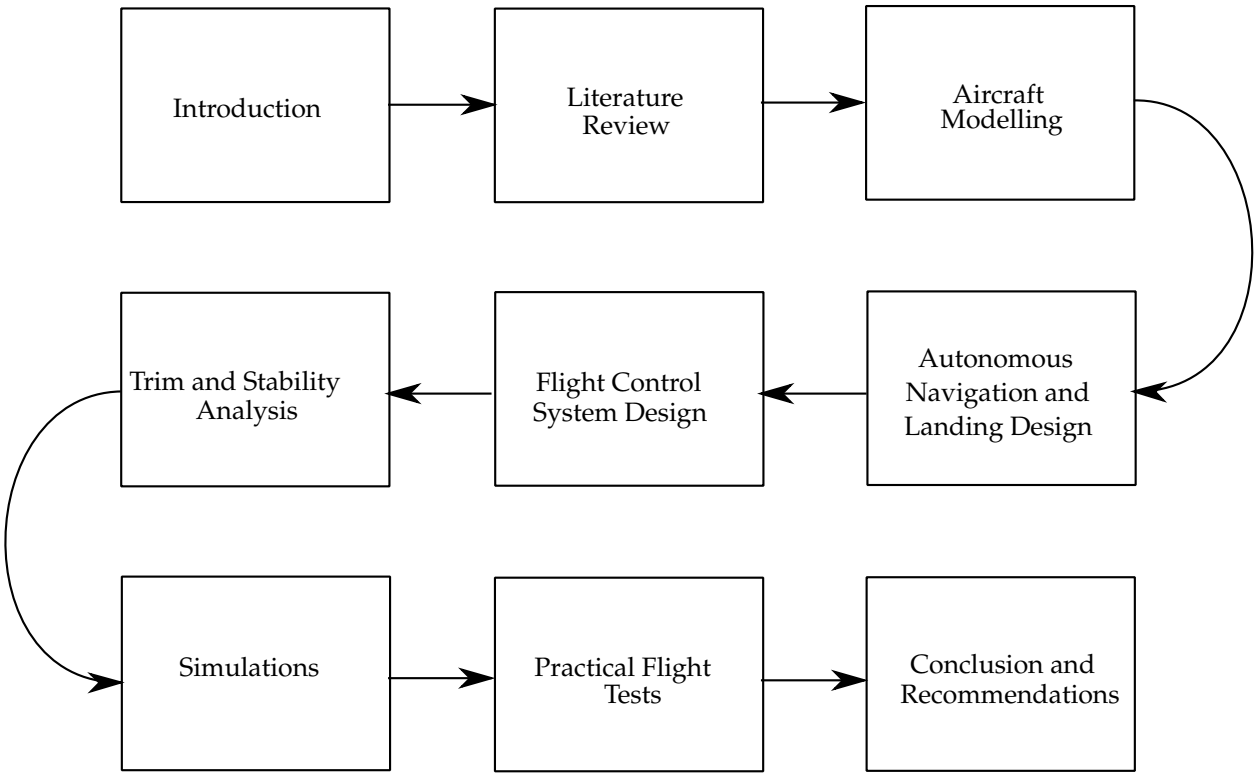

Figure 1.5: Outline of this thesis

Chapter 4 addresses aircraft stability analysis. A static stability analysis is conducted, followed by a dynamic stability analysis. The latter entails finding valid flight equilibriums and linearising the nonlinear aircraft dynamics about the obtained flight equilibriums. The aircraft's natural modes of motion are then investigated as a function of the percentage of wing loss, horizontal stabiliser loss, and vertical stabiliser loss inflicted on the aircraft respectively.

In Chapter 5, the fault-tolerant flight control system is designed to autonomously land the fixed-wing unmanned aircraft that has suffered partial wing loss and stabiliser losses. A linear approach to control system design is adopted. The flight control system architecture and the approach to achieving robustness are described. The controllers are then systematically designed and their performance and robustness are verified.

Chapter 6 describes the navigation and landing strategies that are adopted to allow the aircraft to successfully perform autonomous landings. A navigation strategy which is capable of quickly aligning the aircraft with the runway is described. The landing strategy, containing the procedures followed during the landing, is presented. Furthermore, a state machine that guides the aircraft through the different states during the autonomous flight and landing is developed. Several navigation and landing limitations and constraints are discussed throughout this chapter.

Chapter 7 and 8 discuss the simulation and practical flight test results respectively. The performance and robustness of the flight control system developed in Chapter 5 are verified with a high-fidelity simulation environment and with practical flight tests.

The concluding chapter presents a summary of the research and the results obtained in this thesis. Recommendations for further research and improving the current research are also presented.

In this chapter, a brief review of the existing literature is provided. The literature review starts by providing literature on fault-tolerant control systems, then modelling of damaged aircraft, and finally the auto-landing of fixed-wing aircraft. By presenting a literature review of related work, an approach to the research problem in this project can be identified. Although some research papers on modelling and designing flight control systems for damaged aircraft were found, very little research has been done on the autonomous landing of damaged fixed-wing aircraft. The literature review was therefore presented on fault-tolerant control for damaged aircraft, the modelling of damaged asymmetrical aircraft, and the auto-landing of fixed-wing aircraft.

2.1 Fault-tolerant Control Systems

Fault-tolerant control systems can be classified into two categories, namely passive and active fault-tolerant control. For a passive fault-tolerant control system, deviations of the UAV's plant parameters from their true values may be efficiently compensated for by using a fixed robust feedback controller to ensure the stability of the UAV. If these deviations from the UAV's plant parameters become excessively large, the robust feedback controller might not be able to keep the UAV stable. An active fault-tolerant controller is then needed to extend the fault-tolerant capabilities [1]. An active fault-tolerant controller contains a fault detection and isolation (FDI) system. The FDI system monitors the UAV for any faults or failures that may occur, and informs a reconfiguration mechanism (RM) module about the seriousness of the faults [1]. One of the main disadvantages of active fault-tolerant control in UAVs is that it is much more difficult to obtain airworthiness certification for adaptive controllers than for fixed-gain robust controllers.

2.1.1 Fault-tolerant Control for Damaged Aircraft

Chowdhary et al. presented a paper on *Autonomous Guidance and Control of Airplanes Under Actuator Failures and Severe Structural Damage* [12], in which they described outer-loop guidance and inner-loop attitude control algorithms that ensure safe waypoint navigation for a twin-engine aircraft in the presence of severe structural damage or actuator damage. A combination of passive and active control systems were utilised. The inner-loop attitude controller could either be a PID controller or a model reference adaptive controller. They concluded that the results indicated the possibility of using the presented autonomous flight control methods for ensuring safe flight, and in some cases safe automated landings, for aircraft with severe structural damage.

Arruda presented a masters thesis on *Dynamic Inverse Resilient Control (DIRC) for Damaged Asymmetrical Aircraft* [13]. The DIRC consists of an inverse controller with decoupled flight controls and an adaptive system to correct the command signals for the damaged aircraft. The flight

control system was tested in simulation, and the author concluded that, with wing tip loss, the DIRC could recover the aircraft. The limit of the amount of wing tip loss, however, depended on the available control authority which is needed to counter the asymmetric moments.

Nguyen et al. presented a paper on *Adaptive Control for Stability Recovery of Damaged Asymmetrical Aircraft* [14]. A hybrid direct-indirect neural network, adaptive flight control was proposed as an adaptive law for stabilising the rotational motion of the damaged aircraft. Simulation results showed the effectiveness of the proposed hybrid approach under wing and horizontal stabiliser damage.

Zhao et al. presented a paper on *Fault-tolerant Control for Damaged Aircraft Based on Sliding Mode Control Scheme* [15]. In their paper, a damage-tolerant controller based on an adaptive sliding mode control was proposed which can accommodate vertical stabiliser damage. Simulations were conducted to demonstrate the effectiveness and advantages of the proposed design techniques.

Hitachi presented his masters thesis on *Damage-tolerant Flight Control System Design for Propulsion-controlled Aircraft (PCA)* [16]. A robust PCA control system design using H_∞-based robust control was proposed. The controllers were tested with both linear and nonlinear simulation environments. The results demonstrated the advantages of the robust flight control architecture over the existing optimal controller in dealing with model deviations due to structural damage.

It is clear that adaptive control is the main focus in the literature for flight control systems of damaged aircraft. Furthermore, asymmetric damage, which includes damage to the wings or horizontal stabiliser, is emphasised. Asymmetrical damage is found to severely degrade aircraft handling qualities and will therefore further complicate landings.

2.1.2 Fault-tolerant Control for Model Uncertainties

Several papers on fault-tolerant control that do not necessarily address structural damage were also found.

Kada presented a paper on *Robust PID Controller Design for a UAV Flight Control System* [17]. The paper describes the architecture and design aspects of a robust PID controller for higher-order systems. A robust deadbeat system was successfully implemented and simulation results showed that impressive time-domain performances and robustness were achieved in the presence of modelling uncertainties. Furthermore, the architecture also provided an efficient and practical way to do real-time PID parameter tuning. Standard P, PI, and PID controllers are more intuitive to tune than full state feedback controllers such as LQR controllers.

Sadraey et al. presented a paper on *Robust Nonlinear Controller Design for a Complete UAV Mission* by using a combination of dynamic inversion and H_∞ control [18]. The robust flight control system did not explicitly accommodate structural damage, but the uncertainties considered included uncertainties in stability derivatives, mass, centre of mass location, and airspeed variations. These parameter uncertainties coincides with the expected aircraft parameter changes when the aircraft suffers partial wing loss, partial horizontal stabiliser loss, and partial vertical stabiliser loss.

Prach presented a masters thesis on *Robust Controller Design for Fixed-wing Aircraft* [19]. Two different control design strategies were presented and compared. The first used standard PID controllers and the second robust H_∞ controllers. Comparisons were conducted under model

uncertainties and sensor noise. Prach found that the two flight control systems performed equally well and both achieved the robustness that was required.

2.2 Damaged Asymmetrical Aircraft

Before a flight control system can be developed for an aircraft, the aircraft's dynamics must first be modelled and understood. The standard conventional symmetrical aircraft equations of motion fail to properly reflect the underlying physics of damaged asymmetrical aircraft. In order to analyse the dynamics of damaged aircraft, the dynamic equations of motion must be derived again from first principles to properly capture the underlying physics. One of the most commonly used approaches in the literature is to develop flight dynamics equations of motion for an aircraft which is not necessarily referenced to the aircraft's centre of mass. Such equations can be used when the aircraft loses a portion of its mass and it is desired to track the motion of the aircraft's previous centre of mass now that the centre of mass has moved to a new position [20]. Bacon et al. describes such flight dynamics equations of motion. In the equations of motion developed by Bacon, additional gravitational forces and moment are also introduced. Developing the flight dynamics equations of motion that can model both the flight dynamics of a conventional symmetrical aircraft as well as an unconventional asymmetrical aircraft is critical for this project.

A number of methods exist to determine the aerodynamic stability and control derivative of an airframe. Notable methods are deriving the derivatives from first principles based on empirical data, basic vortex lattice software, high-fidelity computational fluid dynamics, wind tunnel tests and system identification on practical flight test data. Each method has its advantages and disadvantages and therefore the best results will be obtained if a combination of the methods is used. The most common methods used in the literature are obtaining the derivatives from wind tunnel data, empirical data and vortex lattice software.

Shah presented a paper on *The Aerodynamic Effects and Modelling of Damage to Transport Aircraft* [21]. A wind tunnel investigation was conducted to measure the aerodynamic effects of damage on the lifting and stability/control surfaces of a commercial transport aircraft configuration. He found that many assumptions of symmetry may no longer be valid and that new aerodynamic contributions will need to be modelled. The following effects of aircraft asymmetry were highlighted by Shah and should be considered:

- A rolling moment and yawing moment resulting from an angle of attack perturbation.
- A rolling moment due to an asymmetrical elevator deflection may require modelling of individual left and right stabiliser/elevator characteristics instead of as a combined surface.
- A rolling moment resulting from a pitch rate due to asymmetrical damping contribution.
- General aerodynamic characteristics in all axes may be non-symmetric with sideslip.
- A rolling moment resulting from a pitch rate due to asymmetrical normal force damping.
- Due to asymmetrical lift from the wings, roll damping will no longer be symmetric with roll rates - damping from positive and negative roll rates will not be the same.

Shah also investigated the safe landing angle of attack envelope of an aircraft with wing damage. Figure 2.1 shows the angle of attack required to safely land in the presence of wing damage. The figure shows the angle of attack required by the damaged aircraft to achieve the same landing speed as an undamaged aircraft in a no-flap condition. Although it may be possible to stabilise and control a damaged aircraft at higher speeds in cruise flight, it may not be possible to slow down the aircraft sufficiently while maintaining control to allow for a safe landing. The safe landing region can be expanded by increasing the available roll control authority (e.g., spoilers, differential flaps or slats) or by flying at greater sideslip angles, and/or by using high-lift systems (e.g. flaps). It is clear that the amount of partial wing loss that can be accommodated by the flight control system is more constrained by the landing phase than by the cruise flight phase.

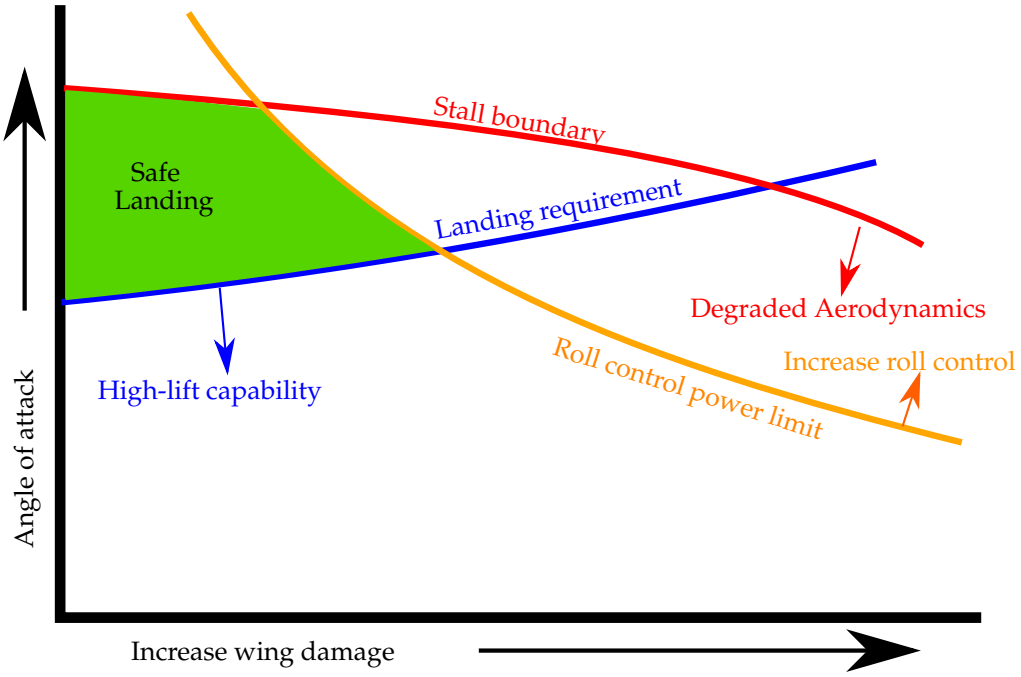

Figure 2.1: Landing angle of attack envelope and restrictions for wing damage [21]. By using high-lift capabilities and increasing the roll control, the safe landing region can be increased

Ouellette et al. presented a paper on *Flight Dynamics and Structural Load Distribution for a Damaged Aircraft* [22]. In this paper, the coupling between the longitudinal and lateral aerodynamic forces was investigated. The aerodynamic coefficients were calculated using Athena Vortex Lattice (AVL), which accounted for non-linearities and couplings. Since the damage considered was only on the lifting surfaces, AVL was able to account for the effects of the damage on the aerodynamics due to the asymmetry of the drag distribution. The changes in the mass distribution, the centre of mass, and the inertia matrix were all taken into account. The flight dynamics model was used to analyse the nonlinear response, the linear stability and the flight loads for a specific aircraft. However, they found that for larger damage cases (greater than 26% wing damage), it was not possible to trim the specific aircraft for straight and level flight.

Cheng et al. presented a paper on *An Approach to Calculating the Flight Trim for Wing-damaged Symmetrical Aircraft* [23]. A numerical method using multidimensional Newton iteration was developed to obtain the fixed points of the nonlinear force and moment equations for trim.

2.3 Fixed-wing Aircraft Auto-landing

Since very little research has been done on the autonomous landing of damaged aircraft, this section provides an overview of previous research on the autonomous landing of healthy, undamaged aircraft. Alberts, a previous student in the Electronic Systems Laboratory at Stellenbosch University, presented his masters thesis on *The Accurate Autonomous Landing of a Fixed-wing UAV* [10]. His thesis presented the analysis, design, simulation and practical implementation of a flight control system for accurate autonomous landing in the presence of wind gust disturbances. Alberts included the concept of direct-lift control that uses the flaps to achieved more accurate longitudinal landing precision. Practical flight test results showed that better accuracy could be obtained by using direct-lift control, especially under greater wind disturbances.

Kargin presented his masters thesis on *The Design of an Autonomous Landing Control Algorithm for a Fixed-wing UAV* [24]. In his thesis the design and development of automatic flight strategies for the autonomous landing of a fixed-wing UAV subjected to severe environmental conditions were presented. The controllers used a model inversion approach based on the dynamic model. Feed-forward and mixing terms were added to improve the performance of the controllers. Simulations were performed for landing under cross wind, head wind, tail wind, wind shear and turbulence conditions. Simulation results demonstrated that the UAV was able to land in all of the aforementioned adverse weather conditions and was able to adequately follow the longitudinal and lateral position commands as well as the descent rate, yaw angle, roll angle and forward velocity commands.

Kurnaz presented a paper on *The Autonomous Navigation and Landing Tasks for Fixed-wing Small UAVs* [25]. Fuzzy logic based autonomous flight and landing system controllers were proposed. Three fuzzy logic modules were developed under the main navigation control system, and three more for the autonomous landing control system, to control the altitude, the airspeed, and the cross track position error to align with the runway. Kurnaz concluded that despite the simple design procedure, the simulated test flights indicated the capability of the approach to achieve the desired performance.

Li et al. presented a paper on *Robust Neuro-H_∞ Controller Design for Aircraft Auto-landing* [26]. They developed a robust neuro-control scheme for aircraft auto-landing under severe wind conditions and partial loss of control surfaces. The performance of this neuro-controller for aircraft auto-landing in severe wind shear along with a partial loss of control effectiveness was analysed and compared to other control schemes. Their simulation results showed that the performance obtained by the neuro-H_∞ control scheme was better than that of other control schemes under failure and extreme wind conditions. However, , the authors cautioned that there is no theoretical guarantee regarding stability and convergence for the neuro-H_∞ control strategy, and that a minimal resource allocating network aided PID controller may still be a better choice for the engineer if the tracking accuracy is not a very important requirement.

2.4 Summary

The literature survey revealed that the two most common approaches to designing damage-tolerant flight control systems are adaptive control and robust control. Robust flight control systems guar-

antee aircraft stability and even a minimum aircraft performance over a given range of parameter variations using fixed-gain control laws. Adaptive flight control laws change the flight control laws to adapt to the changes in the aircraft dynamics resulting from the damage suffered. Physical limitations will establish the maximum controllable damage that an aircraft can suffer. Thereafter, even with a perfect adaptive flight control system or the prior knowledge of the damage the aircraft suffered, neither flight control system configurations will be able to stabilise the aircraft. However, since it is much more difficult to obtain airworthiness certification for adaptive controllers than for fixed-gain robust controllers, it was decided to pursue a robust control approach in this project.

The literature survey also provided a good overview of the approaches used to model aircraft with asymmetrical damage. For this project, it was decided to use the asymmetrical six-degrees-of-freedom equations of motion derived by Bacon [20], to model the changes to the mass, moment of inertia and centre of gravity location with CAD software, and to model the effects of the damage on the aerodynamic stability and control derivatives using the Athena Vortex Lattice software.

The literature survey also highlighted that the landing phase places more severe constraints on the amount of partial wing loss and partial stabiliser loss that can be accommodated by the flight control system than the cruise flight phase.

Since very little research has been done on the autonomous landing of damaged aircraft, the literature review instead provided an overview of previous research on the autonomous landing of healthy, undamaged aircraft. Given the available approaches, it was decided to follow a state-machine based approach to executing the autonomous landing.

Before a stability analysis can be done and the flight control system can be designed, an aircraft model that incorporates the effects of partial wing loss and partial stabiliser losses must be developed. In this chapter, a mathematical aircraft model is developed that will be used for the stability analyses, flight control system design and for simulation purposes. The applicable aircraft notations and definitions required for the modelling process are introduced. The dynamic aircraft model which describes the behaviour of a conventional symmetrical aircraft and an unconventional asymmetrical aircraft is based on an asymmetric, six-degrees-of-freedom equations of motion model. The effects of the partial wing loss and stabiliser losses on the aerodynamic coefficients, mass, centre of mass location, and moments of inertia are calculated as a function of percentage of wing loss, percentage of horizontal stabiliser loss, and percentage of vertical stabiliser loss using vortex lattice techniques and computer-assisted design software respectively. The model also accounts for changes in the aileron, rudder, and elevator control authorities due to partial control surface losses.

3.1 Reference Frame Definitions and Notations

In this section, the reference frames and the standard aircraft notation used throughout this thesis are introduced. These reference frames and notation are used for the mathematical modelling of the aircraft and the control system design. The reference frames include the inertial, body, wind and stability reference frames.

3.1.1 Inertial Reference Frame

The standard North-East-Down (NED) reference frame shown in Figure 3.1 is used as the inertial reference frame. The NED reference frame assumes a flat earth with a non-rotating axis. The centre of the reference frame is chosen to coincide with some convenient reference point on the earth's surface, like the centre of the runway. The X_E-axis points in the north direction, the Y_E-axis points in the east direction and the Z_E-axis points down perpendicular to the local horizontal plane, which completes the right-handed orthogonal axis system. For short range UAV applications as presented in this thesis, the NED axis system is an adequate approximation for a local inertial reference frame.

3.1.2 Body Reference Frame and Aircraft Notations

The second reference frame defined is the body reference frame. The body reference frame shown in Figure 3.2 is a Cartesian coordinate system which is free to rotate and is fixed to the aircraft's

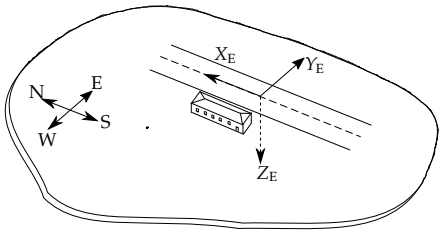

Figure 3.1: Inertial reference frame: Standard North-East-Down reference frame that assumes a flat earth with a non-rotating axis

body, with the origin chosen at some convenient point, e.g. the centre of mass. The X_B-axis points forward through the nose of the aircraft, and the Y_B-axis points through the right wing orthogonal to the X_B-axis. The Z_B-axis points downwards relative to the aircraft's cockpit to complete the right-handed orthogonal axis system. Note that the subscript B denotes body reference frame.

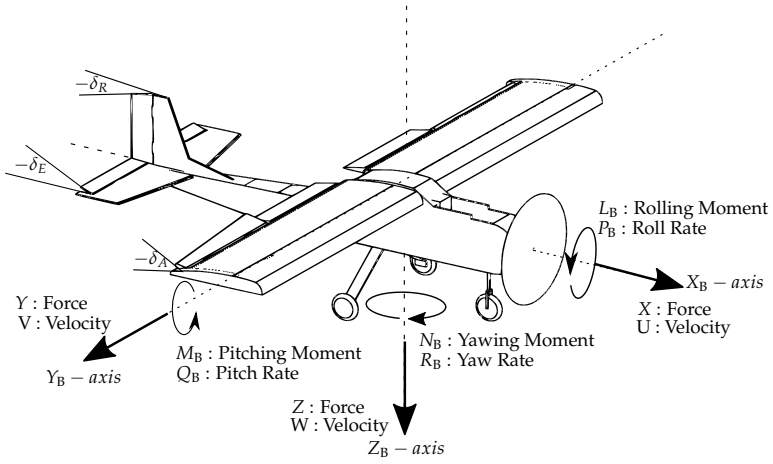

Figure 3.2: Aircraft body reference frame with standard aircraft notation

The aircraft has a velocity U and force X in the direction of the X_B-axis with a rolling moment L_B and roll rate P_B about the X_B-axis; a velocity V and force Y in the direction of the Y_B-axis with a pitching moment M_B and pitch rate Q_B about the Y_B-axis; and a velocity W and force Z in the direction of the Z_B-axis with a yawing moment N_B and yaw rate R_B about the Z_B-axis. The deflection angles of the control surfaces are denoted as δ_A, δ_E, and δ_R and are the aileron, elevator, and rudder control surface deflections respectively. Note that a negative $\delta_{(\bullet)}$ induces a positive moment about an axis, e.g. a negative δ_E induces a positive pitching moment about the Y_B-axis.

3.1.3 Wind and Stability Reference Frame

The final reference frames to be introduced are the wind and stability reference frames. The wind reference frame is similar to the body reference frame, except that its x-axis points in the direction of the aircraft velocity vector instead of through the aircraft's nose. The aircraft's velocity vector can be expressed in spherical coordinates using a magnitude and two angles, as shown in Figure 3.3. The origin of the wind reference frame coincides with the centre of mass of the aircraft. The X_W-axis points in the direction of the aircraft velocity vector and coincides with the direction of travel of the aircraft. The Z_W-axis lies in the aircraft's plane of symmetry, is perpendicular to

the X_W-axis and points downward relative to the cockpit. The Y_W-axis completes the right hand orthogonal axis system. The velocity magnitude $\bar{V}$ is also known as the airspeed of the aircraft. Airspeed is commonly used when modelling the aerodynamic forces and moments of an aircraft. Note that the airspeed of the aircraft will not necessarily be equal to the ground speed of the aircraft ($\alpha \neq \theta$).

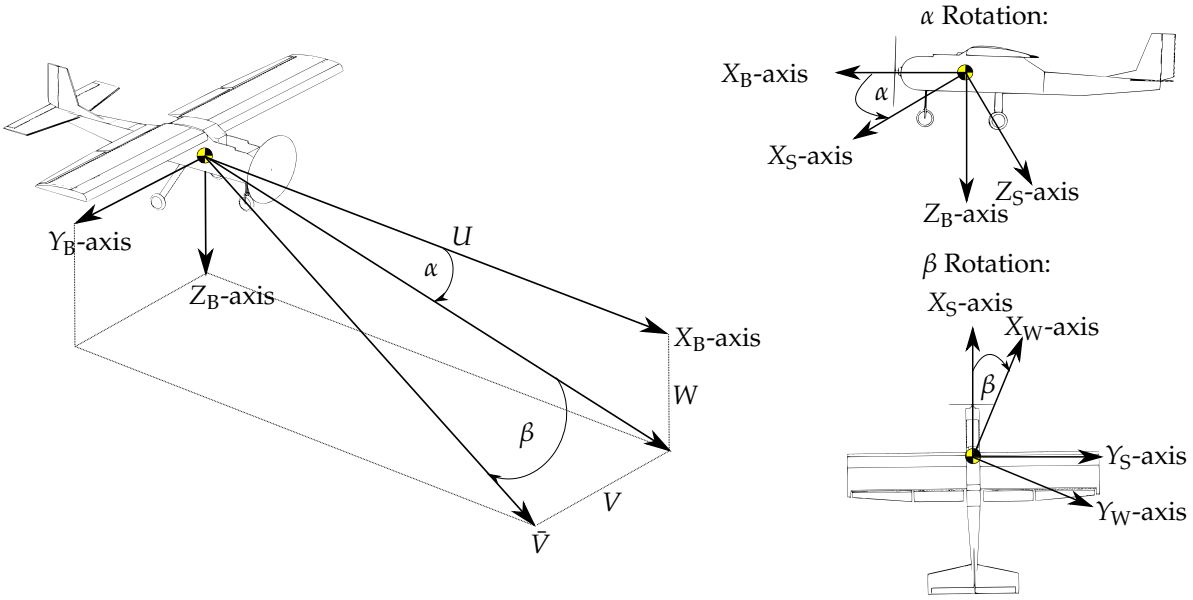

Figure 3.3: Spherical velocity coordinates

The velocity magnitude $\bar{V}$, angle of attack α and sideslip angle β are defined in Spherical coordinates in terms of the body reference frame velocities, with $\bar{V}$ in the direction of travel. Where $\bar{V}$, α, and β are expressed as

$$\bar{V} = \sqrt{U^2 + V^2 + W^2} \tag{3.1.1}$$

$$\alpha = \tan^{-1}\left(\frac{W}{U}\right) \tag{3.1.2}$$

$$\beta = \sin^{-1}\left(\frac{V}{\bar{V}}\right) \tag{3.1.3}$$

The stability reference frame is similar to the wind reference frame, except that there is no sideslip angle rotation. The stability reference frame is an important reference frame because an aircraft's aerodynamic forces and moments are commonly modelled in the stability reference frame. A transformation matrix to relate a three-dimensional vector in the body reference frame to a three-dimensional vector in the wind reference frame is obtained by rotating the body reference frame through α, which will result in the stability reference frame, and then rotating the stability reference frame through β, which results in the wind reference frame, as shown in Figure 3.3. Given a three-dimensional vector $\mathbf{h}_B$ in the body reference frame, when rotated through α, one can show through geometry that the vector $\mathbf{h}_S$ in the stability reference frame is related to the

vector $\mathbf{h}_B$ in the body reference frame through the rotation matrix in (3.1.4).

$$\mathbf{h}_S = \begin{bmatrix} \cos\alpha & 0 & \sin\alpha \\ 0 & 1 & 0 \\ -\sin\alpha & 0 & \cos\alpha \end{bmatrix} \mathbf{h}_B \tag{3.1.4}$$

$$\mathbf{h}_S = \mathbf{R}_\alpha \mathbf{h}_B \tag{3.1.5}$$

The rotation matrix in (3.1.4) allows one to relate a vector in the body reference frame to a vector in the stability reference frame. To obtain the transformation matrix to relate a vector in the body reference frame to a vector in the wind reference frame, a rotation of the stability reference frame through β is also required. The two rotation matrices can then be multiplied to obtain the $DCM_{B\to W}$ in (3.1.8), which relates a vector in the body reference frame to a vector in the wind reference frame.

$$\mathbf{h}_W = \begin{bmatrix} \cos\beta & \sin\beta & 0 \\ -\sin\beta & \cos\beta & 0 \\ 0 & 0 & 1 \end{bmatrix} \mathbf{R}_\alpha \mathbf{h}_B \tag{3.1.6}$$

$$\mathbf{h}_W = \mathbf{R}_\beta \mathbf{R}_\alpha \mathbf{h}_B \tag{3.1.7}$$

$$\mathbf{R}_\beta \mathbf{R}_\alpha = DCM_{B\to W} = \begin{bmatrix} \cos\alpha\cos\beta & \sin\beta & \sin\alpha\cos\beta \\ -\cos\alpha\sin\beta & \cos\beta & -\sin\alpha\sin\beta \\ -\sin\alpha & 0 & \cos\alpha \end{bmatrix} \tag{3.1.8}$$

A transformation matrix to relate a vector in the wind reference frame to a vector in the body reference frame is obtained by taking the inverse of the body to wind transformation matrix, as shown in (3.1.9). Similarly, the rotation matrix from (3.1.4) is inverted to relate a vector from the stability reference frame to a vector in the body reference frame.

$$DCM_{W\to B} = (DCM_{B\to W})^{-1} \tag{3.1.9}$$

3.2 Equations of Motion

There are several approaches that can be followed to describe the general equations of motion for an aircraft. In this thesis the approach described by Bacon et al. is used as the basis for developing the equations of motion [20]. The equations of motion will not necessarily be referenced to the aircraft's centre of mass, but to an arbitrary fixed point on the aircraft's body. This allows one to describe the equations of motion of an aircraft with a non-fixed centre of mass location with respect to an arbitrary fixed point on the aircraft's body. This is desired, as the aircraft's centre of mass is expected to shift when damage occurs. The equations of motion are first derived for a general rigid body and then rewritten in standard aircraft notation.

3.2.1 Equations of Motion for a Rigid Body Referenced to an Arbitrary Fixed Point on the Body

The derivation starts with applying Newton's second law of motion to a rigid body in three-dimensional space to develop the force-driven aircraft equations of motion to an arbitrary fixed point on the body. The moment-driven aircraft equations of motion are then developed using absolute angular moment and the sum of external moments about an arbitrary fixed point on the body (see Figure 3.4).

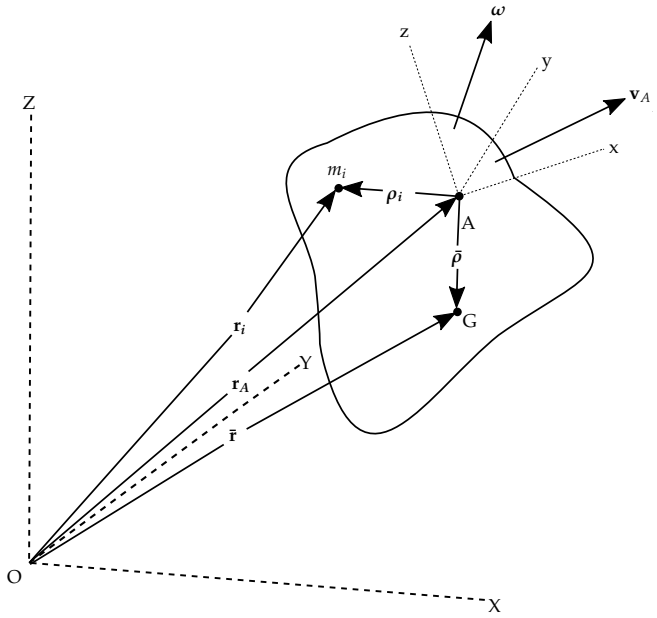

Figure 3.4: Free body diagram in three-dimensional space

3.2.1.1 Translational Accelerations

Consider the rigid body in figure 3.4 with the X-Y-Z reference frame fixed inertially to point O and the x-y-z reference frame fixed to an arbitrary point A on the body which is located $\mathbf{r}_\mathrm{A}$ from point O. The body is free to move and has an angular rate $\boldsymbol{\omega}$ with respect to the inertial reference frame X-Y-Z. G denotes the centre of mass of the rigid body located $\bar{\boldsymbol{\rho}}$ from the arbitrary fixed point A and $\bar{\mathbf{r}}$ from O. Let m_i denote a particle of mass of the rigid body located $\mathbf{r}_i$ from point O and $\boldsymbol{\rho}_i$ from the arbitrary fixed point A. From Varignon's Theorem (see Appendix A), $\bar{\boldsymbol{\rho}}$ and $\bar{\mathbf{r}}$ satisfy $m\bar{\boldsymbol{\rho}} = \sum m_i \boldsymbol{\rho}_i$ and $m\bar{\mathbf{r}} = \sum m_i \mathbf{r}_i$, where m is the total mass of the body. From Newton's second law of motion, the translation of the rigid body is described as,

$$\sum \boldsymbol{F} = \sum m_i (\ddot{\mathbf{r}}_i)_{XYZ} = m(\ddot{\bar{\mathbf{r}}})_{XYZ} \tag{3.2.1}$$

where $\sum \boldsymbol{F}$ is the sum of all the external forces acting on m and $(\ddot{\bar{\mathbf{r}}})_{XYZ}$ is the acceleration of the centre of mass observed from the inertial reference frame X-Y-Z. From Figure 3.4, $\mathbf{r}_i$ is expressed as,

$$\mathbf{r}_i = \mathbf{r}_\mathrm{A} + \boldsymbol{\rho}_i \tag{3.2.2}$$

Equation 3.2.1 is rewritten in terms of components relative to the body frame x-y-z by taking the derivative of (3.2.2) (see Appendix A) with respect to X-Y-Z:

$$(\dot{\mathbf{r}}_i)_{XYZ} = (\dot{\mathbf{r}}_A)_{xyz} + (\dot{\boldsymbol{\rho}}_i)_{xyz} + (\boldsymbol{\omega} \times \boldsymbol{\rho}_i)_{xyz} \tag{3.2.3}$$

where $(\dot{\mathbf{r}}_A)_{xyz}$ is v_A, $\boldsymbol{\omega}$ and $\boldsymbol{\rho}_i$ are expressed in x-y-z components and $\dot{\boldsymbol{\rho}}_i$ is the velocity of m_i observed in the x-y-z reference frame. To obtain the acceleration $(\ddot{\mathbf{r}}_i)_{XYZ}$, the derivative of (3.2.3) with respect to X-Y-Z is taken:

$$\begin{aligned}(\ddot{\mathbf{r}}_i)_{XYZ} &= \frac{d}{dt}(\mathbf{v}_A + \dot{\boldsymbol{\rho}}_i + \boldsymbol{\omega} \times \boldsymbol{\rho}_i) + \boldsymbol{\omega} \times (\mathbf{v}_A + \dot{\boldsymbol{\rho}}_i + \boldsymbol{\omega} \times \boldsymbol{\rho}_i)) \\ &= \dot{\mathbf{v}}_A + \boldsymbol{\omega} \times \mathbf{v}_A + \ddot{\boldsymbol{\rho}}_i + \dot{\boldsymbol{\omega}} \times \boldsymbol{\rho}_i + 2(\boldsymbol{\omega} \times \dot{\boldsymbol{\rho}}_i) + \boldsymbol{\omega} \times (\boldsymbol{\omega} \times \boldsymbol{\rho}_i)\end{aligned} \tag{3.2.4}$$

From (3.2.1),

$$\sum \boldsymbol{F} = \sum m_i(\dot{\mathbf{v}}_A + \boldsymbol{\omega} \times \mathbf{v}_A + \ddot{\boldsymbol{\rho}}_i + \dot{\boldsymbol{\omega}} \times \boldsymbol{\rho}_i + 2(\boldsymbol{\omega} \times \dot{\boldsymbol{\rho}}_i) + \boldsymbol{\omega} \times (\boldsymbol{\omega} \times \boldsymbol{\rho}_i)) \tag{3.2.5}$$

which is simplified using Varignon's Theorem to obtain,

$$\sum \boldsymbol{F} = m(\dot{\mathbf{v}}_A + \boldsymbol{\omega} \times \mathbf{v}_A) + m\ddot{\bar{\boldsymbol{\rho}}} + \dot{\boldsymbol{\omega}} \times m\bar{\boldsymbol{\rho}} + 2(\boldsymbol{\omega} \times m\dot{\bar{\boldsymbol{\rho}}}) + \boldsymbol{\omega} \times (\boldsymbol{\omega} \times m\bar{\boldsymbol{\rho}})) \tag{3.2.6}$$

where $\sum \boldsymbol{F}$ is now expressed in the body fixed reference frame x-y-z. Since the body is rigid, $\dot{\bar{\boldsymbol{\rho}}} = \ddot{\bar{\boldsymbol{\rho}}} = 0$, simplifying (3.2.6) to,

$$\sum \boldsymbol{F} = m(\dot{\mathbf{v}}_A + \boldsymbol{\omega} \times \mathbf{v}_A) + \dot{\boldsymbol{\omega}} \times m\bar{\boldsymbol{\rho}} + \boldsymbol{\omega} \times (\boldsymbol{\omega} \times m\bar{\boldsymbol{\rho}})) \tag{3.2.7}$$

Equation 3.2.7 is formulated in standard aircraft notation (see Figure 3.2) by equating,

$$\sum \boldsymbol{F} = \sum (X\boldsymbol{i} + Y\boldsymbol{j} + Z\boldsymbol{k})$$

$$\boldsymbol{\omega} = P\boldsymbol{i} + Q\boldsymbol{j} + R\boldsymbol{k}$$

$$\bar{\boldsymbol{\rho}} = \Delta x\boldsymbol{i} + \Delta y\boldsymbol{j} + \Delta z\boldsymbol{k}$$

$$\mathbf{v}_A = U_A\boldsymbol{i} + V_A\boldsymbol{j} + W_A\boldsymbol{k}$$

Note that the velocities are subscripted with A to distinguish them from the velocities at the centre of mass. However, if $\bar{\boldsymbol{\rho}} = [0\ 0\ 0]^T$, then the velocities at A are equal to the velocities at the centre of mass. The force-driven aircraft equations of motion referenced about a fixed arbitrary point A on the aircraft's body are therefore,

$$\sum X = m(\dot{U}_A + QW_A - RV_A - (Q^2 + R^2)\Delta x + (QP - \dot{R})\Delta y + (RP + \dot{Q})\Delta z) \tag{3.2.8}$$

$$\sum Y = m(\dot{V}_A + RU_A - PW_A + (PQ + \dot{R})\Delta x - (P^2 + R^2)\Delta y + (QR - \dot{P})\Delta z) \tag{3.2.9}$$

$$\sum Z = m(\dot{W}_A + PV_A - QU_A + (PR - \dot{Q})\Delta x + (QR + \dot{P})\Delta y - (P^2 + Q^2)\Delta z) \tag{3.2.10}$$

Note that if Δx, Δy, and Δz are all set to zero in equations 3.2.8 to 3.2.10, which means that the arbitrary point A coincides with the centre of mass, then the force equations simplify to the standard symmetrical aircraft force equations. The offset $\bar{\boldsymbol{\rho}}$ from the centre of mass introduces new angular rate and acceleration terms that will act on the aircraft. Also note that $\sum X, \sum Y$, and $\sum Z$ include the aerodynamic forces, thrust forces and gravitational forces acting on the aircraft.

3.2.1.2 Angular Accelerations

In this section, momentum principles are used to develop the moment-driven aircraft equations of motion. Again, consider the rigid body in Figure 3.4, as described in the previous section.

The absolute angular moment about point A is,

$$\boldsymbol{H}_{\mathrm{A}} = \sum(\boldsymbol{\rho}_i \times m_i \mathbf{v}_i) \tag{3.2.11}$$

where $\mathbf{v}_i = (\dot{\mathbf{r}}_i)_{XYZ}$ is the velocity of m_i observed from the inertial reference frame X-Y-Z. Now take the derivative of $\boldsymbol{H}_{\mathrm{A}}$ observed from the X-Y-Z reference frame,

$$(\dot{\boldsymbol{H}}_{\mathrm{A}})_{XYZ} = \sum((\dot{\boldsymbol{\rho}}_i)_{XYZ} \times m_i \mathbf{v}_i) + \sum(\boldsymbol{\rho}_i \times m_i (\dot{\mathbf{v}}_i)_{XYZ}) \tag{3.2.12}$$

where $(\dot{\boldsymbol{\rho}}_i)_{XYZ}$ and $(\dot{\mathbf{v}}_i)_{XYZ} = (\ddot{\mathbf{r}}_i)_{XYZ}$ are the derivatives observed from the X-Y-Z reference frame. From Figure 3.4, $(\boldsymbol{\rho}_i)_{XYZ} = (\mathbf{r}_i - \mathbf{r}_{\mathrm{A}})_{XYZ}$ with derivative $(\dot{\boldsymbol{\rho}}_i)_{XYZ} = (\dot{\mathbf{r}}_i - \dot{\mathbf{r}}_{\mathrm{A}})_{XYZ}$. Noting that the sum of the external moments about point A is defined as $\sum \boldsymbol{M}_{\mathrm{A}} = \sum(\boldsymbol{\rho}_i \times m_i \ddot{\mathbf{r}}_i)$, equation (3.2.12) can be rewritten as,

$$\begin{aligned}(\dot{\boldsymbol{H}}_{\mathrm{A}})_{XYZ} &= \sum(((\dot{\mathbf{r}}_i - \dot{\mathbf{r}}_{\mathrm{A}})_{XYZ}) \times m_i \mathbf{v}_i) + \sum(\boldsymbol{\rho}_i \times m_i (\ddot{\mathbf{r}}_i)_{XYZ}) \\ &= \sum(((-\dot{\mathbf{r}}_{\mathrm{A}})_{XYZ}) \times m_i \mathbf{v}_i) + \sum \boldsymbol{M}_{\mathrm{A}}\end{aligned} \tag{3.2.13}$$

Making $\sum \boldsymbol{M}_{\mathrm{A}}$ the subject of the equation gives,

$$\sum \boldsymbol{M}_{\mathrm{A}} = (\dot{\boldsymbol{H}}_{\mathrm{A}})_{XYZ} + (\dot{\mathbf{r}}_{\mathrm{A}})_{XYZ} \times \sum(m_i \mathbf{v}_i) \tag{3.2.14}$$

From Figure 3.4, $\bar{\mathbf{v}}$ is expressed as $\mathbf{v}_{\mathrm{A}} + (\dot{\bar{\boldsymbol{\rho}}})_{XYZ}$. Noting that the linear momentum of a system of particles is equivalent to the linear momentum of a fictitious aggregate particle mass moving with the velocity of the centre of mass of the system [27], $m\bar{\mathbf{v}} = \sum m_i \mathbf{v}_i$ produces the following equation,

$$\sum \boldsymbol{M}_{\mathrm{A}} = (\dot{\boldsymbol{H}}_{\mathrm{A}})_{XYZ} + \mathbf{v}_{\mathrm{A}} \times m(\mathbf{v}_{\mathrm{A}} + (\dot{\bar{\boldsymbol{\rho}}})_{XYZ}) \tag{3.2.15}$$

which using the cross product distributive law simplifies to,

$$\sum \boldsymbol{M}_{\mathrm{A}} = (\dot{\boldsymbol{H}}_{\mathrm{A}})_{XYZ} + \mathbf{v}_{\mathrm{A}} + m(\dot{\bar{\boldsymbol{\rho}}})_{XYZ} \tag{3.2.16}$$

In order to express (3.2.16) in the x-y-z fixed body reference frame, (3.2.11) is rewritten in terms of fixed body reference frame components, noting that the absolute velocity of $\mathbf{v}_i$ is expressed as $\mathbf{v}_{\mathrm{A}} + \dot{\boldsymbol{\rho}}_i + \boldsymbol{\omega} \times \boldsymbol{\rho}_i$(see Appendix A), where $\boldsymbol{\omega}$ is the angular velocity of the body,

$$\boldsymbol{H}_{\mathrm{A}} = \sum(\boldsymbol{\rho}_i \times m_i(\mathbf{v}_{\mathrm{A}} + \dot{\boldsymbol{\rho}}_i + \boldsymbol{\omega} \times \boldsymbol{\rho}_i) \tag{3.2.17}$$

Now vectors $\mathbf{v}_{\mathrm{A}}$, $\dot{\boldsymbol{\rho}}_i$ and $\boldsymbol{\omega} \times \boldsymbol{\rho}_i$ are expressed in the fixed body reference frame x-y-z at A. Since the body is rigid, it implies that $\dot{\boldsymbol{\rho}}_i = 0$, simplifying (3.2.17) to,

$$\boldsymbol{H}_{\mathrm{A}} = \sum(\boldsymbol{\rho}_i \times m_i(\mathbf{v}_{\mathrm{A}} + \boldsymbol{\omega} \times \boldsymbol{\rho}_i) \tag{3.2.18}$$

Now, using Varignon's Theorem, which states that $m\bar{\boldsymbol{\rho}} = \sum m_i \boldsymbol{\rho}_i$ produces,

$$\begin{aligned}\boldsymbol{H}_{\mathrm{A}} &= \bar{\boldsymbol{\rho}} \times m(\mathbf{v}_{\mathrm{A}} + \boldsymbol{\omega} \times \bar{\boldsymbol{\rho}}) \\ &= \bar{\boldsymbol{\rho}} \times m\mathbf{v}_{\mathrm{A}} + \bar{\boldsymbol{\rho}} \times \boldsymbol{\omega} \times m\bar{\boldsymbol{\rho}} \\ &= m\bar{\boldsymbol{\rho}} \times \mathbf{v}_{\mathrm{A}} + \mathbf{I}\boldsymbol{\omega}\end{aligned} \tag{3.2.19}$$

where $\bar{\boldsymbol{\rho}} \times m\boldsymbol{\omega} \times \bar{\boldsymbol{\rho}} = (m\bar{\boldsymbol{\rho}}^2)\boldsymbol{\omega} = \mathbf{I}\boldsymbol{\omega}$ and $\mathbf{I}$ is the moment of inertia matrix of the rigid body referenced to the body fixed reference frame x-y-z. The absolute derivatives with respect to the X-Y-Z reference frame $(\dot{\boldsymbol{H}}_{\mathrm{A}})_{XYZ}$ and $(\dot{\bar{\boldsymbol{\rho}}})_{XYZ}$ from (3.2.16) are obtained by taking the derivatives of equations $(\boldsymbol{H}_{\mathrm{A}})_{XYZ}$ and $(\bar{\boldsymbol{\rho}})_{XYZ}$ relative to the X-Y-Z reference frame.

$$(\dot{\boldsymbol{H}}_{\mathrm{A}})_{XYZ} = (\dot{\boldsymbol{H}}_{\mathrm{A}})_{xyz} + \boldsymbol{\omega} \times \boldsymbol{H}_{\mathrm{A}} \tag{3.2.20}$$

$$(\dot{\bar{\boldsymbol{\rho}}})_{XYZ} = (\dot{\bar{\boldsymbol{\rho}}})_{xyz} + \boldsymbol{\omega} \times \bar{\boldsymbol{\rho}} \tag{3.2.21}$$

Substituting (3.2.17) into (3.2.20) yields,

$$(\dot{\boldsymbol{H}}_{\mathrm{A}})_{XYZ} = \frac{d}{dt}(m\bar{\boldsymbol{\rho}} \times \mathbf{v}_{\mathrm{A}} + \mathbf{I}\boldsymbol{\omega}) + \boldsymbol{\omega} \times (m\bar{\boldsymbol{\rho}} \times \mathbf{v}_{\mathrm{A}} + \mathbf{I}\boldsymbol{\omega}) \tag{3.2.22}$$

simplifying to

$$(\dot{\boldsymbol{H}}_{\mathrm{A}})_{XYZ} = \mathbf{I}\boldsymbol{\omega} + \boldsymbol{\omega} \times \mathbf{I}\boldsymbol{\omega} + m\bar{\boldsymbol{\rho}} \times \dot{\mathbf{v}}_{\mathrm{A}} + \boldsymbol{\omega} \times (m\bar{\boldsymbol{\rho}} \times \mathbf{v}_{\mathrm{A}}) \tag{3.2.23}$$

All the components are now expressed in the fixed body x-y-z reference frame. Equation 3.2.16 can now be rewritten in only body reference frame components:

$$\sum \boldsymbol{M}_{\mathrm{A}} = \mathbf{I}\boldsymbol{\omega} + \boldsymbol{\omega} \times \mathbf{I}\boldsymbol{\omega} + m\bar{\boldsymbol{\rho}} \times \dot{\mathbf{v}}_{\mathrm{A}} + \boldsymbol{\omega} \times (m\bar{\boldsymbol{\rho}} \times \mathbf{v}_{\mathrm{A}}) + \mathbf{v}_{\mathrm{A}} + m(\boldsymbol{\omega} \times \bar{\boldsymbol{\rho}}) \tag{3.2.24}$$

Equation 3.2.24 is formulated in standard aircraft notation (see Figure 3.2) by setting,

$$\sum \boldsymbol{M} = \sum (L_{\mathrm{A}}\boldsymbol{i} + M_{\mathrm{A}}\boldsymbol{j} + N_{\mathrm{A}}\boldsymbol{k})$$

$$\boldsymbol{\omega} = P\boldsymbol{i} + Q\boldsymbol{j} + R\boldsymbol{k}$$

$$\bar{\boldsymbol{\rho}} = \Delta x\boldsymbol{i} + \Delta y\boldsymbol{j} + \Delta z\boldsymbol{k}$$

$$\mathbf{v}_{\mathrm{A}} = U_{\mathrm{A}}\boldsymbol{i} + V_{\mathrm{A}}\boldsymbol{j} + W_{\mathrm{A}}\boldsymbol{k}$$

$$\mathbf{I} = \begin{bmatrix} I_{xx} & -I_{xy} & -I_{xz} \\ -I_{yx} & I_{yy} & -I_{yz} \\ -I_{zx} & -I_{zy} & I_{zz} \end{bmatrix}$$

With no symmetry assumed, the moment-driven aircraft equations of motion are described by,

$$\begin{aligned} \sum L_{\mathrm{A}} =& I_{xx}\dot{P} - I_{xy}\dot{Q} - I_{xz}\dot{R} + I_{xy}PR - I_{xz}PQ + (I_{zz} - I_{yy})QR + (R^2 - Q^2)I_{yz} + \\ & m((PV_{\mathrm{A}} - QU_{\mathrm{A}} + \dot{W}_{\mathrm{A}})\Delta y + (PW_{\mathrm{A}} - RU_{\mathrm{A}} - \dot{V}_{\mathrm{A}})\Delta z) \end{aligned} \tag{3.2.25}$$

$$\begin{aligned} \sum M_{\mathrm{A}} =& -I_{xy}\dot{P} + I_{yy}\dot{Q} - I_{yz}\dot{R} + I_{yz}PQ - I_{xy}QR + (I_{xx} - I_{zz})PR + (P^2 - R^2)I_{xz} + \\ & m((QU_{\mathrm{A}} - PV_{\mathrm{A}} + \dot{W}_{\mathrm{A}})\Delta y + (QW_{\mathrm{A}} - RV_{\mathrm{A}} + \dot{U}_{\mathrm{A}})\Delta z) \end{aligned} \tag{3.2.26}$$

$$\begin{aligned} \sum N_{\mathrm{A}} =& -I_{zx}\dot{P} - I_{yz}\dot{Q} + I_{zz}\dot{R} + I_{xz}QR - I_{yz}PR + (I_{yy} - I_{xx})PR + (Q^2 - P^2)I_{xy} + \\ & m((RU_{\mathrm{A}} - PW_{\mathrm{A}} + \dot{V}_{\mathrm{A}})\Delta x + (RV_{\mathrm{A}} - QW_{\mathrm{A}} - \dot{U}_{\mathrm{A}})\Delta y) \end{aligned} \tag{3.2.27}$$

Once again, the equations are identical to the standard symmetrical aircraft equations if Δx, Δy, and Δz are zero and symmetry about the aircraft $X_{\mathrm{B}}Z_{\mathrm{B}}$-plane is assumed. Take note that $\sum L_{\mathrm{A}}, \sum M_{\mathrm{A}}$ and $\sum N_{\mathrm{A}}$ include the moments due to aerodynamic, thrust and gravitational acting on the aircraft.

3.2.1.3 Modelling Instantaneous centre of Mass Shifts due to Aircraft Damage

In the previous section, the general equations of motion for an aircraft were developed. These equations of motion are referenced to an arbitrary point on the aircraft's body, located $\bar{\boldsymbol{\rho}}$ from the centre of mass of the aircraft. However, when the aircraft is damaged, an instantaneous shift in the centre of mass will occur. Bacon et al. describe two approaches that can be followed to account for this situation: the CM-centric and non-CM approach [20].

Here, the non-CM approach is followed. The non-CM approach assumes that the location of the aircraft's centre of mass with respect to the fixed point A, $\bar{\boldsymbol{\rho}}$,is always known. The fixed point A on the aircraft will not move when the aircraft is damaged, but the centre of mass will move to a new location $\bar{\boldsymbol{\rho}}_{damage}$ from A. From (3.2.8) to (3.2.10) and (3.2.25) to (3.2.27), the velocities and angular rates at point A due to a shift in the centre of mass are written in matrix form as [20],

$$\begin{bmatrix} \dot{\mathbf{v}}_{\mathrm{A}} \\ \dot{\boldsymbol{\omega}} \end{bmatrix} = \begin{bmatrix} m\mathbf{I}_3 & -\mathbf{D}_x \\ \mathbf{D}_x & \mathbf{I} \end{bmatrix}^{-1} \left[\begin{bmatrix} \sum \boldsymbol{F} \\ \sum \boldsymbol{M}_{\mathrm{A}} \end{bmatrix} - \begin{bmatrix} m\boldsymbol{\Omega}_x & -\boldsymbol{\Omega}_x\mathbf{D}_x \\ \boldsymbol{\Omega}_x\mathbf{D}_x & \boldsymbol{\Omega}_x\mathbf{I} - \mathbf{V}_{\mathrm{A}}\boldsymbol{\Omega}_x \end{bmatrix} \begin{bmatrix} \mathbf{v}_{\mathrm{A}} \\ \boldsymbol{\omega} \end{bmatrix} \right] \tag{3.2.28}$$

where,

$$\begin{aligned} \mathbf{D}_x &= \begin{bmatrix} 0 & -m\Delta z & m\Delta y \\ m\Delta z & 0 & -m\Delta x \\ -m\Delta y & m\Delta x & 0 \end{bmatrix}, \ \boldsymbol{\Omega}_x = \begin{bmatrix} 0 & -R & Q \\ R & 0 & -P \\ -Q & P & 0 \end{bmatrix} \\ \mathbf{V}_{\mathrm{A}} &= \begin{bmatrix} 0 & -W_{\mathrm{A}} & V_{\mathrm{A}} \\ W_{\mathrm{A}} & 0 & -U_{\mathrm{A}} \\ -V_{\mathrm{A}} & U_{\mathrm{A}} & 0 \end{bmatrix}, \ \mathbf{I} = \begin{bmatrix} I_{xx} & -I_{xy} & -I_{xz} \\ -I_{yx} & I_{yy} & -I_{yz} \\ -I_{zx} & -I_{zy} & I_{zz} \end{bmatrix} \end{aligned} \tag{3.2.29}$$

When the aircraft is damaged, the mass and moment of inertia of the aircraft change as well as the centre of mass location vector $\bar{\boldsymbol{\rho}}$.

$$\begin{aligned} m &\rightarrow m_{damage} = m - m_{tip} \\ \bar{\boldsymbol{\rho}} &\rightarrow \bar{\boldsymbol{\rho}}_{damage} = (\bar{\boldsymbol{\rho}} - \bar{\boldsymbol{\rho}}_{tip})/m_{damage} \\ I_{ij} &\rightarrow I_{ij_{damage}} = I_{ij} - I_{ij_{tip}} \text{ where, } i,j = x,y,z \end{aligned}$$

where from the parallel axis and parallel plane theorems we have,

$$\begin{aligned} I_{ii_{tip}} &= I_{ii_{tip_{\mathrm{cm}}}} + m_{tip}(\Delta j_{tip}^2 + \Delta k_{tip}^2) \text{ where, } i,j,k = x,y,z \mid i \neq j \ , \ i \neq k \\ I_{ij_{tip}} &= I_{ij_{tip_{\mathrm{cm}}}} + m_{tip}\Delta i_{tip}\Delta j_{tip} \text{ where, } i,j = x,y,z \mid i \neq j \end{aligned}$$

In equation (3.2.29), the velocity vector $\mathbf{v}_{\mathrm{A}}$ is expressed about the fixed point A. However, the angle of attack and sideslip angle is still calculated using the velocity of the aircraft's centre of mass (not the velocity at point A). Given the velocity vector $\mathbf{v}_{\mathrm{A}}$, the angular rate $\boldsymbol{\omega}$, and the centre of mass location vector $\bar{\boldsymbol{\rho}}$ relative to point A, the velocity $\mathbf{v}_{\mathrm{cm}}$ and acceleration $\dot{\mathbf{v}}_{\mathrm{cm}}$ of the centre of mass can be calculated with the following auxiliary equations,

$$\begin{aligned} \mathbf{v}_{\mathrm{cm}} &= \mathbf{v}_{\mathrm{A}} + \boldsymbol{\omega} \times \Delta\bar{\boldsymbol{\rho}}_{damage} \\ \dot{\mathbf{v}}_{\mathrm{cm}} &= \dot{\mathbf{v}}_{\mathrm{A}} + \dot{\boldsymbol{\omega}} \times \Delta\bar{\boldsymbol{\rho}}_{damage} \end{aligned} \tag{3.2.30}$$

When the centre of mass location coincides with point A, then the velocity and acceleration of the centre mass simply equal the velocity and acceleration of point A. Only when the aircraft is damaged and the centre of mass has moved away from point A are these auxiliary equations used.

3.3 Aircraft Kinematics

In this section, the the kinematic equations that relate the aircraft's translational velocity and angular rates to its attitude and position are defined. The kinematic equations represent a set of differential equations that are used to propagate the aircraft's attitude and position with respect to the inertial frame.

3.3.1 Attitude Definition and Dynamics

As mentioned in Section 3.1.2, the body reference frame is a rotating reference frame which is fixed to the aircraft's body, but free to translate and rotate relative to the inertial reference frame. In order to describe the rotation of the body reference frame relative to the inertial frame, a set of Euler angles Ψ, Θ, and Φ are defined, as shown in Figure 3.5. Ψ is called the yaw angle, Θ the pitch angle and Φ the roll angle. In this project, an Euler 3-2-1 sequence is used. This sequence is commonly used for aircraft performing conventional flight (not aerobatic flight) due to a singularity that occurs when the pitch angle is $\pm 90°$.

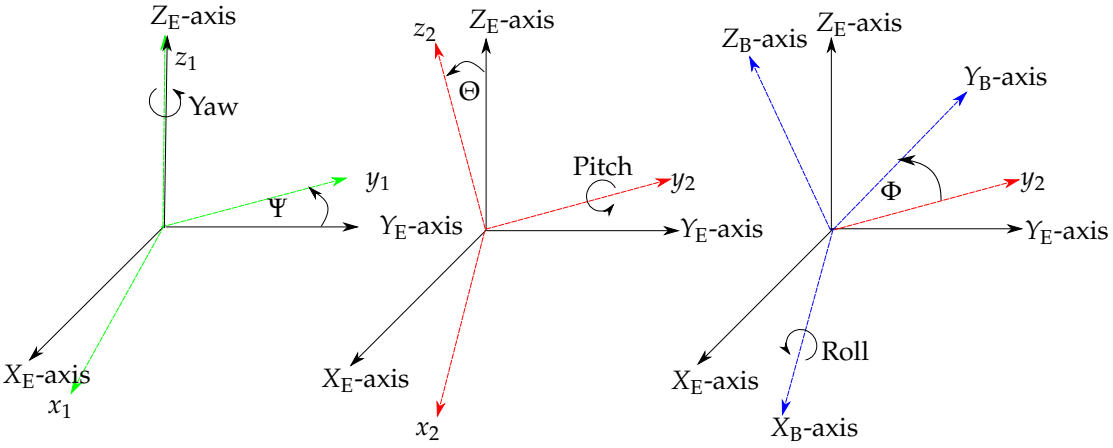

Figure 3.5: Euler 3-2-1 rotations

The Euler 3-2-1 sequence starts with the body reference frame aligned with the inertial reference. The body reference frame is then rotated through a set of ordered rotations. The body reference frame is first rotated about the Z_E-axis through the yaw angle Ψ, resulting in an intermediate axis system $\mathbf{f}_1$, shown in Figure 3.5 in green. The rotation matrix $\mathbf{R}_\Psi$, shown in (3.3.1) mathematically expresses the relationship between the $\mathbf{f}_E$ and $\mathbf{f}_1$ axis systems. The rotation matrix $\mathbf{R}_\Psi$ can therefore be used to relate a vector $\mathbf{h}_E$ from the inertial reference frame to a vector $\mathbf{h}_1$ in the first intermediate axis system $\mathbf{f}_1$, as shown in (3.3.2).

$$\begin{bmatrix} x_1 \\ y_1 \\ z_1 \end{bmatrix} = \begin{bmatrix} \cos\Psi & \sin\Psi & 0 \\ -\sin\Psi & \cos\Psi & 0 \\ 0 & 0 & 1 \end{bmatrix} \begin{bmatrix} X_E \\ Y_E \\ Z_E \end{bmatrix} \tag{3.3.1}$$

$$\mathbf{h}_1 = \mathbf{R}_\Psi \mathbf{h}_E \tag{3.3.2}$$

Secondly, the first intermediate axis system $\mathbf{f}_1$ is rotated about its y_1-axis through the pitch angle Θ, resulting in a second intermediate axis system $\mathbf{f}_2$, shown in Figure 3.5 in red. Again, the rotation

matrix $\mathbf{R}_\Theta$, shown in (3.3.3), expresses the relationship between the $\mathbf{f}_1$ and $\mathbf{f}_2$ axis systems. The rotation matrix $\mathbf{R}_\Theta$ can thus be used to relate a vector $\mathbf{h}_1$ from the axis system $\mathbf{f}_1$ to a vector $\mathbf{h}_2$ in the axis system $\mathbf{f}_2$, as shown in (3.3.4).

$$\begin{bmatrix} x_2 \\ y_2 \\ z_2 \end{bmatrix} = \begin{bmatrix} \cos\Theta & 0 & -\sin\Theta \\ 0 & 1 & 0 \\ \sin\Theta & 0 & \cos\Theta \end{bmatrix} \begin{bmatrix} x_1 \\ y_1 \\ z_1 \end{bmatrix} \tag{3.3.3}$$

$$\mathbf{h}_2 = \mathbf{R}_\Theta \mathbf{h}_1 \tag{3.3.4}$$

Finally, the second intermediate axis system $\mathbf{f}_2$ is rotated about its x_2-axis through the roll angle Φ, resulting in the body reference frame $\mathbf{f}_B$, shown in Figure 3.5 in blue. Again, the rotation matrix $\mathbf{R}_\Phi$, shown in (3.3.5), expresses the relationship between the $\mathbf{f}_2$ and $\mathbf{f}_B$ axis systems. The rotation matrix $\mathbf{R}_\Phi$ can thus be used to relate a vector $\mathbf{h}_2$ from the axis system $\mathbf{f}_2$ to a vector $\mathbf{h}_B$ in the body reference frame $\mathbf{f}_B$, as shown in (3.3.6).

$$\begin{bmatrix} X_B \\ Y_B \\ Z_B \end{bmatrix} = \begin{bmatrix} 1 & 0 & 0 \\ 0 & \cos\Phi & \sin\Phi \\ 0 & -\sin\Phi & \cos\Phi \end{bmatrix} \begin{bmatrix} x_2 \\ y_2 \\ z_2 \end{bmatrix} \tag{3.3.5}$$

$$\mathbf{h}_B = \mathbf{R}_\Phi \mathbf{h}_2 \tag{3.3.6}$$

Combining (3.3.2), (3.3.4) and (3.3.6) yields

$$\mathbf{h}_B = \mathbf{R}_\Phi \mathbf{R}_\Theta \mathbf{R}_\Psi \mathbf{h}_E \tag{3.3.7}$$

where $[\mathbf{R}_\Phi \mathbf{R}_\Theta \mathbf{R}_\Psi]$ is commonly referred to as the Direction Cosine Matrix (DCM). Thus, given the three Euler angles, it is possible to relate any vector in the inertial reference frame to a vector in the body reference frame using the DCM in (3.3.7).

A set of differential equations to propagate the Euler angles can now be derived. Up to this point the dynamics of the aircraft have been derived as a function of the body reference frame angular velocities; therefore, the derivation starts by obtaining a set of differential equations which relates the Euler angular rates to the body reference frame angular velocities. The Euler angular rates are then integrated to propagate the Euler angles. Only for the case of zero Euler angles will the Euler angular rates be equal to the body referenced angular velocities. The relationship between the body angular velocity vector, $[P\ Q\ R]_B^T$, and the rate of change of the Euler angles, $[\dot{\Phi}\ \dot{\Theta}\ \dot{\Psi}]$, is determined by resolving the Euler angular rates into the body reference frame angular velocity, as seen in (3.3.8), where $\dot{\Phi}$ is measured in the body reference frame, $\dot{\Theta}$ is measured in the intermediate reference frame after a Φ rotation, and $\dot{\Psi}$ is measured in the inertial reference frame.

$$\begin{bmatrix} P \\ Q \\ R \end{bmatrix}_B = \mathbf{I}_3 \begin{bmatrix} \dot{\Phi} \\ 0 \\ 0 \end{bmatrix} + \mathbf{R}_\Phi \begin{bmatrix} 0 \\ \dot{\Theta} \\ 0 \end{bmatrix} + \mathbf{R}_\Phi \mathbf{R}_\Theta \begin{bmatrix} 0 \\ 0 \\ \dot{\Psi} \end{bmatrix} \tag{3.3.8}$$

which simplifies to

$$\begin{bmatrix} P \\ Q \\ R \end{bmatrix}_B = \begin{bmatrix} 1 & 0 & -\sin\Theta \\ 0 & \cos\Phi & \sin\Phi\cos\Theta \\ 0 & -\sin\Phi & \cos\Phi\cos\Theta \end{bmatrix} \begin{bmatrix} \dot{\Phi} \\ \dot{\Theta} \\ \dot{\Psi} \end{bmatrix} \tag{3.3.9}$$

$$\begin{bmatrix} P \\ Q \\ R \end{bmatrix}_{\mathrm{B}} = \mathbf{J} \begin{bmatrix} \dot{\Phi} \\ \dot{\Theta} \\ \dot{\Psi} \end{bmatrix} \tag{3.3.10}$$

where $\mathbf{J}$ is the transformation matrix in (3.3.9) with an existing inverse $\mathbf{J}^{-1}$. The Euler angular rates given the body reference frame angular velocities can thus be obtained by,

$$\begin{bmatrix} \dot{\Phi} \\ \dot{\Theta} \\ \dot{\Psi} \end{bmatrix} = \begin{bmatrix} 1 & \sin\Phi\tan\Theta & \cos\Phi\tan\Theta \\ 0 & \cos\Phi & -\sin\Phi \\ 0 & \sin\Phi\sec\Theta & \cos\Phi\sec\Theta \end{bmatrix} \begin{bmatrix} P \\ Q \\ R \end{bmatrix}_{\mathrm{B}} \tag{3.3.11}$$

Note that the transformation matrix $\mathbf{J}$ has a singularity at Θ equal to $\pm 90°$. By integrating the vector $[\dot{\Phi}\ \dot{\Theta}\ \dot{\Psi}]^T$, the attitude of the aircraft $[\Phi\ \Theta\ \Psi]^T$ is propagated. Figure 3.6 shows the aircraft's Euler angles.

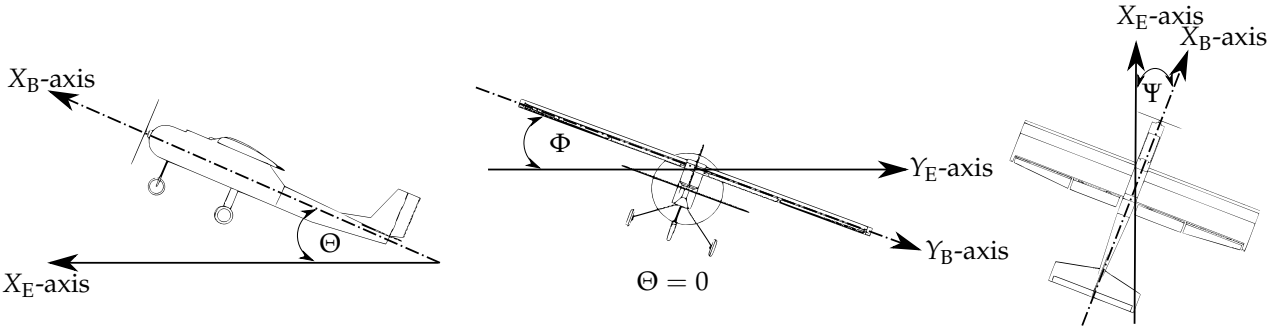

Figure 3.6: Aircraft Euler angles conventions

3.3.2 Position Dynamics

The position of the aircraft is defined as the vector $[N\ E\ D]^T$ from the origin of the inertial reference frame to the origin of the body reference frame, where N is the North position coordinate on the X_{E}-axis, E is the East position coordinate on the Y_{E}-axis, and D is the Down position coordinate on the Z_{E}-axis, as shown in Figure 3.7. The aircraft's translational velocities with respect to the inertial frame can therefore be expressed as the vector $[\dot{N}\ \dot{E}\ \dot{D}]^T$, which is the change in position over time, where $\dot{N}$ is the linear velocity in the X_{E}-axis, $\dot{E}$ is the linear velocity in the Y_{E}-axis and $\dot{D}$ is the linear velocity in the Z_{E}-axis.

Up to this point, the dynamics of the aircraft have been derived as a function of the body reference frame velocities. In Section 3.1.2, the aircraft's linear velocities U, V and W with respect to the body reference frame were defined. Recall from Section 3.3.1, that the DCM in (3.3.7), if given the three Euler angles, relates any vector in the inertial reference frame to a vector in the body reference frame. Note that the inverse is also valid,

$$\mathbf{h}_{\mathrm{E}} = [\mathbf{R}_{\Phi}\mathbf{R}_{\Theta}\mathbf{R}_{\Psi}]^{-1}\mathbf{h}_{\mathrm{B}} \tag{3.3.12}$$

which relates any vector in the body reference frame to a vector in the inertial reference frame. The vector $[U\ V\ W]^T$ can therefore be related to the vector $[\dot{N}\ \dot{E}\ \dot{D}]^T$ using the inverse of the DCM,

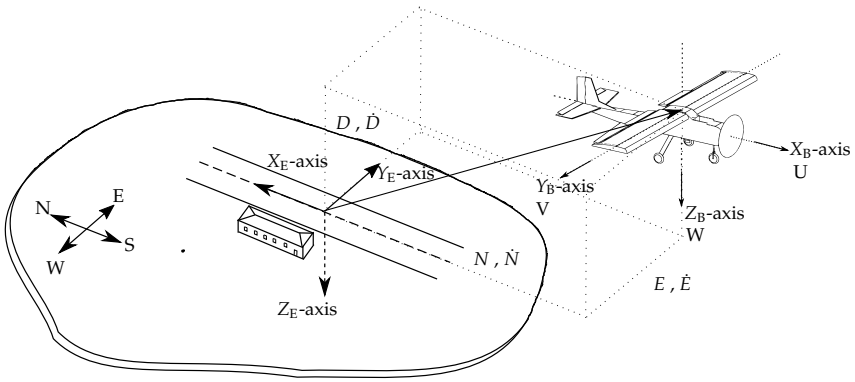

Figure 3.7: Aircraft position relative to the inertial reference frame

as shown in (3.3.12), giving that the Euler angles are known.

$$\begin{bmatrix} \dot{N} \\ \dot{E} \\ \dot{D} \end{bmatrix} = \begin{bmatrix} \cos\Psi\cos\Theta & \sin\Psi\cos\Theta & -\sin\Theta \\ \cos\Psi\sin\Theta\sin\Phi - \sin\Psi\cos\Phi & \sin\Psi\sin\Theta\sin\Phi + \cos\Psi\cos\Phi & \cos\Theta\sin\phi \\ \cos\Psi\sin\Theta\cos\Phi + \sin\Psi\sin\Phi & \sin\Psi\sin\Theta\cos\Phi - \cos\Psi\cos\Phi & \cos\Theta\cos\phi \end{bmatrix}^{-1} \begin{bmatrix} U \\ V \\ W \end{bmatrix} \tag{3.3.13}$$

By integrating the vector $[\dot{N}\ \dot{E}\ \dot{D}]^T$, the position of the aircraft $[N\ E\ D]$, which is defined as the position from the origin of the inertial reference frame to the origin of the body reference frame, is propagated.

3.4 Forces and Moments Acting on the Aircraft

In this section, the forces and moments acting on the aircraft are modelled. For most aircraft, these forces and moments can be classified into three categories,

- Aerodynamic forces and moments produced by the airframe
- Gravitational forces and moments
- Thrust forces and moments produced by the engine

Each category will induce forces and moments acting on the aircraft. The total forces and moments in the body reference frame are given by,

$$\begin{aligned} \boldsymbol{F} &= \boldsymbol{F}^A + \boldsymbol{F}^T + \boldsymbol{F}^G \\ \boldsymbol{M} &= \boldsymbol{M}^A + \boldsymbol{M}^T + \boldsymbol{M}^G \end{aligned} \tag{3.4.1}$$

where $\boldsymbol{F} = [X\ Y\ Z]^T$, $\boldsymbol{M} = [L_B\ M_B\ N_B]^T$ and A, T and G denote aerodynamic, thrust and gravitational components respectively. Each category is discussed in more detail in Sections 3.4.1 to 3.4.3.

3.4.1 Aerodynamics Forces and Moments

The aerodynamics of the airframe makes a fundamental contribution to the stability and control characteristics of the aircraft. Aerodynamic modelling is concerned with the development of models to described the aerodynamic forces and moment acting on the airframe. Due to the complex

nature of describing the aerodynamics of a airframe, simpler approximate mathematical models which represents the aerodynamic properties of the airframe with acceptable accuracy are described [28]. The aerodynamic forces and moments acting on the aircraft in the body reference frame are expressed as,

$$\begin{aligned} X^A &= \bar{q}SC_{x_\mathrm{B}}(\alpha, P_\mathrm{B}, Q_\mathrm{B}, R_\mathrm{B}, \delta_A, \delta_E) \\ Y^A &= \bar{q}SC_{y_\mathrm{B}}(\beta, P_\mathrm{B}, R_\mathrm{B}, \delta_A, \delta_R) \\ Z^A &= \bar{q}SC_{z_\mathrm{B}}(\alpha, P_\mathrm{B}, Q_\mathrm{B}, R_\mathrm{B}, \delta_A, \delta_E) \\ L^A &= \bar{q}SbC_{l_\mathrm{B}}(\alpha, \beta, P_\mathrm{B}, Q_\mathrm{B}, R_\mathrm{B}, \delta_A, \delta_R) \\ M^A &= \bar{q}S\bar{c}C_{m_\mathrm{B}}(\alpha, Q_\mathrm{B}, \delta_E) \\ N^A &= \bar{q}SbC_{n_\mathrm{B}}(\alpha, \beta, P_\mathrm{B}, Q_\mathrm{B}, R_\mathrm{B}, \delta_A, \delta_R) \end{aligned} \tag{3.4.2}$$

where S is the wing reference area, b is the wing span, $\bar{c}$ is the wing mean chord (see Figure 3.8), and $\bar{q}$ is the dynamic pressure which is defined as

$$\bar{q} = \frac{1}{2}\rho\bar{V}^2 \tag{3.4.3}$$

where ρ is the air density and $\bar{V}$ is the airspeed of the aircraft. For altitudes below 11 km, ρ can be calculated with [29],

$$\rho = 1.225(1 - 2.2558 \times 10^{-5}h)^{4.2559} \tag{3.4.4}$$

where h is the altitude of the aircraft above mean see-level (MSL) in meters. The terms $C_{(*)_\mathrm{B}}$ are the non-dimensional aerodynamic force and moment coefficients in the body reference frame. The non-dimensional coefficients are usually modelled in the stability reference frame and must

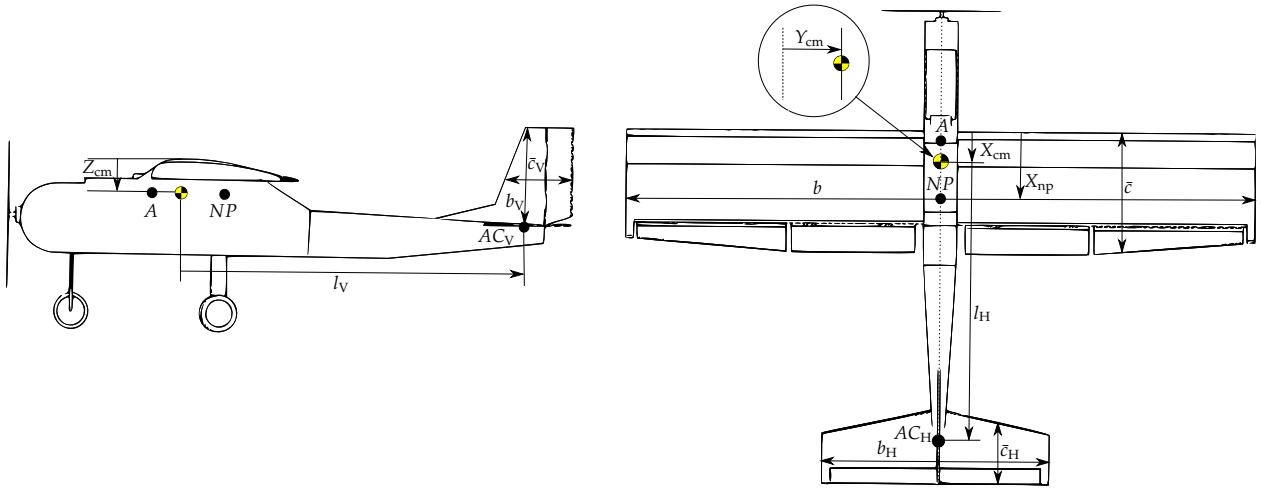

Figure 3.8: Aircraft reference geometry

be transformed to coefficients in the body reference frame using the inverse of the rotation matrix

defined in (3.1.5) to obtain

$$\begin{aligned} C_{x_B} &= -C_D \cos\alpha + C_L \sin\alpha \\ C_{y_B} &= C_y \\ C_{z_B} &= -C_L \cos\alpha - C_D \sin\alpha \\ C_{l_B} &= C_l \cos\alpha - C_n \sin\alpha \\ C_{m_B} &= C_m \\ C_{n_B} &= C_n \cos\alpha + C_l \sin\alpha \end{aligned} \tag{3.4.5}$$

where the coefficients $C_{(*)}$ are in the stability reference frame. The aerodynamic force and moment coefficients for typical subsonic, pre-stall flight in the stability reference frame are given in [29] as,

$$\begin{aligned} C_D &= C_{D_0} + \frac{C_L^2}{\pi A e} \\ C_y &= C_{y_\beta}\beta + C_{y_P}\frac{b}{2\bar{V}}P_S + C_{y_R}\frac{b}{2\bar{V}}R_S + C_{y_{\delta_A}}\delta_A + C_{y_{\delta_R}}\delta_R \\ C_L &= C_{L_0} + C_{L_\alpha}\alpha + C_{L_P}\frac{b}{2\bar{V}}P_S + C_{L_R}\frac{b}{2\bar{V}}R_S + C_{L_Q}\frac{\bar{c}}{2\bar{V}}Q_S + C_{L_{\delta_E}}\delta_E + +C_{L_{\delta_A}}\delta_A \\ C_l &= C_{l_0} + C_{l_\beta}\beta + C_{l_\alpha}\alpha + C_{l_P}\frac{b}{2\bar{V}}P_S + C_{l_R}\frac{b}{2\bar{V}}R_S + C_{l_Q}\frac{\bar{c}}{2\bar{V}}Q_S + C_{l_{\delta_A}}\delta_A + C_{l_{\delta_R}}\delta_R \\ C_m &= C_{m_0} + C_{m_\alpha}\alpha + C_{m_Q}\frac{\bar{c}}{2\bar{V}}Q_S + C_{m_{\delta_E}}\delta_E \\ C_n &= C_{n_0} + C_{n_\beta}\beta + C_{n_\alpha}\alpha + C_{n_P}\frac{b}{2\bar{V}}P_S + C_{n_R}\frac{b}{2\bar{V}}R_S + C_{i_Q}\frac{\bar{c}}{2\bar{V}}Q_S + C_{n_{\delta_A}}\delta_A + C_{n_{\delta_R}}\delta_R \end{aligned} \tag{3.4.6}$$

where subscript D denotes drag force, y denotes side force, L denotes lift force, l denotes rolling moment, m denotes pitching moment, n denotes yawing moment, and the angular rates are in the stability reference frame. The span efficiency factor or Oswald efficiency factor, denoted as e, is used as a parameter to account for the induced drag of the aircraft. The induced drag of the aircraft is the lift-dependent drag term seen in (3.4.6). In the induced drag term, A is the aspect ratio of the wing and is given by [28] as

$$A = \frac{b}{\bar{c}} \tag{3.4.7}$$

The lift-dependent drag term has two components, an inviscid part caused by induced velocities from the wake and a viscous part which is caused by increases in skin friction and pressure drag due to changes in angle of attack [30].

The stability reference frame angular rates P_S, Q_S, and R_S are expressed in terms of the body reference frame angular rates with the rotational matrix in (3.1.5),

$$\begin{bmatrix} P \\ Q \\ R \end{bmatrix}_S = \mathbf{R}_\alpha \begin{bmatrix} P \\ Q \\ R \end{bmatrix}_B \tag{3.4.8}$$

$$\begin{aligned} P_S &= P_B \cos\alpha + R_B \sin\alpha \\ Q_S &= Q_B \\ R_S &= -P_B \sin\alpha + R_B \cos\alpha \end{aligned} \tag{3.4.9}$$

The non-dimensional force and moment coefficients of Equations 3.4.2 are expressed in terms of the aerodynamic derivatives, as seen in Equations 3.4.6. These are called stability and control

derivatives and govern the stability and control behaviour of the aircraft. They are called derivatives as they specify the variation of aerodynamic forces and moments with respect to a small change in the perturbed aircraft state or control input. A particular derivative typically vary with airspeed, altitude, and angle of attack. These derivatives are non-dimensional, and describe the forces and moments acting on the aircraft as functions of α, β, the aircraft's angular rates defined in the stability reference frame P_S, Q_S, R_S, and the control surfaces of the aircraft. The stability and control derivatives are usually modelled in the stability reference frame, and are in the form

$$C_{(*)_{(\bullet)}} = \frac{\delta C_{(*)}}{\delta(\bullet)} \tag{3.4.10}$$

where $C_{(*)_{(\bullet)}}$ is the non-dimensional derivative of $C_{(*)}$ as a function of $(\bullet)$, e.g., C_{L_α} is the non-dimensional stability derivative of the lift produced by the aircraft due to the angle of attack of the aircraft. For a stability derivative, $(\bullet)$ is the aircraft state α, β, P_S, Q_S, or R_S. For a control derivative, $(\bullet)$ is the aircraft control input δ_A, δ_E, δ_R, or δ_F. The non-dimensional derivatives are normalized by the geometry of the aircraft the derivatives were extracted from. This allows the non-dimensional derivatives to be used for any size aircraft with the same design by rescaling them using the specific aircraft's reference geometry. Wind tunnel tests can therefore be performed using a smaller scale aircraft with an identical airframe as a larger aircraft to obtain the non-dimensional derivatives for the larger aircraft.

The aerodynamic stability and control derivatives are difficult to model and introduce most of the uncertainty in the modelled system. Several methods are used to determine the stability and control derivatives for a given airframe. Each method has its own advantages and disadvantages and may produce slightly different results. By using a combination of the methods, more insight into the stability and control derivatives can be obtained. A previous study by Beeton showed that AVL produces good results compared to first-principles methods based on empirical data [9]. AVL is a software package for aerodynamic and flight dynamic analysis of rigid aircraft of arbitrary configuration. It employs an extended vortex lattice model for lifting surface to determine the stability and control derivatives of a rigid aircraft for a described configuration. AVL is used as the primary method to determine the stability and control derivatives of the airframe used in this project.

From Figure 3.8, the horizontal and vertical stabilisers' geometry is defined with subscripts H and V respectively. The horizontal and vertical stabiliser moment arms are also shown in Figure 3.8, and are defined as the distance from the aircraft's centre of mass to the aerodynamic centres of the horizontal and vertical stabiliser respectively. The horizontal stabiliser volume ratio, denoted as $\bar{V}_H$, is another important geometric parameter: the measure of the aerodynamic effectiveness of the horizontal stabiliser as a stabilising device [28].

$$\bar{V}_H = \frac{S_H l_H}{S\bar{c}} \tag{3.4.11}$$

Similar to the above, the vertical stabiliser volume ratio, denoted as $\bar{V}_V$, is also an important geometric parameter which is the measure of the aerodynamic effectiveness of the vertical stabiliser as a directional stabilising device [28].

$$\bar{V}_V = \frac{S_V l_V}{Sb} \tag{3.4.12}$$

The centre of mass, indicated with the standard centre of mass symbol as shown in Figure 3.8, is located $\boldsymbol{\rho}$ from the arbitrary fixed reference point A. The centre of mass location is commonly measured from the leading edge of the standard reference chord. It varies as a function of aircraft loading, and in this project as a function of partial wing loss and stabiliser losses. The moment of inertia for a conventional symmetrical aircraft is given as a diagonal matrix, with I_{xx}, I_{yy} and I_{zz} as the diagonal components. For asymmetrical aircraft, the off-diagonal components also determine the moment of inertia of the aircraft (see (3.2.29)). In this project, the moment of inertia changes as a function of partial wing loss, partial horizontal stabiliser loss, and partial vertical stabiliser loss. The neutral point (NP) of the aircraft, also commonly measured from the leading edge of the standard reference chord, is the location of the centre of mass when the aircraft is statically neutrally stable, so that the centre of mass is equal to the aerodynamic centre of the aircraft [31]. The neutral point is used to determine the static margin of the aircraft which is discussed in detail in Chapter 4.

3.4.1.1 Obtaining the Aircraft's Stability and Control Derivatives

In this project, the focus is on the autonomous landing of a fixed-wing aircraft with partial wing loss and partial stabiliser losses, which is why the modelling of an aircraft with partial wing loss, partial horizontal stabiliser loss, and partial vertical stabiliser loss is required. To accomplish this, the aircraft's non-dimensional stability and control derivatives must be obtained for the aforementioned types of damage cases.

An aircraft with identical geometric properties and dimensions to the Phoenix Trainer 60 is constructed in AVL. A flat fuselage is added to represent the airframe of the aircraft. This is done to try to obtain more feasible lateral influences acting on the aircraft. There is the option to model a slender fuselage in AVL, but this is not recommended by the author due to the possibility of inaccurate results being obtained. The forces and moments are determined with respect to the fixed point A. The reference standard mean chord $\bar{c}$, the reference wing span b and the wing reference area S are all kept constant throughout the modelling process. All the aerodynamic effects of the partial wing loss, partial horizontal stabiliser loss, and partial vertical stabiliser loss are therefore encapsulated within the non-dimensional stability and control derivatives.

Three damage cases are investigated:

- Partial wing loss
- Partial horizontal stabiliser loss
- Partial vertical stabiliser loss

The aerodynamic stability and control derivatives were determined for partial wing and stabiliser losses in increments of 10% of the semi-spans or spans respectively. The damage cases are modelled as "tip losses" due to the modelling constraints encountered by AVL (see Figure 3.9). Control surface loss is also modelled for each damage case. Recall from Section 3.2.1 that the forces and moments are modelled at an arbitrary fixed point A. For the undamaged aircraft, point A coincides with the aircraft's centre of mass, hence the undamaged aircraft's centre of mass position is given to AVL as the arbitrary fixed point A. Note that AVL calculates the stability and control

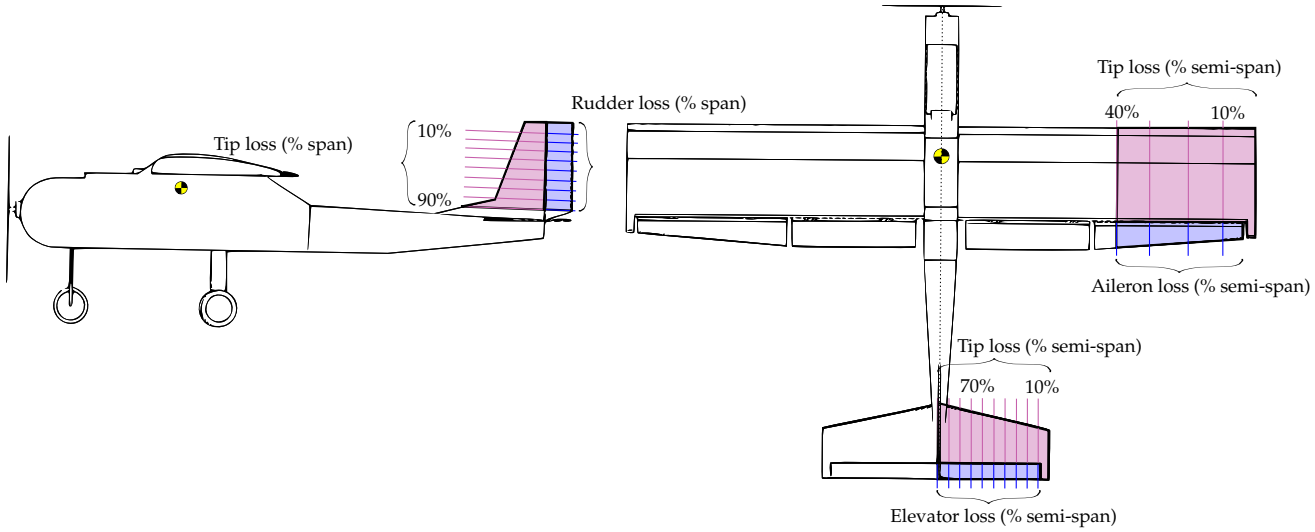

Figure 3.9: Damage cases with, the damage cases modelled as tip losses

derivatives at a given airspeed and angle of attack. The desired cruise airspeed and the expected angle of attack is supplied to AVL. The stability and control derivatives with respect to point A, at the given airspeed and angle of attack, are then determined with AVL. The derivatives that were obtained are used to analyse the effects of the damage cases on the aircraft's static stability and handing qualities.

Only the derivatives that are significant to the aircraft's dynamics and the derivatives that show a large change in magnitude with tip loss will be discussed in more detail in this section. The comprehensive set of stability and control derivative plots as a function of percentage wing and stabiliser losses are provided in Appendix C for the reader's convenience. For more information regarding the stability and control derivatives refer to [31], [32], and[33]. To obtain stability and control derivatives that are more comparable, the non-dimensional stability and control derivatives are scaled with the aircraft's reference geometry. These scaled non-dimensional stability and control derivatives are referred to as the dimensional stability and control derivatives and are denoted as

$$(*)_{(\bullet)} = \bar{q}Sl\frac{\delta C_{(*)}}{\delta(\bullet)}n \tag{3.4.13}$$

where l is $\bar{c}$ for pitching moment derivatives, b for rolling and yawing moment derivatives, and unity for force derivatives. The normalizing factor n is unity for incident and control deflection angles, $\bar{c}/2\bar{V}$ for pitch rate angles, and $b/2\bar{V}$ for roll and yaw rate angles. Note that the dimensional stability and control derivatives $(*)_{(\bullet)}$ are just scaled non-dimensional derivatives $C_{(*)_{(\bullet)}}$, hence the change with tip loss is identical. The dimensional stability and control derivatives are then scaled with the maximum expected aircraft states and control inputs. The maximum expected aircraft states and control inputs remain constant through all the tip loss cases and will therefore only scale the forces and moments and do not change the results. Also note that the non-dimensional stability and control derivatives determined with AVL define the aerodynamic properties of the specific aircraft airframe at a specific airspeed and angle of attack. From this analysis, it cannot necessarily be assumed that all aircraft will behave similarly to identical damage cases.

Partial Wing Loss

For the partial wing loss case, tips from the right wing are removed in increments of 10% up to 40%, as shown in Figure 3.9. Beeton showed that for straight and level flight, the aircraft cannot be trimmed for high percentages of partial wing loss due to aileron saturation [9]. Therefore the partial wing loss case is only modelled up to 40% in this project. Nevertheless, the behaviour of the aircraft due to partial wing loss can still be observed and analysed.

Partial wing loss will result in:

1. Lift limitations
2. A rolling moment due to differential lift on the wings, and lateral control limitations due to aileron loss
3. Effect on the longitudinal stability
4. A yawing moment due to differential drag on the wings

Stability implications are less significant for partial wing loss. Due to the asymmetric nature of partial wing loss, off-axis control is also expected. Partial wing loss does not have a significant effect on the side forces produced by the aircraft and will not be discussed here.

1. Lift Force Derivatives

It is clear from Figure 3.11 (a) and (b) that the overall lift of the aircraft will decrease with partial wing loss. Intuitively this is expected, as the wing is the primary lifting surface of the aircraft. The static lift force derivative $\bar{L}_0$, which quantifies the lift produced by the aircraft at zero angle of attack, is expected to decrease when the aircraft suffers damage to its wing. This is mainly because the static lift force is primarily a result of the camber and size of the wing. Furthermore, the aircraft's lift-curve slope $\bar{L}_\alpha$, which quantifies the increase in lift as a function of angle of attack, also decreases when the aircraft suffers partial wing loss. This is an important derivative which is reflected in the aircraft's stability, control, stall speed, and response to turbulence. With a lower $\bar{L}_\alpha$, a higher angle of attack is necessary to produce the lift required for the aircraft to remain airborne at a given airspeed. The lift-curve shown in Figure 3.10 shows the lift force produced by the aircraft as a function of angle of attack. The decrease in the static lift derivative $\bar{L}_0$ and the lift curve slope $\bar{L}_\alpha$ with partial wing loss is clearly seen in Figure 3.10. Note that at an angle of attack of approximately 14°, which is known as the critical angle of attack, $\bar{L}_\alpha$ equals zero, hence the lift force produced by the aircraft reaches a maximum and starts to decrease with an increase in angle of attack. This is a result of flow separation over the wing which prevents the wing from producing lift, and is known as stall. Also take note that the lift force in the body reference frame is a function of airspeed. From (3.4.2) it is seen that in order to produce a constant lift force in the body reference frame, the angle of attack must increase with a decrease in airspeed and vice versa. This causes the aircraft having a higher stall speed and poses a problem when attempting to land the aircraft due to the higher landing speed required to prevent the aircraft from stalling before touchdown.

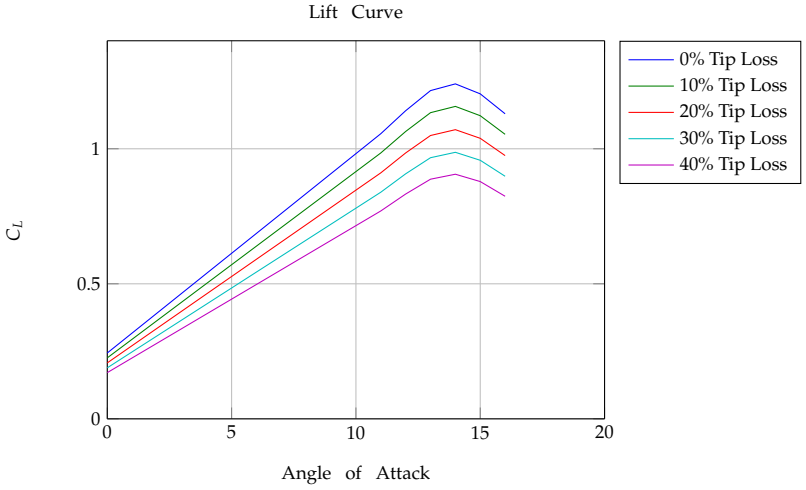

Figure 3.10: Lift curve with partial wing loss

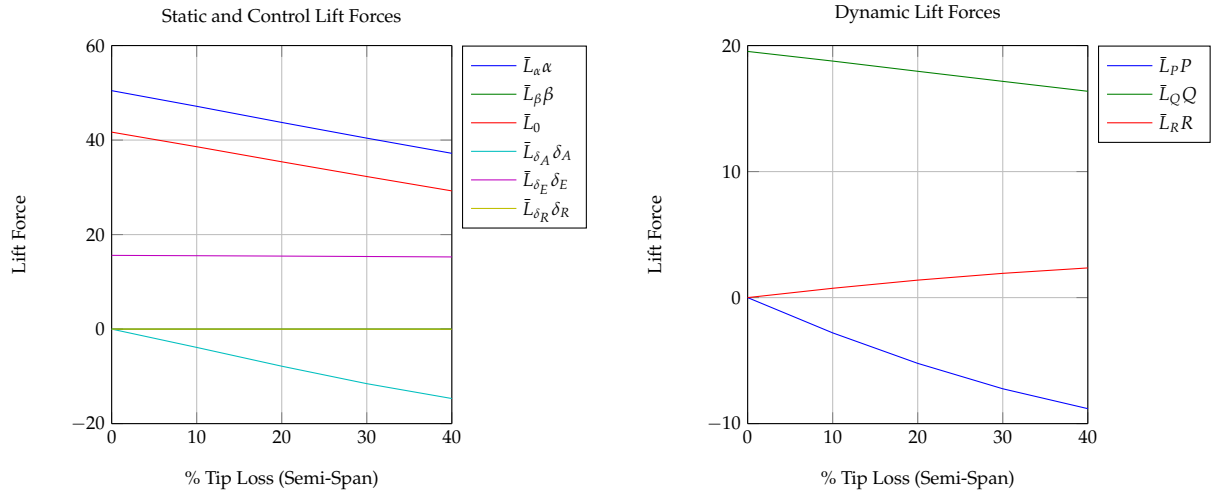

(a) Static and control lift forces

(b) Dynamic lift forces

Figure 3.11: Aerodynamic lift forces with partial wing loss

The dynamic lift forces do not have a significant effect on the lift produced by the aircraft and typically has little to no effect on the aircraft dynamics. Therefore these forces will not be discussed in detail. Nevertheless their effect was as expected and is shown in Figure 3.11 (b). Figure 3.14 (b) shows the drag and zero-lift drag force of the aircraft with partial wing loss. The drag decreases with a decrease in lift. The zero-lift drag D_0 decreases due to the decreasing parasitic drag which resulted from the tip loss.

2. Rolling Moment Derivatives

When an aircraft is symmetrical about its $X_B Z_B$-plane, it tends to produce no static rolling moment, as shown in Figure 3.12 (a). However, this changes when the aircraft suffer partial wing loss and becomes asymmetrical. A static rolling moment derivative L_0 is introduced when the aircraft suffers partial wing loss. This is due to the wing producing differential lift. The static lift produced by the damaged wing is less than the static lift produced by the undamaged wing, resulting in an induced static rolling moment. The static rolling moment quantifies the rolling moment produced by the aircraft at zero angle of attack. The aforementioned also applies to the rolling moment due

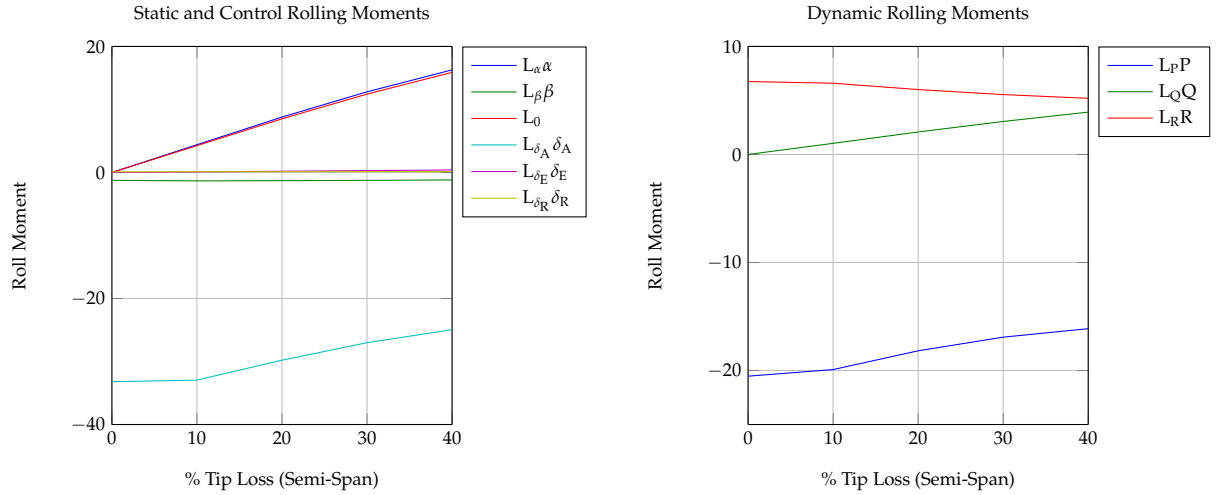

(a) Static and control rolling moments (b) Dynamic rolling moments

Figure 3.12: Aerodynamic rolling moments with partial wing loss

to angle of attack derivative L_α, as shown in Figure 3.12 (a). The lift due to the angle of attack produced by the damaged wing is less than the lift due to the angle of attack produced by the undamaged wing, resulting in an induced rolling moment. Note that if the lift increases with angle of attack, then so will the induced rolling moment. Recall that a positive rolling moment is defined as seen in Figure 3.2, so that when the aircraft suffers partial right wing loss, one would expect the left wing to generate more lift than the right wing, resulting in the aircraft having a rolling moment to the right (positive rolling moment). This agrees with the induced static rolling moments shown in Figure 3.12 (a).

The rolling moment due to body angular rates derivatives, especially L_P and L_R, together with the control rolling moment derivative L_{δ_A} dominate the rolling moment behaviour of a symmetrical aircraft. When the aircraft suffers partial wing loss, the aircraft becomes asymmetrical and the static rolling moments start to dominate the rolling moment behaviour. This will cause the aircraft always experiencing a rolling moment, which needs to be countered by a rolling moment produced by the ailerons if straight and level flight is required. However, from Figure 3.12 (a) it is shown that when the aircraft suffers partial wing loss, the efficiency of the control rolling moment derivative L_{δ_A} decreases significantly due to partial actuator loss, while the induced static rolling moment derivatives L_0 and L_α increase significantly. This poses a problem, because at some point there will not be enough control authority to counter the sum of the static rolling moments produced by the high percentage of partial wing loss. This limits the amount of partial wing loss if straight and level flight is required.

3. Pitching Moment Derivatives

Even though the wing does not produce the majority of the pitching moment, partial wing loss does have an effect on the pitching moment of the aircraft. This effect is due to the aerodynamic centre of the wing not being at the centre of mass of the aircraft, resulting in the lift produced by the wing to induce a pitching moment. From Figure 3.13 (a) and (b) it is shown that the derivatives M_0, M_α and M_{δ_A} is affected by partial wing loss, where M_0 denotes the static pitching moment and quantifies the pitching moment produced by the aircraft at zero angle of attack. Figure 3.13 (a) shows that the aircraft has a negative static pitching moment, therefore the aircraft would nat-

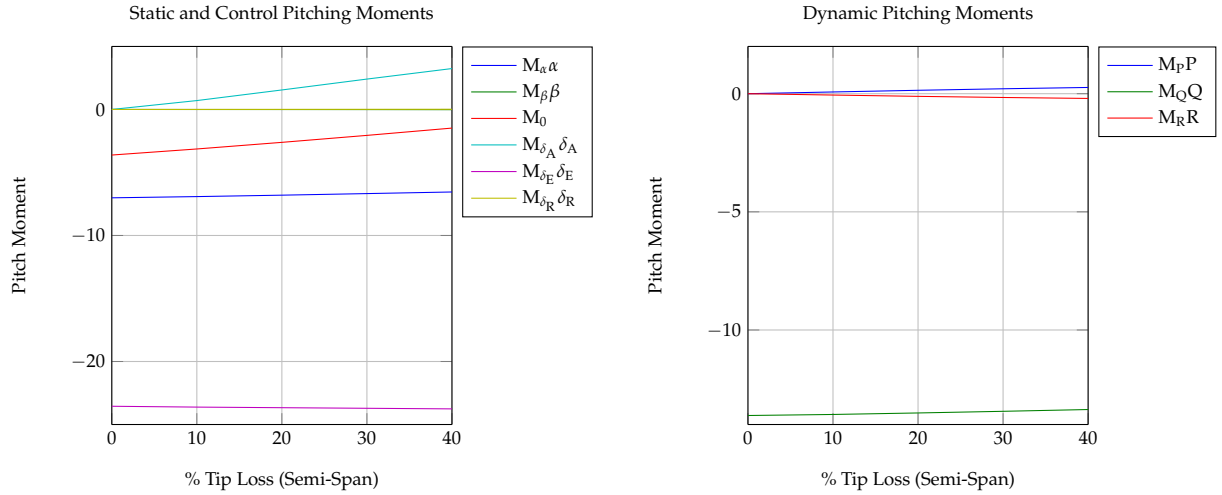

(a) Static and control pitching moments (b) Dynamic pitching moments

Figure 3.13: Aerodynamic pitching moments with partial wing loss

urally tend to pitch nose-down. This tends to become more negative with the increase in airspeed and is referred to as tuck [33]. It can lead to handling quality problems during high-speed dive recoveries [33]. The pitching moment derivative M_α, often referred to as the pitching stiffness, quantifies the degree of static longitudinal stability of the aircraft. This is the aircraft's tendency to return towards its trim condition once disturbed. Figure 3.13 (a) shows a negative M_α. This is expected because a negative M_α implies a longitudinal static stable aircraft. As the aircraft suffers partial wing loss, the aircraft remains longitudinal statically stable. Static stability is discussed in more detail in Chapter 4.

The dynamic pitching moments do not change significantly with partial wing loss and will not be discussed here. The dynamic pitching moments are shown in Figure 3.13 (b). From Figure 3.13 (a) one can note that the control derivative M_{δ_E} produces the majority of the pitching moment of the aircraft and that it is not affected by partial wing loss. Minimal pitching moment control authority is therefore lost.

4. Yawing Moment Derivatives

Similar to the rolling moment, an aircraft that is symmetrical about its $X_B Z_B$-plane does not experience a static yawing moment N_0. However, when the aircraft becomes asymmetrical due to partial wing loss, a static yawing moment is induced, as shown in Figure 3.14 (a). This is expected, because the static differential lift on the wing results in differential drag on the wing, which will induce a yawing moment. Furthermore, a yawing moment is also induced due to the angle of attack N_α. When the aircraft flies at a higher angle of attack, more differential lift is produced, and thus more differential induced drag is also produced (see (3.4.5)). This causes the aircraft to experience a larger yawing moment. Recall that a positive yawing moment was defined in Figure 3.2. It is therefore expected the aircraft with partial right wing loss will have a negative induced yawing moment. This agrees with the induced static yawing moments shown in Figure 3.14 (a). Figure 3.14 (a) shows that a rudder control deflection N_{δ_R} produces the majority of the yawing moment, and that it is not affected by partial wing loss. However, the derivative N_{δ_A}, which quantifies the adverse yawing moment that is a result of the aileron deflections, is affected by partial wing loss. An aileron deflection produces differential lift and thus differential drag across the wing, resulting

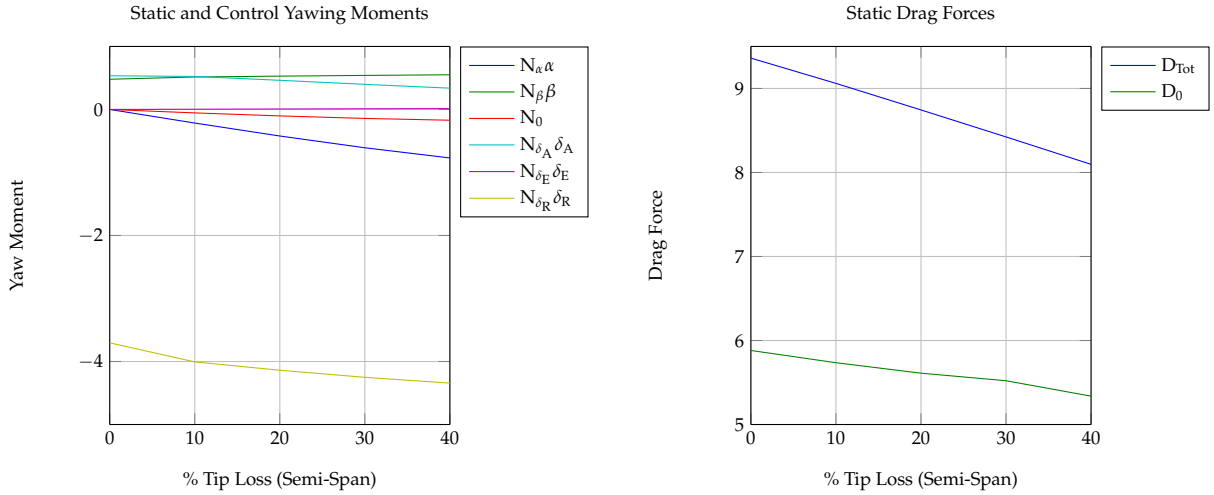

(a) Static and control yawing moments

(b) Static drag forces

Figure 3.14: Aerodynamic yawing moment and drag forces with partial wing loss

in a yawing moment to be produced that tends to yaw the nose of the aircraft into the opposite direction to that of the desired onset of a turn. As shown in Figure 3.14 (a), this effect is reduced with partial wing loss. This is due to less differential drag induced by the smaller aileron.

Partial Horizontal Stabiliser Loss

For the partial horizontal stabiliser loss case, the right side of the horizontal stabiliser is removed in 10% increments up to 100% of the semi-span $0.5b_H$, as shown in Figure 3.9. The horizontal stabiliser's primary function is to stabilise the longitudinal movements of the aircraft. It is therefore expected that partial horizontal stabiliser loss will result in:

1. Decrease in lift due to surface loss
2. Effect on longitudinal stability and longitudinal control limitations

Thus, partial horizontal stabiliser loss primarily affects the aircraft's longitudinal stability, but due to its potential asymmetric nature, off-axis control is also present. Partial horizontal stabiliser loss does not have major effects on the side forces, rolling moments, and yawing moments of the aircraft and will not be discussed here.

1. Lift Force Derivatives

Figure 3.15 shows that the overall lift of the aircraft slightly decreases with partial horizontal stabiliser loss. As mentioned, the wing produces the majority of the aircraft's lift, but some lift is also produced by the horizontal stabiliser and fuselage, as shown in (3.4.14). The non-dimensional derivative C_{L_α} is a combination of the lift produced due to angle of attack from the wing-fuselage and horizontal stabiliser [33],

$$C_{L_\alpha} = C_{L_{\alpha_{WF}}} + \frac{\eta_H S_H C_{L_{\alpha_H}}}{S}\left(1 - \frac{d\epsilon}{d\alpha}\right) \tag{3.4.14}$$

where subscript H denotes horizontal stabiliser, WF denotes wing-fuselage, $\eta_H = \bar{q}_H/\bar{q}$ is the dynamic pressure ratio, and $\frac{d\epsilon}{d\alpha}$ is the change in the downwash angle ϵ with the change in angle of attack. The downwash angle is difficult to predict theoretically and is usually determined

with wind tunnel data [34]. For conceptual purposes, it is assumed that $\frac{d\epsilon}{d\alpha}$ remains the same for all partial horizontal stabiliser loss cases, and it is therefore ignored in the stability and control derivatives (it will only scale these derivatives). A slight decrease in the overall lift is expected due to the decrease in $C_{L_{\alpha_H}}$ and S_H. Note that the decrease in lift is at the aft of the aircraft, and will cause the neutral point to shifting forward. This can pose a problem to the aircraft's longitudinal static stability if the neutral point shifts further forward and past the aircraft's centre of mass.

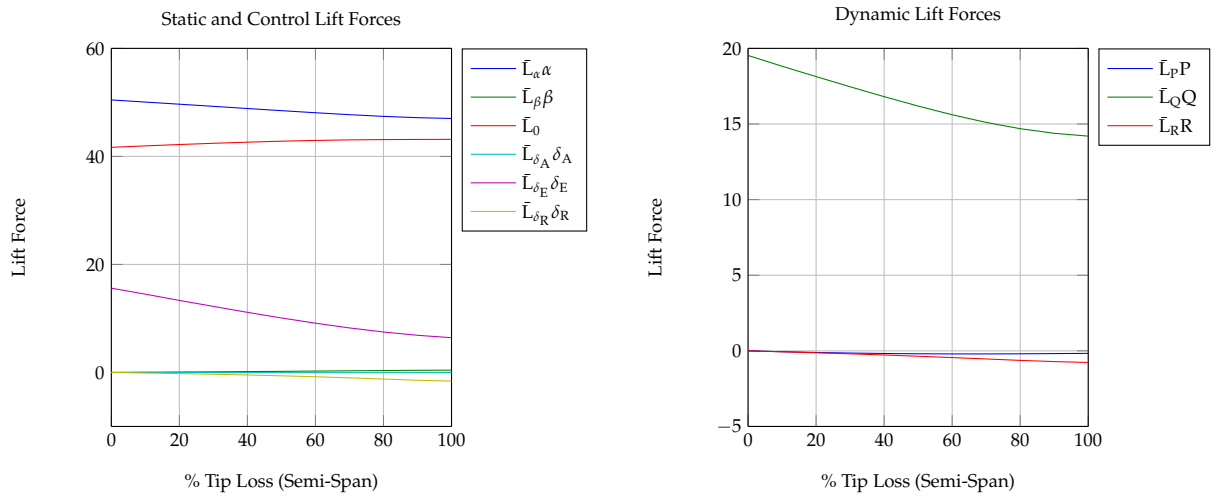

(a) Static and control lift forces

(b) Dynamic lift forces

Figure 3.15: Aerodynamic lift forces with partial horizontal stabiliser loss

2. Pitching Moment Derivatives

As expected, when the aircraft suffers partial horizontal stabiliser loss, a significant effect is observed on the pitching moment stability and control derivatives. The static pitching moment derivative M_0, which quantifies the pitching moment produced by the aircraft at zero angle of attack, increases with horizontal stabiliser loss, as shown in Figure 3.16 (a). Therefore the aircraft will experience a greater nose-down pitching moment. The pitching stiffness derivative M_α, which quantifies the degree of the longitudinal static stability of the aircraft, is given in non-dimensional form by [33] as,

$$C_{m_\alpha} = \frac{C_{L_\alpha}(X_{cm} - X_{ac_{WF}})}{\bar{c}} - C_{L_{\alpha_H}} \bar{V}_H \tag{3.4.15}$$

The non-dimensional derivative M_α becomes less negative with partial horizontal stabiliser loss, but remains negative for all the losses. The aircraft therefore remains longitudinally statically stable for all partial horizontal stabiliser loss cases. As shown in equation (3.4.15), the non-dimensional derivative C_{m_α} is a function of the location and size of the horizontal stabiliser. Note that through $\bar{V}_H$, the location l_H and horizontal stabiliser area S_H change the value of the non-dimensional derivative C_{m_α}. The location l_H of the horizontal stabiliser does not change with tip loss, but the area S_H becomes less. This causes a smaller C_{m_α}, as shown in Figure 3.16. The pitch damping derivative C_{m_Q}, given in its non-dimensional form by [33] as,

$$C_{m_Q} = -\frac{2C_{L_{\alpha_H}} \eta_H \bar{V}_H l_H}{\bar{c}} \tag{3.4.16}$$

quantifies the pitching moment produced by the aircraft due to pitch rate. The pitch damping derivative decreases as the aircraft suffers from horizontal stabiliser loss, as shown in Figure 3.16 (b). This non-dimensional derivative is related to the derivative C_{L_α} through the normalised distance to the tail-plane and the tail volume ratio. The normalised length to the tail-plane $l_H/\bar{c}$ remains constant with partial horizontal stabiliser loss, therefore as C_{L_α} and S_H decreases, C_{m_Q} also decreases. It is interesting to note that the horizontal stabiliser volume ratio $\bar{V}_H$ is an important parameter affecting both C_{m_α} and C_{m_Q}.

The control pitching moment derivative M_{δ_E}, which quantifies the pitching moment produced by an elevator deflection, decreases with horizontal stabiliser loss. This is expected because the elevator control surface becomes smaller. This poses a problem while trying to trim the aircraft for straight and level flight, because the elevator produces the majority of the control pitching moment needed to trim the aircraft. By observing Figure 3.16 (a), one can note that a larger elevator deflection is needed to counter the static pitching moments. This is due to the control derivative decreasing much faster than the static pitching moment derivatives with partial horizontal stabiliser loss .

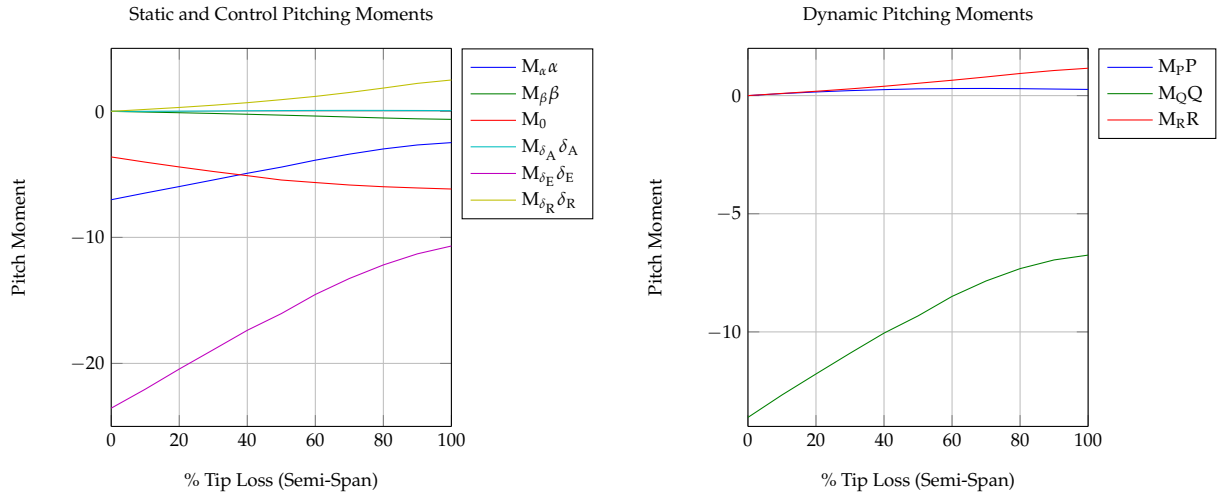

(a) Static and control pitching moments

(b) Dynamic pitching moments

Figure 3.16: Aerodynamic pitching moments with partial horizontal stabiliser loss

Similar to the partial wing loss cases, when the aircraft suffers partial horizontal stabiliser loss, the aircraft becomes asymmetrical, which will cause the aircraft to experience a rolling moment due to differential lift, and a yawing moment due to differential drag. The effect is not as significant as in the partial wing loss case because the horizontal stabiliser produces significantly less lift than the wing.

Partial Vertical Stabiliser Loss

For the partial vertical stabiliser loss case, the vertical stabiliser is removed in 10% increments up to 90% of the span b_V, as shown in Figure 3.9. The primary function of the vertical stabiliser is to reduce aerodynamic sideslip and to provide directional stability to the aircraft. It is therefore expected that partial vertical stabiliser loss will have significant effects on:

1. Side force derivatives and side force control limitations

2. The lateral-directional stability and directional control limitations

Therefore, partial vertical stabiliser loss primarily affects the aircraft's directional stability. Partial vertical stabiliser loss does not have major effects on the lift forces, rolling moments, and pitching moments of the aircraft and will not be discussed here.

1. Side Force Derivatives

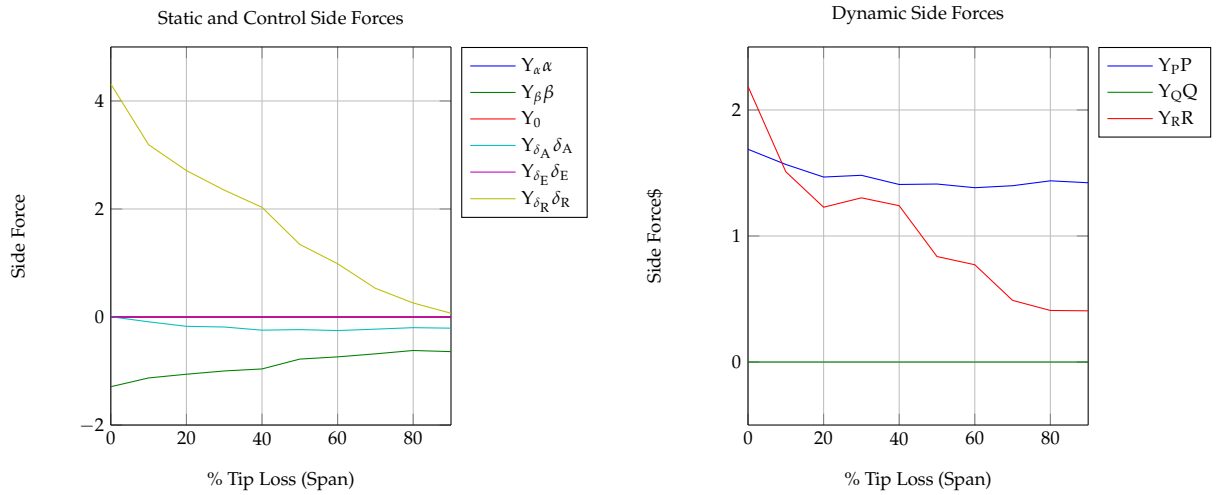

(a) Static and control side forces (b) Dynamic side forces

Figure 3.17: Aerodynamic side forces with partial vertical stabiliser loss

From Figure 3.17 (a), the magnitude of the derivative Y_β, which is an important derivative in Dutch roll dynamics, decreases with partial vertical stabiliser loss. The wing, fuselage, and vertical stabiliser all contribute to the derivative Y_β, but the wing and fuselage contributions are rather small and sometimes negligible. The non-dimensional derivative C_{y_β} is given by [33] as

$$C_{y_\beta} = -\frac{C_{L_{\alpha_V}} \eta_V S_V}{S} \tag{3.4.17}$$

where $C_{L_{\alpha_V}}$ is the lift-curve slope of the vertical tail, $\eta_V = \bar{q}_V / \bar{q}$ is the dynamic pressure ratio, and S_V is the vertical stabiliser area. The derivative C_{y_β} depends strongly on the vertical stabiliser area and the lift-curve slope of the vertical stabiliser. Therefore, a decrease in the derivative Y_β is expected due to the decrease in S_V.

The derivative Y_{δ_R}, which quantifies the side force produced by the rudder, is given in its non-dimensional form by [33] as

$$C_{y_{\delta_R}} = \alpha_{\delta_R} \left(\frac{C_{L_{\alpha_V}} \eta_V S_V}{S} \right) \tag{3.4.18}$$

where α_{δ_R} is the rudder angle-of-attack-effectiveness parameter, which is a function of the rudder-chord-to-vertical-tail-chord ratio ($\bar{c}_R / \bar{c}_H$). Note that the derivative Y_{δ_R} decreases significantly with vertical stabiliser loss (see Figure 3.17 (a)). The aircraft thus loses its control authority or ability to produce a side force at high percentages of partial vertical stabiliser loss. The rudder is the only control surface capable of producing a side force on the aircraft, thus losing part of the rudder can become problematic for aircraft handling qualities. The derivative Y_{δ_R} depends strongly on

the vertical stabiliser area and the lift-curve slope of the vertical stabiliser. The side force Y_R, which quantifies the side force produced due to yaw rate motion, shows a significant change with vertical stabiliser loss, as shown in Figure 3.17 (b). However, it commonly has little significance on the aircraft dynamics and is usually ignored.

2. Yawing Moment Derivatives

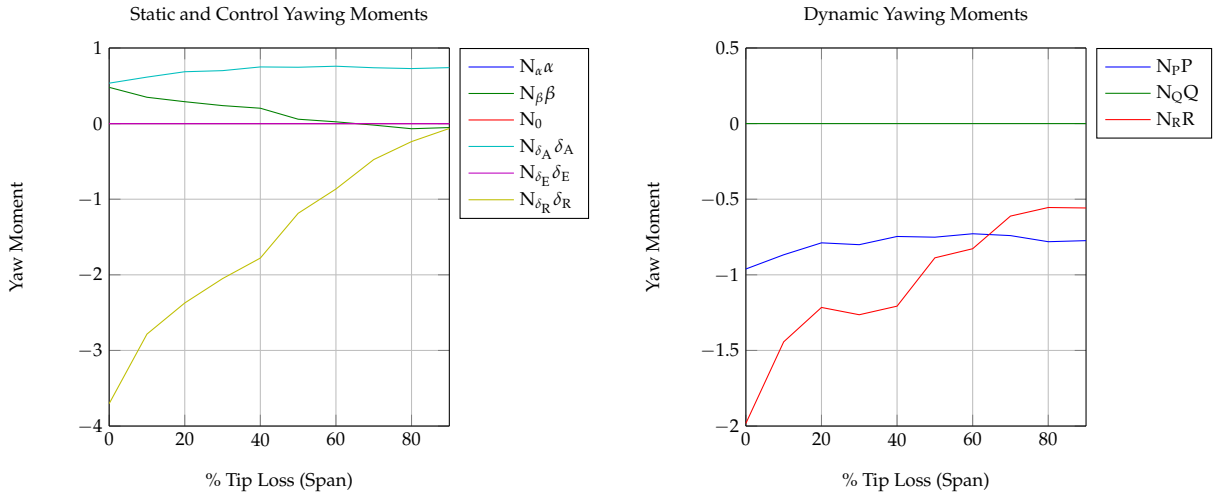

(a) Static and control yawing moments

(b) Dynamic yawing moments

Figure 3.18: Aerodynamics yawing moment with partial vertical stabiliser loss

The yawing moment due to sideslip N_β describes the aircraft's natural tendency to weathercock into the airflow. This derivative quantifies the degree of directional static stability of the aircraft. For a directionally statically stable aircraft, the non-dimensional derivative C_{n_β} must be greater than zero, therefore always positive. This derivative determines the natural frequency of the Dutch roll oscillatory mode, and is of high importance in the lateral-directional static and dynamic stability, and control of the aircraft. The derivative is a combination of yawing moments from the wing, fuselage, and vertical stabiliser. The vertical stabiliser's contribution of this non-dimensional derivative is expressed by [33] as

$$C_{n_{\beta_V}} = C_{L_{\alpha_V}} \eta_V \bar{V}_V \tag{3.4.19}$$

Figure 3.18 shows that the derivative N_β, decreases with partial vertical stabiliser loss. Note that at about 60%, the derivative N_β becomes negative, which means the aircraft becomes directionally statically unstable and will not point into the relative wind direction. Note that (3.4.19) cannot become negative, thus when the derivative N_β becomes negative, the contribution from the wing-fuselage is starting to dominate the yawing moment derivative N_β resulting in it to become negative (static stability is discussed in more detail in Chapter 4). From (3.4.19) it is noted that this derivative depends strongly on the vertical stabiliser volume ratio and the lift-curve slope of the vertical stabiliser. A decrease in N_β is therefore expected due to the decrease in $\bar{V}_V$.

The yaw damping non-dimensional derivative C_{n_R} is generally due to a combination from the wing-fuselage and the vertical stabiliser. The wing and fuselage are not changed when the aircraft suffer vertical stabiliser losses, therefore only the contribution from the vertical stabiliser

is considered. The yaw damping derivative contribution from the vertical stabiliser $C_{n_{R_V}}$ is given by [33] as

$$C_{n_{R_V}} = -\left(\frac{2C_{L_{\alpha_V}}\eta_V l_V \bar{V}_V}{b}\right) \tag{3.4.20}$$

The non-dimensional derivative $C_{n_{R_V}}$ quantifies the yawing moment produced by the aircraft due to a yaw rate motion. This derivative is due to the angle of incidence on the vertical stabiliser during a yaw rate motion and contributes to the damping of the Dutch roll mode of the aircraft in a major way, which will affect the aircraft's handling qualities. From Figure 3.18 (b), the derivative N_R decreases in magnitude with vertical stabiliser loss. Note from (3.4.20) that the derivative depends strongly on the vertical stabiliser volume ratio and the moment arm of the vertical stabiliser. Hence a decrease in the derivative N_R is expected due to a smaller vertical stabiliser volume ratio. A change in damping of the Dutch roll mode is also expected. Dynamic stability is discussed in more detail in Chapter 4.

The comprehensive set of stability and control derivative plots as a function of percentage wing and stabiliser losses are provided in Appendix C for the reader's convenience.

3.4.2 Gravitational Forces and Moments

In the inertial reference frame, forces and moments due to gravity are adequately modelled as $\boldsymbol{F} = [0\ 0\ mg]^T$ in the down direction and $\boldsymbol{M} = \boldsymbol{F} \times \bar{\boldsymbol{\rho}}$ around point A. The forces are with respect to the inertial reference frame and are transformed to the body reference frame forces using the DCM in (3.3.13).

$$\begin{aligned}
\begin{bmatrix} X^G \\ Y^G \\ Z^G \end{bmatrix}_{\mathrm{B}} &= \begin{bmatrix} \cos\Psi\cos\Theta & \sin\Psi\cos\Theta & -\sin\Theta \\ \cos\Psi\sin\Theta\sin\Phi - \sin\Psi\cos\Phi & \sin\Psi\sin\Theta\sin\Phi + \cos\Psi\cos\Phi & \cos\Theta\sin(\phi) \\ \cos\Psi\sin\Theta\cos\Phi + \sin\Psi\sin\Phi & \sin\Psi\sin\Theta\cos\Phi - \cos\Psi\cos\Phi & \cos\Theta\cos(\phi) \end{bmatrix} \begin{bmatrix} 0 \\ 0 \\ mg \end{bmatrix}_{\mathrm{E}} \\
&= \begin{bmatrix} -\sin\Theta \\ \cos\Theta\sin\Phi \\ \cos\Theta\cos\Phi \end{bmatrix}_{\mathrm{B}} mg
\end{aligned}$$

The moments due to gravity in the body reference frame are given by

$$\begin{bmatrix} L^G \\ M^G \\ N^G \end{bmatrix}_{\mathrm{B}} = \begin{bmatrix} -\sin\Theta \\ \cos\Theta\sin\Phi \\ \cos\Theta\cos\Phi \end{bmatrix}_{\mathrm{B}} mg \times \begin{bmatrix} \Delta x \\ \Delta y \\ \Delta z \end{bmatrix}_{\mathrm{B}} \tag{3.4.21}$$

where $[\Delta x\ \Delta y\ \Delta z]^T$ is the position vector from point A to the centre of mass.

3.4.3 Thrust Forces and Moments

The engine or motor thrust T is controlled by a throttle command T_c. The relationship between the thrust and the throttle is modelled as a simple first-order lag response with a time constant τ_T.

$$\dot{T} = -\frac{1}{\tau_T}T + \frac{1}{\tau_T}T_c \tag{3.4.22}$$

For a tractor configuration aircraft, it is assumed that the thrust vector lies along the X_B-axis acting on the undamaged aircraft centre of mass which coincides with the arbitrary fixed point A. The motor is fixed to the body and does not change position due to any of the aforementioned damage cases, and therefore the thrust will only produce a force in the X_B direction. The forces and moments due to thrust can thus be defined as

$$\begin{aligned} X^T = T \ ; \ Y^T = 0 \ ; \ Z^T = 0 \\ L^T = 0 \ ; \ M^T = 0 \ ; \ N^T = 0 \end{aligned} \tag{3.4.23}$$

3.5 Summary

In this chapter, a mathematical representation or model of the aircraft was developed. The model was developed around a number of defined reference frames. The model describes the behaviour of both a conventional symmetrical aircraft and an unconventional asymmetrical aircraft. It accomplishes this by incorporating the full moment of inertia matrix and allowing for a shift of the centre of mass of the aircraft. For a conventional symmetrical aircraft, the former only consists of the diagonal components and the latter is zero.

Furthermore, the forces and moments acting on the aircraft were described in detail. The aerodynamic forces and moments change as a function of percentage of wing loss, percentage of horizontal stabiliser loss, and percentage of vertical stabiliser loss. Figure 3.19 summarises the

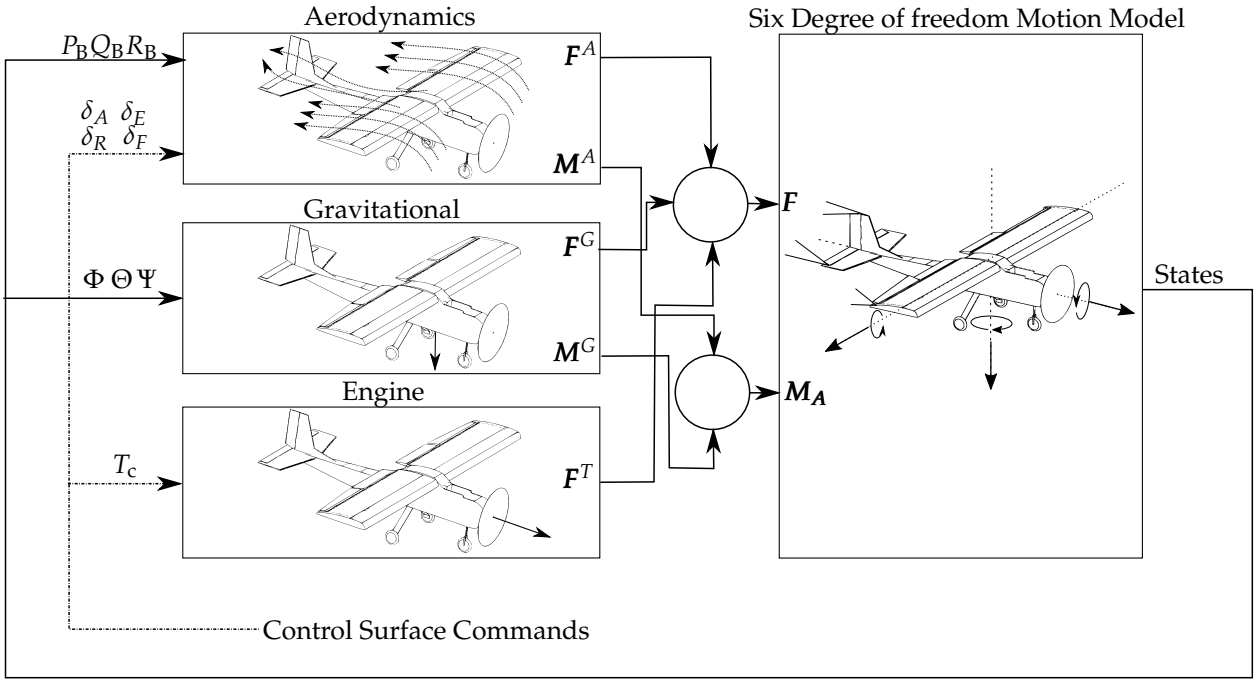

Figure 3.19: Aircraft model block diagram

aircraft model in a block diagram representation. Aerodynamic, gravitational and engine forces and moments, given the aircraft states and control surface deflections, act on the aircraft to change its states. By issuing the appropriate control surface commands, the aircraft can be manipulated or steered to perform the desired manoeuvres.

The notation and reference frames described and model developed in this chapter are used throughout this thesis. The nonlinear dynamic aircraft model that was developed can now be used to analyse the dynamic stability of the aircraft, will serve as the basis for the control system design, and to develop a nonlinear simulation of the aircraft.

In this chapter, the stability and control characteristics of the aircraft, also known as the flying qualities of the aircraft, will be analysed. In this project, the stability and control characteristics of the aircraft change as a function of percentage of wing loss, percentage of horizontal stabiliser loss, and percentage of vertical stabiliser loss respectively. In general, the stability and control characteristics cover the following areas:

- Longitudinal static stability - Speed stability, phugoid and flight path stability.
- Longitudinal dynamic stability - Short-period mode dynamics and longitudinal control.
- Lateral-directional static stability - Static roll stability, static yaw stability.
- Lateral-directional dynamic stability - Dutch roll mode dynamics, roll mode dynamics, spiral stability, roll control and directional control in cross winds.

Consider that at some instant, the aircraft is disturbed from steady equilibrium flight by a control input or an atmospheric influence such as a gust. The aircraft is said to be statically stable if after being disturbed, it eventually returns to a steady flight equilibrium, without active control inputs. The dynamic stability of the aircraft is concerned with the transient behaviour of the aircraft while returning to steady equilibrium flight. An aircraft is said to be dynamically stable if its transient response has acceptable damping. This chapter is divided into two main sections. The first section covers the static stability of the aircraft. This involves the analysis of the longitudinal static stability and the lateral-directional static stability. The second section covers the dynamic stability of the aircraft. This involves using the small perturbation theory to linearise the full nonlinear aircraft dynamics at a convenient flight equilibrium, followed by the analysis of the different natural modes of motion of the aircraft.

4.1 Static Stability Analysis

Static stability is defined as the tendency of an aircraft to produce forces and moments which directly oppose an instantaneous perturbation of a motion variable from a steady state flight condition [33]. Even though several criteria need to be satisfied for an aircraft to be statically stable, only the criteria that are more important to flying qualities are discussed in this chapter. These include the longitudinal, lateral, and directional static stability of the aircraft. An aircraft that is longitudinally, laterally, or directionally statically unstable can still be stabilised given that sufficient control authority is available. A statically unstable manned aircraft is typically stabilised with fly-by-wire control systems that implement stabilising inner-loop control laws through which

the human pilot controls the aircraft. A statically unstable autonomous unmanned aircraft is typically stabilised by the inner-loop control laws and controlled by middle and outer loop control laws.

4.1.1 Longitudinal Static Stability

An aircraft is said to be *longitudinally* statically stable if a small increase/decrease in the angle of attack will produce a pitching moment to decrease/increase the angle of attack of the aircraft. The

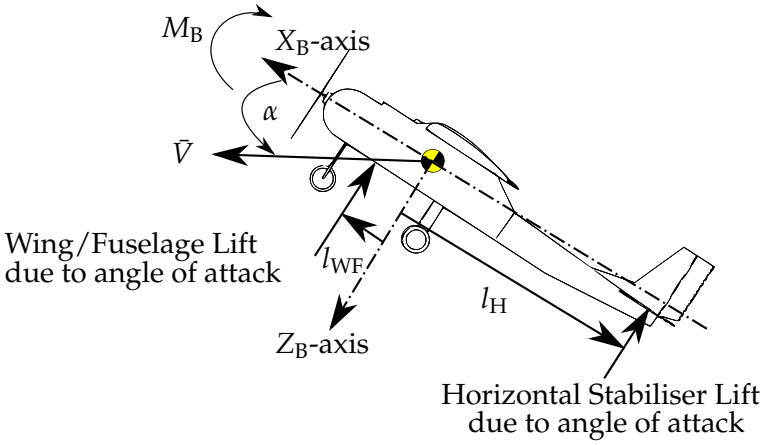

Figure 4.1: Pitching moment due to lift force on the wing/fuselage and horizontal stabiliser

pitching moment derivative with respect to the angle of attack can be expressed in terms of the lift derivative with respect to the angle of attack and the moment arms of the wing-fuselage and horizontal stabiliser respectively [33]:

$$C_{m_\alpha} = \frac{C_{L_\alpha}(X_{\text{cm}} - X_{ac_{\text{WF}}})}{\bar{c}} - C_{L_{\alpha_H}} \bar{V}_{\text{H}} \tag{4.1.1}$$

where $C_{L_\alpha} > 0$ and $C_{L_{\alpha_H}} > 0$. From Figure 4.1 and equation 4.1.2, note that the horizontal stabiliser will have a stabilising effect on the aircraft, and that the wing-fuselage can have either a stabilising or destabilising effect depending on the location of the aerodynamic centre of the wing-fuselage. The lift derivative with respect to angle of attack from the horizontal stabiliser will cause the aircraft experiencing a negative pitching moment.

The pitching moment derivative with respect to the angle of attack can also be rewritten in terms of the total lift derivative with respect to the angle of attack and the neutral point of the aircraft,

$$C_{m_\alpha} = \frac{C_{L_\alpha}(X_{\text{cm}} - X_{\text{np}})}{\bar{c}} \tag{4.1.2}$$

where $C_{L_\alpha} > 0$. A negative C_{m_α} yields a longitudinally statically stable aircraft. Then, if $X_{\text{cm}} < X_{\text{np}}$, the aircraft is longitudinally statically stable. If $X_{\text{cm}} = X_{\text{np}}$, the aircraft is statically neutrally stable, and if $X_{\text{cm}} > X_{\text{np}}$, the aircraft is longitudinally statically unstable. From (4.1.2) the term

$$\text{Static Margin} = -\left(\frac{X_{\text{cm}} - X_{\text{np}}}{\bar{c}}\right) \tag{4.1.3}$$

is known as the static margin of the aircraft, where a positive static margin yields a longitudinally statically stable aircraft and a negative static margin yields a longitudinally statically unstable

aircraft. The static margin of the aircraft strongly depends on the neutral point and centre of mass locations. Note that the neutral point is the most aft location of the centre of mass for which the aircraft would remain longitudinally statically stable.

Figure 4.2 shows how the neutral point and centre of mass of the aircraft used in this project shift with the percentage of wing loss and the percentage of stabiliser losses respectively. The neutral point location always remains more aft than the centre of mass location. The aircraft therefore remains longitudinally statically stable for all the damage cases. As mentioned, the aircraft used for this project is a trainer aircraft. Trainer aircraft are designed to be very stable in order to achieve high handling quality to ensure that amateur RC pilots can fly them. For this reason, the aircraft remains longitudinally statically stable even for a large amount of horizontal stabiliser loss.

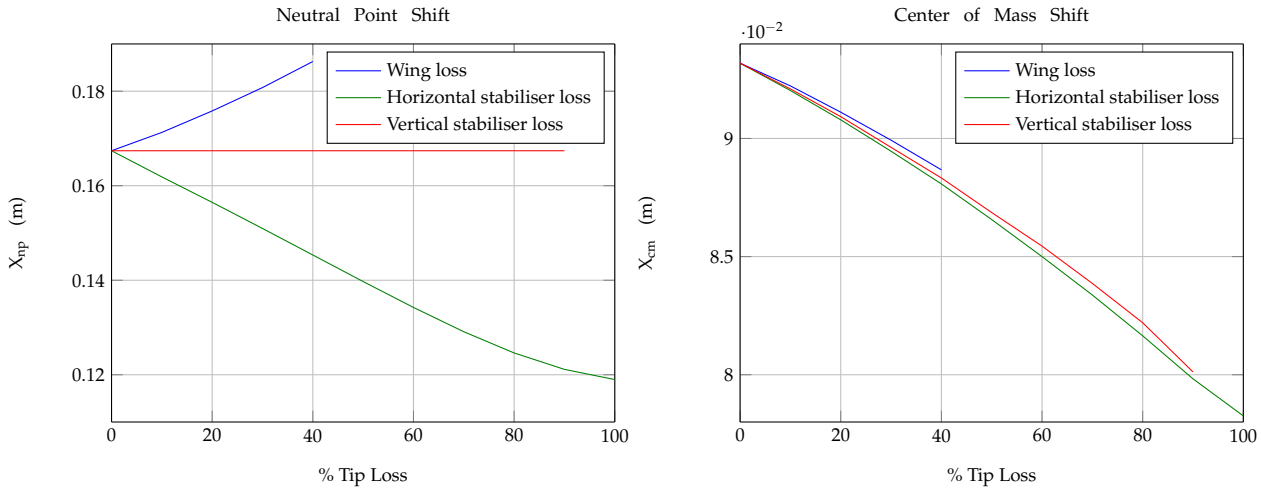

(a) Neutral point location.

(b) centre of mass location.

Figure 4.2: Neutral point and X_{cm} locations for the different damage cases

This is also illustrated by the static margin plotted in Figure 4.3. The static margin remains positive for all the tip loss cases. Note that for the partial wing loss and partial vertical stabiliser loss cases, the static margin improves. This is not the case for partial horizontal stabiliser losses. For the partial wing loss case, the neutral point moves more aft, and at the same time the centre of mass moves more forward. This increases the static margin of the aircraft significantly. For the vertical stabiliser loss cases the neutral point does not move. The centre of mass, on the other hand, moves more forward, causing the static margin to improve.

For the partial horizontal stabiliser loss case, the neutral point moves significantly forward due to the decrease in lift at the aft, and the centre of mass of the aircraft moves forward due to the horizontal stabiliser tip loss. The neutral point shift is much larger than that of the centre of mass, causing the static margin to decrease but to remain positive.

4.1.2 Lateral and Directional Static Stability

An aircraft is said to be *laterally* statically stable if a small perturbation in sideslip produces a rolling moment that tends to return the aircraft to wings level flight. The restoring moment tends to roll the aircraft away from the sideslip disturbance, so for a positive sideslip the aircraft will roll

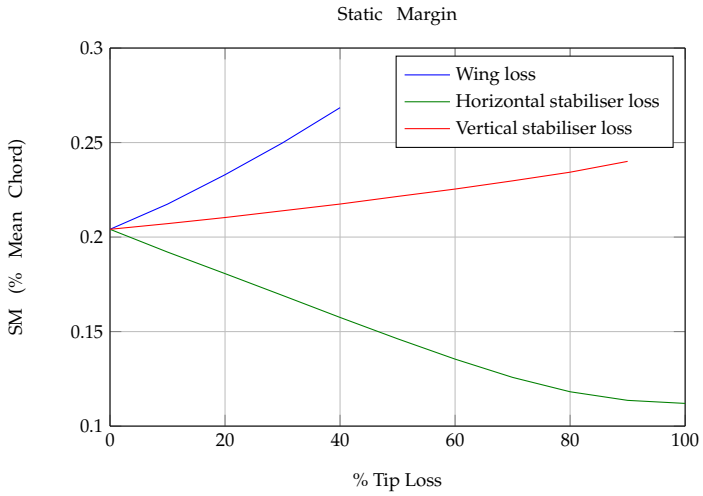

Figure 4.3: Static margin in % mean chord for the different damage cases

left (negative roll). For an aircraft to be laterally statically stable, it is required that $C_{l_\beta} < 0$, where C_{l_β} is the partial derivative of the rolling moment coefficient with respect to sideslip angle.

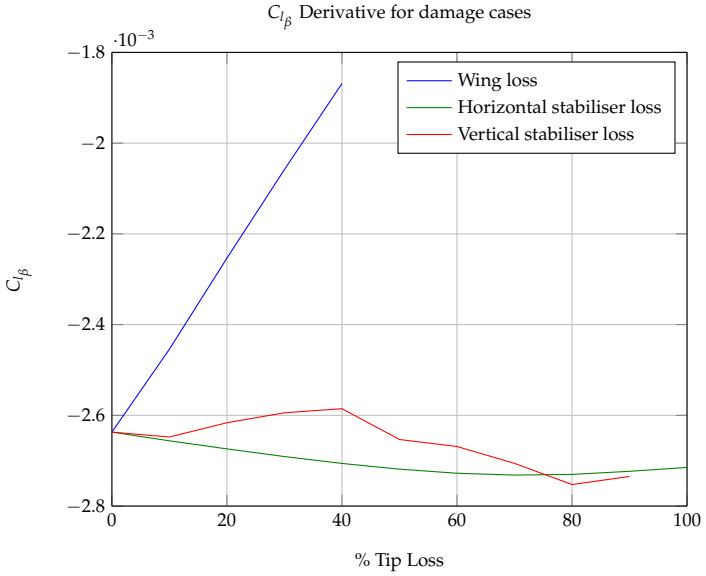

Figure 4.4: Rolling moment derivative with respect to sideslip for the different damage cases

This stability derivative represents contributions of the wing-fuselage, horizontal stabiliser, and vertical stabiliser. Figure 4.4 shows how the derivative C_{l_β} changes with the percentage of wing loss and the percentage of stabiliser losses respectively. Note that the derivative C_{l_β} remains negative throughout all the tip loss cases, hence the aircraft remains laterally statically stable.

An aircraft is said to be *directionally* statically stable if a small increase/decrease in sideslip will produce a yawing moment that tends to decrease/increase the sideslip of the aircraft. The Yawing moment derivative with respect to sideslip C_{n_β} describes the natural tendency of the aircraft to weathercock back into the airflow, which quantifies the directional static stability of the aircraft. For an aircraft to be directionally statically stable, it is required that $C_{n_\beta} > 0$. A positive sideslip will therefore produce a positive yawing moment which tends to reduce the sideslip and thereby

maintain the static stability. The derivative C_{n_β} represents contributions of the wing-fuselage and vertical stabiliser. Figure 4.5 shows how the derivative C_{n_β} changes with the percentage of wing loss and the percentage of stabiliser losses respectively.

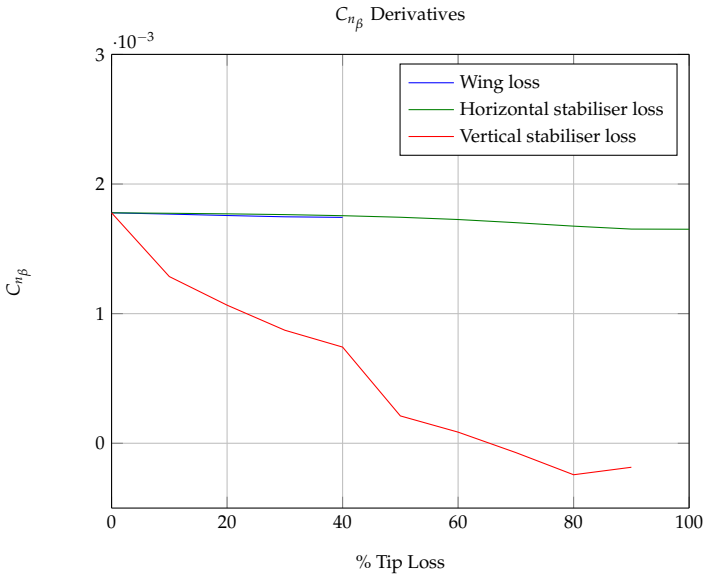

Figure 4.5: Yawing moment derivative with respect to sideslipe for the different damage cases

From Figure 4.5, it is noted that the derivative C_{n_β} decreases significantly more with partial vertical stabiliser loss than with partial wing loss or partial horizontal stabiliser loss. The vertical stabiliser contribution of this derivative can be expressed as

$$C_{n_{\beta_V}} = C_{L_{\alpha_V}} \eta_V \bar{V}_V \tag{4.1.4}$$

and the side force derivative with respect to sideslip is given by [33] as

$$C_{y_{\beta_V}} = \frac{-C_{L_{\alpha_V}} \eta_V S_V}{S} \tag{4.1.5}$$

therefore the yawing moment derivative with respect to sideslip is expressed in terms of the side force derivative with respect to sideslip,

$$C_{n_{\beta_V}} = \frac{-C_{y_{\beta_V}} l_V}{b} \tag{4.1.6}$$

The remaining contribution is thus from the wing-fuselage, which similar to the above, is expressed as

$$C_{n_{\beta_{WF}}} = \frac{-C_{y_{\beta_{WF}}} l_{WF}}{b} \tag{4.1.7}$$

Figure 4.6 shows the side forces that act on the aircraft due to sideslip. Note that each component of side force has a moment arm from the centre of mass of the aircraft to the specific aerodynamic centre through which it acts. In the figure, one will notice that the side force due to sideslip produced by the aircraft's wing-fuselage combination will have a destabilising effect on the aircraft. The wing-fuselage side force will cause the aircraft to experience a negative yawing moment for a positive sideslip.

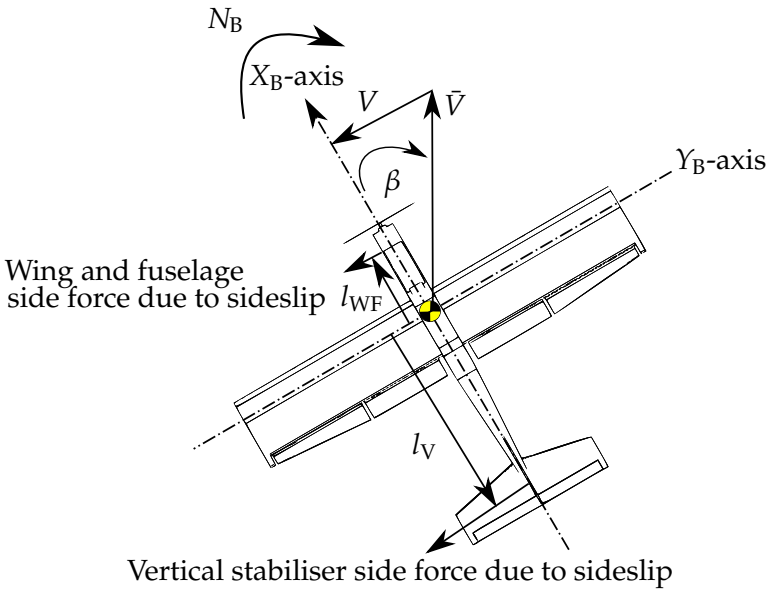

Figure 4.6: Yawing moment due to side force on the wing-fuselage and vertical stabiliser

On the other hand, the side force due to sideslip produced by the vertical stabiliser will have a stabilising effect. The vertical stabiliser side force will cause the aircraft to experience a positive yawing moment for a positive sideslip. If the vertical stabiliser yawing moment is greater than the wing-fuselage yawing moment, then the aircraft will be directionally statically stable. From Figure 4.5, we note that C_{n_β} becomes negative at about 65% vertical stabiliser loss, thus at that point, the yawing moment produced by the damaged vertical stabiliser becomes smaller than the yawing moment produced by the wing-fuselage combination, and therefore the aircraft becomes directionally statically unstable. Recall from Chapter 3 that a flat body was added to the AVL model in order to obtain a better representation of the side forces acting on the aircraft. The wing-fuselage side force is present due to the flat body that was added in the model. Due to limitations of AVL, the flat body does not perfectly resemble the aircraft body and is only an approximation.

4.2 Dynamic Stability Analysis

The purpose of this section is to analyse dynamic stability and control characteristics of the aircraft as a function of partial wing loss, partial horizontal stabiliser loss, and partial vertical stabiliser loss. Dynamic stability is defined as the tendency of the amplitudes of the perturbed motion of an aircraft to decrease to zero or to a value corresponding to a new steady state at some time after the disturbance has stopped [33]. While it is possible to determine the aircraft's dynamic stability by numerically integrating the nonlinear 6DoF equations of motion, it is difficult to establish the cause of the stability or instability.

To better establish the cause of the stability or instability, an approximate analytical theory, the small perturbation theory, is used. The nonlinear 6DoF equations of motion are linearised about a given reference path or flight equilibrium. The linear differential equations are then solved to obtain information about the dynamic stability and control characteristics of the aircraft. The information includes the natural modes of motion of the aircraft and the aircraft's response to control inputs. The linear differential equations are only valid for small perturbations around the

flight equilibrium. Furthermore, linear control techniques can be used on these linear differential equations in the flight control system design process, as discussed in Chapter 5.

The flight equilibriums for straight and level flight are calculated for the aircraft over the range of all tip loss cases. The nonlinear 6DoF equations of motion are then linearised about the calculated flight equilibriums. The dynamic stability of the aircraft is then analysed as a function of partial wing loss and stabiliser losses respectively.

4.2.1 Aircraft Flight Equilibrium

The objective of trimming an aircraft is to bring the forces and moments acting on the aircraft into a state of equilibrium. The trim condition is the condition where the axial force X, the normal force Z, the side force Y, the pitching moment M_{B}, the rolling moment L_{B}, and the yawing moment N_{B} are all exactly zero [28]. In other terms, trim flight is defined as a non-accelerating condition, hence the aircraft must experience zero linear and angular body axis accelerations. The aircraft is then said to be trimmed for a given reference path, and this trim state defines the working point about which the dynamics of the aircraft are linearised for stability analysis and control design purposes.

To achieve flight equilibrium, the aircraft's control surfaces and thrust must be adjusted simultaneously in such a way that the forces and moments add up to zero. These forces and moments include the aerodynamic, gravity and engine forces and moments. An aircraft is usually trimmed at a desired airspeed and altitude (air density). An aircraft can be trimmed for any reference path, but not all reference paths will be useful as a flight equilibrium for linearisation purposes. Common reference paths include steady climb/descent, steady turning flight, and cruise or straight and level flight [31]. Straight and level flight is a common and useful reference path to trim an aircraft at for conventional flight, and a useful reference path to linearise about. That is why straight and level flight trim conditions for the aircraft over the range of all tip loss cases will be determined here.

For straight and level flight, the sum of the forces and moments acting on the aircraft must all be equal to zero; the aircraft should not experience any rotational rates; and the aircraft must travel at a constant airspeed and altitude. From (3.4.11), (3.4.25), and (3.4.27), the force equilibrium equations are written as

$$\mathbf{0} = \boldsymbol{F}^{A}(\alpha, \beta, P_{\mathrm{B}}, Q_{\mathrm{B}}, R_{\mathrm{B}}, \delta_E, \delta_A, \delta_R) + \boldsymbol{F}^{T}(T) + \boldsymbol{F}^{G}(\Theta, \Phi) \tag{4.2.1}$$

and the moment equilibrium equations as

$$\mathbf{0} = \boldsymbol{M}^{A}(\alpha, \beta, P_{\mathrm{B}}, Q_{\mathrm{B}}, R_{\mathrm{B}}, \delta_E, \delta_A, \delta_R) + \boldsymbol{M}^{G}(\Theta, \Phi) \tag{4.2.2}$$

where P_{B}, Q_{B}, R_{B} are zero and $\bar{V}$ and ρ are constant. From the nonlinear equations (4.2.1) and (4.2.2), note that $\boldsymbol{F}^{A}$ and $\boldsymbol{M}^{A}$ are functions of $\alpha, \beta, P_{\mathrm{B}}, Q_{\mathrm{B}}, R_{\mathrm{B}}, \delta_E, \delta_A$, and δ_R; that $\boldsymbol{F}^{G}$ and $\boldsymbol{M}^{G}$ are functions of Θ and Φ; and that $\boldsymbol{F}^{T}$ is a function of T. Also note that for straight and level flight, which implies zero climb rate, the angle of attack is equal to the pitch angle of the aircraft.

When aerodynamic symmetry is lost, due to partial wing loss or partial horizontal stabiliser loss, the aircraft experiences differential lift and drag. Lateral-directional trim adjustments therefore become necessary for the aircraft to achieve flight equilibrium. Longitudinal and lateral-directional trimming is therefore required, which complicates the calculations to determine an

equilibrium solution. From (4.2.1) and (4.2.2) one will note that for straight and level flight, the three force equations and three moment equations have three unknown aircraft states and four unknown aircraft control surface deflections that need to be solved simultaneously for the aircraft to achieve equilibrium. For a conventional symmetrical aircraft, the trim task is reduced to the longitudinal trim only, where the lift generated by the aircraft must oppose the weight of the aircraft, the steady state moment about the Y_B-axis (steady state pitching moment) must be countered by a pitching moment produced by elevator deflection, and the drag must be opposed by the thrust. When aerodynamic symmetry is lost, the ailerons are used to counter the steady state moment about the X_B-axis (steady state rolling moment) and the rudder is used to counter the steady state moment about the Z_B-axis (steady state yawing moment).

The same argument also applies to loss of geometric asymmetry. The position of the centre of mass of the aircraft has a large effect on the trim equilibrium. The centre of mass establishes the moment arms for the aerodynamic pitching, rolling and yawing moments as well as the moment arms for the gravitational pitching, rolling, and yawing moments acting on the aircraft. The position of the centre of mass changes when the aircraft is damaged, and thus also affects the aircraft states to achieve trim equilibrium. For discussion purposes, the aircraft trimming will be divided into two sections and investigated separately here. The two sections are longitudinal trimming and lateral-directional trimming. Note that for an asymmetrical aircraft, the longitudinal and lateral-directional trimming are coupled and therefore should be calculated simultaneously. Note that although the longitudinal and lateral-directional trimming will be discussed conceptually in separate sections, the longitudinal and lateral trims are actually calculated together by solving the full coupled nonlinear trim equations using a Newton-Raphson method.

4.2.1.1 Lateral-Directional Flight Equilibrium

For the asymmetric aircraft, the number of unknown aircraft states and aircraft control surface deflections to be solved is greater than the number of nonlinear trimming equations available. Additional trimming constraints therefore have to be specified before the trim can be calculated by simultaneously solving the set of nonlinear equations. Recall that when aerodynamic symmetry is lost, the aircraft experiences differential lift and drag. The differential lift and drag causes the aircraft to experience undesired steady state yawing and rolling moments that must be opposed using the appropriate aircraft control surface deflections. For a control surface to produce a moment, it deflects which produces a force, and in turn will cause in a moment. To counter the yawing moment due to differential drag, a rudder deflection is necessary. When the rudder deflects, a side force ($qSC_{y_{\delta_R}}\delta_R$) will be produced. To achieve side force equilibrium, note from (4.2.3) that the side force due to rudder can be opposed by either the side force due to sideslip, the side force from the weight of the aircraft when flying at a bank angle, or a combination of the two.

$$0 = qS(C_{y_0} + C_{y_\alpha}\alpha + C_{y_\beta}\beta + C_{y_{\delta_A}}\delta_A + C_{y_{\delta_R}}\delta_R + C_{y_{\delta_E}}\delta_E) + mg\cos\alpha\sin\Phi \tag{4.2.3}$$

This leads to two sensible lateral-directional trim equilibrium configurations for the aircraft:

- Wings-level

- Small bank angle

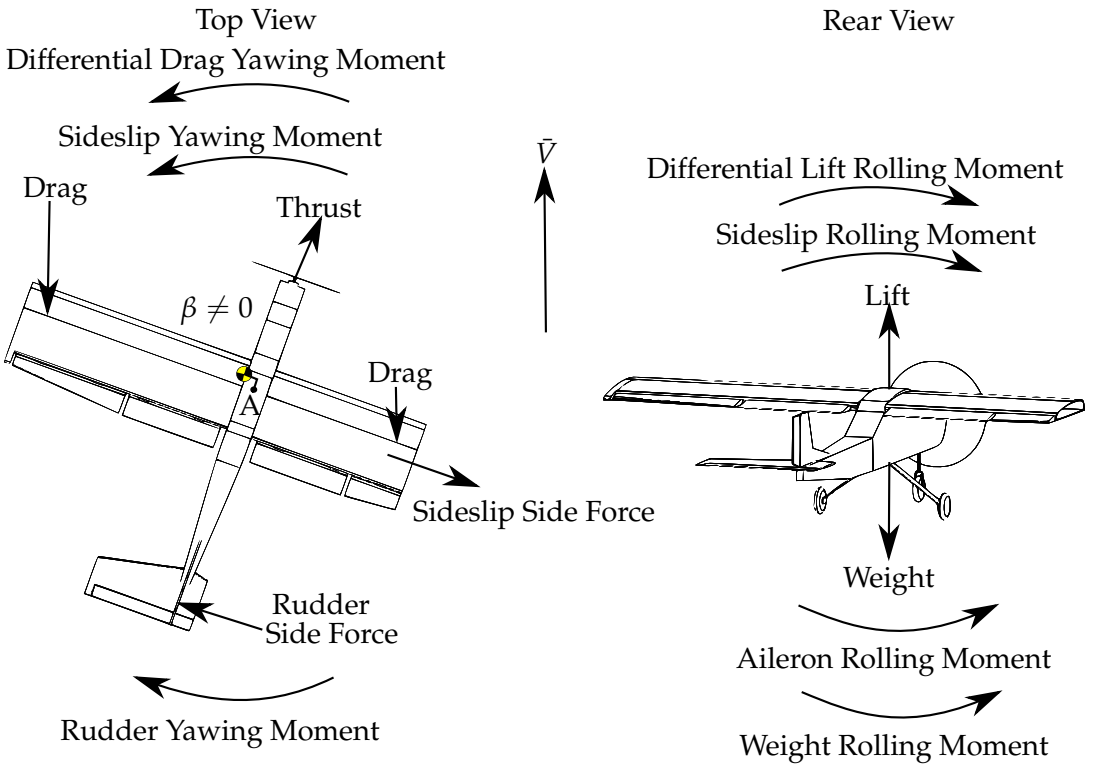

Figure 4.7: Wings-level configuration for lateral-directional trim equilibrium

Figure 4.7 shows the wings-level trim configuration for an aircraft with partial tip losses to its right wing, right horizontal stabiliser and vertical stabiliser. Note that the aircraft flies with a zero roll angle and a non-zero sideslip angle. The aircraft will therefore utilise the side force produced due to sideslip to oppose the side force produced by the rudder deflection. Recall that when flying with a negative sideslip angle, the aircraft will experience a positive side force due to this sideslip. A rudder deflection is used to counter the yawing moment due to differential drag. The rudder deflection causes a side force, which is then opposed by a side force due to sideslip. When an aircraft experiences a sideslip, it tends to produce a yawing moment to weathercock into the direction of airflow. From Figure 4.7 one will note that the produced yawing moment due to sideslip is in the same direction as the differential drag. A larger rudder deflection is therefore necessary to counter the additional yawing moment.

To achieve directional trim, a sideslip angle and rudder deflection must be determined that will result in yawing moment and side force equilibrium. To achieve lateral trim, an aileron deflection must be determined that will produce a rolling moment to counter the rolling moment due to differential lift, and the rolling moment due to flying with a sideslip. Note that the centre of mass shift introduces a weight offset that will produce an additional rolling moment (see Figure 4.7).

Figure 4.8 shows the small bank angle trim configuration for an aircraft with partial tip losses to its right wing, right horizontal stabiliser, and vertical stabiliser. Note that the aircraft now flies with a zero sideslip angle but with a non-zero roll angle. Similar to the wings-level trim configuration, a rudder deflection is used to counter the yawing moment due to differential drag, which results in a rudder side force. Unlike the wings-level trim configuration, the small bank angle trim

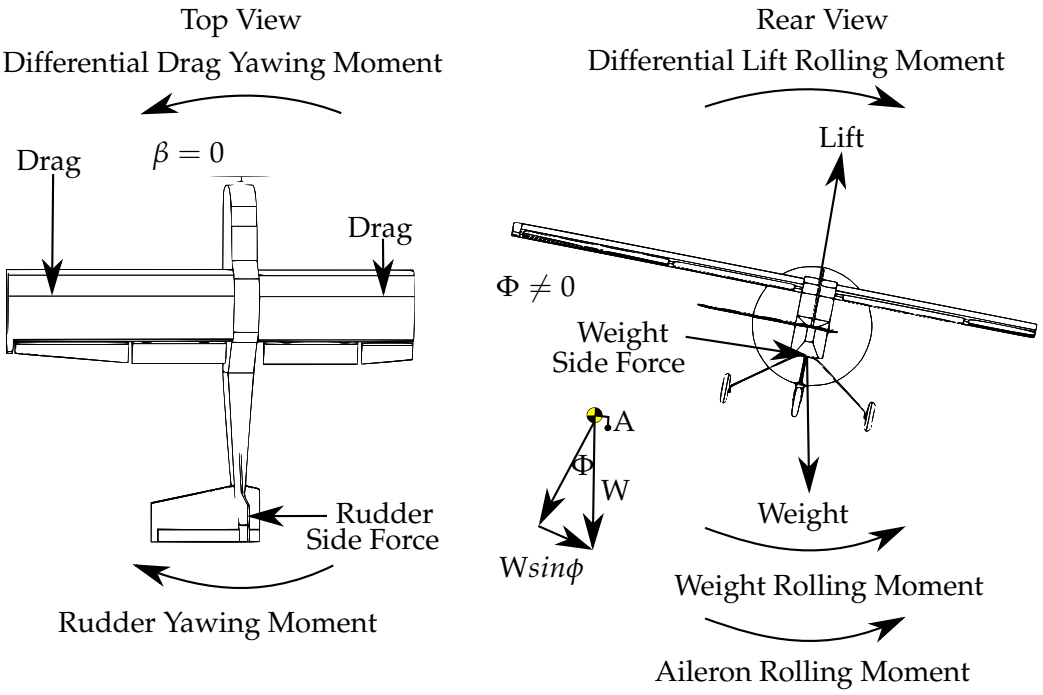

Figure 4.8: Small bank angle configuration for lateral-directional trim equilibrium

configuration utilises the weight of the aircraft to oppose the rudder side force. From (4.2.3), the last term is a function of the roll angle of the aircraft. The aircraft can therefore fly at a bank angle to produce a side force $F_y = \text{mg} \cos\alpha \sin\Phi$. From Figure 4.8, to achieve lateral-directional equilibrium, a rudder deflection is used to counter the yawing moment due to differential drag. The side force produced by the rudder deflection is then opposed by the weight side force due to flying at a bank angle. An aileron deflection is then used to counter the rolling moment due to differential lift. Again an additional rolling moment is present due to the shift in the centre of mass, which introduces a weight offset (see Figure 4.7).

From these two configurations, the small bank angle configuration requires less control authority than the wings-level configuration. For the wings-level configuration, the aircraft flies with a sideslip angle, which results in yawing and rolling moments ($qSbC_{n_\beta}\beta$ and $qSbC_{l_\beta}\beta$) acting on the aircraft. The aircraft will therefore have to use more rudder authority to maintain the non-zero sideslip. For this reason, the aircraft will need more control authority to achieve lateral-directional trim equilibrium. Also note that when the rolling moment due to differential lift is smaller than the weight rolling moment (e.g. in the case of partial horizontal stabiliser loss only), the ailerons should produce a rolling moment in the opposite direction. When landing, the flight equilibrium configuration determines the touchdown orientation of the aircraft. The aircraft will thus have two landing or touchdown configuration options. This is discussed in more detail in Chapter 6.

4.2.1.2 Longitudinal Flight Equilibrium

Lateral-directional stability is designed into most conventional symmetrical aircraft (symmetrical about the $X_B Z_B$-axis). This ensures that most conventional aircraft remain wings-level and tend to weathercock into the wind when the rudder and ailerons are at their centre positions. Thus a conventional symmetrical aircraft will naturally seek a lateral-directional equilibrium without any

trimming required. Therefore the symmetry of a conventional aircraft usually reduces the task to that of longitudinal trimming only. This allows one to eliminate the number of unknown aircraft states from the nonlinear equations (4.2.1) and (4.2.2), which simplifies the trim calculations to only solving for the aircraft state α and the aircraft controls δ_E, and T assuming that the desired trim airspeed and altitude have been specified. From Figure 4.9 the aircraft will be in equilibrium

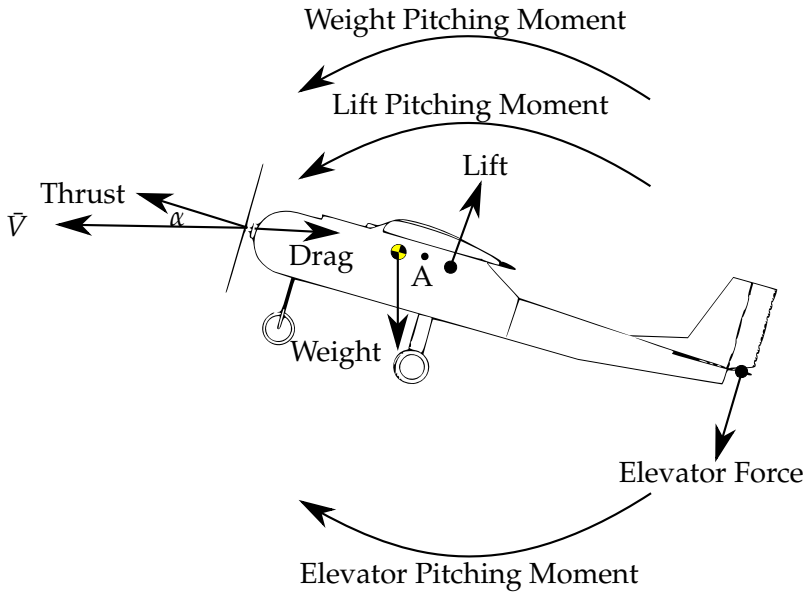

Figure 4.9: Longitudinal trim equilibrium

when the lift generated by the aircraft opposes the weight of the aircraft, the thrust produced by the aircraft opposes the drag, and the steady state moment about the Y_B-axis (the steady state pitching moment) is countered by a pitching moment due to an elevator deflection ($qS\bar{c}C_{m_{\delta_E}}\delta_E$) at the desired trim airspeed and altitude. For the small bank angle configuration, the weight of the aircraft is distributed into a side force and a downwards force. The aircraft can therefore fly with a lower angle of attack because less lift is needed to oppose the reduced weight. Remember that this is not the only coupling between the longitudinal and lateral-direction trimming of an asymmetrical aircraft. The Newton-Raphson method, which can solve the roots for nonlinear equations, is therefore used to solve the trim aircraft states and aircraft control surface deflections for the two trim configurations respectively.

4.2.1.3 Flight Equilibrium Obtained Using the Newton-Raphson Method

In this section, the straight and level flight trim values for the aircraft are obtained using the Newton-Rapshon method. The Newton-Rapshon method is an application of Taylor polynomials for finding the roots of nonlinear functions. The roots of (4.2.1) and (4.2.2) are solved simultaneously to obtain the aircraft trim values. Trim values are determined as a function of the percentage of wing loss and the percentage of stabiliser losses respectively. The effects of the tip loss cases on the aircraft trim values is investigated.

Partial Wing Loss

Figure 4.10 (a) shows how the trim angle of attack changes with the percentage of wing loss (from 0% to 40% semi-span tip loss). The wings are the primary lift-generating surfaces of the aircraft. Hence with partial wing loss the aircraft has to fly at a higher angle of attack to generate the lift required to oppose the weight of the aircraft. Note that the trim angle of attack for the small bank angle configuration is slightly lower as is expected. Figure 4.10 (b) shows how the sideslip angle changes for the wings-level trim configuration, and how the bank angle changes for the small bank angle trim configuration with the percentage of wing loss. As tip loss increases, the differential drag experienced by the aircraft increase. A larger rudder deflection is therefore necessary to counter the yawing moment, and so a larger sideslip angle or bank angle is required to oppose the side force due to rudder deflection. Figure 4.11 (a) shows how the trim aileron deflection

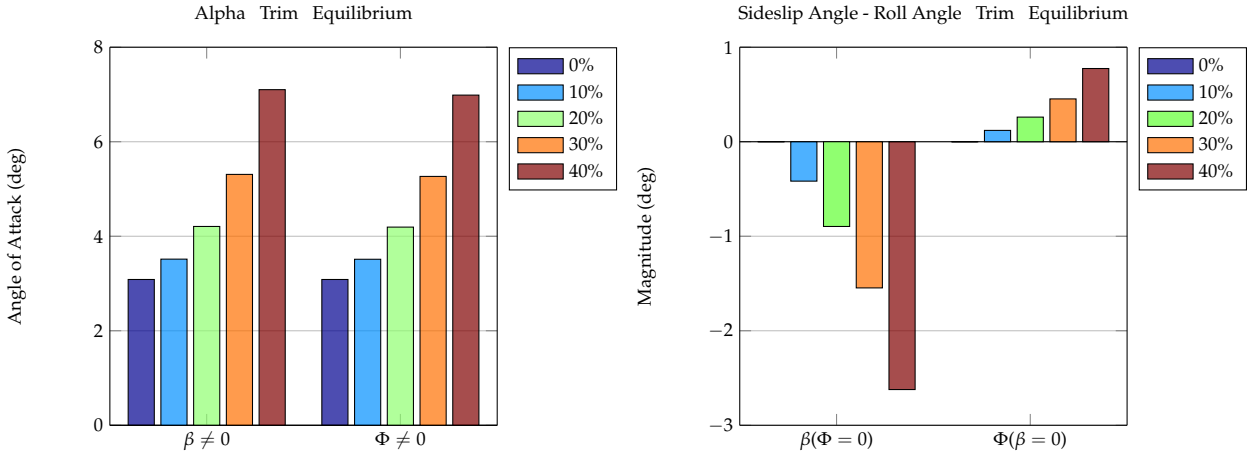

(a) Trim Angle of Attack.

(b) Trim Sideslip Angle and Roll Angle.

Figure 4.10: Aircraft states for wing damage cases

changes with the percentage of wing loss (0% to 40% semi-span tip loss). Note that the aileron deflection required to trim the aircraft increases exponentially. As the differential lift on the wings increases, more aileron deflection is needed to counter the rolling moment due to differential lift. This limits the amount of partial wing loss that the aircraft can suffer. If the aircraft increases its airspeed, thereby increasing the effectiveness of its control surfaces, lower aileron deflections can be obtained. This is only a temporary solution, because the aircraft cannot land at such high airspeeds (assuming no headwind). The ailerons of the Phoenix Trainer 60 aircraft are only capable of deflecting to $\pm 18^{\circ}$. For the aerodynamics to remain in the linear region, this is further limited to $\pm 12.5^{\circ}$. Figure 4.11 (a) shows that the trim aileron deflection for the 30% semi-span case is very close to the maximum deflection angle. If the aircraft is trimmed at such a high aileron deflection, the control authority of the aircraft is limited to one side, which will result in degraded rolling performance and disturbance rejection. Moreover, when the required trim aileron deflection exceeds the aileron deflection limits, then it is no longer possible to trim the aircraft making it impossible to maintain equilibrium flight. The aileron deflection for the small bank angle configuration is slightly lower as is expected.

Figure 4.11 (b) shows how the trim rudder deflection changes with the percentage of wing loss (0% to 40% semi-span tip loss). As the tip loss increases, the differential drag experienced

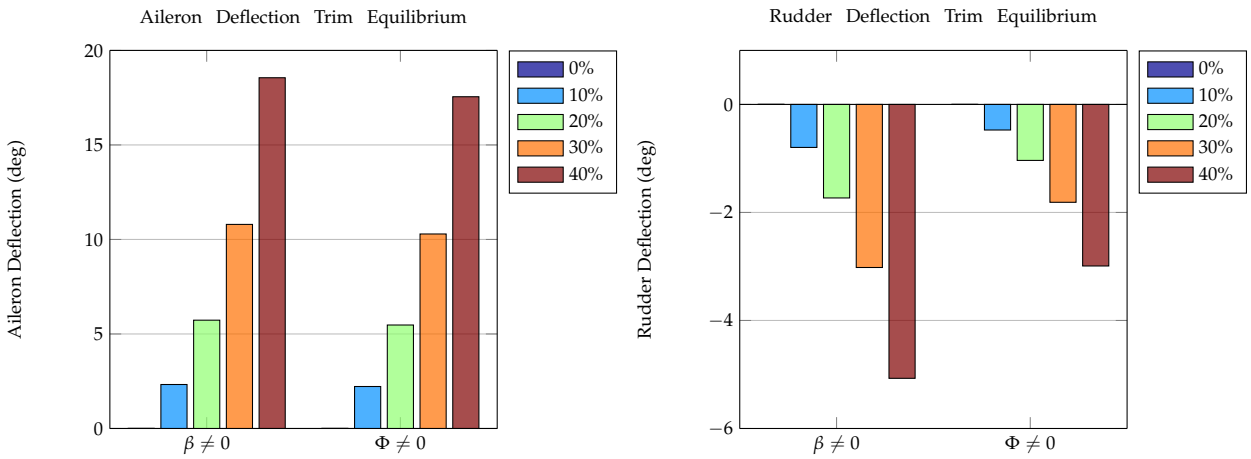

(a) Trim aileron deflection.

(b) Trim rudder deflection.

Figure 4.11: Aircraft control surface deflections for wing damage cases

by the aircraft also increases. A larger rudder deflection is therefore necessary to counter the yawing moment due to differential drag. Trimming the aircraft with the wings-level configuration yields a significantly larger rudder deflection in order to maintain the sideslip. Partial wing loss does not have a significant effect on the trim elevator deflection or trim thrust of the aircraft. From the results above, one can conclude that partial wing loss has a significant effect on both the longitudinal and lateral-directional flight equilibrium of the aircraft.

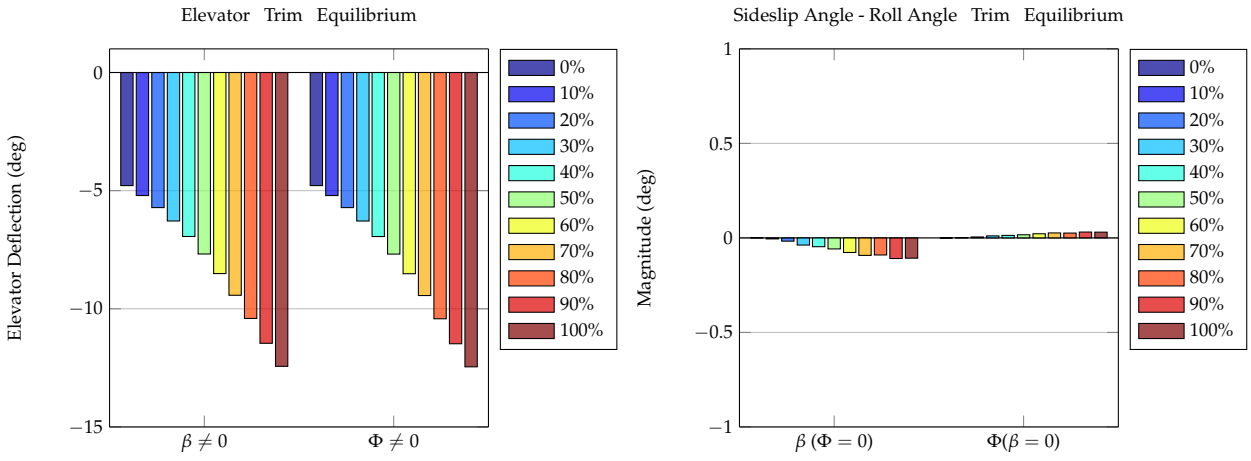

(a) Trim elevator deflection.

(b) Trim sideslip angle and roll angle.

Figure 4.12: Aircraft states and aircraft control surface deflection for horizontal stabiliser damage cases

Partial Horizontal Stabiliser Loss

Figure 4.12 (a) shows how the trim elevator deflection changes with the percentage of horizontal stabiliser loss (0% to 100% semi-span tip loss). The elevator deflection required to trim the aircraft increases exponentially with the percentage of horizontal stabiliser loss. This is due to the loss of control surface effectiveness as the elevator suffer partial loss. Simultaneously, the weight pitching moment increases due to the centre of mass shifting forward towards the nose of the aircraft.

Note that there is also a small amount of lift that is lost, causing the neutral point of the aircraft shifting slightly forward, which will result in a smaller pitching moment due to lift (see Figure 4.9). Therefore the elevator deflection required to trim the aircraft relies strongly on the weight-to-lift ratio of the horizontal stabiliser tip that was lost. Figure 4.12 (b) and Figures 4.13 (a) and (b) shows

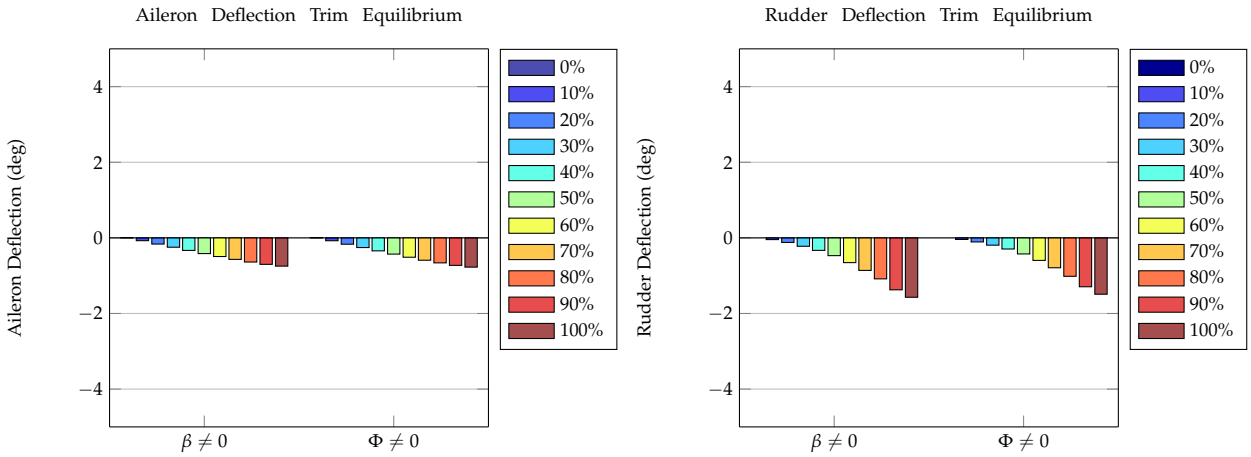

(a) Trim aileron deflection.

(b) Trim rudder deflection.

Figure 4.13: Aircraft control surface deflections for horizontal stabiliser damage cases

how the lateral-directional trim changes with the percentage of horizontal stabiliser loss (0% to 100% semi-span tip loss). The lateral-directional trim values have the same trend as in the partial wing loss case, but are significantly smaller in magnitude. As in the partial wing loss case, partial horizontal stabiliser loss also causes the aircraft to lose symmetry. Unlike with partial wing loss, the differential drag and lift produced due to the partial horizontal stabiliser loss are significantly smaller. From Figure 4.11 and 4.13, note that the trim aileron deflection is of the opposite sign. The rolling moment due to the differential lift is smaller than the weight rolling moment due to the centre of mass shift. The ailerons have to produce a rolling moment in the opposite direction. Partial horizontal stabiliser loss does not have a significant effect on the trim angle of attack or trim thrust of the aircraft. From these results, one can conclude that partial horizontal stabiliser loss has a significant effect on the longitudinal flight equilibrium, and a minor effect on the lateral-directional flight equilibrium of the aircraft.

Partial Vertical Stabiliser Loss

Figure 4.14 shows how the trim elevator deflection changes with the percentage of vertical stabiliser loss (0% to 100% span tip loss). Partial vertical stabiliser loss does not cause the aircraft to become asymmetrical, and thus lateral-directional trim is not required. The small change in trim elevator deflection seen in Figure 4.14 is due to the centre of mass shifting forward towards the nose of the aircraft because of the partial vertical stabiliser tip's mass that is lost. Partial vertical stabiliser loss does not have a significant effect on the trim angle of attack or trim thrust of the aircraft. Even though partial vertical stabiliser loss on its own does not pose any problems, this changes when partial vertical stabiliser loss is combined with partial wing loss or partial horizontal stabiliser loss. With less rudder effectiveness due to the partial vertical stabiliser loss, a larger

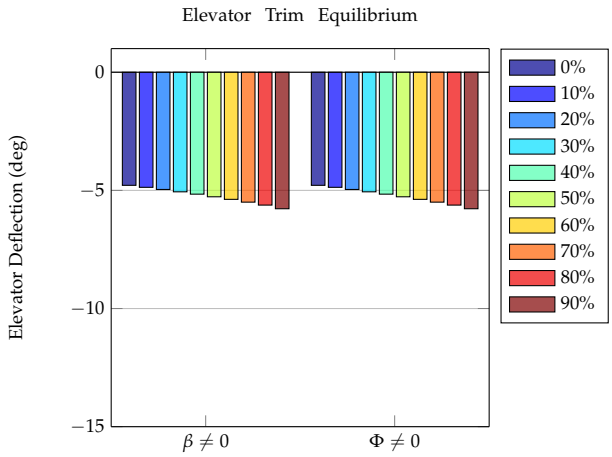

Figure 4.14: Trim elevator deflection for vertical stabiliser damage cases

trim rudder deflection is necessary to counter the yawing moment due to differential drag and to maintain the sideslip in the wings-level trim configuration.

Table 4.1 shows the maximum feasible aircraft states and aircraft control surface deflections that are practically achievable. If the aircraft requires larger states or control surface deflections to achieve flight equilibrium, the partial tip loss case will be seen as infeasible.

Table 4.1: Maximum feasible aircraft states and aircraft control surface deflections

Parameter	Value	Unit
Thrust	48	N
Elevator deflection	12.5	deg
Aileron deflection	12.5	deg
Rudder deflection	12.5	deg
Sideslip angle	5	deg
Roll angle (Navigation)	30	deg
Roll angle (Landing)	19.5	deg

From Figures 4.11 (a) and 4.12 (a), one can conclude that infeasible flight equilibriums are obtained for partial wing losses of more than 30% and partial horizontal stabiliser losses of more than 90%.

4.2.2 Linearised Open-loop Aircraft Dynamics

In this section, the linear open-loop aircraft dynamics will be determined. This is done to better establish and analyse the cause of the dynamic stability or instability of the aircraft. An approximate analytical theory, the small perturbation theory, is used, in which the nonlinear 6DoF equations of motion are linearised about a given reference path or flight equilibrium. In the previous section, the flight equilibriums were obtained as a function of the percentage of wing loss and the percentage of stabiliser losses. Linearisation of the aircraft equations of motion begins with the examination of perturbed flight, which is defined relative to the flight equilibrium condition using a combination of the flight equilibrium and small perturbation control and state variables. The primary dynamics of the aircraft are described by the nonlinear equations (3.2.28) and (3.3.11).

The equations is written in a state space from as

$$\dot{\mathbf{x}} = \mathbf{f}(\mathbf{x}, \mathbf{u}) \tag{4.2.4}$$

with state variables

$$\mathbf{x} = [U_\mathrm{A}\ W_\mathrm{A}\ Q_\mathrm{B}\ \Theta\ V_\mathrm{A}\ P_\mathrm{B}\ R_\mathrm{B}\ \Phi]^T \tag{4.2.5}$$

and control variables

$$\mathbf{u} = [\delta_E\ \ T\ \delta_A\ \delta_R]^T \tag{4.2.6}$$

and where $\mathbf{f}$ is the vector function representing the respective dynamic equations. Perturbed flight can be written as a combination of flight equilibrium $\mathbf{x}_T$ and small perturbation $\mathbf{\Delta x}$ state and control variables

$$\mathbf{x} = \mathbf{x}_T + \mathbf{\Delta x} \tag{4.2.7}$$

$$\mathbf{u} = \mathbf{u}_T + \mathbf{\Delta u} \tag{4.2.8}$$

where the small perturbations are defined as

$$\mathbf{\Delta x} = [u_\mathrm{A}\ w_\mathrm{A}\ q_\mathrm{B}\ \theta\ v_\mathrm{A}\ p_\mathrm{B}\ r_\mathrm{B}\ \phi]^T \tag{4.2.9}$$

$$\mathbf{\Delta u} = [\delta_e\ \Delta T\ \delta_a\ \delta_r]^T \tag{4.2.10}$$

For perturbed flight, we have

$$\dot{\mathbf{x}}_T + \mathbf{\Delta \dot{x}} = \mathbf{f}(\mathbf{x}_T + \mathbf{\Delta x}, \mathbf{u}_T + \mathbf{\Delta u}) \tag{4.2.11}$$

Since $\mathbf{\Delta x}$ and $\mathbf{\Delta u}$ are small perturbations, (4.2.11) can be expanded into a Taylor series about the flight equilibrium states and control variables,

$$\dot{\mathbf{x}}_T + \mathbf{\Delta \dot{x}} = \mathbf{f}(\mathbf{x}_T, \mathbf{u}_T) + \frac{\partial \mathbf{f}}{\partial \mathbf{x}}(\mathbf{x}_T, \mathbf{u}_T)\mathbf{\Delta x} + \frac{\partial \mathbf{f}}{\partial \mathbf{u}}(\mathbf{x}_T, \mathbf{u}_T)\mathbf{\Delta u} \tag{4.2.12}$$

where higher-order terms contain at least quadratic quantities of the small perturbations. Since the perturbations are small, the higher-order terms' squares are even smaller and can thus be ignored. Noting that at flight equilibrium,

$$f(\mathbf{x}_T, \mathbf{u}_T) = \mathbf{0} \tag{4.2.13}$$

linear differential equations are obtained in state space form as

$$\mathbf{\Delta \dot{x}} = \mathbf{A}\mathbf{\Delta x} + \mathbf{B}\mathbf{\Delta u} \tag{4.2.14}$$

Furthermore, the body reference frame velocities in the state vector are expressed in the wind reference frame as a velocity magnitude and two angles. From (3.1.1) to (3.1.3) and (3.2.30), given that the angle of attack and sideslip angle are small and that the flight equilibrium is for straight and level flight,

$$\mathbf{v}_\mathrm{cm} = \mathbf{v}_\mathrm{A} + \boldsymbol{\omega} \times \Delta\bar{\boldsymbol{\rho}}_{damage} = \mathbf{v}_\mathrm{A} \tag{4.2.15}$$

$$\dot{U} = \dot{\bar{V}} \tag{4.2.16}$$

$$\dot{W} = U_T\dot{\alpha} = V_T\dot{\alpha} \tag{4.2.17}$$

$$\dot{V} = \bar{V}\dot{\beta} = V_T\dot{\beta} \tag{4.2.18}$$

The linear aircraft state space model about straight and level flight is given by

$$\begin{bmatrix} \dot{\bar{v}} \\ \dot{\alpha} \\ \dot{q} \\ \dot{\theta} \\ \dot{\beta} \\ \dot{p} \\ \dot{r} \\ \dot{\phi} \end{bmatrix} = \begin{bmatrix} \frac{\partial \dot{U}}{\partial U} & V_T \frac{\partial \dot{U}}{\partial W} & \frac{\partial \dot{U}}{\partial Q} & \frac{\partial \dot{U}}{\partial \Theta} & V_T \frac{\partial \dot{U}}{\partial V} & \frac{\partial \dot{U}}{\partial P} & \frac{\partial \dot{U}}{\partial R} & \frac{\partial \dot{U}}{\partial \Phi} \\ \frac{1}{V_T}\frac{\partial \dot{W}}{\partial U} & \frac{\partial \dot{W}}{\partial W} & \frac{1}{V_T}\frac{\partial \dot{W}}{\partial Q} & \frac{1}{V_T}\frac{\partial \dot{W}}{\partial \Theta} & \frac{\partial \dot{W}}{\partial V} & \frac{1}{V_T}\frac{\partial \dot{W}}{\partial P} & \frac{1}{V_T}\frac{\partial \dot{W}}{\partial R} & \frac{1}{V_T}\frac{\partial \dot{W}}{\partial \Phi} \\ \frac{\partial \dot{Q}}{\partial U} & V_T \frac{\partial \dot{Q}}{\partial W} & \frac{\partial \dot{Q}}{\partial Q} & \frac{\partial \dot{Q}}{\partial \Theta} & V_T \frac{\partial \dot{Q}}{\partial V} & \frac{\partial \dot{Q}}{\partial P} & \frac{\partial \dot{Q}}{\partial R} & \frac{\partial \dot{Q}}{\partial \Phi} \\ \frac{\partial \dot{\Theta}}{\partial U} & V_T \frac{\partial \dot{\Theta}}{\partial W} & \frac{\partial \dot{\Theta}}{\partial Q} & \frac{\partial \dot{\Theta}}{\partial \Theta} & V_T \frac{\partial \dot{\Theta}}{\partial V} & \frac{\partial \dot{\Theta}}{\partial P} & \frac{\partial \dot{\Theta}}{\partial R} & \frac{\partial \dot{\Theta}}{\partial \Phi} \\ \frac{1}{V_T}\frac{\partial \dot{V}}{\partial U} & \frac{\partial \dot{V}}{\partial W} & \frac{1}{V_T}\frac{\partial \dot{V}}{\partial Q} & \frac{1}{V_T}\frac{\partial \dot{V}}{\partial \Theta} & \frac{\partial \dot{V}}{\partial V} & \frac{1}{V_T}\frac{\partial \dot{V}}{\partial P} & \frac{1}{V_T}\frac{\partial \dot{V}}{\partial R} & \frac{1}{V_T}\frac{\partial \dot{V}}{\partial \Phi} \\ \frac{\partial \dot{P}}{\partial U} & V_T \frac{\partial \dot{P}}{\partial W} & \frac{\partial \dot{P}}{\partial Q} & \frac{\partial \dot{P}}{\partial \Theta} & V_T \frac{\partial \dot{P}}{\partial V} & \frac{\partial \dot{P}}{\partial P} & \frac{\partial \dot{P}}{\partial R} & \frac{\partial \dot{P}}{\partial \Phi} \\ \frac{\partial \dot{R}}{\partial U} & V_T \frac{\partial \dot{R}}{\partial W} & \frac{\partial \dot{R}}{\partial Q} & \frac{\partial \dot{R}}{\partial \Theta} & V_T \frac{\partial \dot{R}}{\partial V} & \frac{\partial \dot{R}}{\partial P} & \frac{\partial \dot{R}}{\partial R} & \frac{\partial \dot{R}}{\partial \Phi} \\ \frac{\partial \dot{\Phi}}{\partial U} & V_T \frac{\partial \dot{\Phi}}{\partial W} & \frac{\partial \dot{\Phi}}{\partial Q} & \frac{\partial \dot{\Phi}}{\partial \Theta} & V_T \frac{\partial \dot{\Phi}}{\partial V} & \frac{\partial \dot{\Phi}}{\partial P} & \frac{\partial \dot{\Phi}}{\partial R} & \frac{\partial \dot{\Phi}}{\partial \Phi} \end{bmatrix} \begin{bmatrix} \bar{v} \\ \alpha \\ q \\ \theta \\ \beta \\ p \\ r \\ \phi \end{bmatrix} + \begin{bmatrix} \frac{\partial \dot{U}}{\partial \delta_E} & \frac{\partial \dot{U}}{\partial T} & \frac{\partial \dot{U}}{\partial \delta_A} & \frac{\partial \dot{U}}{\partial \delta_R} \\ \frac{1}{V_T}\frac{\partial \dot{W}}{\partial \delta_E} & \frac{1}{V_T}\frac{\partial \dot{W}}{\partial T} & \frac{1}{V_T}\frac{\partial \dot{W}}{\partial \delta_A} & \frac{1}{V_T}\frac{\partial \dot{W}}{\partial \delta_R} \\ \frac{\partial \dot{Q}}{\partial \delta_E} & \frac{\partial \dot{Q}}{\partial T} & \frac{\partial \dot{Q}}{\partial \delta_A} & \frac{\partial \dot{Q}}{\partial \delta_R} \\ \frac{\partial \dot{\Theta}}{\partial \delta_E} & \frac{\partial \dot{\Theta}}{\partial T} & \frac{\partial \dot{\Theta}}{\partial \delta_A} & \frac{\partial \dot{\Theta}}{\partial \delta_R} \\ \frac{1}{V_T}\frac{\partial \dot{V}}{\partial \delta_E} & \frac{1}{V_T}\frac{\partial \dot{V}}{\partial T} & \frac{1}{V_T}\frac{\partial \dot{V}}{\partial \delta_A} & \frac{1}{V_T}\frac{\partial \dot{V}}{\partial \delta_R} \\ \frac{\partial \dot{P}}{\partial \delta_E} & \frac{\partial \dot{P}}{\partial T} & \frac{\partial \dot{P}}{\partial \delta_A} & \frac{\partial \dot{P}}{\partial \delta_R} \\ \frac{\partial \dot{R}}{\partial \delta_E} & \frac{\partial \dot{R}}{\partial T} & \frac{\partial \dot{R}}{\partial \delta_A} & \frac{\partial \dot{R}}{\partial \delta_R} \\ \frac{\partial \dot{\Phi}}{\partial \delta_E} & \frac{\partial \dot{\Phi}}{\partial T} & \frac{\partial \dot{\Phi}}{\partial \delta_A} & \frac{\partial \dot{\Phi}}{\partial \delta_R} \end{bmatrix} \begin{bmatrix} \delta_e \\ \Delta T \\ \delta_a \\ \delta_r \end{bmatrix} \tag{4.2.19}$$

where the first four states are known as the longitudinal dynamic of the aircraft, and the last four as the lateral-directional dynamics of the aircraft. Equation (4.2.19) is used to describe the dynamic behaviour of the aircraft while operating in flight equilibrium and small perturbations from flight equilibrium. Valuable information about the aircraft's dynamic stability can be extracted from this linear model. The information includes the natural modes of motion of the aircraft and the aircraft's response to control inputs. The linear differential equations described above account for aerodynamic and geometric asymmetry. Linear control techniques can now be used on these linear differential equations in the flight control system design process. The flight control system design is discussed in Chapter 5.

4.2.3 Coupling and Control Efficiency of the Longitudinal and Lateral-Directional Dynamics

For conventional symmetrical aircraft, the longitudinal dynamics have little influence on the lateral-directional dynamics and vice versa. The longitudinal and lateral-directional dynamics are therefore typically decoupled from one another. This decoupling allows one to analyse the longitudinal and lateral-directional dynamics independently. Decoupling also allows one to design the longitudinal and lateral-directional flight control systems independently from one another.

4.2.3.1 Coupling

The linear state space model shown in (4.2.20) describes the linear dynamics for the undamaged aircraft.

$$\begin{bmatrix} \dot{\bar{v}} \\ \dot{\alpha} \\ \dot{q} \\ \dot{\theta} \\ \dot{\beta} \\ \dot{p} \\ \dot{r} \\ \dot{\phi} \end{bmatrix} = \begin{bmatrix} -0.32 & 9.11 & -1.08 & -9.79 & 0 & 0 & 0 & 0 \\ -0.04 & -4.82 & 0.92 & -0.02 & 0 & 0 & 0 & 0 \\ 0 & -100.39 & -7.80 & 0 & -0.02 & 0 & 0 & 0 \\ 0 & 0 & 1 & 0.000 & 0 & 0 & 0 & 0 \\ 0 & 0 & 0 & 0 & -0.23 & 0.05 & -0.99 & 0.48 \\ 0 & 0.13 & 0 & 0 & -36.63 & -11.92 & 3.30 & 0 \\ 0 & 0.01 & 0 & 0 & 11.89 & -1.09 & -0.99 & 0 \\ 0 & 0 & 0 & 0 & 0 & 1 & 0.05 & 0.000 \end{bmatrix} \begin{bmatrix} \bar{v} \\ \alpha \\ q \\ \theta \\ \beta \\ p \\ r \\ \phi \end{bmatrix} + \begin{bmatrix} -0.06 & 0.12 & 0 & 0 \\ -0.46 & 0 & 0 & 0 \\ -107.94 & 0 & -0.09 & 0 \\ 0 & 0.000 & 0 & 0 \\ 0 & 0 & 0.000 & 0.12 \\ -0.04 & 0 & -152.37 & 1.47 \\ 0.01 & 0 & -5.23 & -16.90 \\ 0 & 0 & 0 & 0.000 \end{bmatrix} \begin{bmatrix} \delta_e \\ \Delta T \\ \delta_a \\ \delta_r \end{bmatrix} \tag{4.2.20}$$

The matrix entries filled with orange represent the longitudinal dynamics, and those filled with green the lateral-directional dynamics. The unfilled entries are the cross-coupling terms. For the undamaged aircraft, the coupling terms are typically zero or negligible. Hence, perturbations in the longitudinal states would not cause the lateral-directional states being disturbed and vice versa. The linear state space model shown in (4.2.21) describes the linear dynamics for an aircraft with 20% wing loss, 70% horizontal stabiliser loss and 20% vertical stabiliser loss. The aircraft is now aerodynamically and geometrically asymmetrical. The matrix entries filled with orange represents the longitudinal dynamics, and the matrix entries filled with green the lateral-directional dynamics. However, now the longitudinal dynamics are also a function of the lateral-directional states and vice versa. From (4.2.21) it is clear that when the aircraft experiences a sideslip or roll rate perturbation it will couple into the pitch rate of the aircraft. This contribution to the pitch rate

state derivative is relatively small compared to the that of the angle of attack.

$$\begin{bmatrix} \dot{\bar{v}} \\ \dot{\alpha} \\ \dot{q} \\ \dot{\theta} \\ \dot{\beta} \\ \dot{p} \\ \dot{r} \\ \dot{\phi} \end{bmatrix} = \begin{bmatrix} -0.32 & 10.97 & -1.44 & -9.78 & 0.010 & 0 & -0.34 & 0 \\ -0.04 & -4.13 & 0.94 & -0.03 & -0.05 & 0.03 & 0 & 0 \\ 0.01 & -69.02 & -4.76 & 0 & -11.02 & 0.50 & 0.10 & 0 \\ 0 & 0 & 1 & 0.000 & 0 & 0 & 0 & 0 \\ 0 & 0 & 0 & 0 & -0.19 & 0.07 & -0.99 & 0.48 \\ 0 & 99.19 & 1.52 & 0 & -41.04 & -10.79 & 2.90 & 0 \\ 0.11 & 2.06 & 0.16 & 0 & 7.30 & -1.04 & -0.61 & 0 \\ 0 & 0 & 0 & 0 & 0 & 1 & 0.07 & 0.000 \end{bmatrix} \begin{bmatrix} \bar{v} \\ \alpha \\ q \\ \theta \\ \beta \\ p \\ r \\ \phi \end{bmatrix} + \begin{bmatrix} 0.070 & 0.134 & -0.07 & 0 \\ -0.25 & 0 & 0.23 & 0.02 \\ -63.55 & 0 & 11.34 & 5.11 \\ 0 & 0.000 & 0 & 0 \\ 0 & 0 & 0.000 & 0.08 \\ 10.00 & 0 & -140.41 & 1.64 \\ 2.21 & -0.03 & -6.11 & -12.94 \\ 0 & 0 & 0 & 0.000 \end{bmatrix} \begin{bmatrix} \delta_e \\ \Delta T \\ \delta_a \\ \delta_r \end{bmatrix} \tag{4.2.21}$$

From (4.2.21) it is clear that when the aircraft experiences an angle of attack or pitch rate perturbation, this will couple into its roll rate dynamics. The angle of attack perturbation contributions to the roll rate state derivative is quite significant. When the aircraft is disturbed form its longitudinal flight equilibrium by an elevator input, an atmospheric disturbance like a gust, or a velocity disturbance, the aircraft will experience a rolling moment (this effect was mentioned in Chapter 3). Consider that the aircraft is disturbed by an instantaneous angle of attack perturbation and that the aircraft is required to have zero roll acceleration. Assuming that the other state variables do not change and that no elevator or rudder control inputs are given, an instantaneous aileron control input,

$$\delta_a = \left(\frac{99.19}{140.41}\right)\alpha = 0.70\alpha \tag{4.2.22}$$

is required to achieve zero roll acceleration. Enough aileron authority must be available after the aircraft is trimmed in order to counter the rolling moment disturbance. Note that the angle of attack coupling also affects the yaw acceleration state derivatives. From (4.2.21) it is clear that the coupling between the longitudinal and lateral-directional dynamics affects mostly the angular accelerations. It is also clear that the longitudinal to lateral-directional coupling is dominant.

4.2.3.2 Control Efficiency and Coupling

In this project, the control surfaces are also partially lost along with the tip loss. The control efficiency of the aircraft will therefore be reduced. Equation 4.2.23 shows how the elevator's efficiency to produce pitch acceleration is reduced. The aircraft with 70% horizontal stabiliser tip loss will have to provide 1.7 times the amount of elevator deflection to provide the same amount of pitch acceleration.

$$\delta_{e_{damaged}} = \left(\frac{107.94}{63.55}\right)\delta_{e_{undamaged}} = 1.7\delta_{e_{undamaged}} \tag{4.2.23}$$

Similarly, Equation 4.2.24 shows how the aileron's efficiency to produce roll acceleration is reduced. The aircraft with 20% wing tip loss will have to provide 1.08 times the amount of aileron deflection to provide the same amount of roll acceleration.

$$\delta_{a_{damaged}} = \left(\frac{152.37}{140.41}\right)\delta_{a_{undamaged}} = 1.08\delta_{a_{undamaged}} \tag{4.2.24}$$

In the same way, Equation 4.2.25 shows how the rudder's efficiency to produce yaw acceleration is reduced. The aircraft with 20% vertical stabiliser tip loss will have to provide 1.3 times the amount of rudder deflection to provide the same amount of yaw acceleration.

$$\delta_{r_{damaged}} = \left(\frac{16.9}{12.94}\right)\delta_{r_{undamaged}} = 1.3\delta_{r_{undamaged}} \tag{4.2.25}$$

From (4.2.21) it is clear that the control inputs are also coupled. The pitch acceleration is now also affected by lateral control inputs. An aileron and rudder perturbation will result in the aircraft experiencing a pitch acceleration. The roll acceleration is also affected by longitudinal control inputs. A elevator perturbation will result in the aircraft experiencing both roll and yaw accelerations.

From the analysis above it is clear that the longitudinal and lateral-directional dynamics cannot be fully decoupled. If it is assumed that the system can be decoupled the coupling terms are regarded as disturbances to the system. It is then important to know the effects of the coupling and to make sure that the flight control system can still function as required, and if not, make provision for it.

4.2.4 Dynamic Stability Modes

When an aircraft is disturbed from its equilibrium flight due to a control input or an atmospheric influence such as a gust, the aircraft's stability modes are excited. The dynamic natural modes of motion consist of longitudinal modes of motion and lateral-directional modes of motion. In this section, the change in the dynamic modes is investigated as a function of the percentage of wing loss and the percentage of stabiliser losses respectively.

4.2.4.1 Modes of Motion

The longitudinal modes of motion are the:

- Short Period Mode
- Phugoid Mode

The short period mode is typically a damped oscillation in pitch about the Y_B-axis and describes the aircraft's tendency to realign itself with the velocity vector when disturbed [28]. When an aircraft is disturbed from its pitch flight equilibrium state, the short period mode is excited. The short period mode acts as a classic second-order oscillation, which can be represented as a mass-spring-damper system. The principal state variables are α, q and θ. The natural frequency of this mode is usually fast. The airspeed of the aircraft therefore remains approximately constant over the time scales of the short period motion.

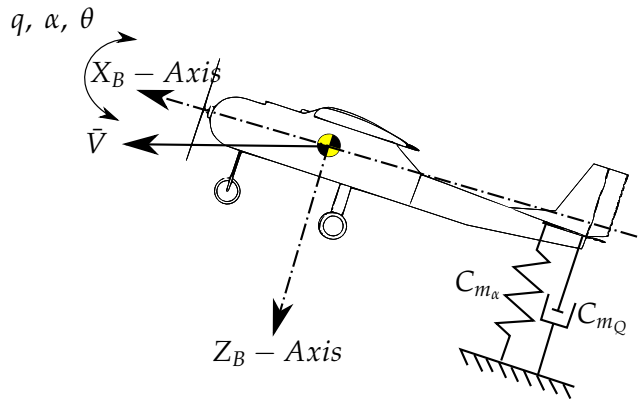

Figure 4.15: Mass-spring-damper representation of the short period mode

Figure 4.15 shows the mass-spring-damper system representation of the short period mode dynamics. When the aircraft is disturbed from its pitch flight equilibrium state, the spring will produce a restoring moment, thereby inducing an oscillation in pitch. The oscillation is then damped, as shown in Figure 4.15. The restoring moment and damping are produced by aerodynamic mechanisms from the airframe. The spring stiffness is a function of the longitudinal static stability C_{m_α}, and the damping is a function of the pitching moment due to pitch rate C_{m_Q}. From Figures 3.13 and 3.16 one saw that the spring stiffness and damping are mostly dominated by the aerodynamics from the horizontal stabiliser.

The phugoid mode is commonly a lightly damped low-frequency oscillation in the aircraft's speed and pitch angle [28]. During the phugoid motion, the angle of attack remains constant. The phugoid mode is a kinematic mode of motion. When the aircraft is disturbed from its flight equilibrium by a positive velocity perturbation, the aircraft will experience additional lift and will therefore pitch up and climb. During the climb, the aircraft decelerates and the aircraft's velocity reduces, causing it to lose lift. The aircraft will then pitch down and descend, causing the aircraft to accelerate and gain velocity. This process repeats itself with the motion damped by the energy removed through aerodynamic drag. Even though the phugoid motion is lightly damped, it generally does not present a control challenge because its timescale is long enough that minor control inputs can compensate for the excitation of this mode. Due to the gentle character of the phugoid mode, it is generally rather the short period mode that needs to be controlled.

To summarise the longitudinal modes of motion, the short period mode is usually a well damped oscillatory mode. The period is mostly determined by the pitching stiffness C_{m_α} of the aircraft, while the damping is primarily determined by the pitching moment due to pitch rate C_{m_Q}. By examining Figure 3.16, one can conclude that the short period mode will change with partial horizontal stabiliser loss. The phugoid mode, on the other hand, is a lightly damped oscillatory mode. The period of the phugoid mode is almost aircraft-independent, and is related to the aircraft's velocity. The damping of this mode is determined by the drag of the aircraft, which is generally low for efficient aircraft. The phugoid mode is therefore not expected to change when the aircraft suffer tip losses.

The lateral-directional modes of motion are the:

- Roll Mode

- Dutch Roll Mode
- Spiral Mode

The roll mode is a non-oscillatory lateral motion which describes the roll rate dynamics of the aircraft [28]. When the aircraft is disturbed from its flight equilibrium in roll, it will experience a roll rate. As the aircraft rolls, differential lift is generated by the wings due to the difference in the induced angle of attack experienced by each wing. This differential lift provides natural roll damping, which acts as a restoring moment in roll. The damping is a function of the rolling moment due to roll rate C_{l_p}. For a constant rolling moment disturbance, the roll rate will increase with an exponential response until the rolling moment due to roll rate balances the disturbing moment. A constant applied rolling moment will therefore result in a constant roll rate in steady state.

The Dutch roll mode is typically a lightly damped oscillation in yaw that couples into roll and sideslip. The Dutch roll mode is the lateral-directional equivalent of the short period mode. It describes the aircraft's tendency to realign itself with the oncoming airflow when disturbed from its flight equilibrium with a sideslip perturbation. However, the vertical stabiliser is generally less effective than the horizontal stabiliser as a damper. The Dutch roll mode is therefore very lightly damped and in most cases the damping is inadequate [28].

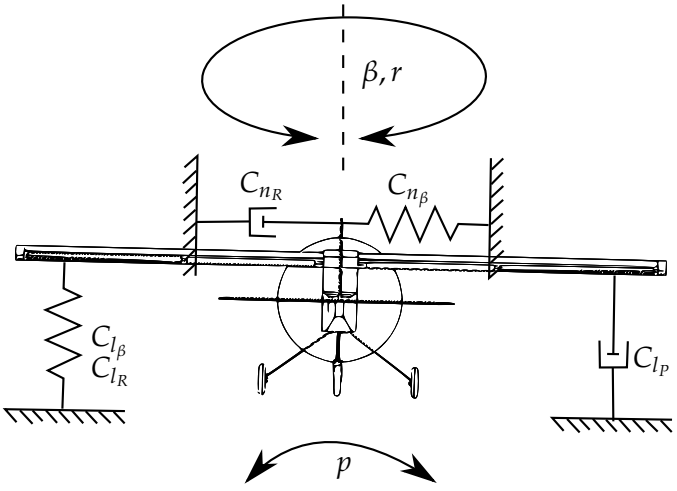

Figure 4.16: Mass-spring-damper representation of the Dutch roll mode

Figure 4.16 shows the mass-spring-damper system representation of the Dutch roll mode. When the aircraft is disturbed from its flight equilibrium with a sideslip perturbation, the spring shown on the vertical stabiliser will produce a restoring yawing moment, thereby inducing an oscillation in yaw. The oscillation is then damped by the resulting yawing moment that opposes the yaw rate, as shown on the vertical stabiliser in Figure 4.16. The spring stiffness is a function of the directional static stability C_{n_β}, and the damping is a function of the yawing moment due to yaw rate C_{n_R}. Both the damping and the spring stiffness in yaw are largely determined by the vertical stabiliser of the aircraft (see Figure 3.18). Furthermore, the sideslip perturbation will cause the aircraft to experience a destabilising rolling moment. The spring shown on the wing will produce a destabilising rolling moment, thereby inducing an oscillation in roll. The oscillation is

then damped by the resulting roll rate, as shown on the wing in Figure 4.16. The spring stiffness is a function of the lateral static stability C_{l_β} and the rolling moment due to yaw rate C_{l_R}, and the damping is a function of the rolling moment due to roll rate C_{l_P}. The net effect is that the aircraft oscillates in both yaw and roll, and when viewed from the back traces out a shrinking eclipse. Note that Figure 4.16 does not include all the aerodynamic contributions to the Dutch roll mode. It is difficult to quantify all the aerodynamic contributions to the Dutch roll mode characteristics with any degree of confidence [28].

The spiral mode is a non-oscillatory lightly damped mode which is slow to develop and involves a roll, yaw and sideslipping motion [28]. The spiral mode describes the tendency of the aircraft to return to or diverge from wings-level flight. The mode's characteristics are very dependent on the lateral-directional static stability of the aircraft (C_{l_β} and C_{n_β}). The spiral mode is therefore expected to change with partial wing loss and partial vertical stabiliser loss (see Figures 4.4 and 4.5). When the aircraft is disturbed from its flight equilibrium by a sideslip perturbation, the aircraft will experience a restoring yawing moment to turn the aircraft into the direction of the airflow. This causes a rolling moment that will roll the aircraft towards the sideslip. Simultaneously, the lateral static stability of the aircraft will generate a rolling moment to roll away from the sideslip and return the aircraft to wings-level. The directional and lateral static stabilities therefore act in opposition, leading to the spiral mode. When the lateral static stability effect is more dominant than the directional static stability effect, the spiral mode is stable. But when the directional static stability effect is more dominant than the lateral static stability effect, the spiral mode will be unstable. The spiral mode usually has a long enough time constant that it presents no difficulty to correct with minor control inputs, even when it is unstable. Due to the gentle character of the spiral mode, it is generally rather the Dutch roll mode and the roll mode that need to be controlled.

To summarise the lateral-directional modes of motion, the roll mode is a non-oscillatory heavily damped mode where the damping is determined by C_{l_P}, hence the roll mode is expected to change with partial wing loss (see Figure 3.12 (b)). The Dutch roll mode is a lightly damped oscillatory mode which consists of a coordinated yawing, rolling and sideslipping motion. The dihedral effect C_{l_β} is generally destabilising, while the directional static stability C_{n_β} is generally stabilising. By examining Figures 3.18 and 3.12, one can conclude that the Dutch roll mode will change with partial wing loss and partial vertical stabiliser loss. The spiral mode is a non-oscillatory lightly damped or unstable mode where the dihedral effect has a stabilising effect and the directional static stability has a destabilising effect; therefore one also expects the spiral mode to change with partial wing loss and partial vertical stabiliser loss.

4.2.4.2 Loci of the Open-loop Poles for Tip Loss Cases

Figures 4.17 and 4.18 illustrate how the natural modes of motion change as a function of the percentage of wing loss and of the percentage of stabiliser losses respectively. The figures plot the loci of the open-loop poles for the full aircraft dynamics, with coupled longitudinal and lateral dynamics, as a function of the percentage wing or stabiliser loss. The open-loop poles were obtained by calculating the eigenvalues of the 8x8 full system matrix over all Tip loss cases.

From Figures 4.17 and 4.18, one will notice that the roll mode of the aircraft is mostly affected by wing loss. The time constant for the aircraft to establish a steady state roll rate increases with partial wing loss. The time constant increases from 84 ms for no tip loss to roughly 113 ms for 40%

semi-span wing tip loss. Horizontal stabiliser and vertical stabilisers tip losses does not affect the roll mode of the aircraft. From Figures 4.17 and 4.18, one will notice that the short period mode of

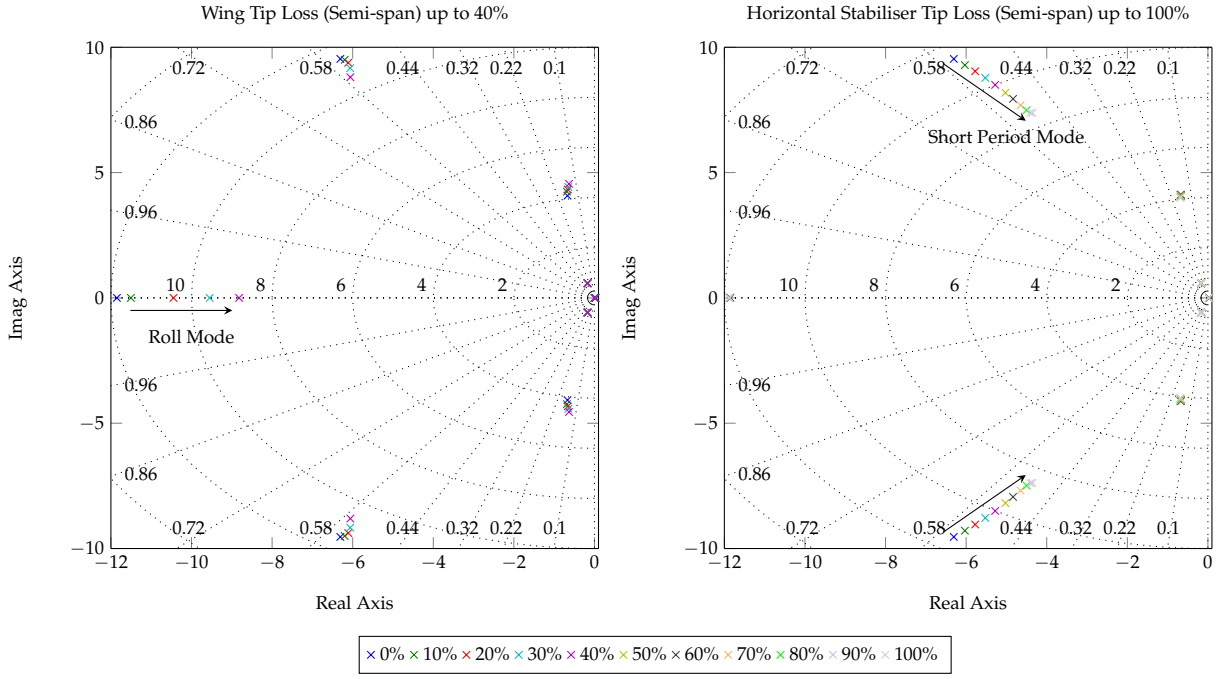

Figure 4.17: Natural modes of motion for wing loss and horizontal stabiliser loss

the aircraft is mostly affected by partial horizontal stabiliser loss. Both the natural frequency and the damping ratio of the short period mode decrease. The natural frequency shows a significant decrease, whereas the damping only shows a minor decrease. This is expected, as discussed above. Partial wing and vertical stabiliser losses only have a minor effect on the short period mode of the aircraft. In Figure 4.17, a slight change in the short period mode due to partial wing loss is observed. The natural frequency and the damping ratio of the short period mode change slightly. Recall from Chapter 3 that the wing also contributes to the C_{m_α} and C_{m_Q} derivatives (see (3.4.15) and (3.4.16)). When the aircraft suffers partial vertical stabiliser loss, the centre of mass of the aircraft will move towards the nose, causing the aircraft to become more statically stable. This is also observed in Figure 4.18. From Figures 4.17 and 4.18, one will notice that the Dutch roll mode of the aircraft is mostly affected by partial vertical stabiliser loss. The Dutch roll mode's natural frequency and damping decreases, and eventually the Dutch roll mode becomes unstable after 70% vertical stabiliser loss. As the Dutch roll mode becomes slower and more lightly damped, the spiral mode becomes faster and more stable. With partial vertical stabiliser loss, the directional static stability C_{n_β} of the aircraft decreases. Due to the directional static stability C_{n_β} having a stabilising effect on the Dutch roll mode and a destabilising effect on the spiral mode, one expects the spiral mode to improve and the Dutch roll mode to degrade with partial vertical stabiliser loss. Partial wing and horizontal stabiliser loss do not noticeably affect the Dutch roll mode of the aircraft. As mentioned above, the phugoid mode is almost aircraft-independent and therefore does not significantly change with tip losses, as seen in Figures 4.17 and 4.18.

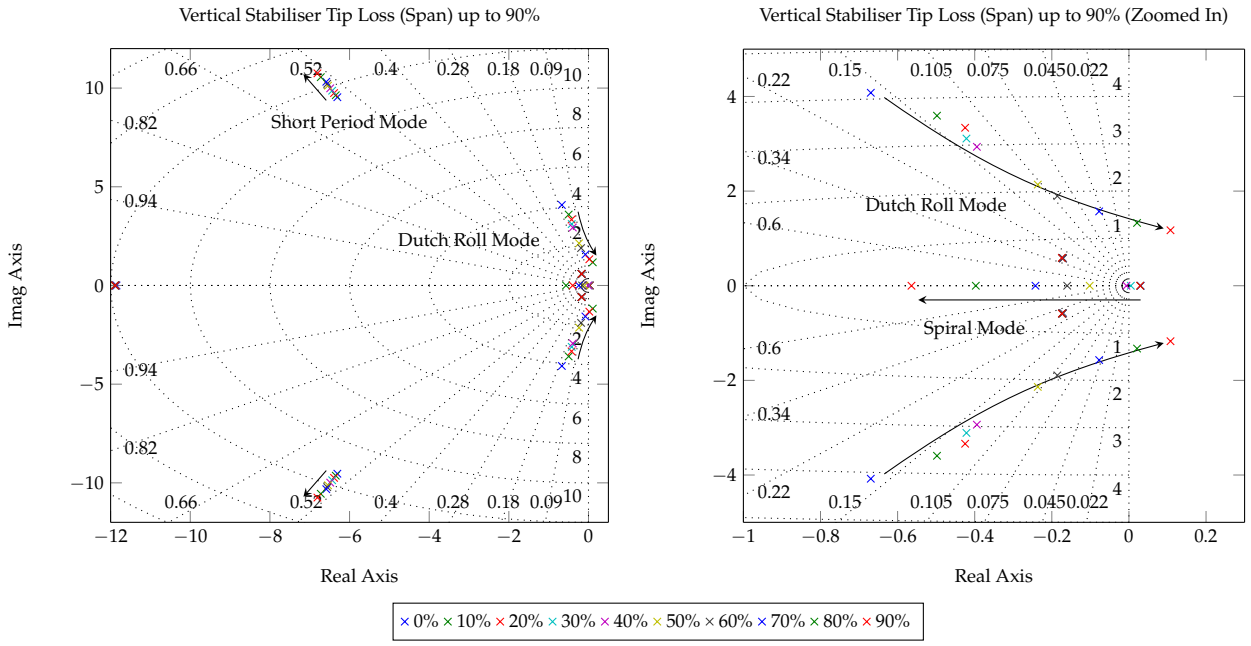

Figure 4.18: Natural modes of motion for vertical stabiliser loss

4.3 Summary

In this chapter, the static stability analysis and dynamics stability analysis of the aircraft with partial wing loss, partial horizontal stabiliser loss, and partial vertical stabiliser loss were investigated. The stability analysis was investigated as a function of percentage tip losses respectively to determine how each tip loss case affects the dynamics of the aircraft. It was found that the aircraft remains longitudinally statically stable for all the partial horizontal stabiliser loss cases (100% semi-span tip loss) and also remains laterally statically stable for all the partial wing loss cases (40% semi-span tip loss). However, it was found that the aircraft becomes directionally statically unstable for partial vertical stabiliser losses of more than approximately 70% (span tip loss).

The full nonlinear aircraft model developed in Chapter 3 was linearised about valid flight equilibrium trim conditions that were obtained for all the tip loss cases respectively. Two lateral-directional trim configurations, namely wings-level and small bank angle, were investigated. From the linearised aircraft model, the aircraft's natural modes of motion were investigated for all the tip loss cases respectively. It was found that partial horizontal stabiliser loss mostly affects the short period mode, partial wing loss mostly affects the roll mode, and partial vertical stabiliser loss mostly affects the Dutch roll mode of the aircraft. Furthermore, the coupling of the longitudinal dynamics into the lateral-directional dynamics and vice versa were investigated. Now that the behaviour of the aircraft under different tip loss cases are better understood, flight controllers can be developed to control the aircraft to perform autonomous navigation and landings.

The flight control system oversees all the tasks required to safely manoeuvre the aircraft throughout a given mission, which are typically all the tasks tat are usually performed by a pilot. Some notable tasks are take-off, navigation, and landing of the unmanned aircraft. The flight control system's architecture must be developed to support the execution of all the required tasks. Furthermore, the flight control system must be reliable, maintainable, and robust while the aircraft operates in uncertain conditions. Uncertain conditions can include a change in atmospheric conditions like wind or a change in the aircraft's dynamics due to structural damage or actuator failure.

In this chapter, an autonomous landing system that is able to land an unmanned aircraft after suffering the partial wing and stabiliser losses is designed. The inner-loop controllers are designed to be robust against the partial wing and stabiliser losses. The outer-loop controllers benefit from the robustness of the inner-loop controllers, enabling the outer-loop controllers to also remain stable over all the tip loss cases. For the purposes of this project, the flight control system must be able to perform two main tasks: waypoint navigation and autonomous landings. The controllers are therefore designed to allow the aircraft to track a glide slope and a cross track position error with zero steady state error.

This chapter starts by proposing a fault-tolerant flight control system architecture, followed by a discussion on how to design it to be robust for an aircraft that has suffered partial wing and stabiliser losses. The controller designs are then discussed in detail and the chapter concludes with a brief summary.

5.1 Flight Control System Architecture

The proposed architecture for the flight control system, as shown in Figure 5.1, is a fixed-gain passive fault-tolerant flight control system. The proposed flight control system can be designed to guarantee the stability of the aircraft given that the uncertainties remain within given bounds. A fixed-gain robust control approach is used instead of an adaptive control approach because it is much more difficult to obtain airworthiness certification for adaptive controllers. The proposed flight control system consists of three main components, namely the inner-loop controllers, the outer-loop controllers, and the navigation and landing state machine. The inner-loop controllers are in direct command of the aircraft's control inputs and control the aircraft's normal and lateral specific acceleration, roll rate, and airspeed. The outer-loop controllers control the aircraft's position and attitude. The navigation and landing state machine supplies the controllers with the appropriate cross track position error, altitude, airspeed and lateral specific acceleration reference commands to manoeuvre the aircraft to perform waypoint navigation or an autonomous landing.

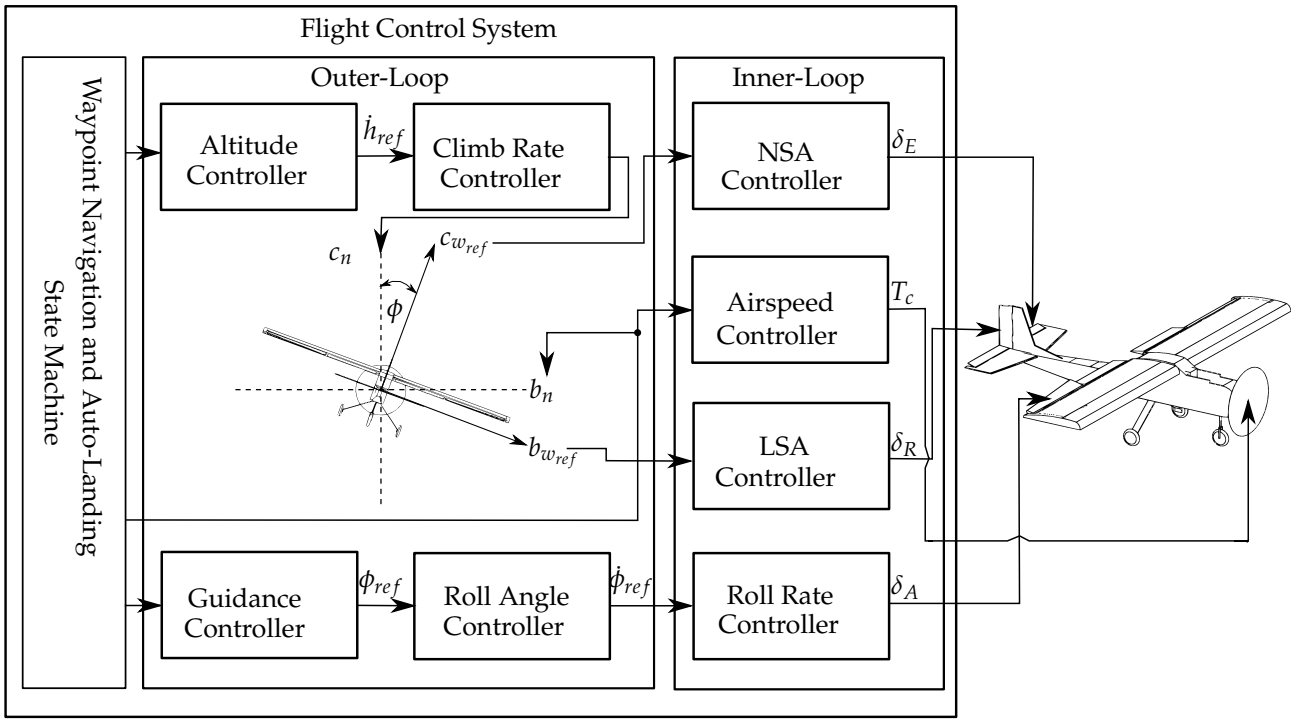

Figure 5.1: Block diagram of the flight control system architecture

Looking at Figure 5.1, the normal specific acceleration (NSA) and lateral specific acceleration (LSA) controllers control the specific accelerations of the aircraft, denoted as c_w and b_w in the wind reference frame respectively. It is important to note that the reference command produced by the climb rate controller is denoted as c_n. When the aircraft flies with a roll angle ϕ, a larger normal acceleration is required to enable the aircraft to remain at a constant climb rate. Therefore the acceleration reference command produced by the climb rate controller c_n is transformed to c_w through the aircraft's roll angle ϕ. The proposed control architecture will trim the aircraft using the wings-level configuration. For straight and level flight, the roll angle controller will keep the aircraft's wings level while the LSA controller regulates the lateral acceleration to zero. The aircraft will fly with a sideslip to balance the forces and moments acting on it. The fact that the LSA controller regulates the lateral acceleration to zero will also enable the aircraft to fly coordinated turns, reducing large sideslip angles when turning.

The design strategy for the flight control system is to ensure that the inner-loop controllers remain stable and within acceptable transient response specifications when the aircraft suffers partial wing and stabiliser losses. The inner-loop controllers are designed to be robust against these partial tip loses. A successive loop closure or cascade control structure is then used to design the outer-loop controllers. This allows the outer-loop controllers to benefit from the robustness of the inner-loop controllers, enabling the outer-loop controllers to also remain stable throughout all tip loss cases. All the uncertainties are captured within the inner-loop controllers, resulting in more robust outer-loop controllers. Furthermore, all the inner-loop controllers are designed with integrators, which enables the flight control system to find the desired straight and level flight trim values, and the outer-loop controllers are design with limited integrators to ensure zero steady state tracking in the presence of sensor biases. All the integrators in the flight control system are equipped with anti wind-up mechanisms to protect them against integral wind-up.

5.2 Approach For Robust Design

The aim of the robust inner-loop controllers is to ensure that the inner-loop controllers remain stable and within acceptable transient response specifications even when the aircraft suffers partial wing and stabiliser losses. Furthermore, this must be achieved without knowing the amount of partial tip loss that the aircraft has suffered and without changing the inner-loop controller structure. The fixed gains of the controllers must be designed so that the flight control system will be robust against partial wing and stabiliser losses. A trade-off between performance and robustness is therefore inevitable. The ideal case would be if the controllers were robust against partial tip losses while retaining their performance. This is not possible with fixed gain controllers, and therefore a trade-off is made. The aircraft will be undamaged for most of its operation, so having a flight control system with poor performance on the undamaged aircraft is not desired. The damaged aircraft must also meet some minimum acceptable performance specification as constrained by the minimum required performance for safely landing the unmanned aircraft. However, it should be noted that it may not be possible to meet the minimum performance requirements for landing over all partial tip loss cases. The design approach is instead to find controller gains that provide the best performance for the undamaged aircraft, while still providing at least the minimum acceptable performance over all tip loss cases. Prior knowledge of the dynamics of the aircraft that has suffered partial wing and stabiliser losses is therefore needed.

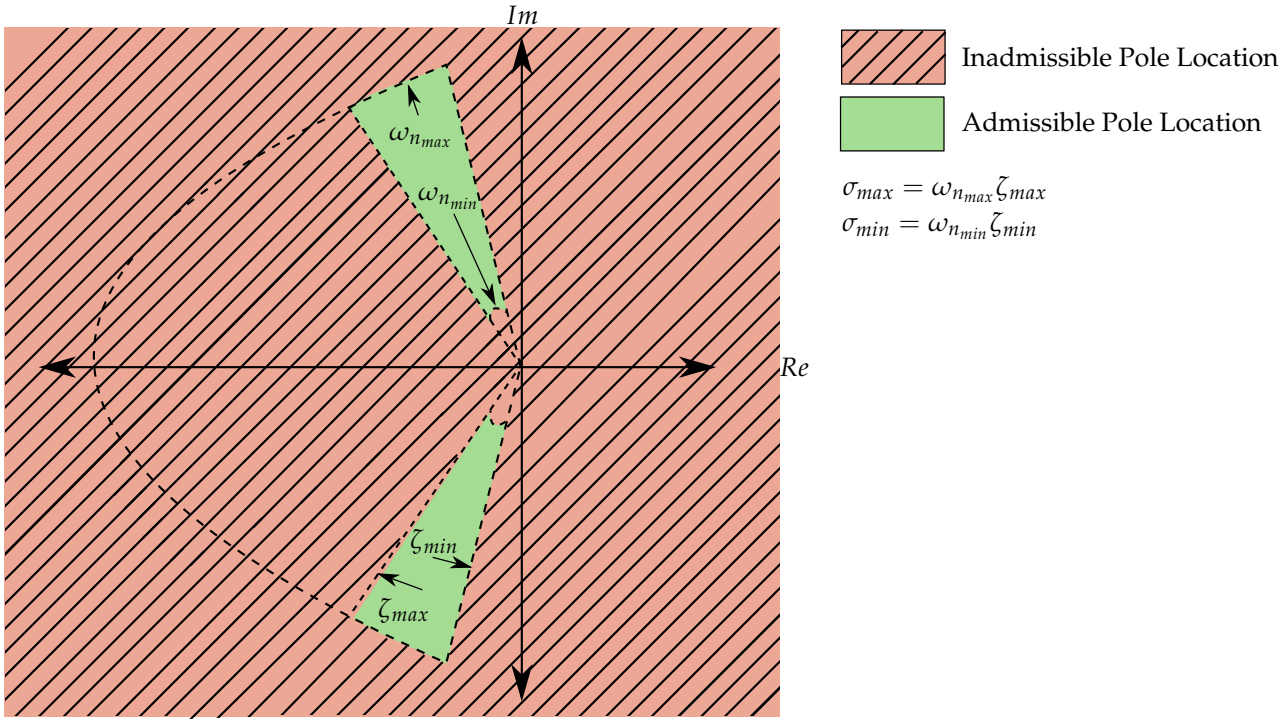

Figure 5.2: Admissible closed-loop pole region required for robustness

For the gains to qualify as robust gains, the closed-loop poles of the system must remain within some admissible pole region as the aircraft suffers partial wing and stabiliser losses. From Figure 5.2, an admissible pole region is defined as the region where the poles have a natural frequency between $\omega_{n_{max}}$ and $\omega_{n_{min}}$ and a damping ratio between ζ_{max} and ζ_{min}. Note that this assumes that

the dominant poles of the system are a complex pole pair, but can easily be adapted to include real poles (e.g $\zeta_{max} = 1$) or to have multiple admissible pole regions.

An iterative algorithm (detailed in Appendix E) is proposed to determine the robust gains for the flight control laws. The algorithm determines gains, if such gains exist, for a controller with different combinations of natural frequencies and damping ratios for all partial tip loss cases until both the desired closed-loop performance and robustness are obtained. If a solution is not found, either the best performance or the minimum acceptable performance specifications are relaxed until an acceptable trade-off between performance and robustness is achieved. The algorithm accomplishes this by first determining controller gains for the undamaged aircraft for some specified natural frequency ω_n and damping ratio ζ. The closed-loop system is then obtained and an admissibility check is done on the closed-loop poles. If the closed-loop poles fall within the given admissible regions, the real part σ of the closed-loop poles is compared to the previous best real part σ obtained. This comparison checks whether the new gains will result in a faster (higher performance) response than the best previously calculated gains. If the gains provide a faster response, then a robustness check is done to see if the controller remains stable and within acceptable transient response specifications over all the partial tip loss cases. The robustness check is done by performing an admissibility check on the closed-loop poles (with the designed gains) for all the given partial tip loss cases. If all the closed-loop poles for all the partial tip loss cases fall within the admissible region, the designed gains and σ of the undamaged aircraft are stored.

The process is repeated with different combinations of ω_n and ζ. Once the algorithm has iterated through all the combinations of natural frequencies ω_n and damping ratios ζ, a check is done to verify if any gains that qualify for the required specifications were found. If none was found, the required specifications and robustness are not possible and either the best performance or the minimum acceptable performance specifications must be relaxed. The whole process can then be repeated until a set of gains is found that provides the best performance for the undamaged aircraft while still providing at least the minimum acceptable performance over all the tip loss cases.

The outer-loop controller gains are then designed on the minimum acceptable performance for the undamaged aircraft. This is done to guarantee the stability of the aircraft given that the tip loss cases remain within the designed bounds. Furthermore, timescale separation between control loops is implemented to enhance the robustness of the outer loops.

5.3 Flight Control System Design

This section describes the design of the fixed-gain passive fault-tolerant flight control system as described by the block diagram in Figure 5.1. A linear approach to control system design is adopted for the design of the flight control system. The inner-loop controllers are designed to be robust against partial wing and stabiliser losses. The inner-loop controllers are then augmented onto the full linear aircraft dynamics, which are used to design the outer-loop controllers. The full uncoupled linear aircraft dynamics are used in order to account for existing coupling terms due to partial wing and stabiliser losses.

From Figure 5.1, one will note that all the inner-loop controllers are independent controllers. Throughout the design it is assumed that each inner-loop controller will reject coupling distur-

bances, for example, if a normal acceleration is commanded, the airspeed will be disturbed, but the airspeed controller will work to reject the disturbance. This approach is used to simplify the control system design proses and the validity of the assumption is evaluated in simulation. Coupling between aircraft states, as discussed in Section 4.2.3, usually forces one to make use of multi-input, multi-output (MIMO) controller design techniques such as Linear Quadratic Regulator (LQR) theory. To achieve sufficient performance from such a controller, an accurate linear aircraft model is required. Full state feedback robust controller techniques do exist, but this requires one to be able to measure or estimate all the aircraft states. In this project, the inner-loop controllers are designed on reduced-order dynamics that are modelled as being decoupled. The coupling is therefore regarded as disturbances to the system. In Section 5.3.1, the controllers will be systematically designed and added to the full linear aircraft dynamics to from a full linear closed-loop system that controls the altitude, velocity, lateral acceleration and cross track position error of the aircraft.

5.3.1 Airspeed Controller

This section describes the design of the airspeed controller. Even though the airspeed controller is an inner-loop controller, it is not designed to be robust to partial tip losses. This is mainly due to the architecture of the reduced-order dynamics which describes the aircraft's change in airspeed when thrust is applied. The only airframe-dependent variable that appears in the reduced-order model is the mass of the aircraft. The mass of the aircraft does not change as significantly as the aerodynamic properties of the aircraft when the aircraft suffers partial tip losses. As mentioned before, all the inner-loop controllers are designed on reduced-order dynamics and thereafter verified on the full linear aircraft dynamics. From Figure 5.1, one will note that the airspeed and longitudinal controllers are independent controllers. Tight coupling between airspeed and the longitudinal dynamics usually forces one to make use of MIMO controller design techniques such as LQR theory. To achieve adequate performance from such a controller, an accurate linear aircraft model is required and one would need to measure or estimate all the aircraft states. It was therefore decided for this project to design independent controllers for airspeed and longitudinal dynamics and thereafter evaluate the design choice.

5.3.1.1 Reduced-Order Design

Before the airspeed controller is designed, a reduced dynamic model that describes the relationship between the airspeed of the aircraft and the throttle commanded by the controller must be obtained. Recall from Chapter 3 that the relationship between the thrust and the commanded throttle is modelled as a first-order lag response. Equation 3.4.22 from Chapter 3 is restated below for convenience.

$$\dot{T} = \left[-\frac{1}{\tau_T} \right] T + \left[\frac{1}{\tau_T} \right] T_c \tag{5.3.1}$$

With small incidence angle simplifications, the wind reference frames' axial acceleration can be written as follows [7]:

$$a_w = \left[\frac{1}{m} \right] T + \left[-\frac{\bar{q} S C_D}{m} \right] \tag{5.3.2}$$

where the axial acceleration a_w can be written as the derivative of the airspeed $\dot{V}$. The linear state space model is then given by

$$\begin{bmatrix} \Delta\dot{T} \\ \dot{\bar{v}} \end{bmatrix} = \begin{bmatrix} -\frac{1}{\tau_T} & 0 \\ \frac{1}{m} & 0 \end{bmatrix} \begin{bmatrix} \Delta T \\ \bar{v} \end{bmatrix} + \begin{bmatrix} \frac{1}{\tau_T} \\ 0 \end{bmatrix} \Delta T_c \tag{5.3.3}$$

where ΔT and $\bar{v}$ are small perturbations from the flight equilibrium. The reduced dynamic state space model in (5.3.3) can now be used to design the airspeed controller. A standard proportional-integral (PI) controller, as seen in Figure 5.3, is used to control and regulate the airspeed of the aircraft, where

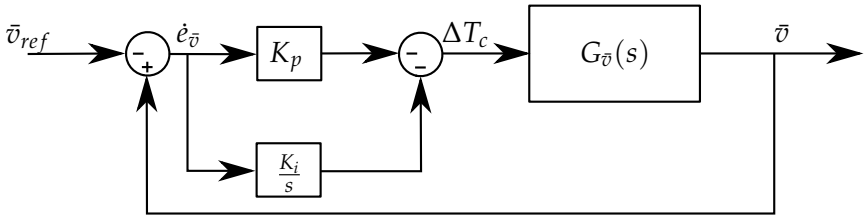

Figure 5.3: Airspeed controller block diagram

$$G_{\bar{v}}(s) = \begin{bmatrix} 0 & 1 \end{bmatrix} \left[\begin{bmatrix} s & 0 \\ 0 & s \end{bmatrix} - \begin{bmatrix} -\frac{1}{\tau_T} & 0 \\ \frac{1}{m} & 0 \end{bmatrix} \right]^{-1} \begin{bmatrix} \frac{1}{\tau_T} \\ 0 \end{bmatrix} \tag{5.3.4}$$

The integrator is used to reject the unmodelled drag, to find trim values, and to reject any other disturbances to the airspeed controller when in steady state. If no initial trim value is specified for the throttle command, then when in straight and level flight the integrator will determine the appropriate throttle command. The integrator integrates the airspeed error, which is expressed mathematically as,

$$\dot{e}_{\bar{v}} = \bar{v} - \bar{v}_{ref} \tag{5.3.5}$$

where $\bar{v}$ is the aircraft's perturbed airspeed and $\bar{v}_{ref}$ the perturbed airspeed reference. After augmenting the integrator dynamics to (5.3.3), the system becomes

$$\begin{bmatrix} \Delta\dot{T} \\ \dot{\bar{v}} \\ \dot{e}_{\bar{v}} \end{bmatrix} = \begin{bmatrix} -\frac{1}{\tau_T} & 0 & 0 \\ \frac{1}{m} & 0 & 0 \\ 0 & 1 & 0 \end{bmatrix} \begin{bmatrix} \Delta T \\ \bar{v} \\ e_{\bar{v}} \end{bmatrix} + \begin{bmatrix} \frac{1}{\tau_T} \\ 0 \\ 0 \end{bmatrix} \Delta T_c + \begin{bmatrix} 0 \\ 0 \\ -1 \end{bmatrix} \bar{v}_{ref} \tag{5.3.6}$$

A PI control law is defined that generates a throttle command T_c proportional to the weighted sum of the airspeed error and the time integral of the airspeed error:

$$T_c = -K_p \dot{e}_{\bar{v}} - K_i e_{\bar{v}} \tag{5.3.7}$$

The control law is now substituted into the system and the closed-loop system becomes

$$\begin{bmatrix} \Delta\dot{T} \\ \dot{\bar{v}} \\ \dot{e}_{\bar{v}} \end{bmatrix} = \begin{bmatrix} -\frac{1}{\tau_T} & -\frac{K_p}{\tau_T} & -\frac{K_i}{\tau_T} \\ \frac{1}{m} & 0 & 0 \\ 0 & 1 & 0 \end{bmatrix} \begin{bmatrix} \Delta T \\ \bar{v} \\ e_{\bar{v}} \end{bmatrix} + \begin{bmatrix} \frac{K_p}{\tau_T} \\ 0 \\ -1 \end{bmatrix} \bar{v}_{ref} \tag{5.3.8}$$

Calculating the closed-loop characteristic equation gives

$$|sI - A| = s^3 + \frac{1}{\tau_T} s^2 + \frac{K_p}{m\tau_T} s + \frac{K_i}{m\tau_T} \tag{5.3.9}$$

For pole placement, a desired characteristic equation for the airspeed dynamics is defined as

$$\alpha_{cl}(s) = (s^2 + 2\zeta\omega_n s + \omega_n^2)(s + a) \tag{5.3.10}$$

where ω_n can be written as

$$\omega_n = \frac{1 - a\tau_T}{2\zeta\tau_T} \tag{5.3.11}$$

From (5.3.9) and (5.3.10), the control gains are calculated as

$$K_p = m\tau_T(2\zeta\omega_n a + \omega_n^2) \tag{5.3.12}$$

$$K_i = m\tau_T\omega_n^2 a \tag{5.3.13}$$

Designing the airspeed controller therefore involves selecting a damping ratio ζ and natural frequency ω_n, and the real closed-loop pole a corresponding to the open-loop integrator. The value of the thrust time constant τ_T as well as the maximum thrust are determined with a static thrust test [5]. The damping ratio and closed-loop natural frequency are selected such that the airspeed is controlled fast enough to counter climb rate disturbances but not to use excessive throttle commands. Thus,

$$\zeta_{cl} = 1 \qquad\qquad \omega_{n_{cl}} = 0.8 \text{ rad/s} \tag{5.3.14}$$

The pole placement and step response of the airspeed controller are shown in Figure 5.4. From Figure 5.4 (b), one will note that even though the controller is designed to have no overshoot, overshoot is present. This is due to the zero that is introduced by the PI controller, which is one of its disadvantages. Alternatively, the airspeed control law used by Alberts could be used to minimise the overshoot, but this could slow down the response [10].

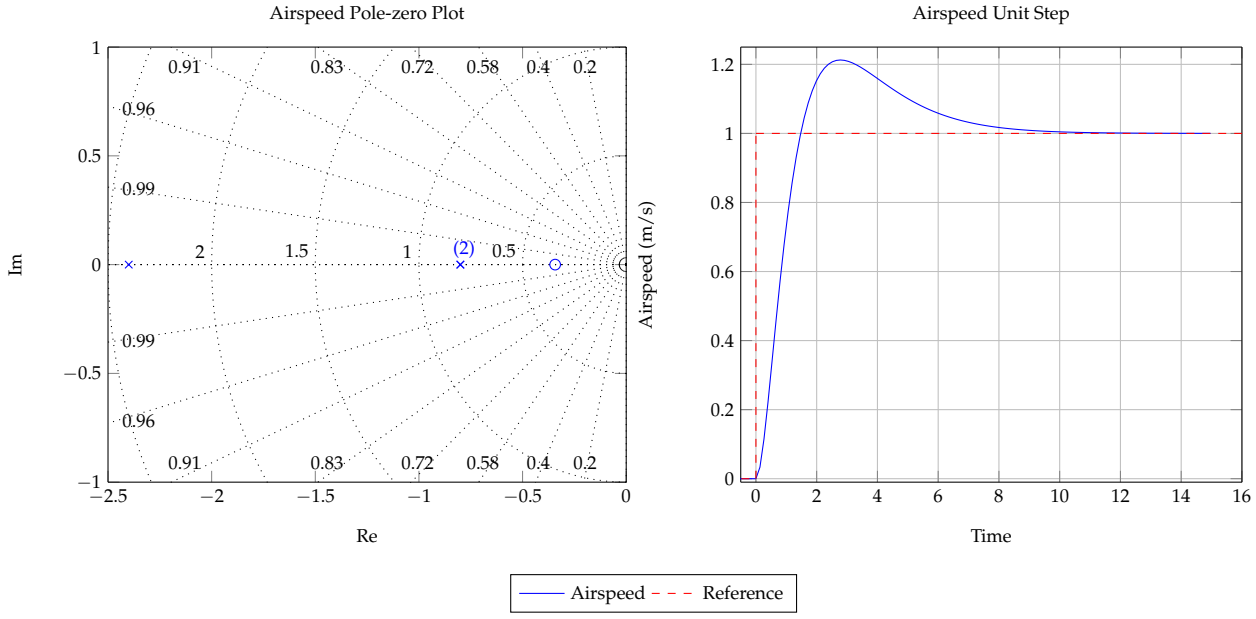

Figure 5.4: Airspeed pole-zero plot and unit step response

5.3.1.2 Closed-Loop System

The airspeed controller is now added to the full linear dynamics of the aircraft. Equation 5.3.15 states the full linear aircraft dynamics as derived in Section 4.2.2.

$$\dot{\mathbf{x}} = \mathbf{A}\mathbf{x} + \mathbf{B}\mathbf{u} \tag{5.3.15}$$

where

$$\mathbf{B} = \begin{bmatrix} \boldsymbol{B}_{\delta_e} & \boldsymbol{B}_T & \boldsymbol{B}_{\delta_a} & \boldsymbol{B}_{\delta_r} \end{bmatrix} \tag{5.3.16}$$

The engine lag dynamics are now augmented to the full linear aircraft dynamics.

$$\begin{bmatrix} \dot{\mathbf{x}} \\ \Delta\dot{T} \end{bmatrix} = \begin{bmatrix} \mathbf{A} & \boldsymbol{B}_T \\ \mathbf{0}_{1\times 8} & -\frac{1}{\tau} \end{bmatrix} \begin{bmatrix} \mathbf{x} \\ T \end{bmatrix} + \begin{bmatrix} \boldsymbol{B}_{\delta_e} & \mathbf{0}_{8\times 1} & \boldsymbol{B}_{\delta_a} & \boldsymbol{B}_{\delta_r} \\ 0 & \frac{1}{\tau_T} & 0 & 0 \end{bmatrix} \begin{bmatrix} \delta_e \\ \Delta T_c \\ \delta_a \\ \delta_r \end{bmatrix} \tag{5.3.17}$$

The integrator dynamics can now be augmented.

$$\begin{bmatrix} \dot{\mathbf{x}} \\ \Delta\dot{T} \\ \dot{e}_{\bar{v}} \end{bmatrix} = \begin{bmatrix} \mathbf{A} & \boldsymbol{B}_T & \mathbf{0}_{8\times 1} \\ \mathbf{0}_{1\times 8} & -\frac{1}{\tau} & 0 \\ \begin{bmatrix} 1 & \mathbf{0}_{1\times 7} \end{bmatrix} & 0 & 0 \end{bmatrix} \begin{bmatrix} \mathbf{x} \\ T \\ e_{\bar{v}} \end{bmatrix} + \begin{bmatrix} \boldsymbol{B}_{\delta_e} & \mathbf{0}_{8\times 1} & \boldsymbol{B}_{\delta_a} & \boldsymbol{B}_{\delta_r} \\ 0 & \frac{1}{\tau_T} & 0 & 0 \\ 0 & 0 & 0 & 0 \end{bmatrix} \begin{bmatrix} \delta_e \\ \Delta T_c \\ \delta_a \\ \delta_r \end{bmatrix} + \begin{bmatrix} \mathbf{0}_{8\times 1} \\ 0 \\ -1 \end{bmatrix} \bar{v}_{ref} \tag{5.3.18}$$

Finally, the control law from (5.3.7) is added as follows:

$$\begin{bmatrix} \dot{\mathbf{x}} \\ \Delta\dot{T} \\ \dot{e}_{\bar{v}} \end{bmatrix} = \begin{bmatrix} \mathbf{A} & \boldsymbol{B}_T & \mathbf{0}_{8\times 1} \\ \begin{bmatrix} -\frac{K_p}{\tau_T} & \mathbf{0}_{1\times 7} \end{bmatrix} & -\frac{1}{\tau} & -\frac{K_i}{\tau_T} \\ \begin{bmatrix} 1 & \mathbf{0}_{1\times 7} \end{bmatrix} & 0 & 0 \end{bmatrix} \begin{bmatrix} \mathbf{x} \\ T \\ e_{\bar{v}} \end{bmatrix} + \begin{bmatrix} \boldsymbol{B}_{\delta_e} & \mathbf{0}_{8\times 1} & \boldsymbol{B}_{\delta_a} & \boldsymbol{B}_{\delta_r} \\ 0 & \frac{K_p}{\tau_T} & 0 & 0 \\ 0 & -1 & 0 & 0 \end{bmatrix} \begin{bmatrix} \delta_e \\ \bar{v}_{ref} \\ \delta_a \\ \delta_r \end{bmatrix} \tag{5.3.19}$$

The closed-loop state space model now has a subscript $\bar{v}$, indicating that the airspeed controller has been added. Note that the input vector has changed. The airspeed reference is now an input to the system.

$$\dot{\mathbf{x}}_{\bar{v}} = \mathbf{A}_{\bar{v}}\mathbf{x}_{\bar{v}} + \mathbf{B}_{\bar{v}}\mathbf{u} \tag{5.3.20}$$

Now define

$$\mathbf{B}_{\bar{v}} = \begin{bmatrix} \boldsymbol{B}_{\delta_e} & \boldsymbol{B}_{\bar{v}_{ref}} & \boldsymbol{B}_{\delta_a} & \boldsymbol{B}_{\delta_r} \end{bmatrix} \tag{5.3.21}$$

The closed-loop transfer function from $\bar{v}_{ref}$ to $\bar{v}$ can now be obtained.

$$G_{\bar{v}_{cl}}(s) = \frac{\bar{v}}{\bar{v}_{ref}} = \boldsymbol{C}_{\bar{v}}(s\mathbf{I}_{10} - \mathbf{A}_{\bar{v}})^{-1}\boldsymbol{B}_{\bar{v}_{ref}} \tag{5.3.22}$$

where

$$\boldsymbol{C}_{\bar{v}} = \begin{bmatrix} 1 & \mathbf{0}_{1\times 9} \end{bmatrix} \tag{5.3.23}$$

5.3.2 Normal Specific Acceleration Controller

This section describes the design and robustness of the normal specific acceleration (NSA) controller. The controller design is based on the linear, decoupled rigid body rotational dynamics model derived by Peddle [7]. As mentioned, the longitudinal controllers are designed completely separately from the airspeed controller on the assumption that the airspeed is maintained sufficiently well by the airspeed controller while performing a normal acceleration manoeuvre. The NSA controller is a high-bandwidth controller that encapsulates all of the aircraft-specific uncertainties. Since the NSA controller is a high-bandwidth controller that operates at acceleration level, it has the ability to reject disturbances before they manifest to the slower controller dynamics. The NSA controller uses the aircraft's elevator to produce a pitching moment that changes the angle of attack of the aircraft, thereby changes the amount of lift generated by the wings of the aircraft. This is also known as pitch-moment-based longitudinal control.

In the case of pitch-moment-based control, the normal dynamics can simply be thought of as the short period mode dynamics [7]. Therefore the NSA controller will essentially control the short period dynamics of the aircraft. In Chapter 4, it was concluded that the short period mode dynamics are mostly dominated by the horizontal stabiliser of the aircraft. With horizontal stabiliser loss, the short period mode dynamics reduces both in natural frequency and in damping ratio. For the NSA controller to be robust against horizontal stabiliser loss, the NSA controller is designed to be robust against the change in short period mode dynamics. The technique discussed in Section 5.2 will be used to find controller gains that are robust against the given amount of partial horizontal stabiliser tip losses.

The abovementioned technique requires one to specify an upper and lower bound for both natural frequency and damping ratio. The upper and lower bounds of the natural frequency are obtained from the NSA design assumptions discussed by Peddle. First, it is assumed that

$$\left| \frac{L_Q}{mV_T} \right| \ll 1 \tag{5.3.24}$$

This assumption should be met by all the partial horizontal stabiliser loss cases. Secondly, the effective length to the tail-plane l_H and the effective damping arm length l_D should be of similar magnitude. The length between l_H and l_D should be shorter than the length between l_H and l_N, where [7]

$$l_H = -\frac{M_{\delta_E}}{L_{\delta_E}} \tag{5.3.25}$$

$$l_D = -\frac{M_Q}{L_Q} \tag{5.3.26}$$

$$l_N = -\frac{M_\alpha}{L_\alpha} \tag{5.3.27}$$

with l_N the length to the neutral point.

For most aircraft, these assumptions are valid because the pitch damping arises from the horizontal stabiliser which is also typically where the elevator control surface is located. If the abovementioned conditions are met, Peddle shows conditions under which the effects of a right-hand plane (RHP) zero become negligible. This allows one to ignore the non-minimum-phase (NMP)

nature of the system. The design of the NSA controller can then continue based on a set of simplified reduced-order dynamics that do not capture the NMP nature of the system. The condition under which the NMP can be neglected fall within an upper natural frequency band given by [7] as

$$\omega_n < \frac{1}{3}\left|\sqrt{\frac{L_\alpha(l_H - l_N)}{I_{yy}}}\right| \tag{5.3.28}$$

It is important to note that both the open-loop and closed-loop normal dynamics should fall within the upper bound limit given by (5.3.28). A lower bound is also specified by Peddle. The normal dynamics must be timescale-separated from the velocity magnitude and air density dynamics. The velocity magnitude typically has a higher bandwidth than the air density dynamics, and is therefore considered to be the limiting factor. A commonly used design rule is that the normal dynamics bandwidth should be at least five times greater than the velocity magnitude bandwidth for sufficient timescale-separation [7]. Unlike the upper bound, only the closed-loop poles need to satisfy the lower bound. However if the open-loop poles are significantly slower than the lower limit, a large amount of control effort will be required to move the poles within the lower bound, which could result in actuator saturation. Figure 5.5 shows the aircraft-dependent admissibility

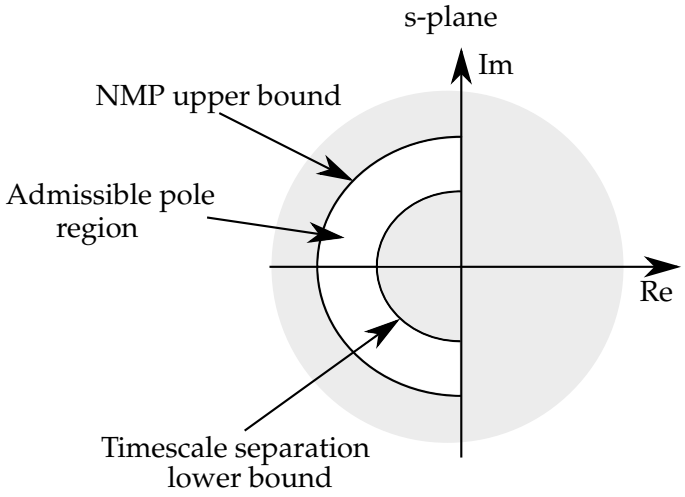

Figure 5.5: Admissible pole placement region

region where the closed-loop pole must fall within in order to make use of the NSA controller. These bounds can be used for the robust design technique that is discussed in Section 5.2.

5.3.2.1 Reduced-Order Design

Assuming that all the abovementioned frequency bounds are met, the design of the NSA controller can proceed with the following reduced-order normal dynamics given by [7] as

$$\begin{bmatrix}\dot{\alpha}\\ \dot{q}\end{bmatrix} = \begin{bmatrix}-\frac{L_\alpha}{mV_T} & 1\\ \frac{M_\alpha}{I_{yy}} & \frac{M_Q}{I_{yy}}\end{bmatrix}\begin{bmatrix}\alpha\\ q\end{bmatrix} + \begin{bmatrix}0\\ \frac{M_{\delta_E}}{I_{yy}}\end{bmatrix}\delta_e \tag{5.3.29}$$

$$c_w = \begin{bmatrix}-\frac{L_\alpha}{m} & 0\end{bmatrix}\begin{bmatrix}\alpha\\ q\end{bmatrix} \tag{5.3.30}$$

where c_w is the normal specific acceleration perturbation in the wind reference frame and the short period mode dynamics are approximated by (5.3.29). Figure 5.6 shows the feedback control system in block diagram form, where

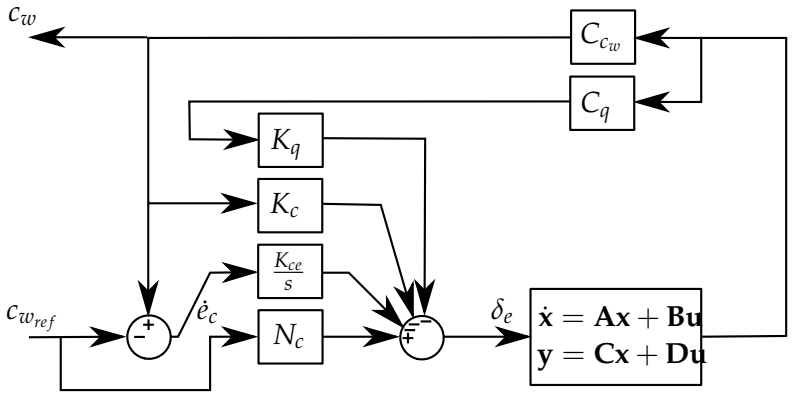

Figure 5.6: Normal acceleration control system block diagram

$$C_{c_w} = \begin{bmatrix} -\frac{L_\alpha}{m} & 0 \end{bmatrix} \tag{5.3.31}$$

and

$$C_q = \begin{bmatrix} 0 & 1 \end{bmatrix} \tag{5.3.32}$$

The control law consists of a PI controller, a pitch rate damper, and a feed-forward term to cancel the transient effects of the integral term. The integral term of the control law is introduced to ensure that the normal specific acceleration is robustly tracked with zero steady state error. Offset disturbances such as static lift and static pitching moments were ignored in the design, knowing that the integrator would work to fix the error. Through dynamic inversion and using (5.3.29), (5.3.34), and (5.3.35), Peddle develops a reduced-order closed-loop state space model:

$$\begin{bmatrix} \ddot{c}_w \\ \dot{c}_w \\ \dot{e}_c \end{bmatrix} = \begin{bmatrix} \left(\frac{M_Q}{I_{yy}} - \frac{L_\alpha}{mV_T} - \frac{M_{\delta_E}}{I_{yy}} K_q\right) & \left(\frac{M_\alpha}{I_{yy}} + \frac{L_\alpha M_Q}{mV_T I_{yy}} + \frac{L_\alpha M_{\delta_E}}{mV_T} K_c - \frac{L_\alpha M_{\delta_E}}{mV_T I_{yy}} K_q\right) & \left(\frac{L_\alpha M_{\delta_E}}{mI_{yy}} K_e\right) \\ 1 & 0 & 0 \\ 0 & 1 & 0 \end{bmatrix} \begin{bmatrix} \dot{c}_w \\ c_w \\ e_c \end{bmatrix} + \begin{bmatrix} -\frac{(N_c L_\alpha M_{\delta_E})}{mI_{yy}} \\ 0 \\ -1 \end{bmatrix} c_{w_{ref}} \tag{5.3.33}$$

where the control law is defined as

$$\delta_e = -K_q q - K_c c_w - K_e e_c + N_c c_{w_{ref}} \tag{5.3.34}$$

and the error is defined as

$$\dot{e}_c = c_w - c_{w_{ref}} \tag{5.3.35}$$

If all the frequency bounds are met, (5.3.33) is an adequate closed-loop representation and can be used to design the gains for the NSA controller. Given the desired closed-loop characteristic

equation for the normal dynamics,

$$\alpha_{cl}(s) = (s^2 + 2\zeta\omega_n s + \omega_n^2)(s + a) \tag{5.3.36}$$

$$\alpha_{cl}(s) = s^3 + \alpha_2 s^2 + \alpha_1 s + \alpha_0 \tag{5.3.37}$$

where

$$\alpha_2 = 2\zeta\omega_n + a \tag{5.3.38}$$

$$\alpha_1 = 2\zeta\omega_n a + \omega_n^2 \tag{5.3.39}$$

$$\alpha_0 = \omega_n^2 a \tag{5.3.40}$$

the closed form solution feedback gains are calculated

$$K_q = \frac{I_{yy}}{M_{\delta_E}}\left(\alpha_2 + \frac{M_Q}{I_{yy}} - \frac{L_\alpha}{mV_T}\right) \tag{5.3.41}$$

$$K_c = -\frac{mI_{yy}}{L_\alpha M_{\delta_E}}\left(\alpha_1 + \frac{M_\alpha}{I_{yy}} - \frac{L_\alpha}{mV_T}\left(\alpha_2 - \frac{L_\alpha}{mV_T}\right)\right) \tag{5.3.42}$$

$$K_e = \frac{mI_{yy}}{L_\alpha M_{\delta_E}}\alpha_0 \tag{5.3.43}$$

$$N_c = -\frac{K_e}{a} \tag{5.3.44}$$

where N_c is the feed-forward gain. The controller design is reduced to placing three poles that govern the closed-loop normal dynamics. From (5.3.36), the three poles are placed by specifying a natural frequency and damping ratio for the normal dynamics, and the real closed-loop pole a corresponding to the open-loop integrator pole. With the frequency bounds and the reduced-order closed-loop normal dynamics derived, the robust design technique discussed in Section 5.2 can be used to find controller gains that are robust against a given amount of partial horizontal stabiliser loss.

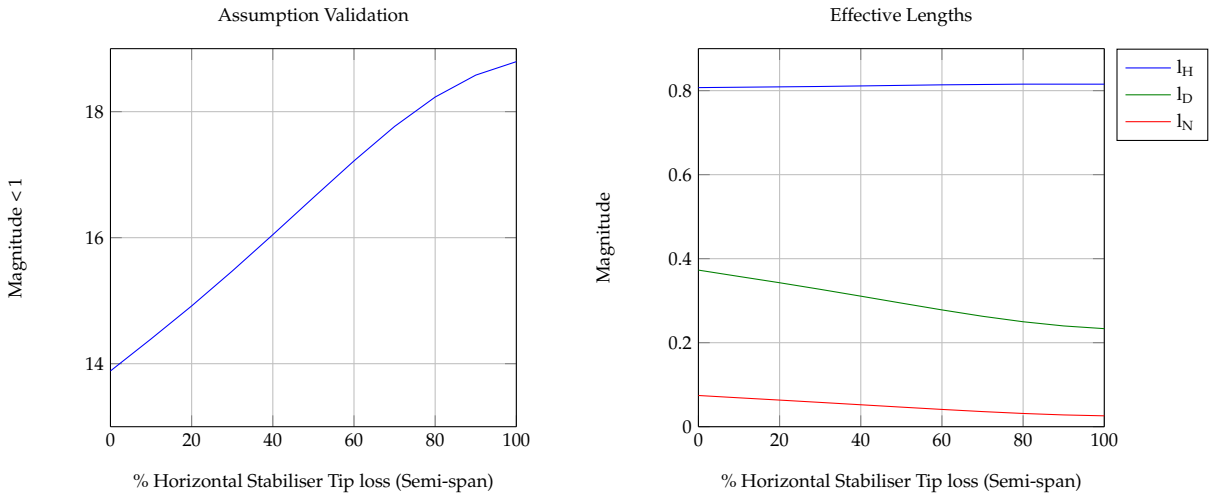

(a) Small lift due to pitch rate assumption (b) Effective length

Figure 5.7: Lift due to pitch rate and effective lengths: assumptions validation

Before the NSA controller design can proceed, the assumptions and constraints made in order to obtain the reduced-order dynamics must be validated. This includes the assumption of (5.3.24), and that (5.3.25) and (5.3.26) are of similar magnitude, and finally the constraint that the open-loop normal dynamics must fall within the upper frequency bound. Figure 5.7 (a) shows the small lift due to pitch rate assumption for partial horizontal stabiliser of up to 100%. This figure thus validates that the aircraft meets the requirements of the first assumption for all partial horizontal stabiliser loss cases. The second assumption is shown in Figure 5.7 (b). When the aircraft suffers partial horizontal stabiliser loss, l_H and l_D tend to become less similar. Note that the length between l_H and l_N also increases, thus it will still dominate or be greater than the length between l_H and l_D. One can therefore say that the second assumption is also valid for all partial horizontal stabiliser loss cases. Ideally one would like to define a common upper bound that must

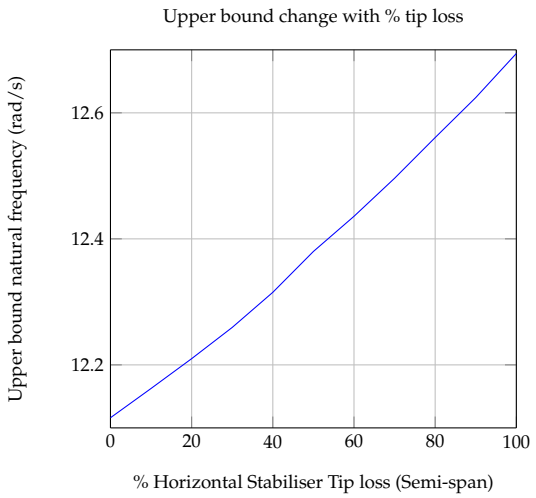

(a) Upper bound frequency constraint

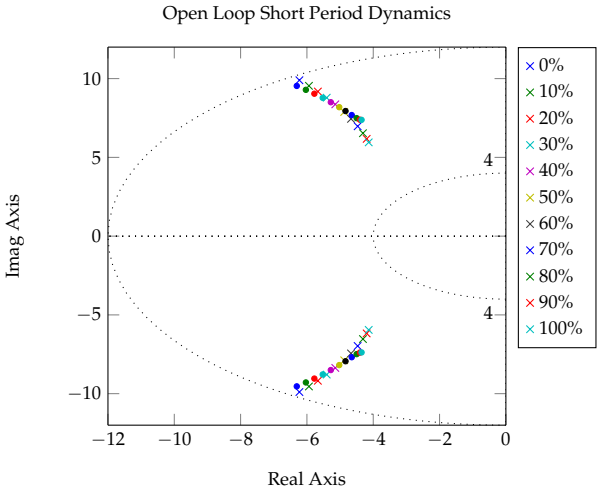

(b) Open-loop normal dynamics.

Figure 5.8: Upper bound and approximated short period dynamics

be met by all the partial horizontal stabiliser loss cases. The lowest upper bound of all the partial horizontal stabiliser loss cases is therefore chosen. Figure 5.8 (a) shows how the upper frequency bound changes with partial horizontal stabiliser loss. The upper bound of the undamaged aircraft is therefore used as the natural frequency design upper bound. Figure 5.8 (b) shows the open-loop normal dynamics poles as a function of the percentage of horizontal stabiliser loss. It is clear that all the open-loop poles fall within the upper bound. Also note the difference between the reduced-order short period dynamics (indicated with an x) and the short period dynamics (indicated with a dot). The difference is due to the centre of mass shift not included in the reduced-order model developed by Peddle. Now that all the assumptions have been validated and the constraints have been met, one can design the controller gains (5.3.41) to (5.3.44) for the NSA controller.

Consider the following maximum and minimum natural frequencies and damping ratios to bound the normal dynamics poles:

$$80\% \text{ of NMP upper bound} \geq \omega_n \geq \text{timescale-separation lower bound} \tag{5.3.45}$$

$$0.9 \geq \zeta \geq 0.6 \tag{5.3.46}$$

where a is only constrained by the natural frequency bound and not by the damping. The algorithm finds a set of gains that will keep the closed-loop poles within the admissible pole region defined in (5.3.46).

Figure 5.9 shows the pole-zero plot and a unit step response for a set of controller gains that satisfy all the above supplied boundaries while obtaining a robustness of partial horizontal stabiliser losses of up to 70%. Note that the normal dynamics for partial horizontal stabiliser losses of up to 70% remain within the admissible pole region. The set of robust controller gains obtained

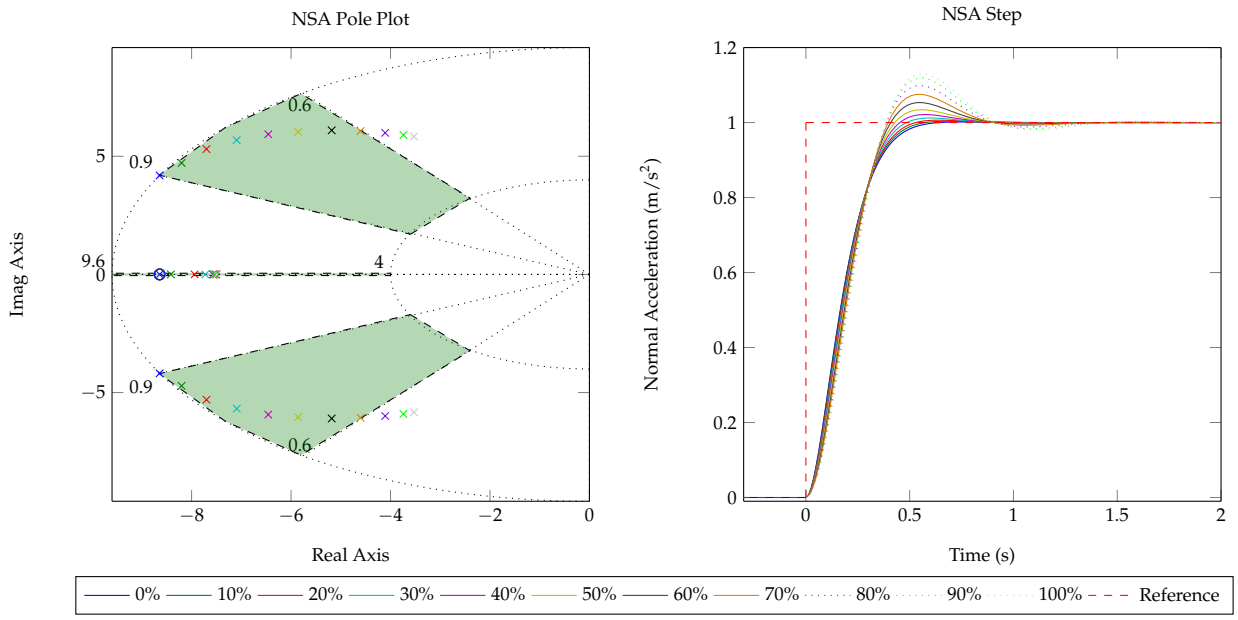

Figure 5.9: NSA unit step response and pole plot

will therefore guarantee that the closed-loop system remains within acceptable transient response specifications when the aircraft suffers partial horizontal stabiliser losses of up to 70%. Note that even though the closed-loop system remains stable for partial horizontal stabiliser losses of 80% to 100%, it does not meet the defined specifications. The NSA controller dynamics can now be added to, and verified on the full linear dynamics of the aircraft.

5.3.2.2 Closed-loop System

The NSA controller is now verified on the full linear dynamics of the aircraft. Equation 5.3.20 states the full linear aircraft dynamics with the airspeed controller dynamics included. First the integrator dynamics given in (5.3.35) are added.

$$\begin{bmatrix} \dot{\mathbf{x}}_{\bar{v}} \\ \dot{e}_c \end{bmatrix} = \begin{bmatrix} \mathbf{A}_{\bar{v}} & \mathbf{0}_{10\times 1} \\ \begin{bmatrix} 0 & -\frac{L_\alpha}{m} & -\frac{L_Q}{m} \end{bmatrix} & \mathbf{0}_{1\times 8} \end{bmatrix} \begin{bmatrix} \mathbf{x}_{\bar{v}} \\ e_c \end{bmatrix} + \begin{bmatrix} \boldsymbol{B}_{\delta_e} & \boldsymbol{B}_{\bar{v}_{ref}} & \boldsymbol{B}_{\delta_a} & \boldsymbol{B}_{\delta_r} \\ -\frac{L_{\delta_E}}{m} & 0 & 0 & 0 \end{bmatrix} \begin{bmatrix} \delta_e \\ \bar{v}_{ref} \\ \delta_a \\ \delta_r \end{bmatrix} + \begin{bmatrix} \mathbf{0}_{10\times 1} \\ -1 \end{bmatrix} c_{w_{ref}} \tag{5.3.47}$$

where

$$c_w = -\frac{L_\alpha}{m}\alpha - \frac{L_Q}{m}q - \frac{L_{\delta_E}}{m}\delta_e \tag{5.3.48}$$

Note that the full-order normal acceleration dynamics are augmented and not the reduced-order normal acceleration dynamics. The control law given in (5.3.34) is added to the system.

$$\begin{bmatrix}\dot{\mathbf{x}}_{\bar{v}}\\ \dot{e}_c\end{bmatrix} = \left[\begin{bmatrix}\mathbf{A}_{\bar{v}} & \mathbf{0}_{10\times 1}\\ \begin{bmatrix}0 & -\frac{L_\alpha}{m} & -\frac{L_Q}{m}\end{bmatrix} & \mathbf{0}_{1\times 8}\end{bmatrix} + \begin{bmatrix}\boldsymbol{B}_{\delta_e}\\ -\frac{L_{\delta_E}}{m}\end{bmatrix}\begin{bmatrix}0 & \left(\frac{K_c\frac{L_\alpha}{m}}{1-K_c\frac{L_{\delta_E}}{m}}\right) & \left(\frac{-K_q+Kc\frac{L_Q}{m}}{1-K_c\frac{L_{\delta_E}}{m}}\right) & \mathbf{0}_{1\times 7} & \left(\frac{-K_e}{1-K_c\frac{L_{\delta_E}}{m}}\right)\end{bmatrix}\right]\begin{bmatrix}\mathbf{x}_{\bar{v}}\\ e_c\end{bmatrix} + \begin{bmatrix}\boldsymbol{B}_{\delta_e}\left(\frac{N_c}{1-K_c\frac{L_{\delta_E}}{m}}\right) & \boldsymbol{B}_{\bar{v}_{ref}} & \boldsymbol{B}_{\delta_a} & \boldsymbol{B}_{\delta_r}\\ \left(-1-\frac{L_{\delta_E}N_c}{m-K_cL_{\delta_E}}\right) & 0 & 0 & 0\end{bmatrix}\begin{bmatrix}c_{w_{ref}}\\ \bar{v}_{ref}\\ \delta_a\\ \delta_r\end{bmatrix} \tag{5.3.49}$$

The closed-loop state space model now has a subscript c_w, indicating that the NSA controller has been added. Note that the input vector has changed. The NSA reference is now an input to the system.

$$\dot{\mathbf{x}}_{c_w} = \mathbf{A}_{c_w}\mathbf{x}_{c_w} + \mathbf{B}_{c_w}\mathbf{u} \tag{5.3.50}$$

Now define

$$\mathbf{B}_{c_w} = \begin{bmatrix}\boldsymbol{B}_{c_{w_{ref}}} & \boldsymbol{B}_{\bar{v}_{ref}} & \boldsymbol{B}_{\delta_a} & \boldsymbol{B}_{\delta_r}\end{bmatrix} \tag{5.3.51}$$

The output of the NSA controller is given as

$$y_{c_w} = \boldsymbol{C}_{c_w}\mathbf{x}_{c_w} + \boldsymbol{D}_{c_w}\mathbf{u} \tag{5.3.52}$$

where

$$\boldsymbol{C}_{c_w} = \begin{bmatrix}0 & \left(-\frac{L_\alpha}{m} - \frac{L_{\delta_E}}{m}\left(\frac{K_c\frac{L_\alpha}{m}}{1-K_c\frac{L_{\delta_E}}{m}}\right)\right) & \left(-\frac{L_Q}{m} - \frac{L_{\delta_E}}{m}\left(\frac{-K_q+Kc\frac{L_Q}{m}}{1-K_c\frac{L_{\delta_E}}{m}}\right)\right) & \mathbf{0}_{1\times 7} & \left(\frac{L_{\delta_E}K_e}{m-K_cL_{\delta_E}}\right)\end{bmatrix} \tag{5.3.53}$$

and

$$\boldsymbol{D}_{c_w} = -\left(\frac{L_{\delta_E}N_c}{m-K_cL_{\delta_E}}\right) \tag{5.3.54}$$

The closed-loop transfer function from $c_{w_{ref}}$ to c_w can now be obtained.

$$G_{c_{w_{cl}}}(s) = \frac{c_w}{c_{w_{ref}}} = \boldsymbol{C}_{c_w}(s\mathbf{I}_{11} - \mathbf{A}_{c_w})^{-1}\boldsymbol{B}_{c_{w_{ref}}} + \boldsymbol{D}_{c_w} \tag{5.3.55}$$

5.3.2.3 Robustness to Horizontal Stabiliser Tip Loss

Figure 5.10 shows the robustness of the NSA controller on the full linear aircraft model. Note that the pole locations on the full linear aircraft model are slightly different than those on the reduced-order model. This is mainly due to the centre of mass shift not being accounted for in the reduced-order. However, the centre of mass shift for partial horizontal stabiliser loss is small, causing its effect to also being small. Nevertheless, the NSA controller remains robust against partial horizontal stabiliser loss.

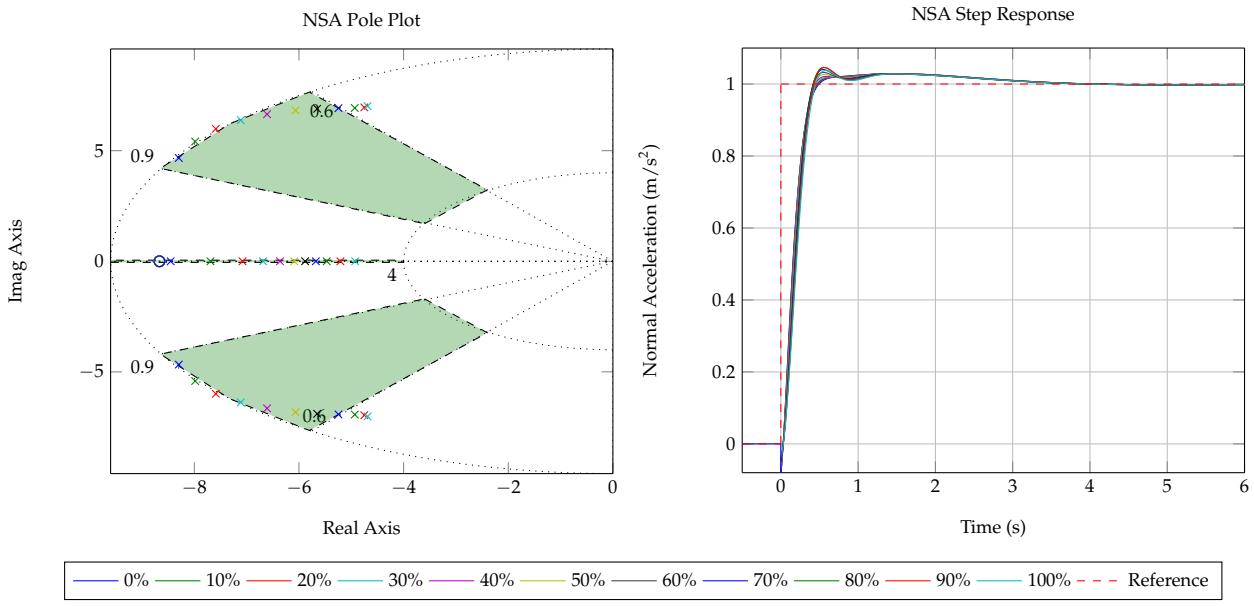

Figure 5.10: NSA unit step response and pole-zero plot for horizontal stabiliser loss

5.3.3 Climb Rate Controller

This section describes the design and robustness of the climb rate controller. The climb rate controller regulates the climb rate of the aircraft by making use of the NSA controller. A positive climb rate is define as $-\dot{D}$ and is produced by a negative normal acceleration. The climb rate controller therefore generates a normal acceleration c_n, which is supplied to the NSA controller after a roll angle conversion and sign inversion (see Figure 5.1). In turn, the NSA controller issues an elevator command that changes the flight path angle of the aircraft, causing the aircraft to climb or descend.

5.3.3.1 Design

The climb rate of the aircraft is related to the longitudinal states by linearising and decoupling the down velocity component from (3.3.13),

$$\dot{D} = -U\sin\Theta + V\cos\Theta\sin\Phi + W\cos\Theta\cos\Phi \tag{5.3.56}$$

Linearising the equation about straight and level flight equilibrium using small angle approximation yields

$$-\dot{d} = \dot{h} = u\theta - w \tag{5.3.57}$$

and noting that $w = u\alpha$ and $u = V_T$ at trim,

$$\dot{h} = V_T(\theta - \alpha) \tag{5.3.58}$$

where $\theta - \alpha = \gamma$ is known as the flight path angle of the aircraft. Figure 5.11 shows the climb rate feedback control system in block diagram form. The open-loop transfer function of the aircraft's climb rate dynamics is given by

$$G_{\dot{h}}(s) = \boldsymbol{C}_{\dot{h}}\left[s\mathbf{I}_{11} - \mathbf{A}_{c_w}\right]^{-1}\boldsymbol{B}_{c_{w_{ref}}} \tag{5.3.59}$$

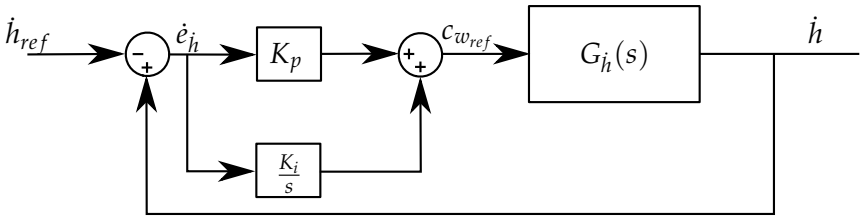

Figure 5.11: Climb rate controller block diagram

where

$$\boldsymbol{C}_{\dot{h}} = \begin{bmatrix} 0 & -V_T & 0 & V_T & \mathbf{0}_{1\times 7} \end{bmatrix} \tag{5.3.60}$$

From Figure 5.11, the transfer function $G_{\dot{h}}(s)$ has a free integrator given that $c_{w_{ref}} = -\ddot{h}$, and is therefore a type one system. Zero steady state tracking of a step command is therefore achievable and only a proportional controller is required to achieve the desired transient specifications. Nevertheless, a PI controller is used, as seen in Figure 5.11. The integral component is added for robustness to normal acceleration control biases due to mounting or sensor biases and parameter uncertainties. The integrator will ensure that the climb rate controller can track a step reference with zero steady state error. Note that the integral component will cause the closed-loop system to have a slower response with higher overshoot.

A PI control law is defined that generates a normal acceleration command c_n proportional to the weighted sum of the airspeed error and the time integral of the airspeed error,

$$c_n = -K_p \dot{e}_{\dot{h}} - K_i e_{\dot{h}} \tag{5.3.61}$$

where $c_{w_{ref}} = -c_n$ for the linearised dynamics, and the climb rate error is defined as

$$c_{w_{ref}} = K_p \dot{e}_{\dot{h}} + K_i e_{\dot{h}} \tag{5.3.62}$$

$$\dot{e}_{\dot{h}} = \dot{h} - \dot{h}_{ref} \tag{5.3.63}$$

where $\dot{h}$ is the climb rate perturbation and $\dot{h}_{ref}$ is the climb rate perturbation reference. The root locus design technique is used to determine the controller gains K_p and K_i. Note that the negative of $G_{\dot{h}}(s)$ must be used due to the fact that a positive climb rate will result from a negative normal acceleration. Figure 5.12 shows the root locus design and the closed-loop unit step response of the climb rate controller.

Suppose the aircraft is travelling on the glide slope at an airspeed of 16 m/s. If the glide slope has a length of approximately 250 m at an angle of 4°, the aircraft will reach the touchdown point in roughly 16 s. At this point, if the aircraft is required to land accurately, the longitudinal controllers must therefore track the references exactly. In Figure 5.1, note that an altitude controller supplies the climb rate controller with a reference. Due to the successive loop closure architecture, the altitude controller dynamics will be slower than that of the climb rate controller. To land accurately the altitude controller is required to track the reference exactly before 16 s. The climb rate controller should therefore have a faster settling time. To achieve adequate overshoot, the integrator dynamics are made relatively slow. The controller is designed to meet a settling time specification of 13 s while still achieving adequate overshoot, as seen in Figure 5.12. The climb rate controller dynamics can now be added to, and verified on the full linear dynamics of the aircraft.

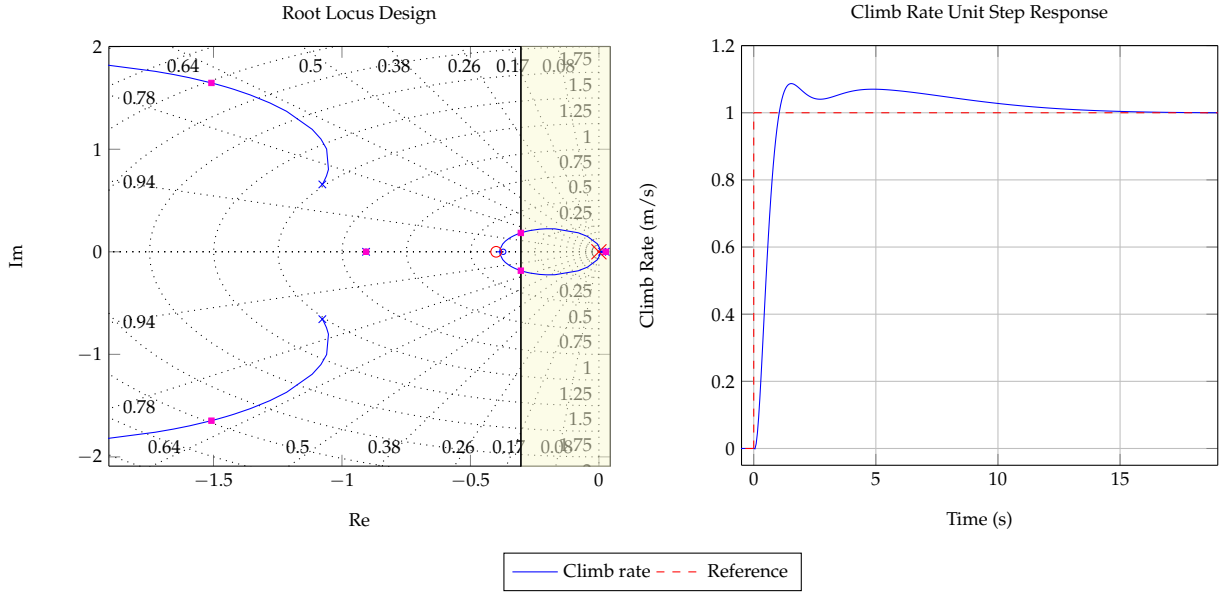

Figure 5.12: Climb rate unit step response and root locus design

5.3.3.2 Closed-Loop System

The climb rate controller dynamics is now verified on the full linear dynamics of the aircraft. Equation 5.3.50 states the full linear aircraft dynamics with the NSA controller dynamics included. First, the integrator dynamics given in (5.3.63) are added to the system.

$$\begin{bmatrix} \dot{\mathbf{x}}_{c_w} \\ \dot{e}_{\dot{h}} \end{bmatrix} = \begin{bmatrix} \mathbf{A}_{c_w} & \mathbf{0}_{11\times 1} \\ \begin{bmatrix} 0 & -V_T & 0 & V_T \end{bmatrix} & \mathbf{0}_{1\times 8} \end{bmatrix} \begin{bmatrix} \mathbf{x}_{c_w} \\ e_{\dot{h}} \end{bmatrix} + \begin{bmatrix} \boldsymbol{B}_{c_{w_{ref}}} & \boldsymbol{B}_{\bar{v}_{ref}} & \boldsymbol{B}_{\delta_a} & \boldsymbol{B}_{\delta_r} \\ 0 & 0 & 0 & 0 \end{bmatrix} \begin{bmatrix} c_{w_{ref}} \\ \bar{v}_{ref} \\ \delta_a \\ \delta_r \end{bmatrix} + \begin{bmatrix} \mathbf{0}_{11\times 1} \\ -1 \end{bmatrix} \dot{h}_{ref} \tag{5.3.64}$$

The control law given in (5.3.62) is then added to the system.

$$\begin{bmatrix} \dot{\mathbf{x}}_{c_w} \\ \dot{e}_{\dot{h}} \end{bmatrix} = \left[\begin{bmatrix} \mathbf{A}_{c_w} & \mathbf{0}_{11\times 1} \\ \begin{bmatrix} 0 & -V_T & 0 & V_T \end{bmatrix} & \mathbf{0}_{1\times 8} \end{bmatrix} + \begin{bmatrix} \boldsymbol{B}_{c_{w_{ref}}} \\ 0 \end{bmatrix} \begin{bmatrix} 0 & -K_p V_T & 0 & K_p V_T & \mathbf{0}_{1\times 7} & K_i \end{bmatrix} \right] \begin{bmatrix} \mathbf{x}_{c_w} \\ e_{\dot{h}} \end{bmatrix} + \begin{bmatrix} -\boldsymbol{B}_{c_w} K_p & \boldsymbol{B}_{\bar{v}_{ref}} & \boldsymbol{B}_{\delta_a} & \boldsymbol{B}_{\delta_r} \\ -1 & 0 & 0 & 0 \end{bmatrix} \begin{bmatrix} \dot{h}_{ref} \\ \bar{v}_{ref} \\ \delta_a \\ \delta_r \end{bmatrix} \tag{5.3.65}$$

The closed-loop state space model now has a subscript $\dot{h}$ to indicate that the climb rate controller has been added. Note that the input vector has changed. The climb rate reference is now an input to the system.

$$\dot{\mathbf{x}}_{\dot{h}} = \mathbf{A}_{\dot{h}} \mathbf{x}_{\dot{h}} + \mathbf{B}_{\dot{h}} \mathbf{u} \tag{5.3.66}$$

Now define

$$\mathbf{B}_{\dot{h}} = \begin{bmatrix} \boldsymbol{B}_{\dot{h}_{ref}} & \boldsymbol{B}_{\bar{v}_{ref}} & \boldsymbol{B}_{\delta_a} & \boldsymbol{B}_{\delta_r} \end{bmatrix} \tag{5.3.67}$$

The output of the climb rate controller is given as

$$y_{\dot{h}} = \boldsymbol{C}_{\dot{h}} \mathbf{x}_{\dot{h}} \tag{5.3.68}$$

where

$$\boldsymbol{C}_{\dot{h}} = \begin{bmatrix} 0 & -V_T & 0 & V_T & \mathbf{0}_{1\times 8} \end{bmatrix} \tag{5.3.69}$$

The closed-loop transfer function from $\dot{h}_{ref}$ to $\dot{h}$ can now be obtained.

$$G_{\dot{h}_{cl}}(s) = \frac{\dot{h}}{\dot{h}_{ref}} = \boldsymbol{C}_{\dot{h}}(s\mathbf{I}_{12} - \mathbf{A}_{\dot{h}})^{-1}\boldsymbol{B}_{\dot{h}_{ref}} \tag{5.3.70}$$

5.3.3.3 Robustness to Horizontal Stabiliser Tip Loss

Figure 5.13 shows the robustness of the climb rate controller on the full linear aircraft model. Note that only the higher-frequency poles move slightly, while the dominant closed-loop poles remain unchanged. The majority of the uncertainties were captured within the NSA inner-loop controller, resulting in a robust climb rate controller. The climb rate controller achieves the level of robustness it was designed for (at least up to 70% semi-span horizontal stabiliser loss).

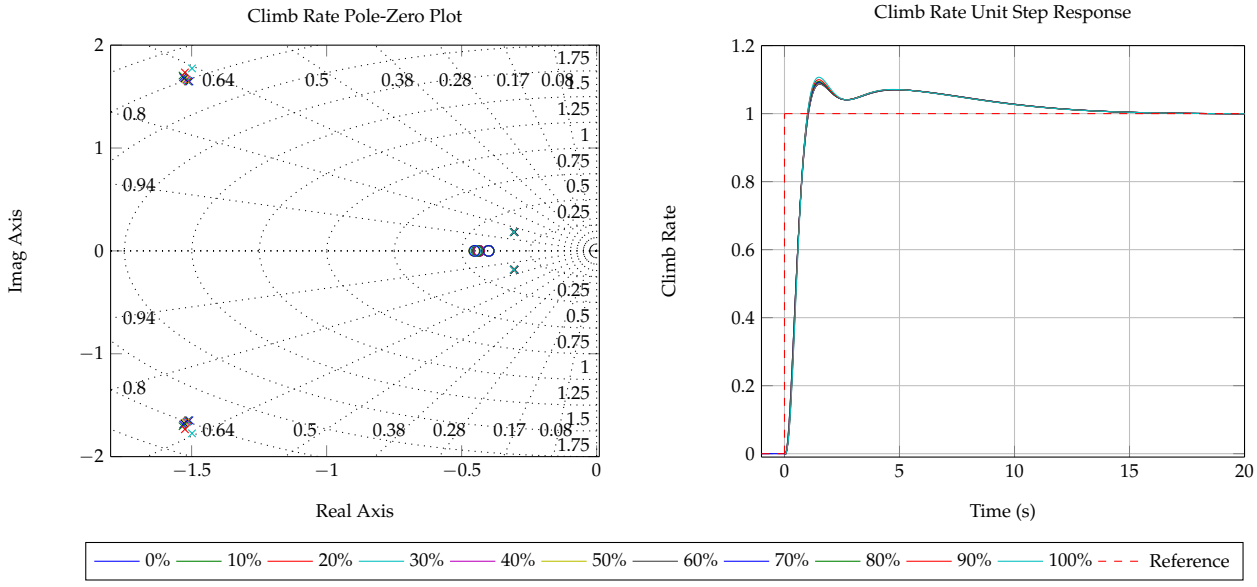

Figure 5.13: Climb rate unit step response and pole-zero plot for horizontal stabiliser loss

5.3.4 Altitude Controller

This section describes the design and robustness of the altitude controller. The altitude controller controls and regulates the altitude of the aircraft by making use of the climb rate controller. The altitude is controlled with respect to the inertial reference frame. It is therefore assumed that the climb rate vector of the aircraft is always normal to the North-East plane of inertial reference frame and that the flight path angle remains small. A positive altitude perturbation h is defined as a $-d$ perturbation and is produced by a positive climb rate. To perform an autonomous landing, the altitude controller must be capable of controlling the aircraft to track a ramp reference with a zero steady state error. This is necessary for accurate glide slope tracking. The altitude controller design is therefore done with the autonomous landing application in mind.

5.3.4.1 Design

The altitude of the aircraft is related to the longitudinal states by adding an altitude state to the full linear dynamics of the aircraft. Equation 5.3.58 is added to the full linear dynamics of the aircraft given in (5.3.66) to obtain the system

$$\begin{bmatrix} \dot{\mathbf{x}}_h \\ \dot{h} \end{bmatrix} = \begin{bmatrix} \mathbf{A}_h & \mathbf{0}_{12\times 1} \\ \begin{bmatrix} 0 & -V_T & 0 & V_T \end{bmatrix} & \mathbf{0}_{1\times 9} \end{bmatrix} \begin{bmatrix} \mathbf{x}_h \\ h \end{bmatrix} + \begin{bmatrix} \boldsymbol{B}_{\dot{h}_{ref}} & \boldsymbol{B}_{\bar{v}_{ref}} & \boldsymbol{B}_{\delta_a} & \boldsymbol{B}_{\delta_r} \\ 0 & 0 & 0 & 0 \end{bmatrix} \begin{bmatrix} \dot{h}_{ref} \\ \bar{v}_{ref} \\ \delta_a \\ \delta_r \end{bmatrix} \tag{5.3.71}$$

The open-loop transfer function $G_h(s)$ of the aircraft's altitude dynamics is given by

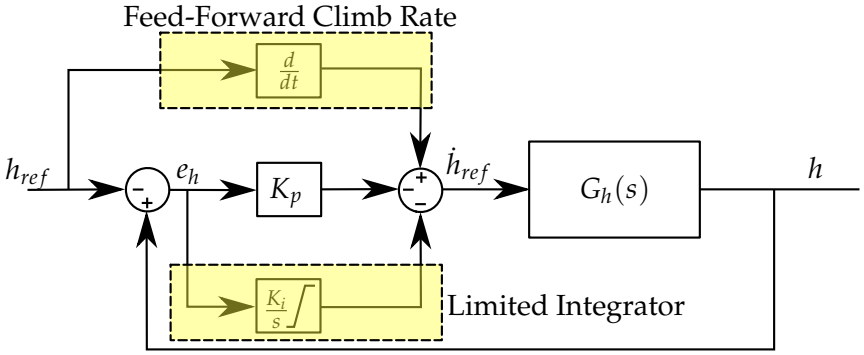

Figure 5.14: Altitude controller block diagram

$$G_h(s) = \boldsymbol{C}_h \left[s\mathbf{I}_{13} - \begin{bmatrix} \mathbf{A}_h & \mathbf{0}_{12\times 1} \\ \begin{bmatrix} 0 & -V_T & 0 & V_T \end{bmatrix} & \mathbf{0}_{1\times 9} \end{bmatrix} \right]^{-1} \begin{bmatrix} \boldsymbol{B}_{\dot{h}_{ref}} \\ 0 \end{bmatrix} \tag{5.3.72}$$

where

$$\boldsymbol{C}_h = \begin{bmatrix} \mathbf{0}_{1\times 12} & 1 \end{bmatrix} \tag{5.3.73}$$

For conceptual purposes, the system $G_h(s)$ can be seen as a pure integrator. This is verified from Figure 5.14. The input of the system is climb rate and the output is altitude, hence $\dot{h}$ is integrated to obtain h. The system $G_h(s)$ is therefore a type one system, which means it can follow a step reference with zero steady state error, but can only follow a ramp reference with a finite steady state error. Following a ramp reference signal requires the system to be type two. The system type must therefore be incremented from a type one to a type two system. This can be achieved with a PI controller. As mentioned before, PI controllers usually slow down the closed-loop system and result in the closed-loop system having a large amount of overshoot. This is usually not desired for altitude control, especially not when autonomous landings need to be performed. Suppose that only a proportional (P) controller is used to control the altitude.

$$D_h(s) = K_p \tag{5.3.74}$$

The steady state error when tracking a unit ramp is given by

$$e_{ss} = \frac{1}{K_v} \tag{5.3.75}$$

where

$$K_v = \lim_{s \to 0} sG_h(s)D_h(s) \tag{5.3.76}$$

The steady state error when following a unit ramp is therefore also given by

$$e_{ss} = \frac{1}{K_p} \tag{5.3.77}$$

If the controller gain K_p is small, the steady state error will be large. This can be catastrophic for the aircraft while attempting to land, because the aircraft may land a large distance before or after the designated touchdown point. An alternative method is to supply the climb rate controller with the required climb rate reference, which will result in the desired altitude ramp. An altitude ramp translates to a step or constant climb rate that must be maintained. In the previous section, a climb rate controller capable of tracking a step input with zero steady state error was designed. This method will therefore yield a valid solution. The climb rate required to cause the desired altitude ramp is obtained by differentiating the altitude reference, as seen in Figure 5.14. The differentiated altitude reference can be supplied to the climb rate controller as reference. If the aircraft is never disturbed, it will follow the desired altitude trajectory by controlling only climb rate. A climb rate reference is thus fed forward. the Feed-forward component is combined with a P controller. The P controller is used to control and regulate the altitude of the aircraft. When the aircraft is disturbed while on a ramp trajectory, the P controller will generate the appropriate climb rate reference required to reject the disturbance. The combination of the P controller and climb rate feed-forward component is therefore capable of controlling the aircraft to track step and ramp references with zero steady state error. Note that the climb rate feed-forward component will only contribute to the climb rate reference when the altitude reference is a ramp or acceleration function. Otherwise the altitude control system will behave like a normal P controller.

A proportional control law is defined that generates a climb rate $\dot{h}_{ref}$ proportional to the altitude error.

$$\dot{h}_{ref} = -K_p e_h \tag{5.3.78}$$

where

$$e_h = h - h_{ref} \tag{5.3.79}$$

The root locus design technique is used to determine the controller gain K_p. Figure 5.15 shows the root locus design and the closed-loop unit step response of the altitude controller.

The altitude controller is designed to be timescale-separated from at least the higher-bandwidth closed-loop climb rate dynamics (see Figure 5.13). This is to ensure that the altitude closed-loop response is not affected by a change in the climb rate response, and to ensure that when the altitude controller is added, it does not change the closed-loop climb rate response. For the altitude controller to achieve timescale separation from the slower climb rate dynamics, the altitude controller will become practically too slow, which will not be feasible. Following the same argument as with the design of the climb rate controller, the aircraft will have approximately 16 s to track and settle if an accurate landing is desired. From Figure 5.15, it is clear that the altitude controller will be within 2% of its value before the aircraft will touch down. A limited integrator term, as seen in Figure 5.14 is added to the altitude controller to ensure that the correct altitude steady state error is achieved, even with climb rate sensor biases present. The limits are chosen as the maximum

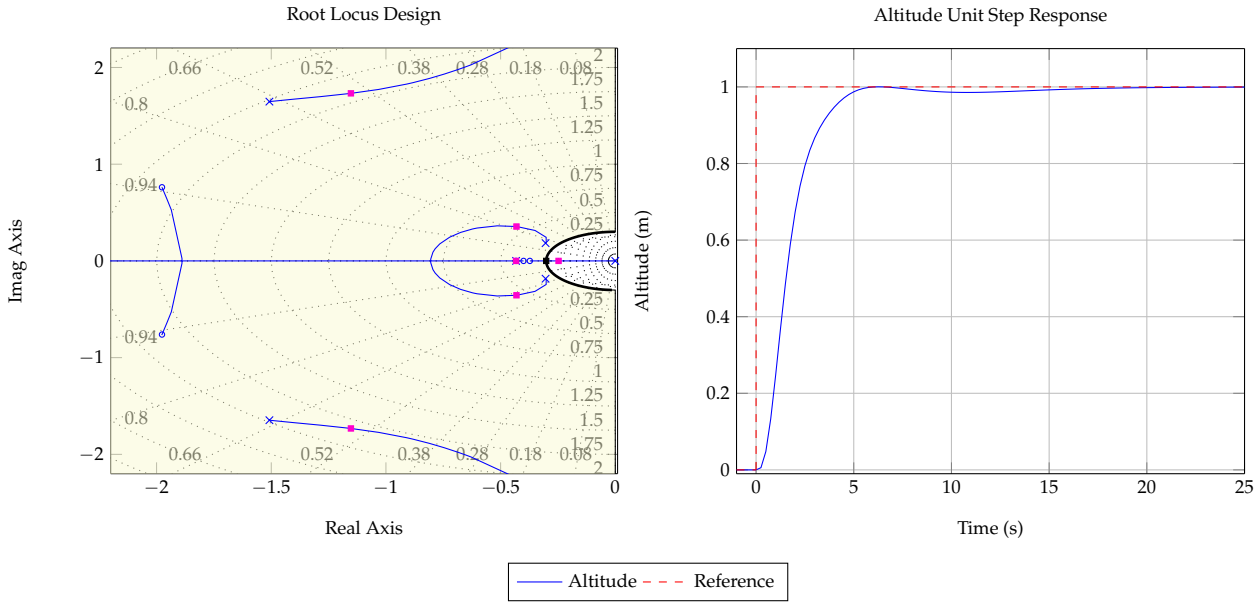

Figure 5.15: Altitude unit step response and root locus design

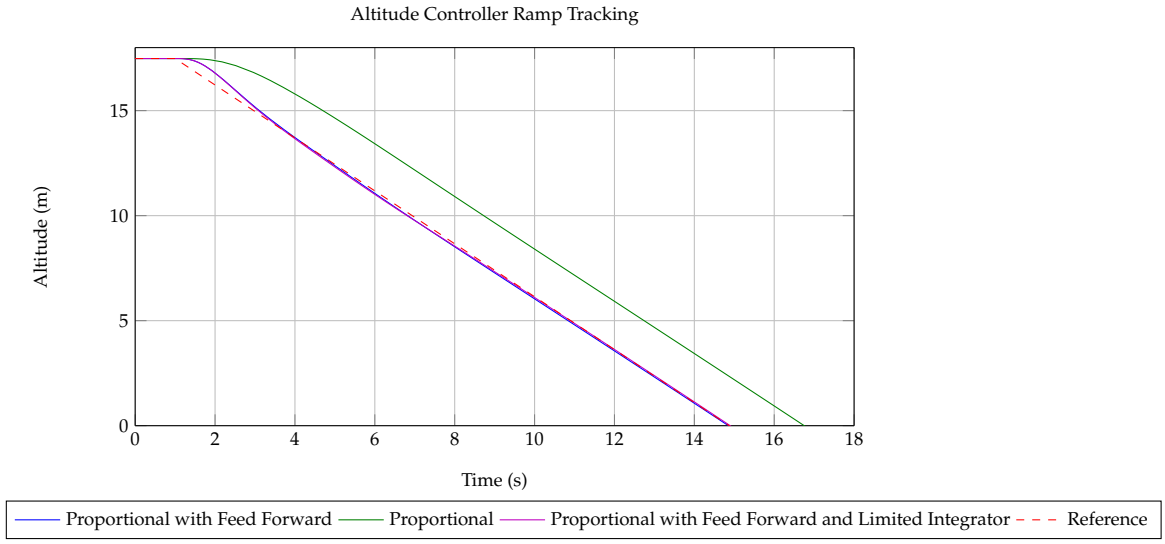

Figure 5.16: Altitude ramp tracking for each controller architecture

expected climb rate sensor bias, and the integrator gain K_i is determined iteratively. Figure 5.16 shows the altitude controller's ability to track a ramp reference. Note the steady state error when only a proportional controller is used. This will not be practically feasible because the aircraft will overshoot the touchdown point. Also note that the limited integrator does not significantly affect the transient response of the controller, but will affect the steady state. The altitude controller dynamics can now be added to, and be verified on the full linear dynamics of the aircraft.

5.3.4.2 Closed-Loop System

The altitude controller in verified on the full linear dynamics of the aircraft. Equation 5.3.66 states the full linear aircraft dynamics with the climb rate controller dynamics included. The control law

given in (5.3.78) is added to the system.

$$\begin{bmatrix}\dot{\mathbf{x}}_h\\ \dot{h}\end{bmatrix} = \left[\begin{bmatrix}\mathbf{A}_h & \mathbf{0}_{12\times 1}\\ \begin{bmatrix}0 & -V_T & 0 & V_T\end{bmatrix} & \mathbf{0}_{1\times 9}\end{bmatrix} + \begin{bmatrix}\boldsymbol{B}_{\dot{h}_{ref}}\\ 0\end{bmatrix}\begin{bmatrix}\mathbf{0}_{1\times 12} & -K_p\end{bmatrix}\right]\begin{bmatrix}\mathbf{x}_h\\ h\end{bmatrix} + \begin{bmatrix}\boldsymbol{B}_{\dot{h}}K_p & \boldsymbol{B}_{\bar{v}_{ref}} & \boldsymbol{B}_{\delta_a} & \boldsymbol{B}_{\delta_r}\\ 0 & 0 & 0 & 0\end{bmatrix}\begin{bmatrix}h_{ref}\\ \bar{v}_{ref}\\ \delta_a\\ \delta_r\end{bmatrix} \tag{5.3.80}$$

The closed-loop state space model now has a subscript h, indicating that the altitude controller has been added. Note that the input vector has changed. The altitude reference is now an input to the system.

$$\dot{\mathbf{x}}_h = \mathbf{A}_h\mathbf{x}_h + \mathbf{B}_h\mathbf{u} \tag{5.3.81}$$

Now define

$$\mathbf{B}_h = \begin{bmatrix}\boldsymbol{B}_{h_{ref}} & \boldsymbol{B}_{\bar{v}_{ref}} & \boldsymbol{B}_{\delta_a} & \boldsymbol{B}_{\delta_r}\end{bmatrix} \tag{5.3.82}$$

The output of the altitude controller is given as

$$y_h = \boldsymbol{C}_h\mathbf{x}_h \tag{5.3.83}$$

where

$$\boldsymbol{C}_h = \begin{bmatrix}\mathbf{0}_{1\times 12} & 1\end{bmatrix} \tag{5.3.84}$$

The closed-loop transfer function from h_{ref} to h can now be obtained.

$$G_{h_{cl}}(s) = \frac{h}{h_{ref}} = \boldsymbol{C}_h(s\mathbf{I}_{13} - \mathbf{A}_h)^{-1}\boldsymbol{B}_{h_{ref}} \tag{5.3.85}$$

5.3.4.3 Robustness to Horizontal Stabiliser Tip Loss

Figure 5.17 shows the robustness of the altitude controller on the full linear aircraft model. Note that the dominant poles remain unchanged over the desired range of partial horizontal stabiliser loss cases. The designed altitude controller therefore achieves the level of robustness it was designed for.

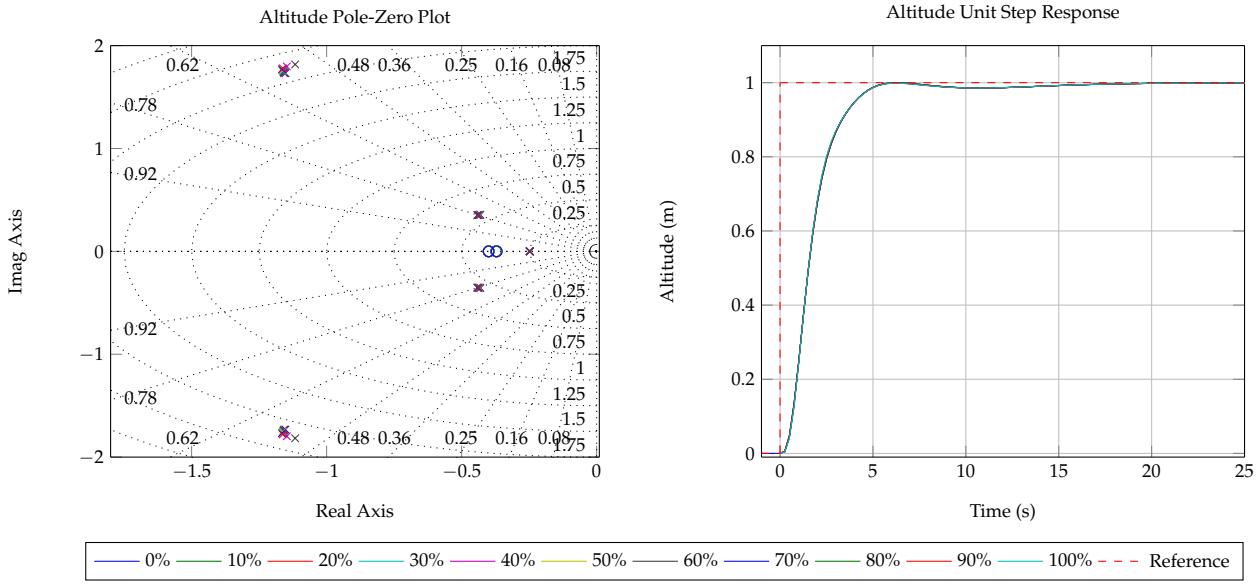

Figure 5.17: Altitude unit step response and pole-zero plot for horizontal stabiliser loss

5.3.5 Lateral Specific Acceleration Controller

This section describes the design and robustness of the lateral specific acceleration (LSA) controller. The lateral-directional dynamics of the aircraft can be considered to be well approximated by the standard roll/Dutch roll dynamics [7]. Peddle shows that under certain conditions, typically met by most conventional aircraft, the lateral-directional dynamics are decoupled into lateral and directional dynamics respectively. This allows two independent inner-loop controllers to be designed, both based on their decoupled dynamics. The first controller is designed to regulate roll rate about the velocity vector, and the second controller is design to regulate the lateral specific acceleration. The roll rate controller will essentially control the roll mode of the aircraft, and the LSA controller will damp and control the Dutch roll mode of the aircraft. This section describes the design of the LSA controller and the next section the design of the roll rate controller. In the dynamic stability analysis in Chapter 4, it was found that the Dutch roll mode of the aircraft is mostly affected by partial vertical stabiliser loss. The LSA controller will therefore be designed to be robust against partial vertical stabiliser loss.

For the lateral-directional dynamics to be decoupled into lateral and directional dynamics respectively, a number of conditions and constraints must be met. First, the side force due to roll rate and aileron deflection should be close to zero.

$$Y_P \approx 0 \tag{5.3.86}$$

$$Y_{\delta_A} \approx 0 \tag{5.3.87}$$

Figure 5.18 (a) shows how Y_P and Y_{δ_A} change as a function of the percentage of vertical stabiliser loss. Figure 5.18 (a) shows that Y_P and Y_{δ_A} remain relatively constant and small with partial vertical stabiliser loss. Furthermore, the yawing moments due to roll rate and aileron deflection must be significantly smaller than the yawing moments due to yaw rate, sideslip, rudder deflection,

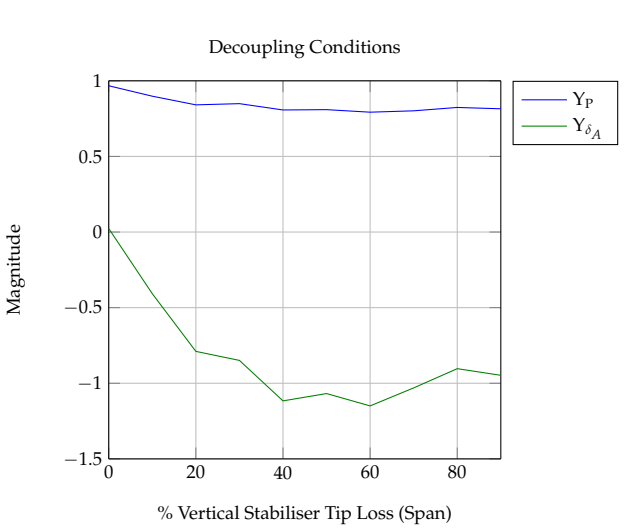

(a) Side force due to lateral perturbations

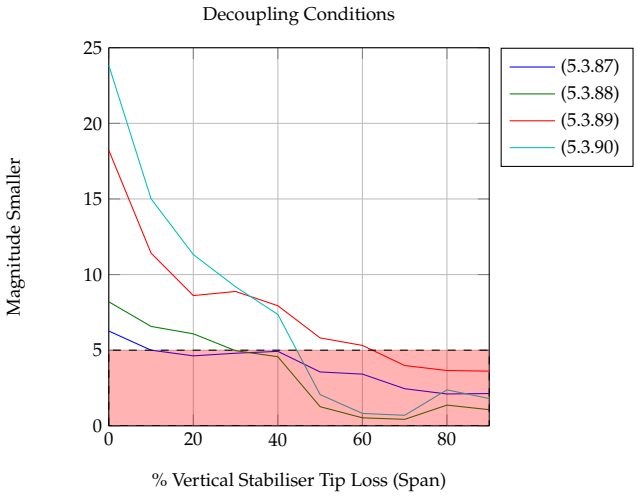

(b) Decoupling conditions.

Figure 5.18: Conditions to be met for decoupling lateral-directional dynamics

and vice versa. Hence lateral dynamics should have little effect on directional dynamics and directional dynamics should have little effect on lateral dynamics. These conditions are usually met by conventional aircraft, but must also be validated for when the aircraft suffers partial vertical stabiliser losses. The conditions are given mathematically by [7] as

$$\left|\frac{C_{n_p}}{C_{l_p}}\right| \ll \left|\frac{C_{n_r}}{C_{l_r}}\right| \tag{5.3.88}$$

$$\left|\frac{C_{n_p}}{C_{l_p}}\right| \ll \left|\frac{C_{n_\beta}}{C_{l_\beta}}\right| \tag{5.3.89}$$

$$\left|\frac{C_{n_{\delta_A}}}{C_{l_{\delta_A}}}\right| \ll \left|\frac{C_{n_r}}{C_{l_r}}\right| \tag{5.3.90}$$

$$\left|\frac{C_{n_{\delta_A}}}{C_{l_{\delta_A}}}\right| \ll \left|\frac{C_{n_\beta}}{C_{l_\beta}}\right| \tag{5.3.91}$$

$$\left|\frac{C_{n_p}}{C_{l_p}}\right| \ll \left|\frac{C_{n_{\delta_R}}}{C_{l_{\delta_R}}}\right| \tag{5.3.92}$$

$$\left|\frac{Y_R}{mV_T}\right| \ll 1 \tag{5.3.93}$$

Figure 5.18 (b) and 5.19 (a) show the order of times less that lateral dynamics influence directional dynamics and vice versa. It is clear that these conditions become less valid as the aircraft suffers partial vertical stabiliser losses. Note the large decay from 0% to approximately 40%. If a magnitude of at least five times less is required, decoupling the lateral dynamics from the directional dynamics is not valid for partial vertical stabiliser losses of higher than approximately 40%. If decoupling is assumed for higher loss cases, the reduced-order decoupled directional dynamics or the approximated Dutch roll dynamics will be poorly approximated. Figure 5.19 (b) shows the comparison between the approximated decoupled lateral and directional dynamics (denoted

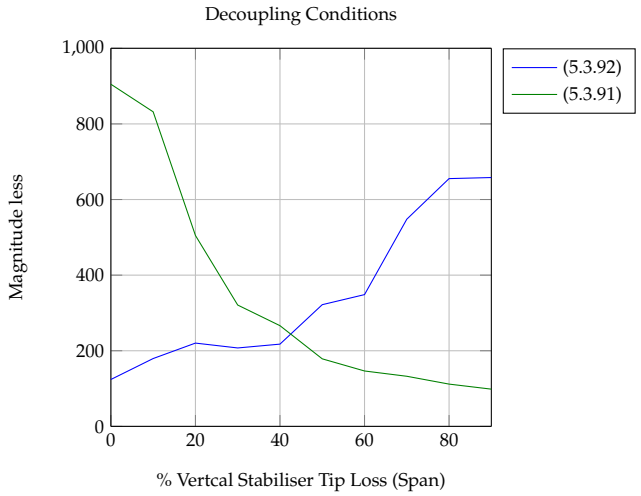

(a) Decoupling conditions

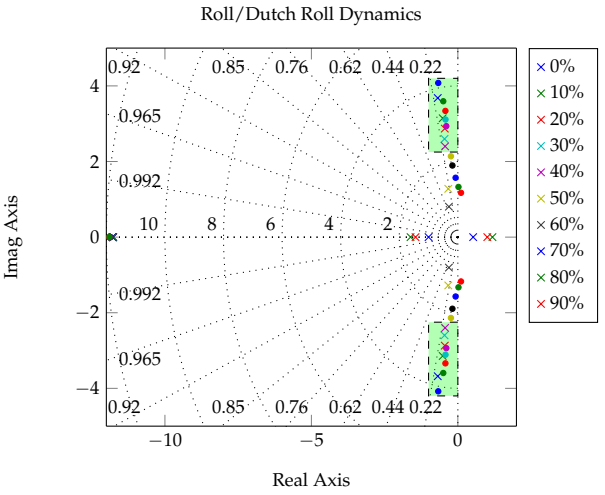

(b) Reduced-order lateral-directional dynamics

Figure 5.19: Conditions to be met for decoupling lateral-directional dynamics and reduced-order Dutch roll dynamics.

with an x) and the true lateral-directional dynamics (denoted with a dot). From Figure 5.19 (b) it is clear that the lateral-directional dynamics can only be decoupled for partial vertical stabiliser losses of up to 40%. The Dutch roll mode poles included within the green bounded area indicate the approximated Dutch roll poles and the true Dutch roll poles for vertical stabiliser losses of 0% up to 40%.

Under the conditions of (5.3.86) to (5.3.93), for control system design purposes, the lateral-directional dynamics are decoupled into lateral and directional dynamics respectively. However, it is important to note that the conditions above do not fully decouple the lateral-directional dynamics, not even for the undamaged aircraft, and that aileron deflections will still excite directional dynamics, and rudder deflections will excite lateral dynamics [7]. This is known as adverse yaw and rudder-induced roll respectively and are considered to be disturbances to the decoupled systems.

The LSA controller is designed on the reduced-order decoupled directional dynamics by taking the abovementioned constraints into account. The robust design technique discussed in Section 5.2 is used to design an LSA controller that is robust to partial vertical stabiliser loss.

5.3.5.1 Reduced-Order Design

Assuming that all the abovementioned conditions and constraints are met, the design of the LSA controller can proceed with the following reduced-order directional dynamics given by [7] as

$$\begin{bmatrix} \dot{\beta} \\ \dot{r} \end{bmatrix} = \begin{bmatrix} \frac{Y_\beta}{mV_T} & -1 \\ \frac{N_\beta}{I_{zz}} & \frac{N_R}{I_{zz}} \end{bmatrix} \begin{bmatrix} \beta \\ r \end{bmatrix} + \begin{bmatrix} \frac{Y_{\delta_R}}{mV_T} \\ \frac{N_{\delta_r}}{I_{zz}} \end{bmatrix} \delta_r \tag{5.3.94}$$

$$b_w = \begin{bmatrix} \frac{Y_\beta}{m} & \frac{Y_R}{m} \end{bmatrix} \begin{bmatrix} \beta \\ r \end{bmatrix} + \begin{bmatrix} \frac{Y_{\delta_R}}{m} \end{bmatrix} \delta_r \tag{5.3.95}$$

where b_w is the lateral specific acceleration perturbation in the wind reference frame, and the Dutch roll mode dynamics are approximated by (5.3.94). Figure 5.20 shows the feedback control system in block diagram form, where

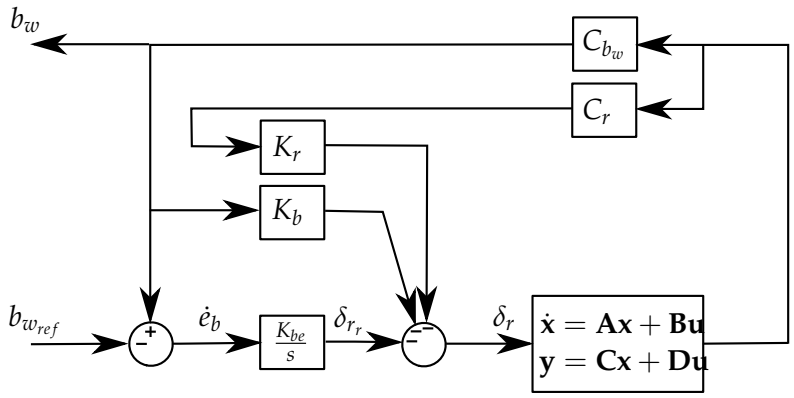

Figure 5.20: Lateral specific acceleration controller block diagram

$$C_r = \begin{bmatrix} 0 & 1 \end{bmatrix} \tag{5.3.96}$$

The LSA controller is designed as described by Peddle [7]. It consists of two controller loops. First, the reduced decoupled directional dynamics are used to design a controller that allows the Dutch roll mode poles to be moved arbitrarily. This controller is used for stability augmentation only and does not regulate the lateral specific acceleration. A second, outer level controller is then designed to regulate the lateral specific acceleration. This second controller ensures that the closed-loop LSA regulation bandwidth does not exceed the NMP upper frequency bound given by [7] as,

$$\omega_{n_{cl}} < \frac{1}{3}\left|\sqrt{\frac{-Y_\beta(l_V - l_W)}{I_{zz}}}\right| \tag{5.3.97}$$

which is required for a practically feasible controller, and

$$l_W = -\frac{N_\beta}{Y_\beta} \tag{5.3.98}$$

$$l_D = -\frac{N_r}{Y_r} \tag{5.3.99}$$

$$l_V = -\frac{N_{\delta_R}}{Y_{\delta_R}} \tag{5.3.100}$$

where l_W is the weathercock arm length, l_D is the damping arm length and l_V is the effective length to the vertical stabiliser. The design of the second control system assumes that the stability augmentation controller places the Dutch roll poles such that a timescale separation exists between the stability augmentation controller and the LSA regulation controller. This assumption allows the full dynamic model from rudder to lateral specific acceleration to be approximated by a steady state gain. Figure 5.21 shows the admissible pole regions for the stability-augmented Dutch roll poles and the admissible pole region for the LSA regulation pole. Note that a timescale separation must exist between the two regions. Roughly five times the timescale of the outer-loop bandwidth is commonly used in practice.

Define the stability augmentation control law

$$\delta_r = -K_r r - K_b b_w + \delta_{r_r} \tag{5.3.101}$$

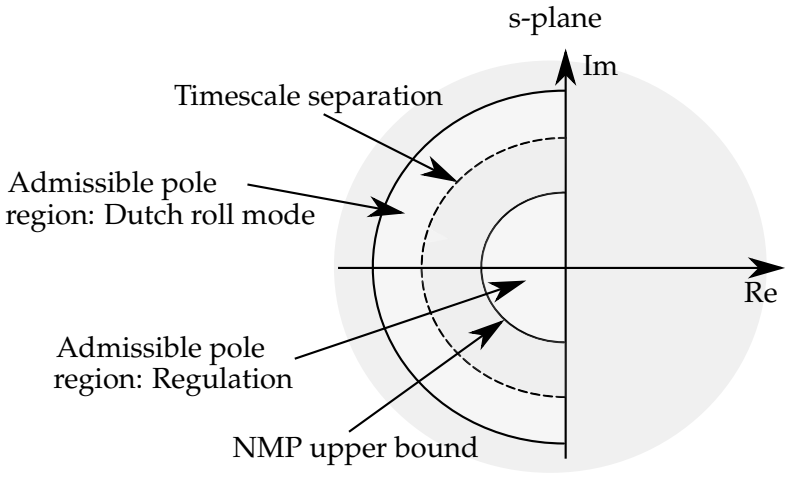

Figure 5.21: Lateral specific acceleration admissible pole regions

where δ_{r_r} is the reference input for the regulation control law. Given the desired closed-loop directional dynamics characteristic equation,

$$\alpha_c(s) = s^2 + \alpha_1 s + \alpha_0 \tag{5.3.102}$$

where

$$\alpha_0 = \omega_n^2 \tag{5.3.103}$$

$$\alpha_1 = 2\zeta\omega_n \tag{5.3.104}$$

Peddle shows that the stability augmentation feedback gains can be determined where

$$K_b = \frac{\frac{Y_\beta}{mV_T}\frac{N_R}{I_{zz}} + \frac{N_\beta}{I_{zz}} - \alpha_0}{\frac{Y_{\delta_R}}{m}\left[\alpha_0 - \frac{Y_\beta}{I_{zz}}\left(\frac{N_\beta}{Y_\beta} - \frac{N_{\delta_R}}{Y_{\delta_R}}\right)\right]} \tag{5.3.105}$$

$$K_r = \frac{I_{zz}}{N_{\delta_R}}\left[\frac{Y_\beta}{mV_T} + \frac{N_R}{I_{zz}} + \alpha_1\left(1 + K_b\frac{Y_{\delta_R}}{m}\right)\right] \tag{5.3.106}$$

The Dutch roll mode can now be damped and the natural frequency changed to ensure timescale separation from the LSA regulation controller. The stability augmentation controller can therefore be designed by selecting a damping ratio ζ_{cl} and a natural frequency $\omega_{n_{cl}}$.

With the stability augmentation controller placed, and assuming that the closed-loop directional dynamics poles will be timescale-separated from the LSA regulator pole, Peddle shows that the transfer function from rudder through to lateral specific acceleration can be well approximated by,

$$b_w \approx K_{ss}\delta_{r_r} \tag{5.3.107}$$

where K_{ss} is the steady state gain of the transfer function given as

$$K_{ss} = \frac{1}{\alpha_0}\frac{\frac{Y_{\delta_R}}{m}\frac{Y_\beta}{I_{zz}}\left(\frac{N_\beta}{Y_\beta} - \frac{N_{\delta_R}}{Y_{\delta_R}}\right)}{1 + K_b\frac{Y_{\delta_R}}{m}} \tag{5.3.108}$$

where α_0 refers to the final term in the desired characteristic equation of (5.3.102). An integral control law for the LSA regulator is defined:

$$\delta_{r_r} = -K_e e_b \tag{5.3.109}$$

and

$$\dot{e}_b = b_w - b_{w_{ref}} \tag{5.3.110}$$

where $b_{w_{ref}}$ is the reference lateral specific acceleration perturbation command. The closed-loop dynamics are then given by [7] as

$$\dot{e}_b = \left[-K_{ss}K_e\right] e_b + \left[-1\right] b_{w_{ref}} \tag{5.3.111}$$

Given the desired characteristic equation or equivalently pole location

$$\alpha_c(s) = s + \alpha_0 \tag{5.3.112}$$

the integrator feedback gain is calculated as follows:

$$K_e = \frac{\alpha_0}{K_{ss}} \tag{5.3.113}$$

The design freedom of the LSA regulator is therefore left by choosing the real closed-loop pole corresponding to the open-loop integrator pole that falls within the admissible pole region, as shown in Figure 5.21. Note that the LSA regulation pole will dominate the LSA response, which will ensure that a practically feasible controller is designed. The stability augmentation controller provides fast disturbance rejection at acceleration level, but due to the timescale separation, it will not dominate the LSA response.

Consider the following maximum and minimum natural frequencies and damping ratios to bound the directional dynamics poles:

$$\text{Twice timescale separation lower bound} \geq \omega_n \geq \text{Timescale separation lower bound} \tag{5.3.114}$$

$$0.9 \geq \zeta \geq 0.6 \tag{5.3.115}$$

and maximum and minimum natural frequencies for the LSA regulation pole:

$$\text{NMP Upper frequency bound} \geq \omega_n \geq 0 \tag{5.3.116}$$

$$\zeta \geq 1 \tag{5.3.117}$$

The algorithm finds a set of controller gains that keeps the closed-loop poles within the admissible pole region defined above.

Figure 5.22 shows the pole-zero plot and a unit step response for a set of controller gains that satisfies all the above boundaries while providing robustness to partial vertical stabiliser losses up to 20%. Note that the closed-loop directional dynamics and the LSA regulation pole remain within the admissible pole region for partial vertical stabiliser losses up to 20% . The set of robust controller gains determined will guarantee that the closed-loop system remains stable and within acceptable transient response specifications when the aircraft suffers partial vertical stabiliser losses up to 20%. Note that even though the closed-loop system remains stable for partial vertical stabiliser losses of 30% to 50%, it does not meet the damping or timescale separation specifications. Also note that the natural frequency of the Dutch roll dynamics is significantly increased in order to achieve the required timescale separation. The open-loop Dutch roll dynamics of the aircraft is relatively slow and very lightly damped, which complicates the design of the LSA controller and reduces the robustness that can be achieved. The LSA controller dynamics is added to, and verified on the full linear dynamics of the aircraft.

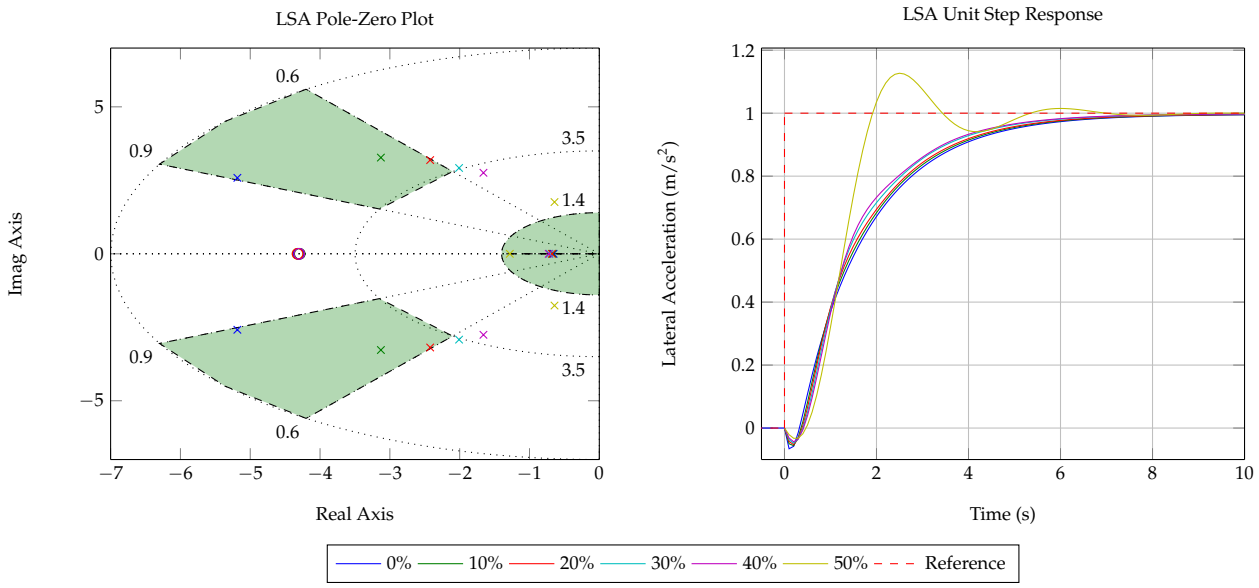

Figure 5.22: LSA unit step response and pole plot

5.3.5.2 Closed-Loop System

The LSA controller dynamics is now verified on the full linear dynamics of the aircraft. Equation 5.3.81 states the full linear aircraft dynamics with the all the longitudinal controller dynamics included. First, the stability augmentation control law given in (5.3.101) is added:

$$\begin{bmatrix}\dot{\mathbf{x}}_h\end{bmatrix} = \begin{bmatrix}\mathbf{A}_h - \boldsymbol{B}_{\delta_r}\boldsymbol{H}_1\end{bmatrix}\begin{bmatrix}\mathbf{x}_h\end{bmatrix} + \begin{bmatrix}\boldsymbol{B}_h & \boldsymbol{B}_{\bar{v}_{ref}} & \boldsymbol{B}_{\delta_a} - \boldsymbol{B}_{\delta_r}\left(\frac{K_b Y_{\delta_A}}{m+K_B Y_{\delta_R}}\right) & \boldsymbol{B}_{\delta_r}\left(\frac{1}{1+\frac{K_b Y_{\delta_R}}{m}}\right)\end{bmatrix}\begin{bmatrix}h_{ref}\\ \bar{v}_{ref}\\ \delta_a\\ \delta_{r_r}\end{bmatrix} \tag{5.3.118}$$

where

$$b_w = \begin{bmatrix}\frac{Y_\beta}{m} & \frac{Y_P}{m} & \frac{Y_R}{m}\end{bmatrix}\begin{bmatrix}\beta\\ p\\ r\end{bmatrix} + \begin{bmatrix}\frac{Y_{\delta_A}}{m} & \frac{Y_{\delta_R}}{m}\end{bmatrix}\begin{bmatrix}\delta_a\\ \delta_r\end{bmatrix} \tag{5.3.119}$$

and

$$\boldsymbol{H}_1 = \begin{bmatrix}\mathbf{0}_{1\times 4} & -\left(\frac{K_b Y_\beta}{m+K_B Y_{\delta_R}}\right) & -\left(\frac{K_b Y_P}{m+K_B Y_{\delta_R}}\right) & -\left(\frac{K_r}{1+\frac{K_b Y_{\delta_R}}{m}} + \frac{K_b Y_R}{m+K_b Y_{\delta_R}}\right) & \mathbf{0}_{1\times 6}\end{bmatrix} \tag{5.3.120}$$

Note that the full-order lateral acceleration dynamics were augmented in (5.3.119), and not the reduced-order lateral acceleration dynamics. For the sake of convenience, (5.3.118) is written as follows:

$$\dot{\mathbf{x}}_{b_{sa}} = \mathbf{A}_{b_{sa}}\mathbf{x}_{b_{sa}} + \mathbf{B}_{b_{sa}}\mathbf{u} \tag{5.3.121}$$

where subscript *sa* denotes that the stability augmentation is added to the full linear dynamics. The LSA regulation integrator state given in (5.3.110) is now added to the system

$$\begin{bmatrix}\dot{\mathbf{x}}_{b_{sa}}\\ \dot{e}_b\end{bmatrix}=\begin{bmatrix}\mathbf{A}_{b_{sa}} & \mathbf{0}_{13\times1}\\ \boldsymbol{H}_2 & 0\end{bmatrix}\begin{bmatrix}\mathbf{x}_{b_{sa}}\\ e_b\end{bmatrix}+\begin{bmatrix}\boldsymbol{B}_{h_{ref}} & \boldsymbol{B}_{\bar{v}_{ref}} & \boldsymbol{B}_{\delta_a} & \boldsymbol{B}_{\delta_{r_r}}\\ 0 & 0 & \frac{Y_{\delta_A}}{m}-\frac{Y_{\delta_R}}{m}\left(\frac{K_bY_{\delta_A}}{m+K_BY_{\delta_R}}\right) & \frac{Y_{\delta_R}}{m+K_bY_{\delta_R}}\end{bmatrix}\begin{bmatrix}h_{ref}\\ \bar{v}_{ref}\\ \delta_a\\ \delta_{r_r}\end{bmatrix}+\begin{bmatrix}\mathbf{0}_{13\times1}\\ -1\end{bmatrix}b_{w_{ref}} \tag{5.3.122}$$

where

$$\boldsymbol{H}_2=\begin{bmatrix}\mathbf{0}_{1\times4} & \frac{Y_\beta}{m}-\frac{Y_{\delta_R}}{m}\left(\frac{K_bY_\beta}{m+K_BY_{\delta_R}}\right) & \frac{Y_P}{m}-\frac{Y_{\delta_R}}{m}\left(\frac{K_bY_P}{m+K_BY_{\delta_R}}\right) & \frac{Y_R}{m}-\frac{Y_{\delta_R}}{m}\left(\frac{K_r}{1+\frac{K_bY_{\delta_R}}{m}}+\frac{K_bY_R}{m+K_bY_{\delta_R}}\right) & \mathbf{0}_{1\times6}\end{bmatrix} \tag{5.3.123}$$

The LSA regulation control law given in (5.3.109) is substituted,

$$\begin{aligned}\begin{bmatrix}\dot{\mathbf{x}}_{b_{sa}}\\ \dot{e}_b\end{bmatrix}=&\left(\begin{bmatrix}\mathbf{A}_{b_{sa}} & \mathbf{0}_{13\times1}\\ \boldsymbol{H}_2 & 0\end{bmatrix}+\begin{bmatrix}\boldsymbol{B}_{\delta_{r_r}}\\ \frac{Y_{\delta_R}}{m+K_bY_{\delta_R}}\end{bmatrix}\begin{bmatrix}\mathbf{0}_{1\times13} & -Ke\end{bmatrix}\right)\begin{bmatrix}\mathbf{x}_{b_{sa}}\\ e_b\end{bmatrix}\\ &+\begin{bmatrix}\boldsymbol{B}_{h_{ref}} & \boldsymbol{B}_{\bar{v}_{ref}} & \boldsymbol{B}_{\delta_a} & 0\\ 0 & 0 & \frac{Y_{\delta_A}}{m}-\frac{Y_{\delta_R}}{m}\left(\frac{K_bY_{\delta_A}}{m+K_BY_{\delta_R}}\right) & -1\end{bmatrix}\begin{bmatrix}h_{ref}\\ \bar{v}_{ref}\\ \delta_a\\ b_{w_{ref}}\end{bmatrix}\end{aligned} \tag{5.3.124}$$

The closed-loop state space model now has a subscript b_w, indicating that the LSA controller has been added. Note that the input vector has changed. The LSA reference is now an input to the system.

$$\dot{\mathbf{x}}_{b_w}=\mathbf{A}_{b_w}\mathbf{x}_{b_w}+\mathbf{B}_{b_w}\mathbf{u} \tag{5.3.125}$$

where

$$\mathbf{B}_{b_w}=\begin{bmatrix}\boldsymbol{B}_{c_{w_{ref}}} & \boldsymbol{B}_{\bar{v}_{ref}} & \boldsymbol{B}_{\delta_a} & \boldsymbol{B}_{b_{w_{ref}}}\end{bmatrix} \tag{5.3.126}$$

The output of the LSA controller is given as

$$y_{b_w}=\boldsymbol{C}_{b_w}\mathbf{x}_{b_w} \tag{5.3.127}$$

Now define

$$\boldsymbol{C}_{b_w}=\begin{bmatrix}0 & \left(-\frac{L_\alpha}{m}-\frac{L_{\delta_E}}{m}\frac{L_\alpha}{m}K_c\right) & \left(-\frac{L_Q}{m}+\frac{L_{\delta_E}}{m}K_q-\frac{L_{\delta_E}}{m}\frac{L_Q}{m}K_c\right) & \mathbf{0}_{1\times7} & \left(-\frac{L_{\delta_E}}{m}K_e\right)\end{bmatrix} \tag{5.3.128}$$

The closed-loop transfer function from $b_{w_{ref}}$ to b_w can now be obtained.

$$G_{b_{w_{cl}}}(s)=\frac{b_w}{b_{w_{ref}}}=\boldsymbol{C}_{b_w}(s\mathbf{I}_{14}-\mathbf{A}_{b_w})^{-1}\boldsymbol{B}_{b_{w_{ref}}} \tag{5.3.129}$$

5.3.5.3 Robustness to Vertical Stabiliser Tip Loss

Figure 5.23 shows the robustness of the LSA controller on the full linear aircraft model. Note that the closed-loop pole locations differ from the reduced-order pole locations. This is mainly due to the decoupling assumptions that were adopted during the reduced-order design. Furthermore, the reduced-order design does not account for the centre of mass shift. The centre of mass shift is,

however, very small and its effect even smaller. The 20% vertical stabiliser loss case's Dutch roll mode poles, which were within the admissible pole region for the reduced design, now fall outside of the admissible pole region. The LSA regulation poles, on the other hand, remain approximately at the designed locations.

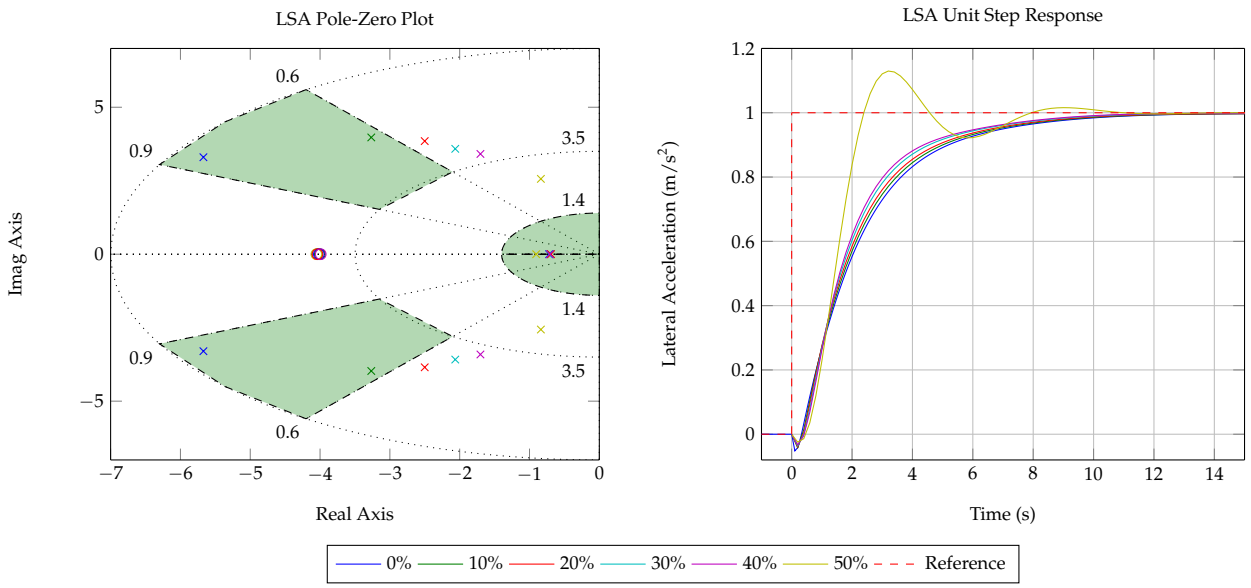

Figure 5.23: LSA unit step response and pole-zero plot for vertical stabiliser loss

5.3.6 Roll Rate Controller

This section describes the design and robustness of the roll rate controller. The roll rate dynamics of the aircraft can be considered to be well approximated by the lateral or roll mode dynamics. As discussed in the previous section, the lateral-directional dynamics of the aircraft are decoupled into lateral and directional dynamics respectively. The conditions and constraints under which the decoupling is valid were described in the previous section.

The decoupled reduced-order model is used for control system design purposes. From the dynamic stability analysis in Chapter 4, it was found that the roll mode of the aircraft is mostly affected by partial wing loss. The roll rate controller will therefore be designed to be robust against partial wing loss. Similar to what was done in the partial vertical stabiliser loss cases, it must also be validated whether the lateral-directional decoupling is valid for the partial wing loss cases. From Figures 5.24 and 5.25, it is clear that all the conditions and constraints as described by Peddle are met, and that the lateral-directional dynamics can be decoupled for all partial wing loss cases. From Figure 5.25 (b), note the error between the reduced-order roll mode pole (denoted with an x) and the roll mode pole (denoted with a dot). The reduced-order approximation remains accurate for partial wing losses of up to 30%. Designing the controller on the reduced-order roll dynamics is therefore a valid design approach.

The roll rate controller is designed on the reduced-order decoupled dynamics. The robust design technique discussed in Section 5.2 is used to design a roll rate controller that is robust against partial wing loss.

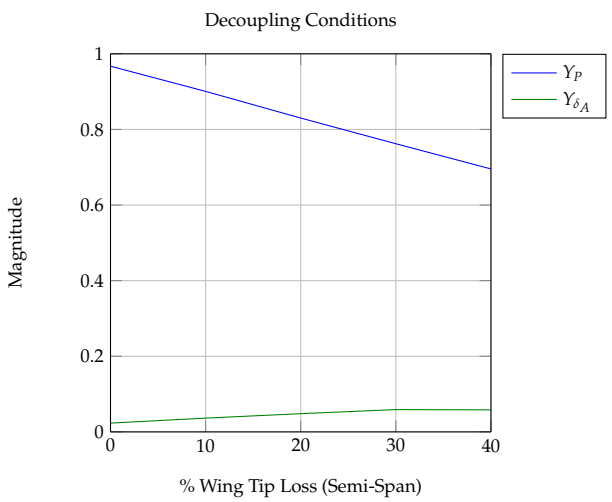

(a) Side force due to lateral perturbations

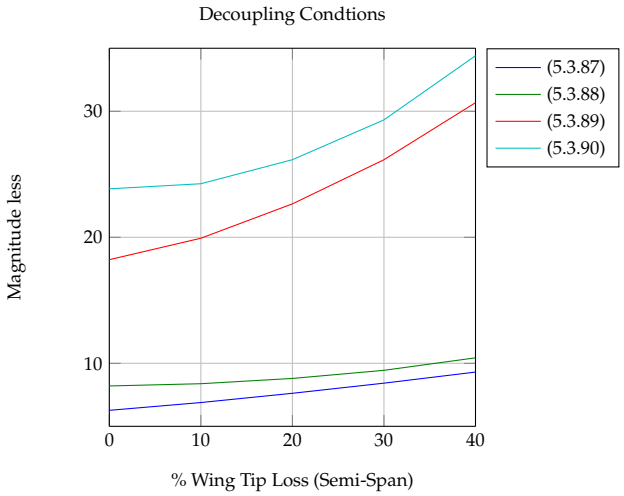

(b) Decoupling conditions.

Figure 5.24: Conditions to be met for decoupling lateral-directional dynamics

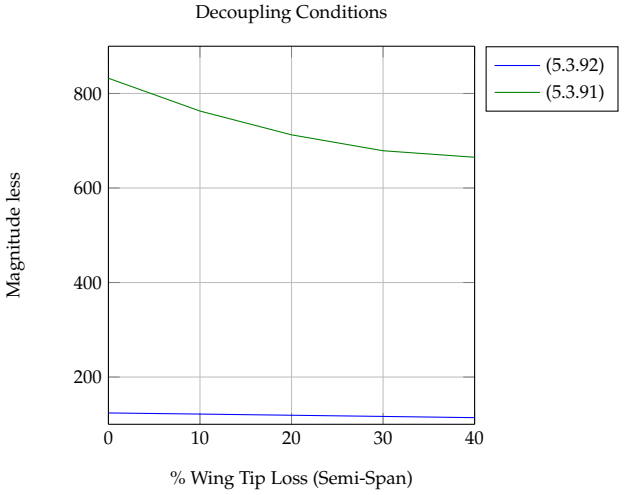

(a) Decoupling conditions

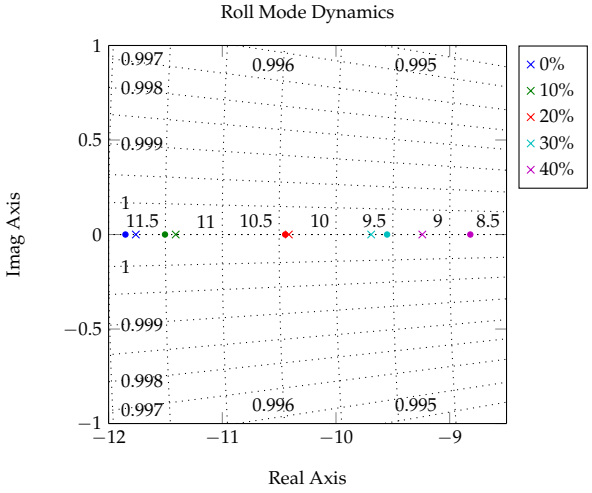

(b) Reduced-order roll rate dynamics

Figure 5.25: Conditions to be met for decoupling lateral-directional dynamics and reduced-order roll rate dynamics.

5.3.6.1 Reduced-Order Design

Assuming that all the abovementioned conditions and constraints are met, the design of the roll rate controller can proceed with the following reduced-order roll dynamics given by [7] as

$$\dot{p} = \left[\frac{L_p}{I_{xx}}\right] p + \left[\frac{L_{\delta_A}}{I_{xx}}\right] \delta_a \tag{5.3.130}$$

Figure 5.26 shows the feedback control system in block diagram form, where

$$G_p(s) = \left[1\right] \left[s \quad - \quad \frac{L_p}{I_{xx}}\right]^{-1} \left[\frac{L_{\delta_A}}{I_{xx}}\right] \tag{5.3.131}$$

A PI control law is defined that generates an aileron deflection δ_a proportional to the weighted sum of the roll rate error and the time integral of the roll rate error:

$$\delta_a = -K_p \dot{e}_p - K_i e_p \tag{5.3.132}$$

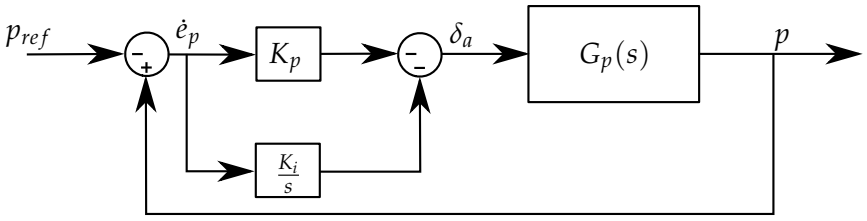

Figure 5.26: Roll rate controller block diagram

where the roll rate error is defined as

$$\dot{e}_p = p - p_{ref} \tag{5.3.133}$$

where p_{ref} is the roll rate perturbation reference. The integrator is used to reject any model uncertainties when in steady state to ensure that the correct aileron deflection is deflected to obtain the correct roll rate. Furthermore, the integrator will find the aileron trim value of the aircraft. After added the integrator dynamics to (5.3.130) and substituting the control law (5.3.132), the closed-loop system becomes

$$\begin{bmatrix} \dot{p} \\ \dot{e}_p \end{bmatrix} = \begin{bmatrix} \frac{L_P}{I_{xx}} - K_p \frac{L_{\delta_A}}{I_{xx}} & -K_i \frac{L_{\delta_A}}{I_{xx}} \\ 1 & 0 \end{bmatrix} \begin{bmatrix} p \\ e_p \end{bmatrix} + \begin{bmatrix} K_p \frac{L_{\delta_A}}{I_{xx}} \\ -1 \end{bmatrix} p_{ref} \tag{5.3.134}$$

For pole placement, a desired characteristic equation for the roll rate dynamics is defined as

$$\alpha_{cl}(s) = s^2 + \alpha_1 s + \alpha_0 \tag{5.3.135}$$

The roll rate controller gains are calculated by solving (5.3.135) and the characteristic equation of (5.3.134) to obtain

$$K_p = \frac{L_p - I_{xx}\alpha_1}{L_{\delta_A}} \tag{5.3.136}$$

$$K_i = \frac{I_{xx}}{L_{\delta_A}} \alpha_0 \tag{5.3.137}$$

The design freedom of the roll rate controller is therefore left to choosing a natural frequency and damping ratio that will result in the closed-loop poles falling within an admissible pole region.

Consider the following maximum and minimum natural frequencies and damping ratios to bound the roll rate dynamics:

$$0.7\frac{L_P}{I_{xx}} \geq \omega_n \geq 0 \tag{5.3.138}$$

$$\zeta \geq 0.9 \tag{5.3.139}$$

The algorithm finds a set of gains that will keep the closed-loop poles within the admissible pole region defined above. Figure 5.27 shows the pole-zero plot and a unit step response for a set of controller gains that satisfy all the above boundaries while having a robustness to partial wing loss of up to 40%. Note that the closed-loop poles remain within the admissible pole region. The set of robust controller gains obtained will therefore guarantee that the closed-loop system remains stable and within acceptable transient response specifications when the aircraft suffers partial wing loss (up to 40%). Even though the controller is robust against partial wing loss of up to 40%, equilibrium flight can only be achieved for partial wing loss of up to 20%. The roll rate controller dynamics is added to, and verified on the full linear dynamics of the aircraft.

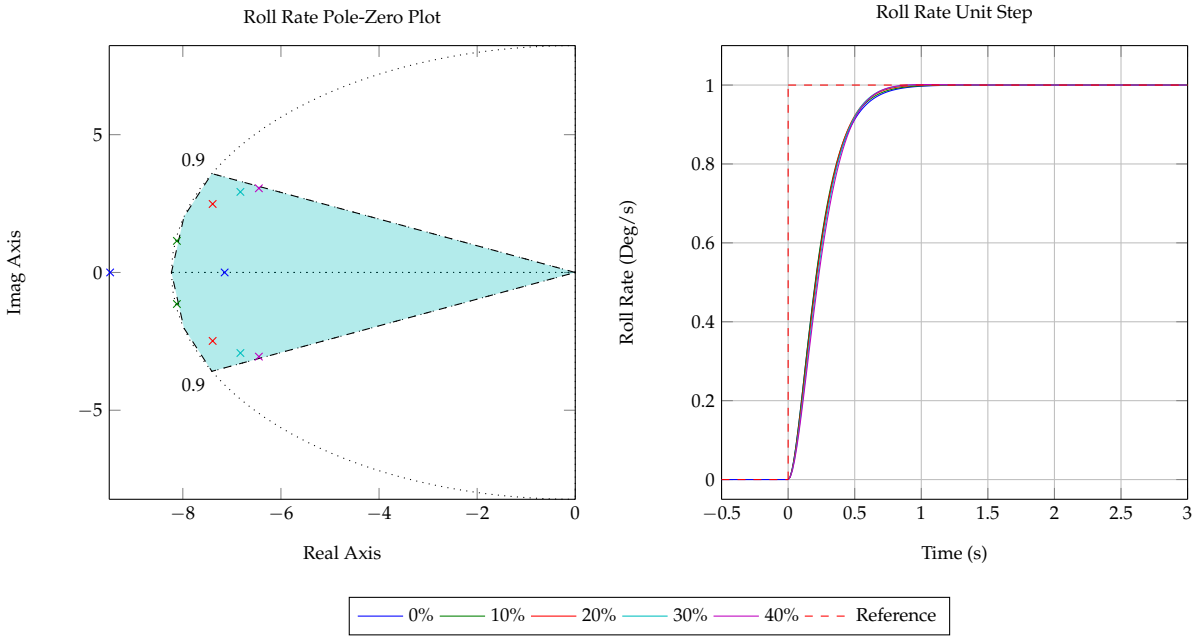

Figure 5.27: Roll rate unit step response and pole-zero plot

5.3.6.2 Closed-Loop System

The roll rate controller dynamics is now verified on the full linear dynamics of the aircraft. Equation (5.3.125) states the full linear aircraft dynamics with the LSA and longitudinal controller dynamics included. First the integrator dynamics given in (5.3.133) are added.

$$\begin{bmatrix} \dot{\mathbf{x}}_{b_w} \\ \dot{e}_p \end{bmatrix} = \begin{bmatrix} \mathbf{A}_{b_w} & \mathbf{0}_{14\times 1} \\ \begin{bmatrix} \mathbf{0}_{1\times 5} & 1 \end{bmatrix} & \mathbf{0}_{1\times 9} \end{bmatrix} \begin{bmatrix} \mathbf{x}_{b_w} \\ e_p \end{bmatrix} + \begin{bmatrix} \boldsymbol{B}_{h_{ref}} & \boldsymbol{B}_{\bar{v}_{ref}} & \boldsymbol{B}_{\delta_a} & \boldsymbol{B}_{b_{w_{ref}}} \\ 0 & 0 & 0 & 0 \end{bmatrix} \begin{bmatrix} h_{ref} \\ \bar{v}_{ref} \\ \delta_a \\ b_{w_{ref}} \end{bmatrix} + \begin{bmatrix} \mathbf{0}_{14\times 1} \\ -1 \end{bmatrix} p_{ref} \tag{5.3.140}$$

The control law given in (5.3.132) is then added to the system.

$$\begin{aligned} \begin{bmatrix} \dot{\mathbf{x}}_{b_w} \\ \dot{e}_p \end{bmatrix} = \left[\begin{bmatrix} \mathbf{A}_{b_w} & \mathbf{0}_{14\times 1} \\ \begin{bmatrix} \mathbf{0}_{1\times 5} & 1 \end{bmatrix} & \mathbf{0}_{1\times 9} \end{bmatrix} + \begin{bmatrix} \boldsymbol{B}_{\delta_a} \\ 0 \end{bmatrix} \begin{bmatrix} \mathbf{0}_{1\times 5} & -K_p & \mathbf{0}_{1\times 8} & -K_i \end{bmatrix} \right] \begin{bmatrix} \mathbf{x}_{b_w} \\ e_p \end{bmatrix} \\ + \begin{bmatrix} \boldsymbol{B}_{h_{ref}} & \boldsymbol{B}_{\bar{v}_{ref}} & \boldsymbol{B}_{\delta_a} K_p & \boldsymbol{B}_{b_{w_{ref}}} \\ 0 & 0 & -1 & 0 \end{bmatrix} \begin{bmatrix} h_{ref} \\ \bar{v}_{ref} \\ p_{ref} \\ b_{w_{ref}} \end{bmatrix} \end{aligned} \tag{5.3.141}$$

The closed-loop state space model now has a subscript p, indicating that the roll rate controller has been added. Note that the input vector has changed. The roll rate reference is now an input to the system.

$$\dot{\mathbf{x}}_p = \mathbf{A}_p \mathbf{x}_p + \mathbf{B}_p \mathbf{u} \tag{5.3.142}$$

Now define

$$\mathbf{B}_p = \begin{bmatrix} \boldsymbol{B}_{h_{ref}} & \boldsymbol{B}_{\bar{v}_{ref}} & \boldsymbol{B}_{p_{ref}} & \boldsymbol{B}_{b_{w_{ref}}} \end{bmatrix} \tag{5.3.143}$$

The output of the roll rate controller is given as

$$y_p = \boldsymbol{C}_p \mathbf{x}_p \tag{5.3.144}$$

where

$$\boldsymbol{C}_p = \begin{bmatrix} \mathbf{0}_{1\times 5} & 1 & \mathbf{0}_{1\times 9} \end{bmatrix} \tag{5.3.145}$$

The closed-loop transfer function from p_{ref} to p can now be obtained.

$$G_{p_{cl}}(s) = \frac{p}{p_{ref}} = \boldsymbol{C}_p(s\mathbf{I}_{15} - \mathbf{A}_p)^{-1}\boldsymbol{B}_{p_{ref}} \tag{5.3.146}$$

5.3.6.3 Robustness to Wing Tip Loss

Figure 5.28 shows the robustness of the roll rate controller on the full linear aircraft model. There is a significant change in the pole locations between the reduced-order and full linear model. The dominant pole is placed at a much lower frequency than what it was designed for. Note that the aircraft is still unstable after the roll rate controller is added, resulting in the roll rate increasing over time. This makes it difficult to design the roll rate controller using the full non-linear aircraft model. Nonetheless, the dominant closed-loop poles remain within the admissible pole region and therefore remains robust to partial wing loss.

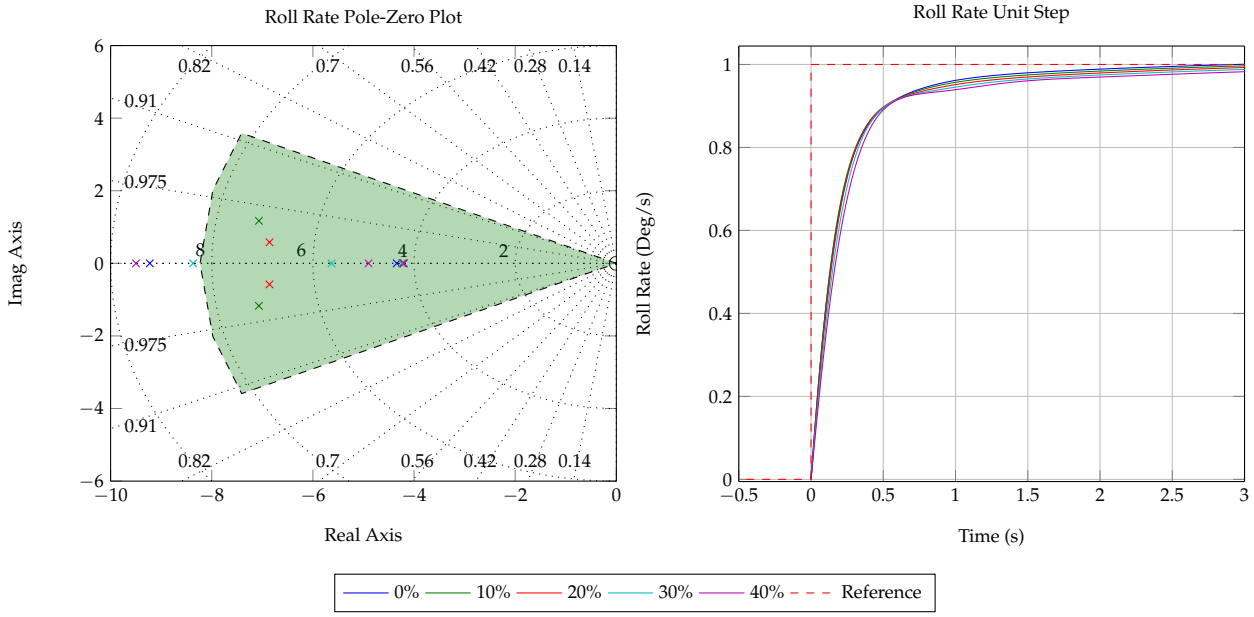

Figure 5.28: Roll rate unit step response and pole-zero plot for wing loss

5.3.7 Roll Angle Controller

This section describes the design and robustness of the roll angle controller. The roll angle controller regulates the aircraft's roll angle by making use of the roll rate controller. The roll angle that is controlled is the angle ϕ, which is the angle of the body reference frame with respect to the inertial reference frame. A positive instantaneous roll angle perturbation will cause the aircraft to experience a positive roll rate perturbation.

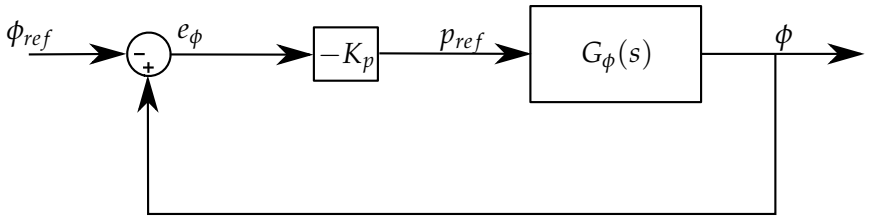

Figure 5.29: Roll angle controller block diagram

5.3.7.1 Design

Figure 5.29 shows the feedback control system in block diagram form, where the open-loop transfer function of the aircraft's roll angle dynamics is given by

$$G_\phi(s) = \boldsymbol{C}_\phi \left[s\mathbf{I}_{15} - \mathbf{A}_p \right] \boldsymbol{B}_{p_{ref}} \tag{5.3.147}$$

where

$$\boldsymbol{C}_\phi = \begin{bmatrix} \mathbf{0}_{1\times 7} & 1 & \mathbf{0}_{1\times 7} \end{bmatrix} \tag{5.3.148}$$

A proportional control law is defined that generates a roll rate p_{ref} proportional to the roll angle error:

$$p_{ref} = -K_p e_\phi \tag{5.3.149}$$

where the roll angle error is defined as

$$e_\phi = \phi - \phi_{ref} \tag{5.3.150}$$

The root locus design technique is used to determine the controller gain K_p. Figure 5.30 shows the root locus design and the closed-loop unit step response of the roll angle controller. The roll

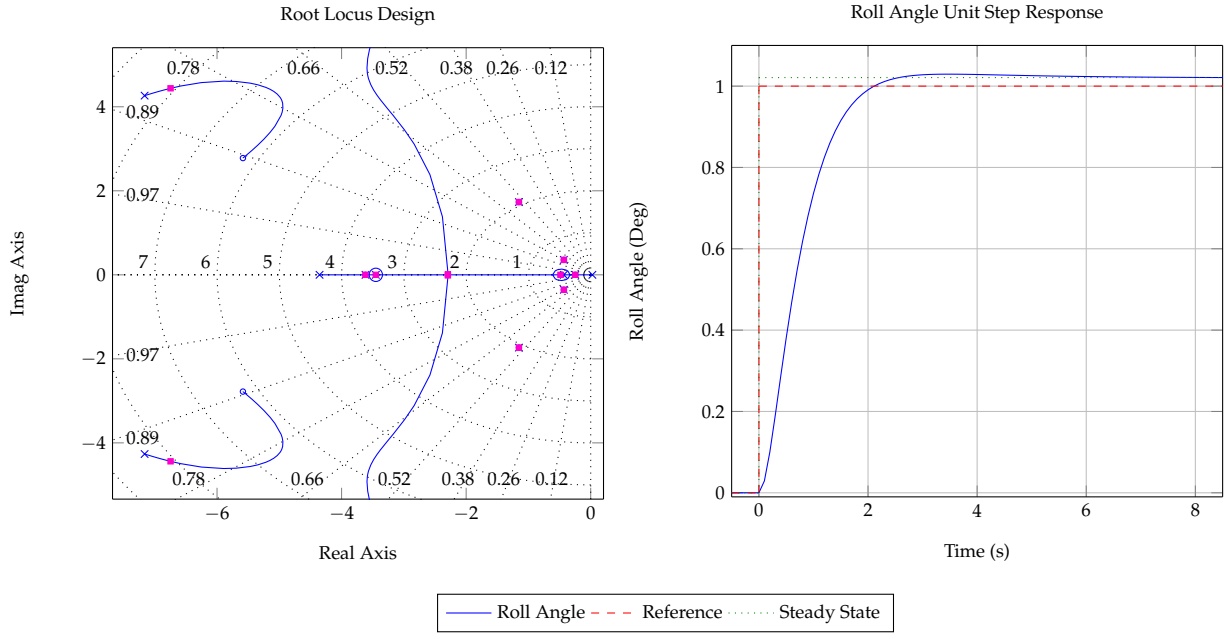

Figure 5.30: Roll angle unit step response and root locus design

angle controller is designed to be well damped with minimum overshoot. Note that the open-loop

roll angle dynamics does not have a free integrator, resulting in the roll angle controller tracking the unit step reference with a finite steady state error. An approximately 2% error is made on the tracking of the reference. A PI controller can be implemented, but this will result in a slow roll angle controller with a large amount of overshoot. The guidance controller, which is described in the next section will be designed with the ability to correct for the roll angle steady state error. The roll angle controller dynamics is added to, and verified on the full linear dynamics of the aircraft.

5.3.7.2 Closed-Loop System

The roll angle controller dynamics is now verified on the full linear dynamics of the aircraft. Equation (5.3.142) states the full linear aircraft dynamics with the roll rate and longitudinal controller dynamics included. The control law given in (5.3.149) is added to the system.

$$\begin{aligned}\begin{bmatrix}\dot{\mathbf{x}}_p\end{bmatrix} = \left[\begin{bmatrix}\mathbf{A}_p\end{bmatrix} + \begin{bmatrix}\boldsymbol{B}_p\end{bmatrix}\begin{bmatrix}\mathbf{0}_{1\times 7} & -K_p & \mathbf{0}_{1\times 7}\end{bmatrix}\right]\begin{bmatrix}\mathbf{x}_p\end{bmatrix} \\ + \begin{bmatrix}\boldsymbol{B}_{h_{ref}} & \boldsymbol{B}_{\bar{v}_{ref}} & \boldsymbol{B}_p K_p & \boldsymbol{B}_{b_{w_{ref}}}\end{bmatrix}\begin{bmatrix} h_{ref} \\ \bar{v}_{ref} \\ \phi_{ref} \\ b_{w_{ref}}\end{bmatrix}\end{aligned} \tag{5.3.151}$$

The closed-loop state space model now has a subscript ϕ, indicating that the roll angle controller has been added. Note that the input vector has changed. The roll angle reference is now an input to the system.

$$\dot{\mathbf{x}}_\phi = \mathbf{A}_\phi \mathbf{x}_\phi + \mathbf{B}_\phi \mathbf{u} \tag{5.3.152}$$

Now define

$$\mathbf{B}_\phi = \begin{bmatrix}\boldsymbol{B}_{h_{ref}} & \boldsymbol{B}_{\bar{v}_{ref}} & \boldsymbol{B}_{\phi_{ref}} & \boldsymbol{B}_{b_{w_{ref}}}\end{bmatrix} \tag{5.3.153}$$

The output of the roll angle controller is given as

$$y_\phi = \boldsymbol{C}_\phi \mathbf{x}_\phi \tag{5.3.154}$$

where

$$\boldsymbol{C}_\phi = \begin{bmatrix}\mathbf{0}_{1\times 7} & 1 & \mathbf{0}_{1\times 7}\end{bmatrix} \tag{5.3.155}$$

The closed-loop transfer function from ϕ_{ref} to ϕ can now be obtained.

$$G_{\phi_{cl}}(s) = \frac{\phi}{\phi_{ref}} = \boldsymbol{C}_\phi (s\mathbf{I}_{15} - \mathbf{A}_\phi)^{-1} \boldsymbol{B}_{\phi_{ref}} \tag{5.3.156}$$

5.3.7.3 Robustness to Wing Tip Loss

Figure 5.31 shows the robustness of the roll angle controller on the full linear aircraft model. From the unit step response, one will note that the roll angle controller remains robust against partial wing loss, but the steady state error increases. As mentioned, the angle error made by the roll angle controller will be corrected by the guidance controller, therefore the increase in roll angle error is not a major concern.

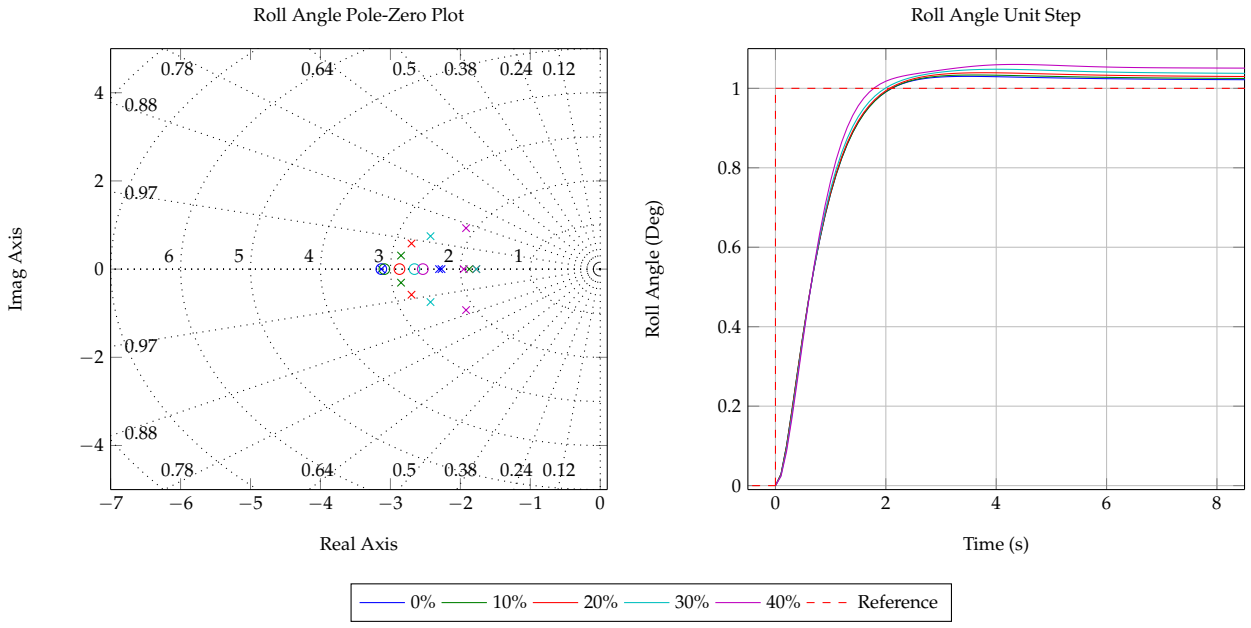

Figure 5.31: Roll angle unit step response and pole-zero plot for wing loss

5.3.8 Guidance Controller

This section describes the design and robustness of the guidance controller. The guidance controller's task is to guide the aircraft to follow a series of straight-line segments which connect predefined waypoints. The waypoints are described by north and east coordinates in the inertial reference frame.

Consider two waypoints, as seen in Figure 5.32; the source waypoint denoted with subscript "src" and the destination waypoint denoted with subscript "dst". The purpose of the guidance controller is to guide the aircraft onto the ground track, which has a length

$$L_{track} = \sqrt{(N_{dst} - N_{src})^2 + (E_{dst} - E_{src})^2} \tag{5.3.157}$$

that connects the source and the destination waypoints. This is achieved by controlling the cross track position error y, which is the perpendicular length from the aircraft to the ground track, to zero. The in-track position x, which is the distance of the aircraft's projection onto the ground

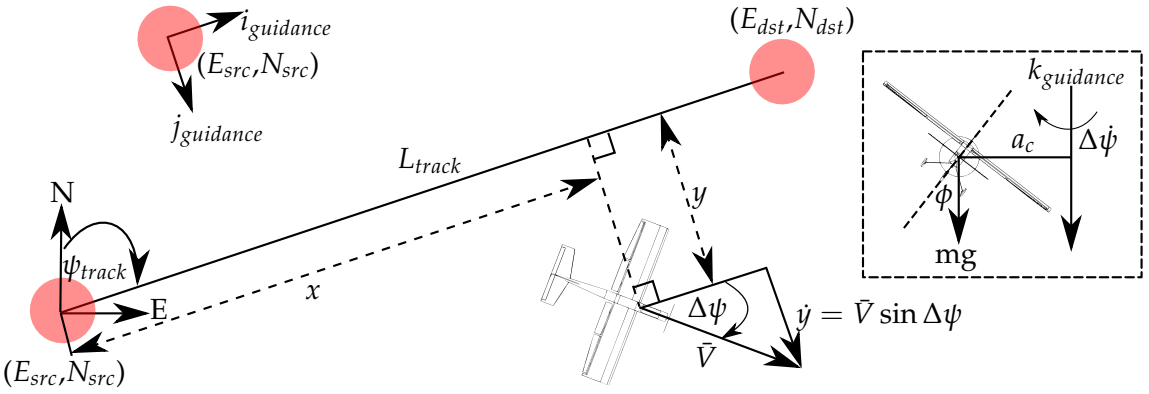

Figure 5.32: Guidance reference frame

track from the source waypoint, is used to determine how far the aircraft has travelled or must still travel before completing the current waypoint leg.

To obtain the cross track position error and the in-track distance given inertial reference frame positions, another reference frame is defined. This reference frame, called the guidance reference frame, has its origin at the source waypoint with its x-axis ($i_{guidance}$) parallel to the ground track and its y-axis ($j_{guidance}$) perpendicular to the ground track. The aircraft's NED position is transformed to the guidance reference frame with a rotation matrix given as

$$\mathbf{R}_{\psi_{track}} = \begin{bmatrix} \cos\psi_{track} & \sin\psi_{track} \\ -sin\psi_{track} & \cos\psi_{track} \end{bmatrix} \tag{5.3.158}$$

$$\begin{bmatrix} x \\ y \end{bmatrix} = \mathbf{R}_{\psi_{track}} \begin{bmatrix} N - N_{src} \\ E - E_{src} \end{bmatrix} \tag{5.3.159}$$

where ψ_{track} is the ground track heading relative to north, which from Figure 5.32 is given as

$$\psi_{track} = \tan\left(\frac{E_{dst} - E_{src}}{N_{dst} - N_{src}}\right)^{-1} \tag{5.3.160}$$

5.3.8.1 Design

The cross track position error of the aircraft is related to the lateral states by adding a cross track position error state to the full linear aircraft dynamics. From Figure 5.32, the cross track position error rate is given as

$$\dot{y} = \bar{V}\sin\Delta\psi = \bar{V}\Delta\psi \tag{5.3.161}$$

where $\bar{V}$ is the ground speed and $\Delta\psi$ is the aircraft heading relative to the guidance reference frame. Furthermore, the aircraft's centripetal acceleration is expressed as

$$a_c = \bar{V}\Delta\dot{\psi} = g\tan\phi \tag{5.3.162}$$

resulting in a heading rate of

$$\Delta\dot{\psi} = \frac{g\phi}{\bar{V}} \tag{5.3.163}$$

By differentiating (5.3.161) and then substituting (5.3.163), and by assuming small angles, the cross track position acceleration is obtained.

$$\ddot{y} = g\phi \tag{5.3.164}$$

The cross track error acceleration can therefore be expressed in terms of the roll angle of the aircraft. The cross track position error state (5.3.164) is added to the full linear aircraft dynamics.

$$\begin{bmatrix} \dot{\mathbf{x}}_\phi \\ \dot{y} \\ \ddot{y} \end{bmatrix} = \begin{bmatrix} \mathbf{A}_\phi & \mathbf{0}_{15\times1} & \mathbf{0}_{15\times1} \\ \mathbf{0}_{1\times15} & 0 & 1 \\ g\boldsymbol{C}_\phi & 0 & 0 \end{bmatrix} \begin{bmatrix} \mathbf{x}_\phi \\ y \\ \dot{y} \end{bmatrix} + \begin{bmatrix} \boldsymbol{B}_{h_{ref}} & \boldsymbol{B}_{\bar{v}_{ref}} & \boldsymbol{B}_{\phi_{ref}} & \boldsymbol{B}_{b_{w_{ref}}} \\ 0 & 0 & 0 & 0 \\ 0 & 0 & 0 & 0 \end{bmatrix} \begin{bmatrix} h_{ref} \\ \bar{v}_{ref} \\ \phi_{ref} \\ b_{w_{ref}} \end{bmatrix} \tag{5.3.165}$$

Figure 5.33 shows the feedback control system in block diagram form, where the open-loop cross

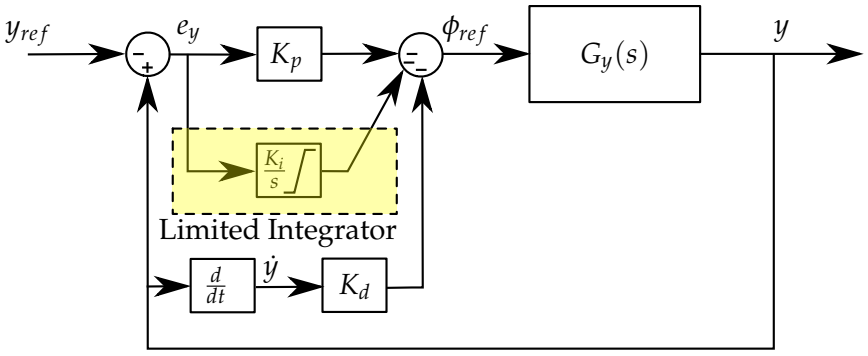

Figure 5.33: Guidance controller block diagram

track position error transfer function is

$$G_y(s) = \begin{bmatrix} \mathbf{0}_{1\times 15} & 1 & 0 \end{bmatrix} \left[s\mathbf{I}_{17} - \begin{bmatrix} \mathbf{A}_\phi & \mathbf{0}_{15\times 1} & \mathbf{0}_{15\times 1} \\ \mathbf{0}_{1\times 15} & 0 & 1 \\ g\boldsymbol{C}_\phi & 0 & 0 \end{bmatrix} \right]^{-1} \begin{bmatrix} \boldsymbol{B}_{\phi_{ref}} \\ 0 \\ 0 \end{bmatrix} \tag{5.3.166}$$

A proportional derivative (PD) control law is defined that generates a roll angle ϕ_{ref} proportional to the weighted sum of the altitude error and the time derivative of the cross track position error,

$$\phi_{ref} = -K_p e_y - K_d \dot{y} \tag{5.3.167}$$

where the error is defined as

$$e_y = y - y_{ref} \tag{5.3.168}$$

The root locus design technique is used to determine the controller gains K_p and K_d. Figure 5.34 shows the root locus design and the closed-loop unit step response of the guidance controller. The

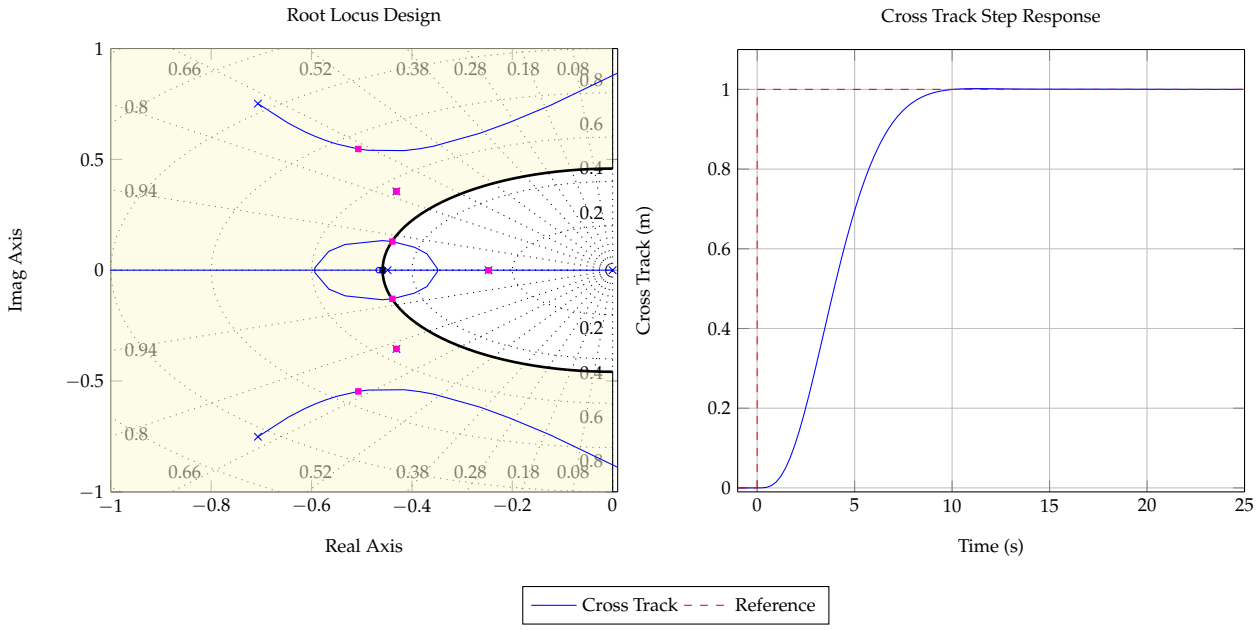

Figure 5.34: Cross track unit step response and root locus design

guidance controller is designed to be timescale-separated from the roll angle controller dynamics

to ensure that the guidance controller is not affected by changes to these dynamics. This will also ensure that the roll angle dynamics do not change drastically. Note from Figure 5.33 that a limited integrator term is introduced into the controller. The integrator will ensure that the guidance controller can track the ground track with zero steady state error, even if a roll angle sensor bias is present. This bias could be a mounting or measurement bias. The limits of the integrator are chosen such that they coincide with the maximum expected roll angle bias. The integrator gain K_i is iteratively obtained. The guidance controller will guide the aircraft onto the ground track from a source waypoint to a destination waypoint. Once the destination waypoint is reached, it becomes the new source waypoint and a new destination waypoint is supplied. The navigation of the aircraft is discussed in more detail in Chapter 6. The guidance controller dynamics is added to, and verified on the full linear dynamics of the aircraft.

5.3.8.2 Closed-Loop System

The guidance controller dynamics is now verified on the full linear dynamics of the aircraft. Equation (5.3.170) states the full linear aircraft dynamics with the roll angle and longitudinal controller dynamics included. First, the cross track position error dynamics given in (5.3.164) is added, and then the control law (5.3.167) is added.

$$\begin{bmatrix} \dot{\mathbf{x}}_\phi \\ \dot{y} \\ \ddot{y} \end{bmatrix} = \left[\begin{bmatrix} \mathbf{A}_\phi & \mathbf{0}_{15\times 1} & \mathbf{0}_{15\times 1} \\ \mathbf{0}_{1\times 15} & 0 & 1 \\ g\boldsymbol{C}_\phi & 0 & 0 \end{bmatrix} + \begin{bmatrix} \boldsymbol{B}_{\phi_{ref}} \\ 0 \\ 0 \end{bmatrix} \begin{bmatrix} \mathbf{0}_{15\times 1} & -K_p & -K_d \end{bmatrix} \right] \begin{bmatrix} \mathbf{x}_\phi \\ y \\ \dot{y} \end{bmatrix} + \begin{bmatrix} \boldsymbol{B}_{h_{ref}} & \boldsymbol{B}_{\bar{v}_{ref}} & \boldsymbol{B}_{\phi_{ref}} K_p & \boldsymbol{B}_{b_{w_{ref}}} \\ 0 & 0 & 0 & 0 \\ 0 & 0 & 0 & 0 \end{bmatrix} \begin{bmatrix} h_{ref} \\ \bar{v}_{ref} \\ y_{ref} \\ b_{w_{ref}} \end{bmatrix} \tag{5.3.169}$$

The closed-loop state space model now has a subscript y, indicating that the guidance controller has been added. Note that the input vector has changed. The cross track position error reference is now an input to the system.

$$\dot{\mathbf{x}}_y = \mathbf{A}_y \mathbf{x}_y + \mathbf{B}_y \mathbf{u} \tag{5.3.170}$$

Now define

$$\mathbf{B}_y = \begin{bmatrix} \boldsymbol{B}_{h_{ref}} & \boldsymbol{B}_{\bar{v}_{ref}} & \boldsymbol{B}_{y_{ref}} & \boldsymbol{B}_{b_{w_{ref}}} \end{bmatrix} \tag{5.3.171}$$

The output of the guidance controller is given as

$$y_y = \boldsymbol{C}_y \mathbf{x}_y \tag{5.3.172}$$

where

$$\boldsymbol{C}_y = \begin{bmatrix} \mathbf{0}_{1\times 15} & 1 & 0 \end{bmatrix} \tag{5.3.173}$$

The closed-loop transfer function from y_{ref} to y can now be obtained.

$$G_{y_{cl}}(s) = \frac{y}{y_{ref}} = \boldsymbol{C}_y (s\mathbf{I}_{17} - \mathbf{A}_y)^{-1} \boldsymbol{B}_{y_{ref}} \tag{5.3.174}$$

5.3.8.3 Robustness to Wing Tip Loss

Figure 5.31 shows the robustness of the guidance controller on the full linear aircraft model. Note that the dominant poles remain mostly unchanged as the aircraft suffers partial wing loss. The roll rate and roll angle controllers have captured most of the uncertainties, resulting in a very robust outer-loop controller. The guidance controller has achieved the level of robustness required and will be able to control both the undamaged and damaged aircraft with good performance.

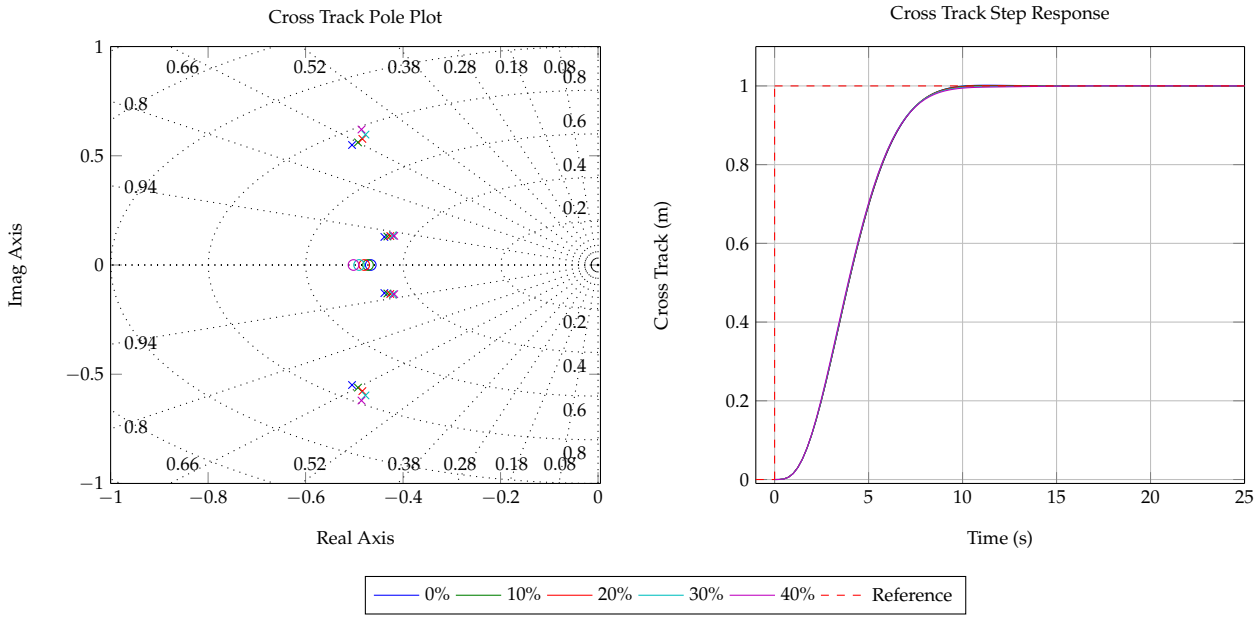

Figure 5.35: Cross track unit step response and pole-zero plot for wing loss

5.4 Summary

In this chapter, a passive fault-tolerant flight control system capable of controlling an aircraft with partial wing loss, partial horizontal stabiliser loss, and partial vertical stabiliser loss was developed. A design strategy was adopted whereby the inner-loop controllers were designed to be robust to partial wing loss and stabiliser losses. A successive loop closure control structure was used to design the required outer-loop controllers. This allows the outer-loop controllers to benefit from the robustness of the inner-loop controllers, enabling the outer-loop controllers to also remain stable throughout all the tip loss cases. The design approach is to find controller gains that provide the best performance for the undamaged aircraft while still providing at least the minimum acceptable performance over all the tip loss cases. The flight control system was developed for autonomous landings, which is why controller limitations and sensor biases were taken into account during the design phases.

The longitudinal controllers achieved good performance while being robust to partial horizontal stabiliser loss of up to 70% semi-span. The lateral controllers achieved good performance while being robust to partial wing loss of up to 40% semi-span. However, due to control surface deflection limitations, straight and level flight equilibrium only exists for partial wing loss of up to 20% semi-span. The directional controllers achieved good performance while being robust to

partial vertical stabiliser loss of up to 20% span. The performance of the flight control system can be relaxed if more robustness is desired. The flight control system developed in this chapter can now be verified and validated in a simulation environment and with practical flight tests.

A fully autonomous UAV is capable of performing autonomous take-off, navigation and landings, which all form part of typical aircraft operation phases or tasks. Of all these tasks, landing the aircraft is the most difficult. Landing typically entails aligning the aircraft with the runway, reducing the aircraft's airspeed (while still keeping the airspeed well above the stall speed) and following a glide path at a certain sink rate until touchdown. The aircraft will then perform a ground roll until rest.

In this chapter, a navigation strategy to align the aircraft with the runway effectively and elegantly is discussed. Practical and aircraft-dependent constraints that directly influence the autonomous landing procedures are discussed before developing the landing strategies and state machine that are required to perform autonomous landings for a fixed-wing unmanned aircraft that has suffered partial wing loss and stabiliser losses.

6.1 Autonomous Navigation Strategy

In this section, the navigation strategy used to autonomously navigate the aircraft and to prepare it for an autonomous landing is discussed. A waypoint scheduler is used to supply the altitude, guidance, and airspeed controllers with the appropriate reference commands in order to make the aircraft follow a predetermined flight trajectory. Circular turns are introduced to help the aircraft to turn and align itself with the runway more effectively and elegantly. Circular turns eliminate excessive or aggressive roll angles and allows the aircraft to align itself with the runway more quickly.

The aircraft navigates between four waypoints that are arranged in a rectangular configuration. As can be seen in Figure 6.1, the runway leg (waypoint 4 to waypoint 1) and the down leg (waypoint 2 to waypoint 3) are of equal length and are longer than the distances between waypoints 1 and 2 and waypoints 3 and 4. Circular turns are performed to travel between waypoints 1 and 2 and waypoint 3 and 4. Aligning the aircraft with the runway is very important for accurate autonomous landings. The circular turns are based on a turn radius concept. The aircraft performs coordinated turns, which have a number of favourable features such as no net lateral acceleration, which means no skidding or slipping, and the fact that the aircraft can maintain a constant turn radius for circular turns. From Figure 6.1, the horizontal component of lift F_h provides the centripetal force and is given by

$$F_h = mg \tan \phi \tag{6.1.1}$$

The centripetal force can also be expressed through the centripetal acceleration.

$$F_c = ma_c = m\frac{V_g^2}{r} \tag{6.1.2}$$

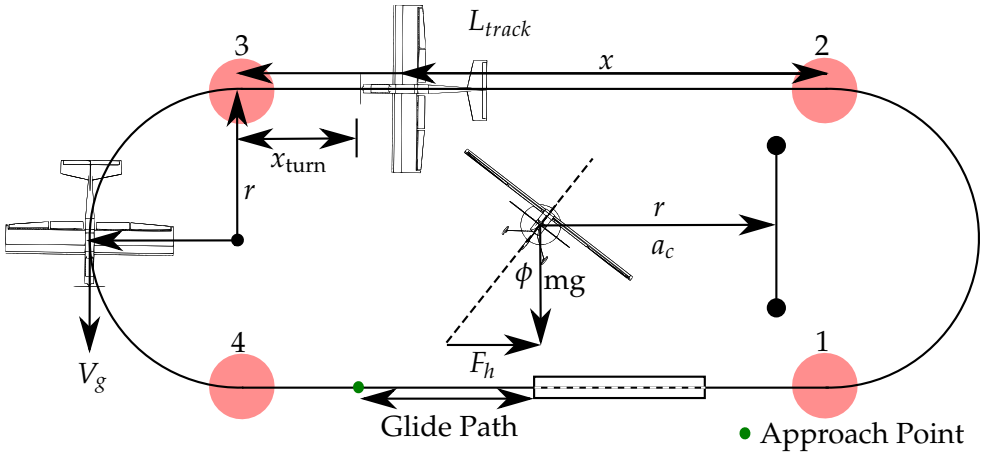

Figure 6.1: Autonomous navigation strategy

where F_c is the centripetal force, a_c is the centripetal acceleration, r the turn radius and V_g is the aircraft's ground speed. Note that the turn radius is half the ground track length of the two waypoints. From (6.1.1) and (6.1.2), the roll angle at which the aircraft is required to bank in order to have the given turn radius is

$$\phi_{\text{turn}} = \tan^{-1}\left(\frac{V_g^2}{gr}\right) \tag{6.1.3}$$

If the aircraft could change its roll angle instantaneously to the calculated roll angle value, it would navigate a perfect circular turn from one waypoint to another. However, this is not practically achievable due to controller bandwidth limitations and steady state errors. Firstly, the roll angle controller exhibits a transient response with a time constant τ_ϕ to reach its final value. Secondly, the roll angle controller tracks a step reference with a finite steady state error, as discussed in Chapter 5. To account for the aforementioned controller limitations, the aircraft is required to turn a distance

$$x_{\text{turn}} = V_g \tau_\phi \tag{6.1.4}$$

before the destination waypoint at a roll angle of

$$\phi_{ref} = \frac{\phi_{\text{turn}}}{1 + e_{ss}} \tag{6.1.5}$$

where e_{ss} is the steady state error of the roll angle controller for a unit step. The aircraft should therefore schedule the new waypoints a short distance before reaching the current destination waypoint, in other words when

$$x + x_{\text{turn}} \geq L_{\text{track}} \tag{6.1.6}$$

The navigation strategy adopted above enables the aircraft to avoid excessive roll angles and to align itself with the runway more quickly than achievable with only the pure guidance controller. Figure 6.2 shows the comparison between the navigation strategy adopted and navigating using the guidance controller without any additions. It is clear that by performing circular turns, a more elegant navigation path is achieved and that the aircraft aligns itself with the runway more quickly.

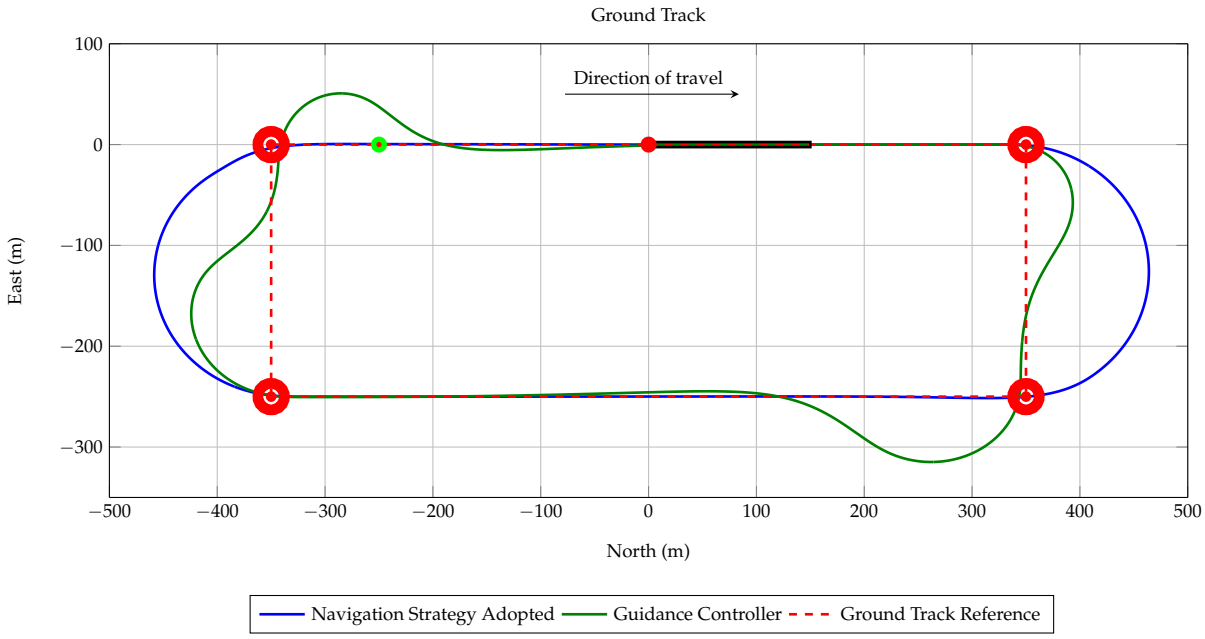

Figure 6.2: Autonomous navigation strategy comparison

6.2 Autonomous Landing Constraints

Landing typically entails aligning the aircraft with the runway, reducing the aircraft's airspeed (while still keeping the airspeed well above the stall speed) and following a glide path at a certain sink rate until touchdown. To accomplish a successful landing, a number of constraints must be considered. In this section, practical limitations and aircraft-dependent constraints that will influence the autonomous landing of the aircraft are investigated. The aircraft-dependent constraints are investigated for partial wing loss and stabiliser losses respectively to ensure that a valid landing strategy is adopted to autonomously land both the undamaged aircraft and the damaged aircraft with acceptable accuracies.

6.2.1 Aircraft Approach Speed Constraint and Sink Rate Constraint

Ideally, a low approach speed is desired. A low approach speed will result in a lower sink rate and a shorter ground run distance. The lowest maintainable airspeed is achieved when the aircraft is producing its maximum lift. Recall from Figure 3.10 that the aircraft produces its maximum lift when it is at critical angle of attack. Thereafter, as the angle of attack increases, the produced lift will decrease, causing the aircraft to stall. From (3.4.15)

$$C_{z_{\text{tot}}} = -C_{D_{\text{tot}}} \sin\left(\alpha_{\text{critical}}\right) - C_{L_{\text{tot}}} \cos\left(\alpha_{\text{critical}}\right) \tag{6.2.1}$$

From (3.4.16), the stall speed of the aircraft is given by

$$\bar{V}_{\text{Stall}} = \sqrt{\frac{2mg}{\rho S |C_{z_{\text{tot}}}|}} \tag{6.2.2}$$

For safety purposes, the approach speed is required to be a factor higher than the stall speed, and is taken to be [31]

$$\bar{V}_{TD} = 1.3\bar{V}_{\text{Stall}} \tag{6.2.3}$$

Figure 6.3 shows how the stall speed and minimum required landing approach speed change as a function of the percentage of wing loss and the percentage of stabiliser losses respectively. Note

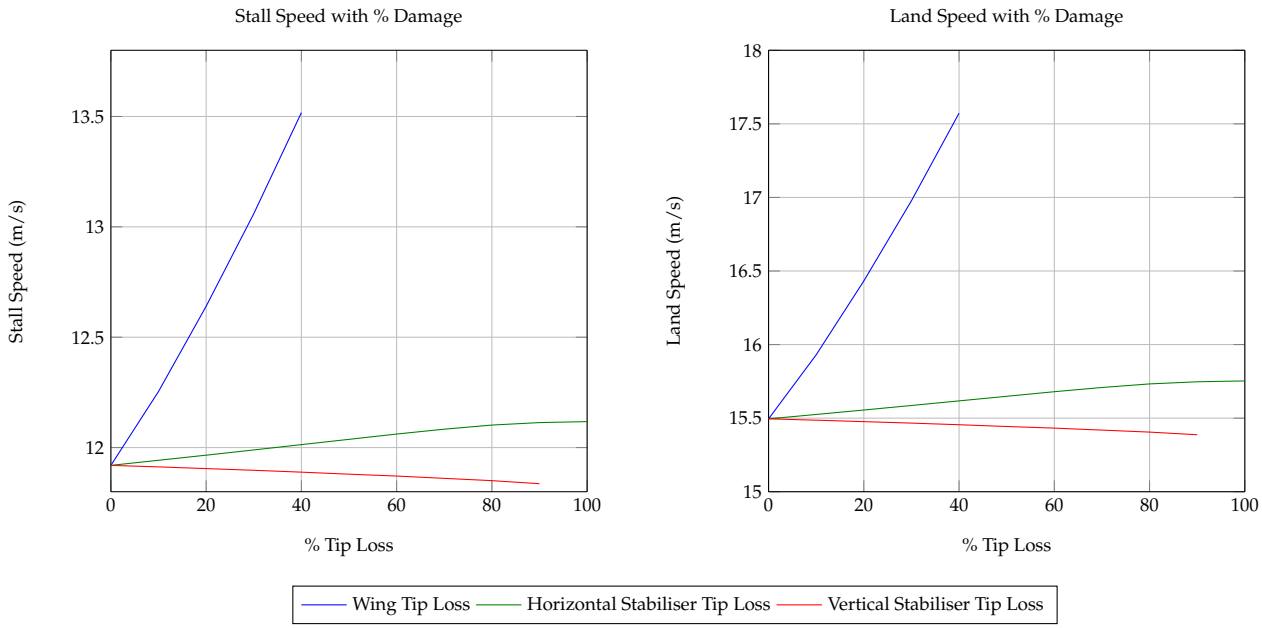

Figure 6.3: Calculated stall and minimum required approach speed based on 14° critical angle of attack

that the approach speed increases significantly with partial wing loss. It is clear that the aircraft will have to approach the touchdown point with a significantly higher airspeed if it has suffered partial wing loss. This is to avoid stalling before touchdown. A faster approach speed will lead to the aircraft touching down with a higher sink rate. The sink rate of the aircraft is a function of the aircraft's airspeed and glide slope angle γ at which the aircraft is approaching the touchdown point. A steeper glide slope angle will result in a larger sink rate and vice versa. A shallower glide slope angle is therefore preferred in order to achieve a softer landing. To determine if the landing gear of the aircraft can withstand the touchdown force given the sink rate at which the aircraft is approaching the touchdown point, a "drop test" is performed. Suppose that the aircraft is free-falling from a height h_0, then

$$\ddot{h} = -g \tag{6.2.4}$$

A height equation which describes the aircraft's height over time is obtained by taking the time integral of (6.2.4) twice, which yields

$$h = h_0 + \dot{h}_0 t - 0.5gt^2 \tag{6.2.5}$$

Before the aircraft is released to fall, its initial climb rate $\dot{h}_0$ is zero. The final height h, which is the height of the aircraft when it touches down on the ground, is also zero. By taking the time integral of (6.2.4) and noting that $\dot{h}_0 = 0$, one can obtain the rate of change in height.

$$\dot{h} = -gt \tag{6.2.6}$$

Substituting (6.2.6) into (6.2.5) leads to an equation that determines the equivalent height that the aircraft dropped (h_0) in a "drop test" for a given sink rate ($-\dot{h}$).

$$h_0 = \frac{(-\dot{h})^2}{2g} \tag{6.2.7}$$

Note that this is the height from the base of the wheels of the aircraft, and not its centre of mass. If the aircraft has a touchdown airspeed of 18 m/s at a glide slope angle of 4°, the aircraft will have a sink rate of 1.2556 m/s. If it has a sink rate of 1.2556 m/s, the equivalent height that the aircraft must be dropped in the "drop test" is 8 cm. Therefore, the aircraft was dropped from a height of 8 cm for the "drop test". The landing gear proved to be strong enough to absorb the landing force. This technique works well for small aircraft like the one used in this project, but might not be practical for larger aircraft.

6.2.2 Practical Limitations and Touchdown Accuracy

Before an landing strategy can be devised, some practical limitations must be considered. Firstly, because this is experimental work, the approach altitude of the aircraft should not be too low. If the safety pilot needs to recover the aircraft from an incident, sufficient height is usually required. Secondly, the aircraft must remain within line of sight, not only for the communication link but also for the safety pilot. Consider a set of four waypoints, as shown in Figure 5.32. If the ground station and the safety pilot are situated at the runway, waypoints 1 to 4 should be arranged such that the aircraft is never out of line of sight. This obviously limits the length that the glide slope can be. Third, the size of the runway must be considered. The guidance controller must be able to guide the aircraft onto the ground track within the boundaries of the runway width before touchdown, and the aircraft must come to rest before the runway ends. Taking these practical limitations into consideration, a glide slope length, approach height and glide slope angle can be determined that will result in an adequate autonomous landing.

The touchdown accuracy that can be expected depends on the flight control system bandwidths, as well as external disturbances. As mentioned above, the cross track accuracy depends on how fast the guidance controller can track the ground track and how well the ground track is regulated. The in-track accuracy depends on how fast the altitude controller can track the glide slope trajectory with zero steady state error, and how well the altitude controller can reject disturbances while on the glide slope. The in-track touchdown accuracy also degrades due to a phenomenon called ground effect. From about one wing span above the ground, the pressure below the wing increases, thereby increasing the lift produced by the aircraft. Furthermore, the lift vector rotates more vertically while maintaining the same angle of attack, causing a decrease in the induced drag. Essentially, ground effect makes the wing more efficient, since it improves the lift-to-drag ratio. In ground effect, the lift and induced drag coefficients are scaled with nonlinear altitude function gains $G_L(h)$ and $G_D(h)$, and become [31],

$$C_L = G_L(h)C_L \tag{6.2.8}$$

$$C_D = C_{D_0} + G_D(h)\left(\frac{C_L^2}{\pi A e}\right) \tag{6.2.9}$$

where $G_L(h) \geq 1$ and $G_D(h) \leq 1$ are given by [31]

$$G_L(h) = 1 + (0.00211 - 0.0003(A-3))e^{5.2(1-h/b)} \tag{6.2.10}$$

$$G_D(h) = 1.111 + 5.555\frac{h}{b} - \sqrt{29.8\left(\frac{h}{b} + 0.02\right)^2 + 0.817} \tag{6.2.11}$$

where h is the altitude of the aircraft, A is the aspect ratio of the wing and b the wing span. The gain G_D is valid for $h < 0.9b$, otherwise, G_D is just unity. Figure 6.4 shows how the gains G_L and G_D change as a function of altitude for altitudes between one wing span and ground level. The lift

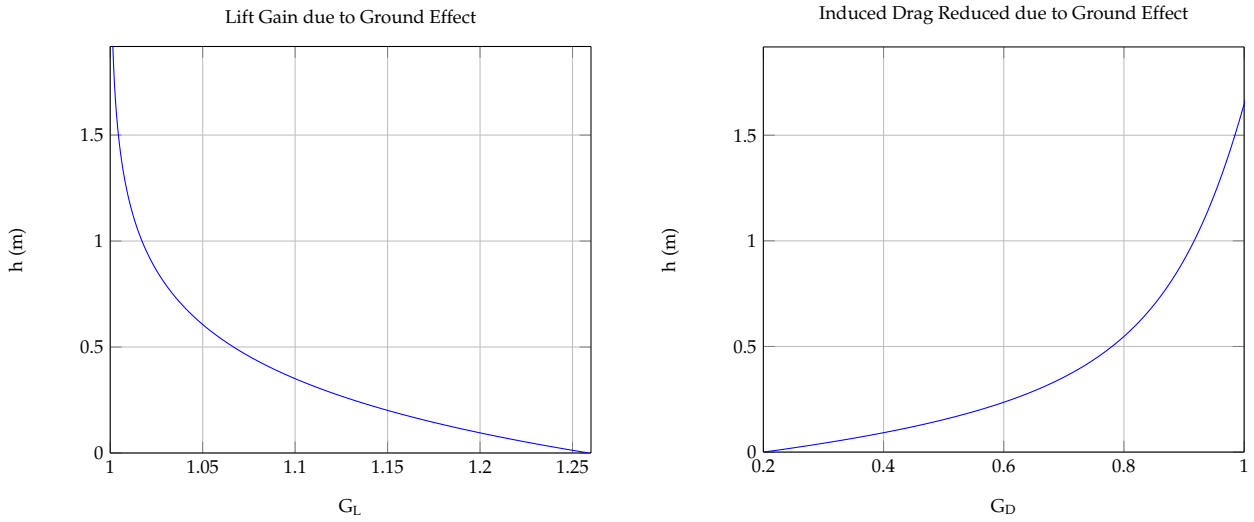

Figure 6.4: Lift and induced drag gains due to ground effect

starts to increase as the aircraft comes within one wing span from the ground, and increases up to 1.25 times when grounded. However, the induced drag decreases as the aircraft comes within one wing span from the ground, and upon touch down the induced drag is 20% lower than when out of ground effect.

Given these limitations, a practically achievable touchdown accuracy can be specified. In this project, a touchdown accuracy of within a 1.5 m circle is considered an accurate landing, and within the width of the runway (2.5 m) an adequately accurate landing.

6.3 Autonomous Landing Strategy

With all the constraints and limitations considered, landing strategies can be devised. In this section, landing strategies are proposed to autonomously land the aircraft that has suffered partial wing loss and stabiliser losses. Figure 6.5 shows the proposed glide phases that will guide the aircraft to perform an autonomous landing. A state machine guides the aircraft through a number of states to ensure that the aircraft navigates and touches down safely. The first state, called the navigation phase, is the default aircraft state. During the navigation phase, the aircraft will navigate a circuit (as described in section 6.1) at cruise speed with an altitude equal to the approach altitude H_{aa}. The second state, called the landing phase, is entered when the aircraft is commanded to land. In the landing phase, the aircraft will continue to navigate the circuit until it reaches the approach point. At the approach point the aircraft will enter a third state, called the long final phase. During this phase, the airspeed of the aircraft is reduced to the approach airspeed, and the

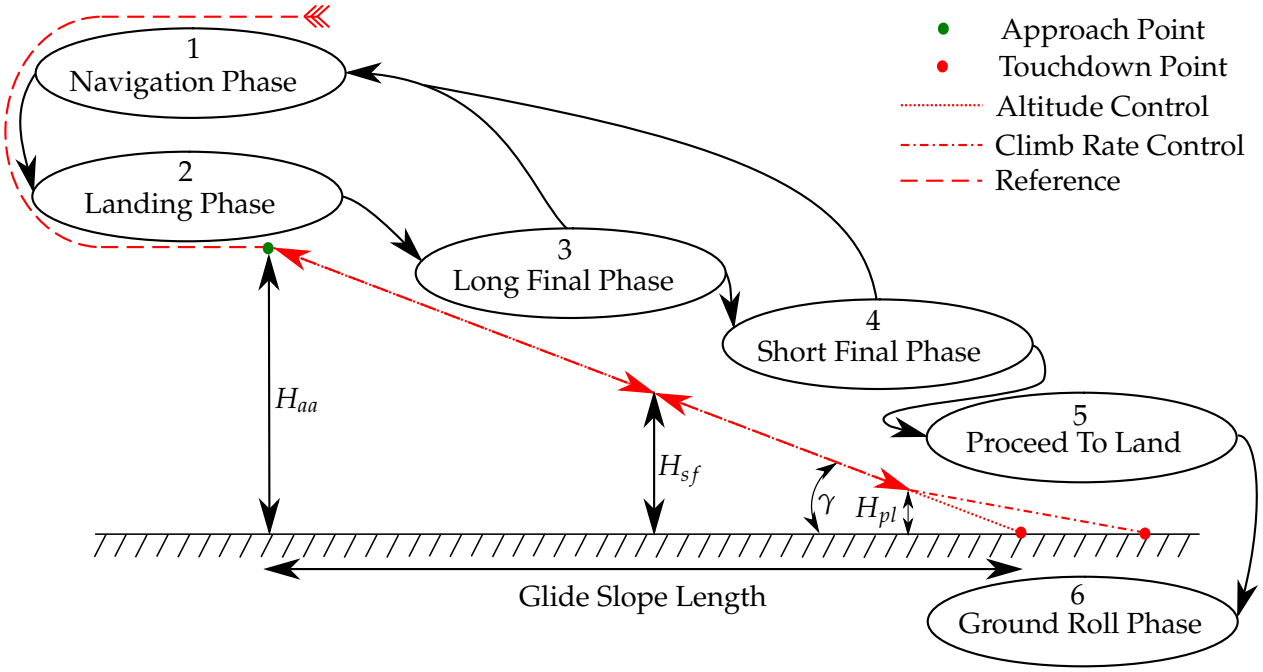

Figure 6.5: Landing glide path and approach strategy

altitude controller starts to track a glide slope reference, calculated with

$$h_{ref} = x \tan \gamma \tag{6.3.1}$$

where x is the in-track distance to the touchdown point, γ is the glide slope angle, and the touchdown point is situated at zero north and zero east. During the long final phase, the flight controllers have the same control authority as when in the navigation phase in order to rapidly reduce any altitude and cross track position errors. A fourth state, called the short final phase, is entered when the aircraft reaches an altitude H_{sf}, and the altitude and cross track position errors are within given bounds. Otherwise the aircraft will abandon the landing attempt and return to the default navigation phase. During the short final phase, the control authority is restricted. Restrictions are put on the maximum roll angle that can be commanded. This is done to prevent the aircraft from making any excessive manoeuvres close to the ground. A fifth state, called the "proceed to land" state, is entered when the aircraft reaches an altitude H_{pl}, and the altitude error and cross track error are within given bounds. Once the aircraft enters this state, it cannot abort and must proceed with the landing. The aircraft cannot change its direction of travel instantaneously, which means that aborting at a low altitude can lead to the aircraft connecting with the ground while trying to abort.

The aircraft will touch down using one of two methods. The first method is to continue regulating the altitude to track the glide slope. This method is followed when the sink rate that accompanies the approach airspeed is low enough to land safely without damaging the aircraft's landing gear. The touchdown sink rate is given by

$$-\dot{h} = \bar{V}_{TD} \sin \gamma \tag{6.3.2}$$

The first method achieves a more accurate landing, but with an approach airspeed and glide slope angle dependent sink rate. For the second method, the altitude controller is disabled and the

climb rate controller controls the aircraft's sink rate at a lower sink rate than the sink rate that was dependent on the approach airspeed and glide slope angle. Controller the sink rate and not the altitude allows one to choose the touchdown sink rate, and thereby implicitly to choose how hard the aircraft will land. This method may cause the aircraft to touchdown with an in-track error. The in-track touchdown error depends on the controlled sink rate. The in-track touchdown error is a function of the enabled altitude H_{pl} (the height where the altitude controller was deactivated and the climb rate controller was activated) and the desired sink rate:

$$\text{Touchdown in-track error} = \frac{H_{pl}}{\tan\left(\sin\left(\frac{-\dot{h}}{\bar{V}_{TD}}\right)\right)} - \frac{H_{pl}}{\tan\gamma} \tag{6.3.3}$$

The final state, called the ground roll phase, is entered when the aircraft touches down. Upon touchdown, the flight control system is disabled and runway controllers are enabled. The runway controllers are designed to push the nose of the aircraft down ($\theta = 0$), keep the roll angle zero, and guide the aircraft down the middle of the runway until it comes to rest. Although runway controllers were designed, they are beyond the scope of this project, and therefore the details of their design will not be presented in this thesis.

Considering all these constraints and limitations, and referring to Figure 6.5, the autonomous landing parameters given in Table 6.1 are proposed.

Table 6.1: Feasible autonomous landing parameters

Landing Parameter	Value	Unit
Glide Slope Length	250	m
Approach Altitude (H_{aa})	17.5	m
Glide Slope Angle (γ)	4	deg
Approach Speed ($\bar{V}_{TD}$)	18	m/s
Sink Rate	1.2556	m/s
H_{sf}	5	m
H_{pl}	2	m
Waypoint 1	(0,100)	(E,N) m
Waypoint 2	(-250,100)	(E,N) m
Waypoint 3	(-250,-350)	(E,N) m
Waypoint 4	(0,-350)	(E,N) m

Recall from Chapter 4 that the aircraft has two lateral-directional flight equilibrium trim configurations: the wings-level and the small bank angle configurations. The aircraft therefore also has two touchdown configurations. Figure 6.6 shows the top view and rear view of the aircraft before touchdown for both the wings-level and the small bank angle configurations. When trimmed for the wings-level configuration, the aircraft will touch down with a crabbed orientation. In a crabbed landing, the travel direction of the landing gear points in a different direction than that of the aircraft's travel direction. For small crab angles (typically when $|\psi_{runway} - \psi| < 5°$), this is not a problem [35]. The aircraft will experience a small lateral-directional deviation upon touchdown, at which point the runway controllers will minimise the error and move the aircraft towards the centre of the runway. Alternatively, a de-crab manoeuvre can be performed moments before

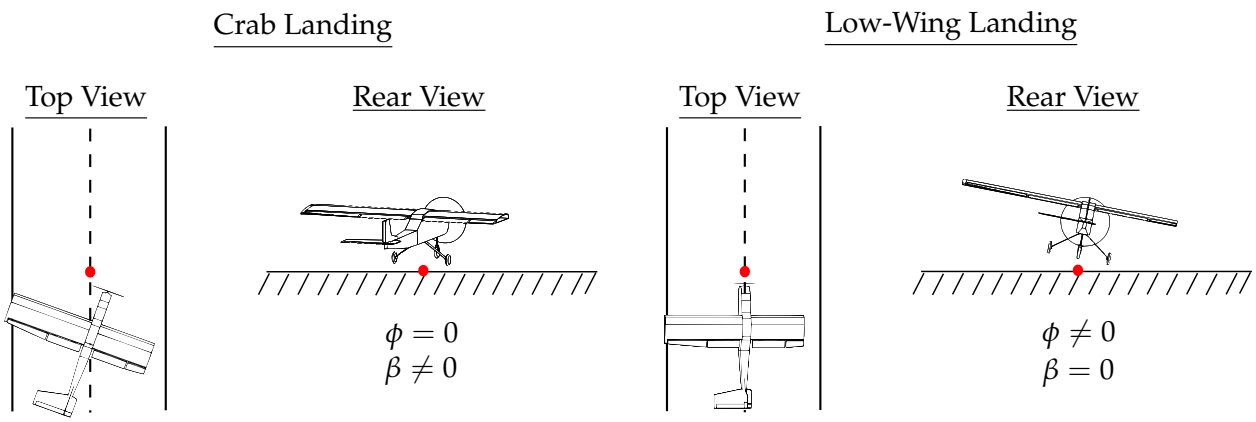

Figure 6.6: Landing configurations based on flight equilibriums

touchdown to align the aircraft heading with the runway heading. This was not deemed necessary for this project due to the small crab angles experienced by the aircraft when damaged, and was therefore not considered in this project.

When trimmed for the small bank angle configuration, the aircraft will touch down with a low-wing orientation. The aircraft will touch down with its heading aligned with the runway heading, but with a small bank angle, hence the name of the configuration. The main landing gear's wheel on the low wing side will touch down first, followed by the other main landing gear wheel. A low-wing landing will minimise the lateral-directional deviation upon touchdown, thereby requiring less effort from the runway controllers to keep the aircraft on the centre line. Due to the high wing configuration of this particular aircraft, the low-wing landing configuration is valid for roll angles up to $\pm 19.5^\circ$, as seen in Figure 6.7. For aircraft with a low wing configuration, the valid roll angles become significantly smaller. Another important aircraft state to consider during touchdown is the

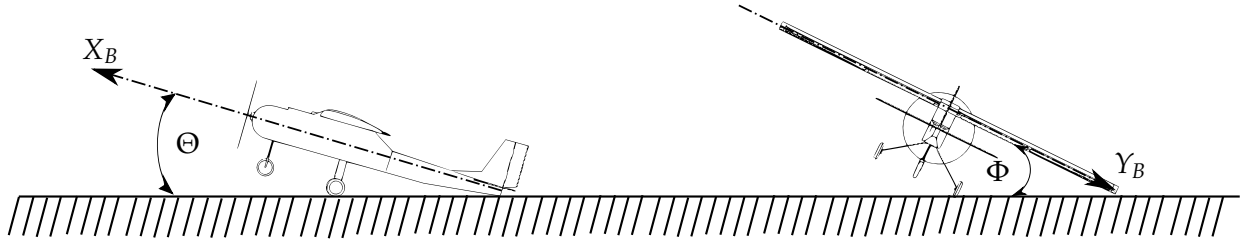

Figure 6.7: Pitch angle and roll angle limitations upon landing

pitch angle. Ideally, the aircraft should touch down on its main landing gear. The main landing gear is designed to absorb the impact upon touchdown. Therefore the pitch angle of the aircraft should be positive on touchdown. However, if the pitch angle upon touch down is too large, then the aircraft tail-plane will strike the ground. This limits the maximum allowable pitch angle on touchdown, as illustrated in Figure 6.7. The pitch angle limits are therefore chosen as,

$$0^\circ < \Theta < 12.5^\circ \tag{6.3.4}$$

6.4 Summary

In this chapter, the most suitable waypoint navigation and autonomous landing strategies required to achieve the research objectives were proposed. The navigation strategy is structured in such a way that the aircraft can optimally align itself with the runway with minimal cross track position error deviation to ensure an accurate landing. To accomplish an accurate landing, an open-loop roll angle control circular turns strategy was adopted. Performing circular turns allows the aircraft to align itself quickly with the runway without excessive roll angle manoeuvres.

Two landing strategies were proposed: a single glide slope crabbed landing, and a single glide slope crabbed landing with a complementary sink rate control before touchdown. The former will result in a more accurate landing, but with an approach airspeed and glide slope angle dependent sink rate, and the latter in a less accurate landing, but with an explicitly controlled sink rate. Both the navigation strategy and the landing strategies adhere to the limitations and constraints which were discussed in the chapter.

In this chapter, a high-fidelity nonlinear simulation environment which combines hardware and software is introduced and utilised to verify the performance and robustness of the flight control system designed in Chapter 5, as well as the autonomous navigation and landing discussed in Chapter 6. This is done to ensure the correct functionality of the system as a whole (hardware and software) before any flight tests are attempted.

First, a brief overview of the simulation environment and all the components involved is discussed. The simulation results are then presented. The linear approach for aircraft control system design that was used in Chapter 5 is validated by comparing the linear step responses to the nonlinear step responses obtained from the nonlinear simulation environment. Next, coupling between the longitudinal, lateral, and directional dynamics is investigated and the ability of the controller's to reject the coupling disturbances is verified. The autonomous landing of a fixed-wing aircraft with partial wing loss, partial horizontal stabiliser loss, and partial vertical stabiliser loss is simulated, and the functionality, performance, and robustness of the flight control system are verified.

7.1 Nonlinear Simulation Environment

A hardware-in-the-loop (HIL) simulation that connects the onboard computer running the flight software to a full nonlinear aircraft simulation running on a desktop computer, is used to verify the correct operation of the flight control system. A diagram of the hardware-in-the-loop simulation setup is shown in Figure 7.1. The nonlinear aircraft simulation running on the desktop computer mimics the behaviour of the actual aircraft and interfaces to the onboard computer via a HIL board. The HIL board receives the simulated sensor measurements from the desktop computer, packages it into the correct format, and sends it to the onboard computer. The flight control software running on the onboard computer processes the simulated sensor measurements and calculates the appropriate commands for the aircraft's control surfaces and throttle. The actuator commands are transmitted back to the HIL board which in turn transmits them back to the desktop computer to continue the simulation. Each component of the hardware-in-the-loop simulation illustrated in Figure 7.1 is discussed in more detail below.

7.1.1 Software Simulation

A nonlinear aircraft simulation running on the desktop computer mimics the behaviour of the actual aircraft. The nonlinear aircraft simulation includes the nonlinear equations of motion, nonlinear aircraft aerodynamics including ground effect, atmospheric or wind model, nonlinear ground

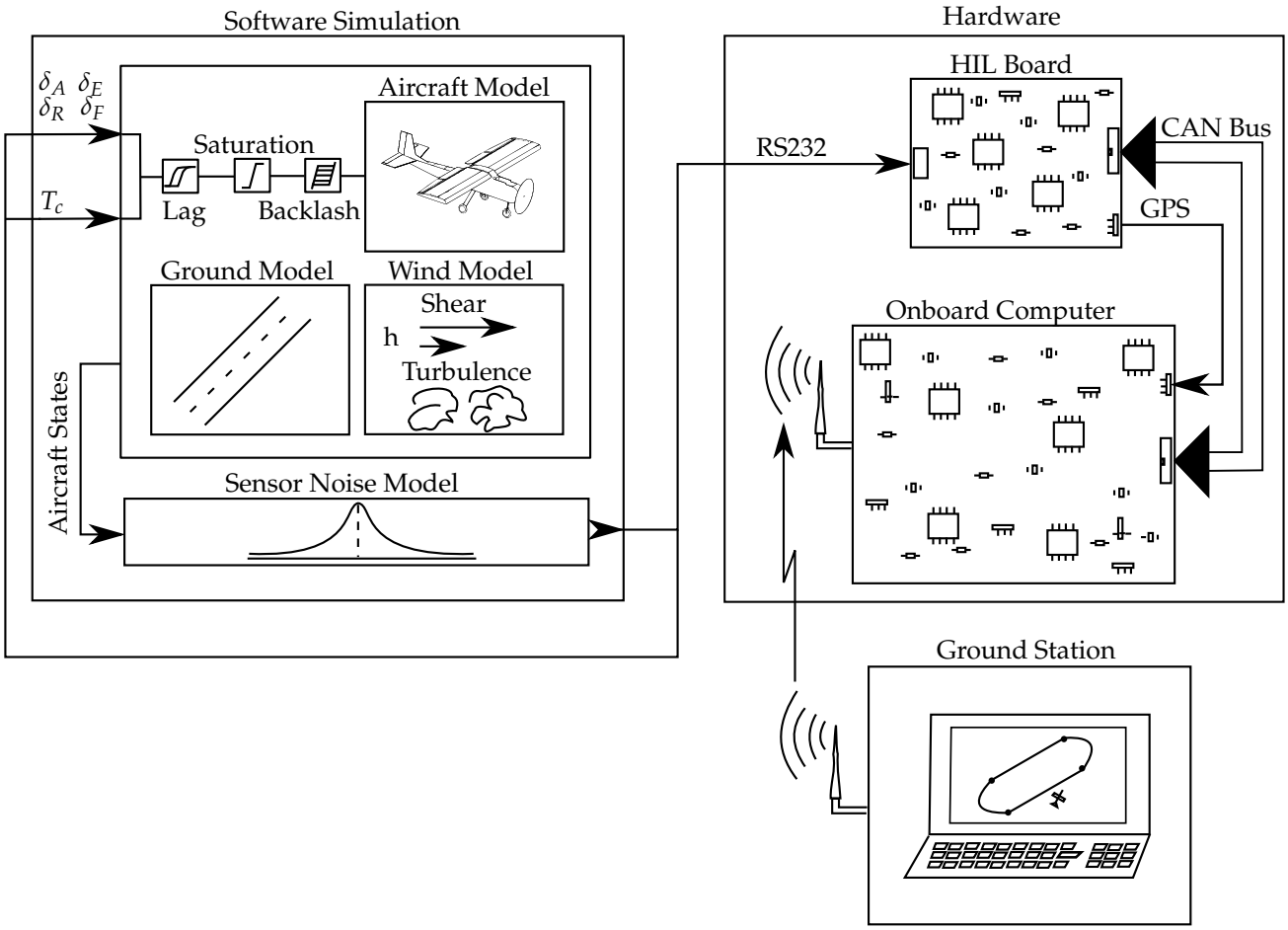

Figure 7.1: High-fidelity nonlinear simulation environment

or runway model, sensor noise model, and aircraft control surface non-linearities like saturation and actuator backlash.

The software simulation describes how the aircraft translates and rotates through inertial space given certain atmospheric condition and control inputs. The nonlinear equations of motion given by (3.2.28), the kinematic equations (3.3.11), and the position dynamics (3.3.13) developed in Chapter 3 are used to describe the translational and rotational motion of the aircraft in inertial space given the forces and moments acting on the aircraft. The forces and moments acting on the aircraft are modelled by (3.4.17), (3.4.26), and (3.4.28), which are the forces and moments due to aerodynamics, gravity and the engine of the aircraft respectively. Note that all of these equations are non-linear. The lag dynamics and saturation of the control surface actuators are also incorporated in the aircraft model. This ensures that more realistic control inputs are passed to the aircraft model. Backlash is also included in the actuator models to represent actuator and control surface rod backlash. Sensor measurements are simulated by adding the appropriate sensor noise to the aircraft states. Measurement delays are also included in the sensor models to represent the measurement update delays that are present in some sensors, such as the GPS sensor. The sensors that are modelled include the inertial measurement unit (IMU), the airspeed sensor, the magnetometer, and the GPS sensor. Based on the assumption that the DGPS sensor does not drift, GPS sensor drift is not included in the model and only GPS sensor measurement noise is added. The sensor noise is modelled as Gaussian noise, with a zero mean and a variance which is sensor dependent.

The variances of the sensors are obtained from the experimentally measured sensor data or from the data sheets of the specific sensors.

The software simulation also contains a full nonlinear runway or ground model. The ground model represents the interaction between the aircraft and the ground. The model assumes a tricycle undercarriage and was developed by Roos [3]. The ground model calculates forces and moments that are produced by the interaction between the undercarriage of the aircraft and the ground. The forces modelled include normal forces, cornering forces, and friction forces. Each of these forces acts on the aircraft's undercarriage at a distance from the centre of mass, thus each force produces a moment as well. All the ground model forces and moments are modelled with nonlinear equations. A detailed description and design of the ground model can be found in [3].

The software simulation also contains an atmospheric or wind model developed at Stellenbosch University. The wind model simulates wind gust, wind shear, turbulence, and static wind. All of these elements are modelled from the guidelines given by the U.S. Military Specifications MIL-F-8785C and MIL-HDBK-1797 [36],[37]. The wind model produces additional body velocities and angular rates that are experienced by the aircraft. The gust is modelled as a piecewise function with a "build-up" profile represented by an one minus cosine function, and a "fading-out" profile of an inverted one minus cosine function. Figure 7.2 illustrates the piecewise function for wind gust magnitude over the distance travelled by the aircraft starting at time t_s, where V_m is the

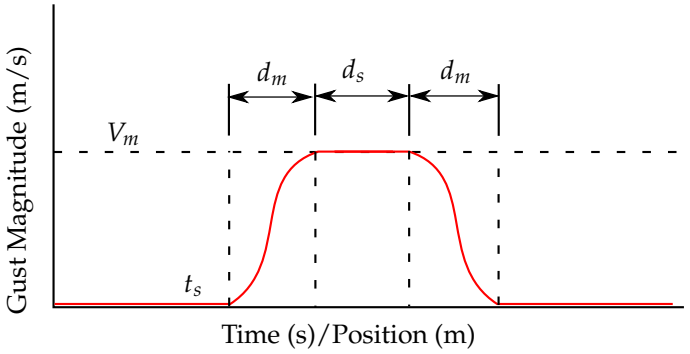

Figure 7.2: Piecewise gust magnitude function

gust's maximum amplitude, d_m is the gust's build/fade distance, and d_s is the distance for which the gust stays at its maximum strength before fading. The gust direction and elevation can also be specified in the model. Note that the gust magnitude is in the inertial reference frame and must be transformed to the aircraft body reference frame using the DCM. A detailed description and design of the gust model can be found in MIL-HDBK-1797 [37].

Turbulence is modelled as velocity and angular rate disturbances which are realised by passing band-limited white noise through forming filters to achieve either the Dryden or Von Kármán spectral forms. The U.S. Military Specifications MIL-F-8785C and MIL-HDBK-1797 describe turbulence as a stochastic process defined by velocity spectra [36],[37]. A detailed description of the turbulence model can be found in MIL-HDBK-1797 [37]. Wind shear is modelled as a change in wind magnitude experienced by the aircraft as a function of its altitude. Figure 7.3 illustrates the wind shear magnitude. The shear model is implemented as described by U.S. Military Specification MIL-F-8785C [36]. Note that the wind shear magnitude is in the inertial reference frame and

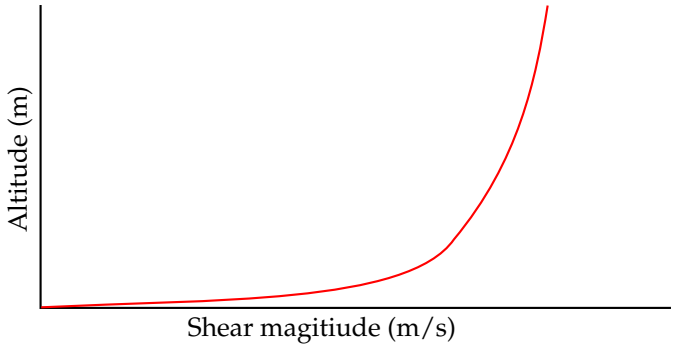

Figure 7.3: Shear magnitude as a function of altitude

must be transformed to the aircraft body reference frame using the DCM. A detailed description and design of the shear model can be found in MIL-F-8785C [36].

The software simulation is developed in a Matlab/Simulink environment which consists of a combination of Simulink block diagrams and s-functions. The high-fidelity software simulation provides a simulation platform with which the control systems, the aircraft autonomous navigation, and the autonomous landing can be simulated and verified to gain confidence in the system before performing a real flight test.

7.1.2 Hardware

Hardware is used in conjunction with the abovementioned software simulation to allow for a HIL environment. A HIL board acts as interface between the software simulation and the onboard computer. The HIL board receives all the simulated sensor measurements generated by the software simulation via the serial port of the desktop computer. The HIL board then processes the sensor measurements and packages them into the correct format for the onboard computer. All of the sensor measurements, except for the GPS measurements, are transmitted to the onboard computer via a CAN bus. The simulated GPS measurements are transmitted to the onboard computer via a serial port. Due to the physical design of the onboard computer, the simulated GPS sensor measurements are transferred from the HIL board to the onboard computer on a separate serial port than the other sensor measurements, as shown in Figure 7.1. When operating in HIL mode, the onboard computer ignores the CAN packets from the real sensors and the serial packets from the real GPS sensor and uses the simulated sensor values received from the HIL board.

The flight control system, which includes the control laws designed in Chapter 5 and the landing state machine designed in Chapter 6, is implemented in software with C code, and is executed on the onboard computer hardware. Both the HIL board and onboard computer were developed in-house and have been refined throughout the years to address the needs of the research projects at Stellenbosch University. The hardware-in-the-loop simulation environment described in this chapter is used to verify not only the flight control system design, but also the correct operation of the hardware and software that implements the flight control system. In the next section, the simulation environment is used to verify the performance of the flight control system for both the undamaged and damaged aircraft.

7.2 Simulation Results

In this section, the flight control system's performance and robustness are verified in the high-fidelity simulation environment described in the previous section. In Chapters 4 and 5, a linear approach to aircraft stability analysis and control design was adopted. The flight controllers are therefore designed to function at a specific flight equilibrium with small perturbations. If the perturbations become too large, the system will tend to behave more nonlinearly and the linear approximation of the aircraft dynamics may become less valid. Furthermore, a number of approximations were made to allow the decoupling between longitudinal, lateral, and directional dynamics in order to simplify the control design process. The coupling between the normal acceleration and the airspeed was ignored based on the argument that the airspeed controller will maintain the airspeed of the aircraft during climbs and dives if they are not aggressive. The nonlinear simulations performed in this section are used to check that the linearisation and decoupling approximations are valid.

The flight control system's performance is verified for both the undamaged aircraft and the damaged aircraft. The damage case used for the nonlinear simulations is an aircraft that has suffered 20% wing loss, 70% horizontal stabiliser loss, and 20% vertical stabiliser loss.

Firstly, simulations are performed to validate the linearisation and decoupling assumptions that were used in the control system design. Step responses are performed with the full coupled nonlinear simulation model and are then compared to the step responses of the linear decoupled models. The coupling effects between the longitudinal, lateral, and directional dynamics are also investigated. The nonlinear step responses are performed without sensor noise or wind disturbances so that they can be more clearly compared to the linear step responses. The control surface lag dynamics are also augmented into the linear models to yield more comparable results.

After verifying the step responses of the individual control laws, the full autonomous waypoint navigation and autonomous landing is simulated with sensor noise and wind disturbances included.

7.2.1 Airspeed Controller

Figure 7.4 shows the unit airspeed step responses for both the damaged and undamaged aircraft. Note that the linear responses has slightly higher overshoots than the nonlinear simulated responses. Factors that contribute to the slight differences are the unmodelled drag and the coupling between the climb rate and the airspeed of the aircraft.

The effect of the coupling between the aircraft's airspeed and normal acceleration on the airspeed control is investigated by observing the airspeed response when a normal specific acceleration step command is given. Although it was assumed that the airspeed controller keeps the airspeed constant during normal acceleration manoeuvres, this is not exactly true. A small increase or decrease in airspeed is observed when a normal acceleration command is given. In response to an increase in the normal specific acceleration command, the NSA controller increases the angle of attack to increase the lift. When the lift increases, the associated drag also increases. The increased lift also causes the flight path angle to increase, and as the flight path angle increases, the component of gravity that opposes the aircraft velocity also increase. The result is that the airspeed of the aircraft decreases due to a combination of increased drag and an increased component of gravity

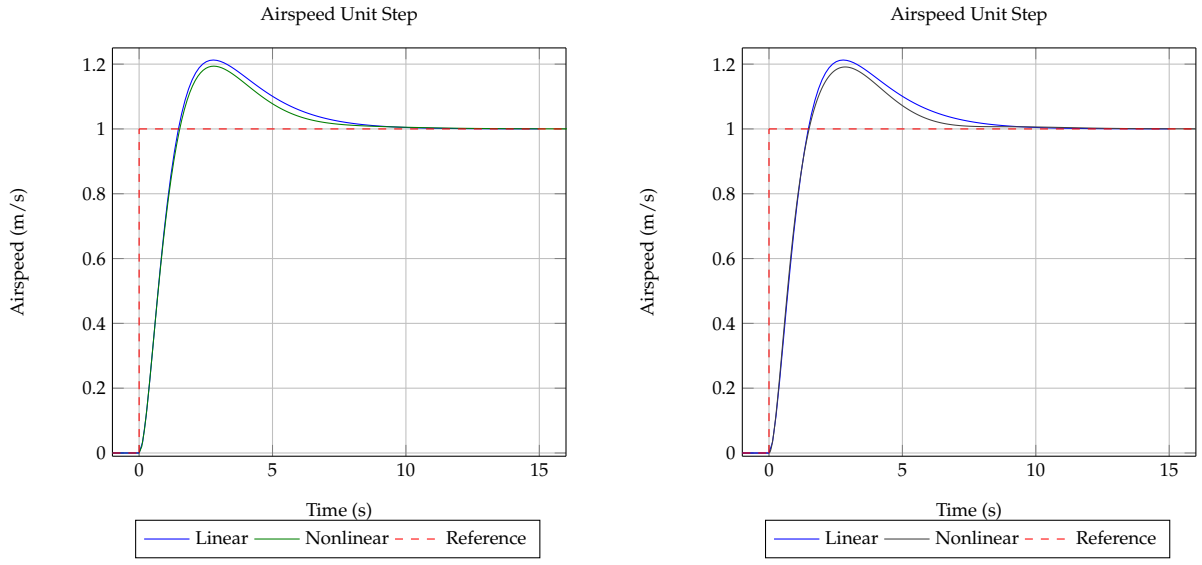

(a) Undamaged aircraft. (b) Damaged aircraft.

Figure 7.4: Linear vs nonlinear unit step airspeed responses

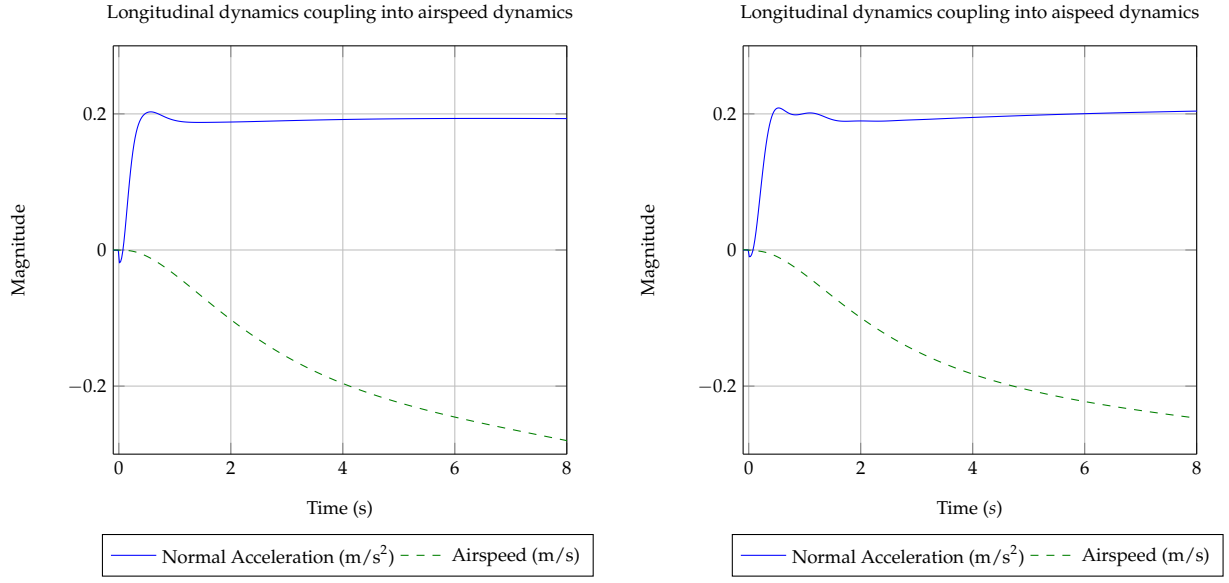

(a) Undamaged aircraft (b) Damaged aircraft

Figure 7.5: Decrease in airspeed while experiencing a constant normal acceleration

that opposes the airspeed. Following the same argument, a decrease in the normal specific acceleration causes an increase in the airspeed due to a combination of reduced drag and an increased component of gravity that accelerates the aircraft. The airspeed controller sees the disturbance but due to the relatively low bandwidth of the airspeed controller it is slow to reject the disturbance (see Figure 7.14). If the aircraft experiences a constant normal acceleration as seen in Figure 7.5, the airspeed of the aircraft decreases. This is clearly the case for both the undamaged and damaged aircraft. The reduced-order linear dynamics for normal acceleration given by (5.3.48) assumes a constant dynamic pressure and therefore a constant airspeed. All three dimensional derivatives in (5.3.48) will in reality change with airspeed.

7.2.2 Normal Specific Acceleration Controller

Figure 7.6 shows the normal acceleration unit step responses for both the undamaged and the damaged aircraft. The transient normal acceleration experienced by the aircraft is less due to the fact that the airspeed decreases during the response. The airspeed coupling was ignored in the design of the normal acceleration controller, resulting in the difference between the linear and nonlinear responses due to a lower dynamic pressure.

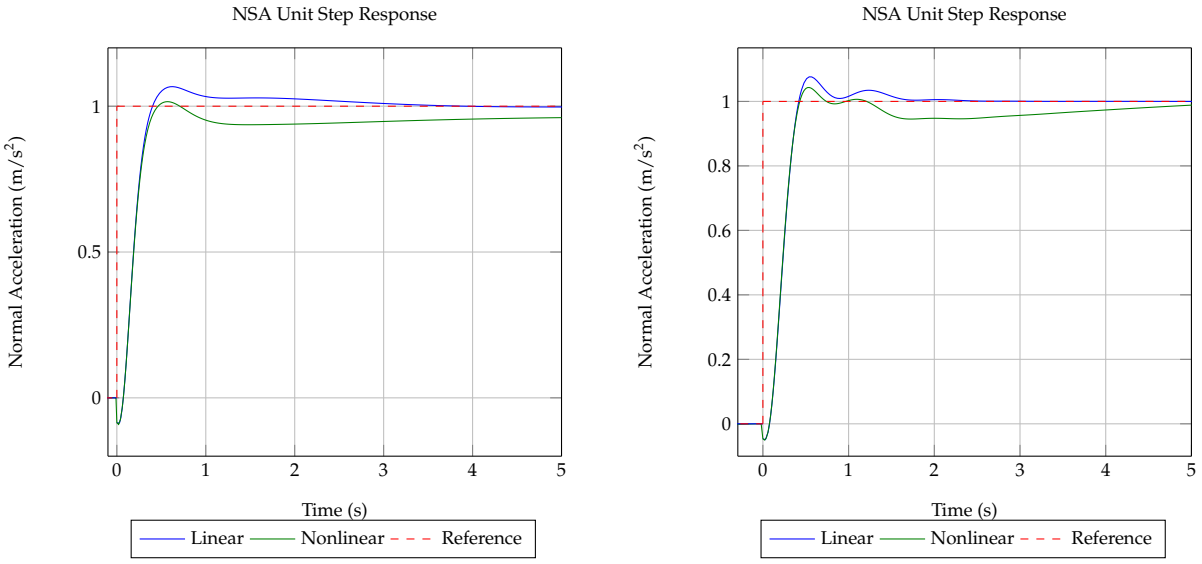

(a) Undamaged aircraft (b) Damaged aircraft

Figure 7.6: Linear vs nonlinear unit step NSA responses

From Figure 7.5 the airspeed continues to decrease when a constant normal acceleration is commanded, which results in the steady state error. Also note that the coupling does not get worse for the damaged aircraft. The airspeed coupling into the normal acceleration will affect all the longitudinal controllers that use the NSA controller as an inner-loop. Fortunately, the coupling does not compromise the robustness of the normal acceleration controller, as seen in Figure 7.6.

7.2.3 Climb Rate Controller

Figure 7.7 shows the unit climb rate step responses for both the undamaged and the damaged aircraft. More overshoot is observed in the nonlinear climb rate responses. Note that in both cases faster settling times are achieved. It is clear that the damage has almost no effect on the response of the climb rate controller.

7.2.4 Altitude Controller

Figure 7.8 shows the unit altitude step responses for both the undamaged and the damaged aircraft. Due to a more aggressive climb rate, the altitude response has a faster rise time. Note that the altitude responses for the undamaged and damaged aircraft are almost identical. It is clear that the damage has almost no effect on the response of the altitude controller.

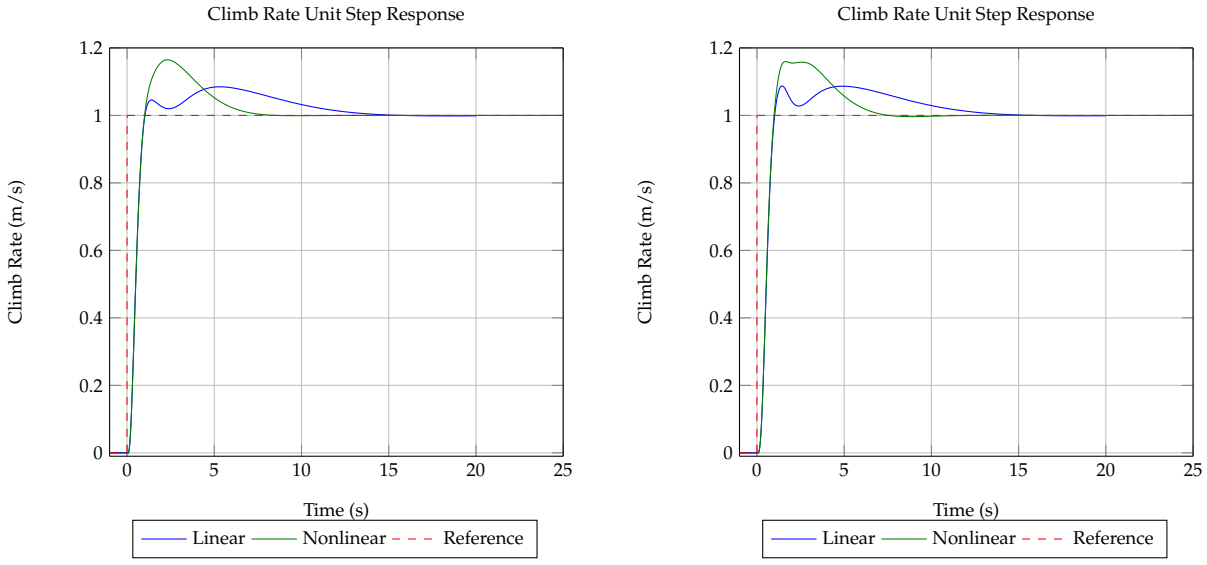

(a) Undamaged aircraft (b) Damaged aircraft

Figure 7.7: Linear vs nonlinear unit step climb rate responses

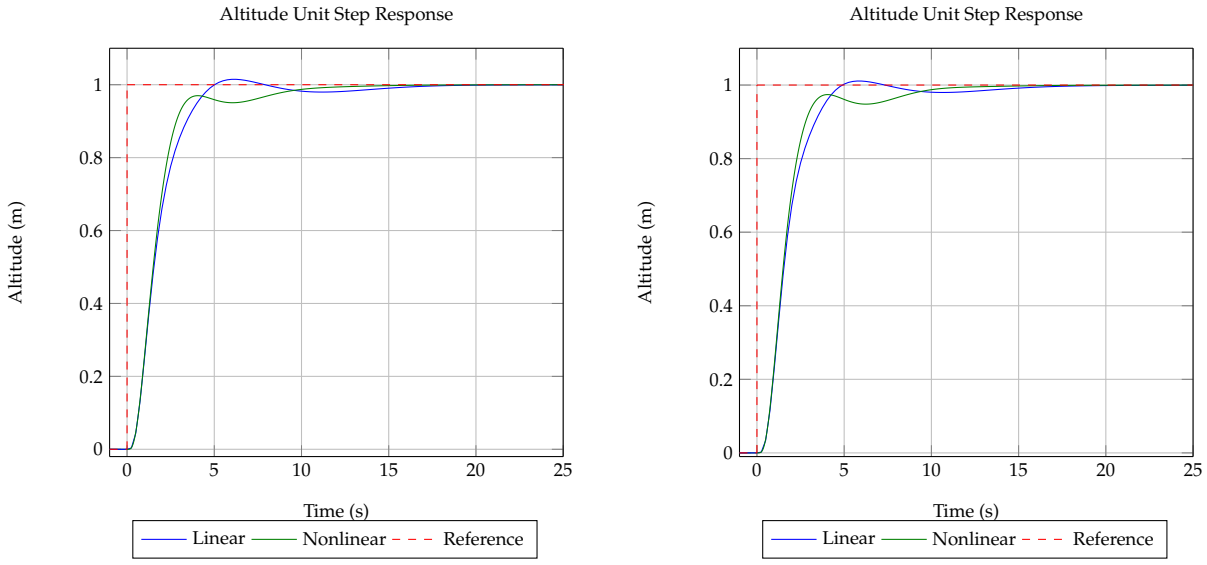

(a) Undamaged aircraft (b) Damaged aircraft

Figure 7.8: Linear vs nonlinear unit step altitude responses

The slight differences between the linear and the nonlinear responses of the longitudinal controllers can be ascribed to the fact that the coupling between the airspeed and the normal acceleration was not explicitly taken into account in the control design. Nevertheless the airspeed, NSA, climb rate and altitude controller's performances remain acceptable for an aircraft that has suffered 20% wing loss, 70% horizontal stabiliser loss, and 20% vertical stabiliser loss. Fortunately, the coupling does not compromise the robustness of the normal acceleration controller, and even less so the robustness of the middle and outer-loop controllers. The robustness is clearly seen in Figures 7.7 and 7.8.

7.2.5 Lateral Specific Acceleration Controller

Figure 7.9 illustrates lateral acceleration unit step responses for both the undamaged and damaged aircraft. The lateral and directional dynamics are not tightly coupled to airspeed perturbations. However, the coupling between the lateral and directional dynamics are observed. After decoupling the lateral and directional dynamics from one another, it was assumed that when commanding a lateral acceleration, the roll rate would stay constant and vice versa. This is not exactly true, especially not for the damaged aircraft where lateral and directional coupling are more significant. The effects of the coupling are less significant in the lateral acceleration dynamics due to the low bandwidth LSA regulation pole. The roll rate pole operates at a much higher bandwidth than the LSA regulation pole. The nonlinear lateral acceleration step response for the undamaged aircraft

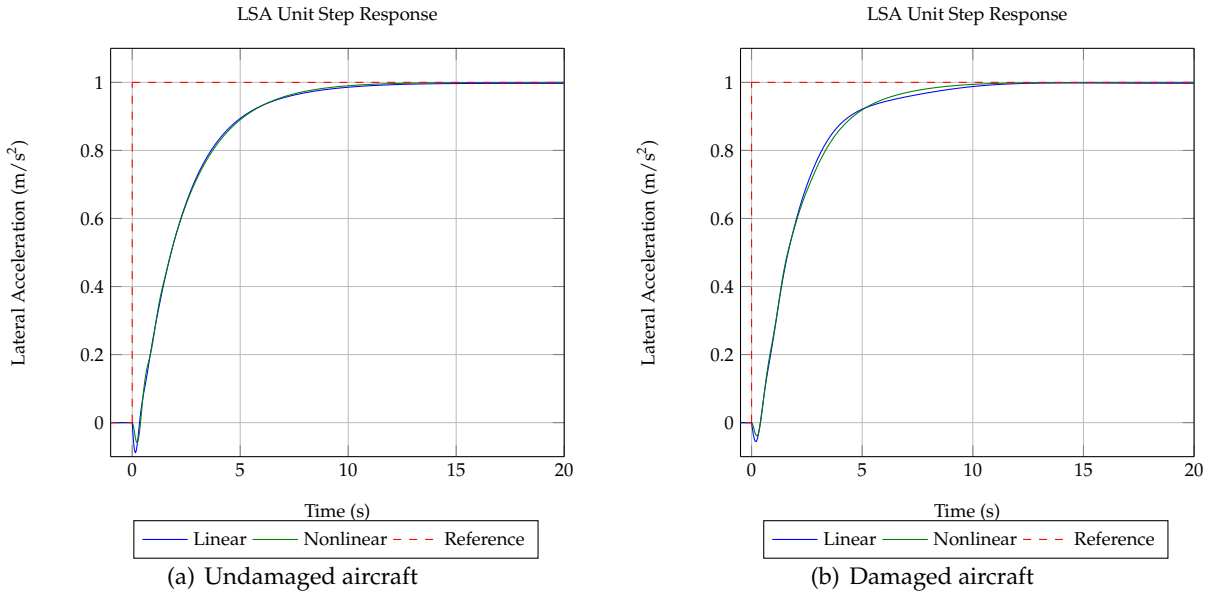

(a) Undamaged aircraft (b) Damaged aircraft

Figure 7.9: Linear vs nonlinear unit step LSA responses

corresponds well to the linear step response. However, the lateral coupling is clearly visible in the lateral acceleration step response for the damaged aircraft. This results in the nonlinear response having a slight deviation from the linear response, as seen in Figure 7.9 (b). It is clear that the damage has almost no effect on the response of the LSA controller.

7.2.6 Roll Rate Controller

Figure 7.10 shows the roll rate unit step responses for both the undamaged and damaged aircraft. The lateral-directional coupling is more visible in the roll rate dynamics. This is due to the higher bandwidth LSA stability augmentation (Dutch roll) poles, which operate at more similar bandwidths, coupling into the roll dynamics. The coupling is more significant for the damaged aircraft. Nonetheless, the nonlinear roll angle step responses corresponds well to the linear step responses. The lateral-directional decoupling assumptions that were made are thus valid.

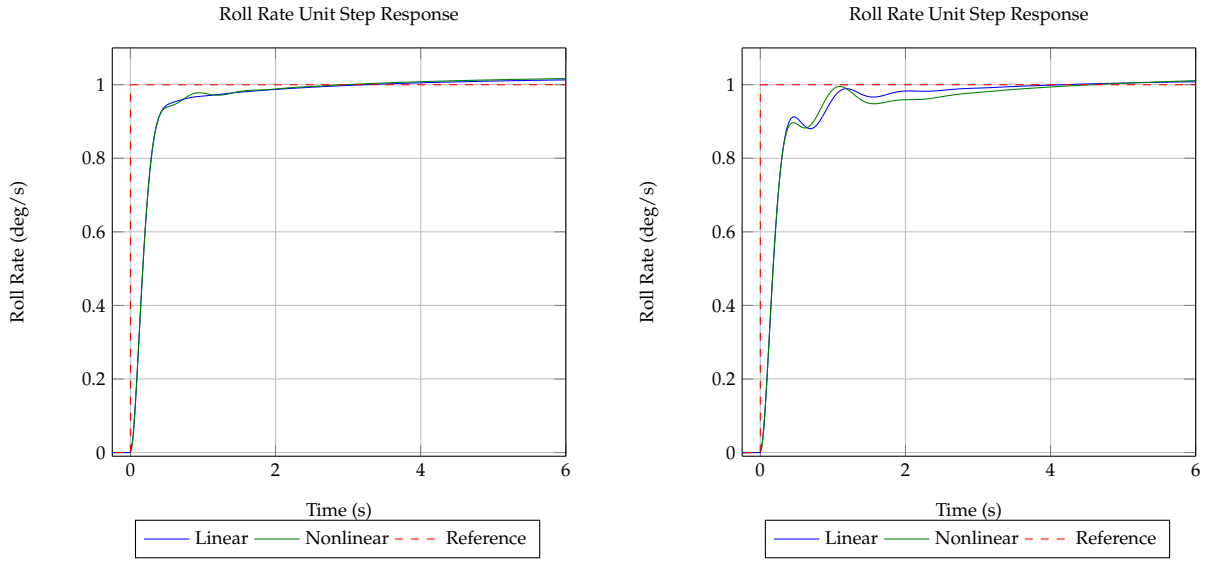

(a) Undamaged aircraft (b) Damaged aircraft

Figure 7.10: Linear vs nonlinear unit step roll rate responses

7.2.7 Roll Angle Controller

Figure 7.11 shows the roll angle unit step responses for both the undamaged and the damaged aircraft. Since the linear and nonlinear responses of the inner-loop controllers already correspond very well, and because the inner-loop controllers encapsulate the plant uncertainty, the roll angle nonlinear step responses also correspond well with the linear step responses. It is clear that the damage has almost no effect on the response of the roll angle controller.

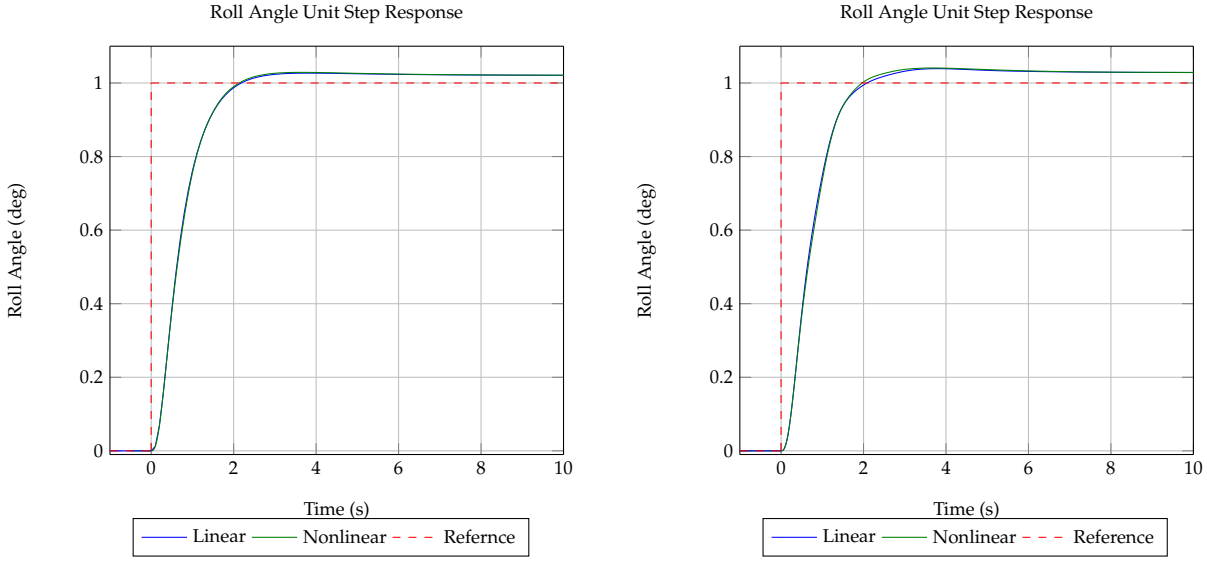

(a) Undamaged aircraft (b) Damaged aircraft

Figure 7.11: Linear vs nonlinear unit step roll angle responses

7.2.8 Guidance Controller

Figure 7.12 shows the cross track unit step responses for both the undamaged and the damaged aircraft. Since the linear and nonlinear responses of the roll angle controller already correspond very well, the cross track nonlinear step responses also correspond well with the linear step responses. Note from the cross track step responses that the robustness of the lateral-directional controllers remain intact in the nonlinear environment. It is clear that the damage has almost no effect on the response of the guidance controller.

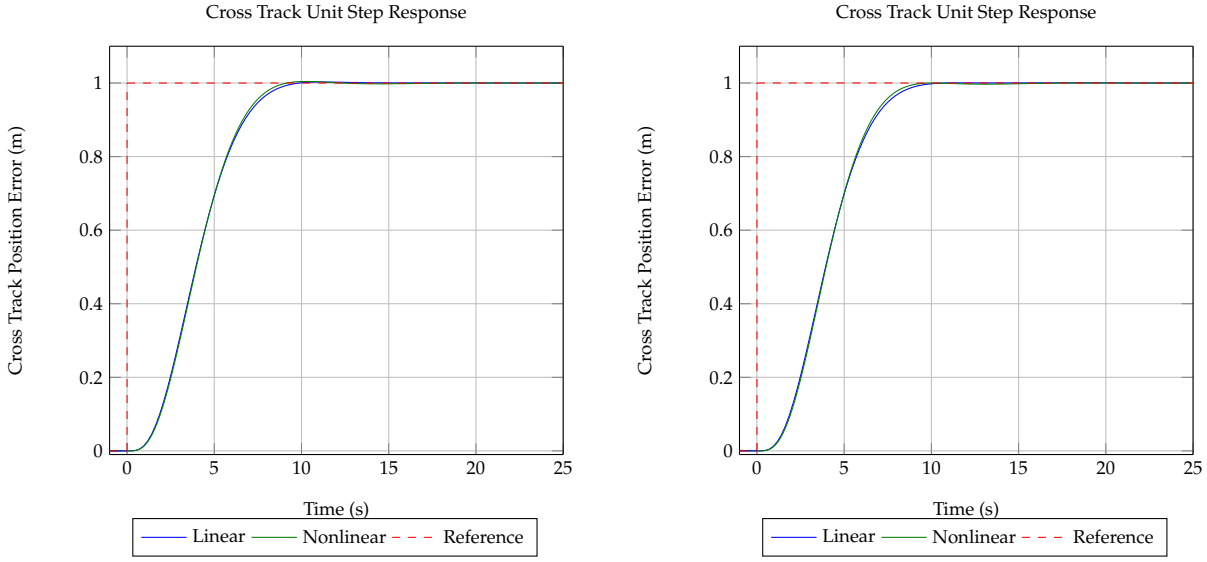

(a) Undamaged aircraft (b) Damaged aircraft

Figure 7.12: Linear vs nonlinear unit step cross track position error responses

Overall the linear approach to stability analysis and control design yielded good results, with the nonlinear step responses corresponding well to the linear step responses. The robustness of the controllers remained intact in the nonlinear environment, and decoupling the lateral-directional dynamics was shown to be a valid approach.

7.2.9 Coupling between Longitudinal and Lateral Dynamics

In Chapter 4, it was noted that if an aircraft suffers damage that causes asymmetry, the longitudinal dynamics will couple into the lateral-directional dynamics. The majority of the coupling occurs through the angle of attack. The most significant effect is that an angle of attack perturbation will cause the aircraft to experience a large rolling moment disturbance. Figure 7.13 (a) illustrates the effect of an angle of attack perturbation on the lateral-directional dynamics of the damaged aircraft. The angle of attack perturbation couples into the lateral dynamics, which causes the aircraft to experience a rolling moment and a yawing moment. The rolling and yawing moments cause large roll rate perturbations and smaller yaw rate perturbations. The roll rate and yaw rate propagate into roll angle and sideslip angle perturbations. It is therefore required of the roll rate and LSA controllers to reject the coupling disturbances.

From (4.2.22) it was noted that an aileron deflection of about 70% of the angle of attack perturbation is needed to counter the induced rolling moment. Figure 7.13 (b) shows the aileron

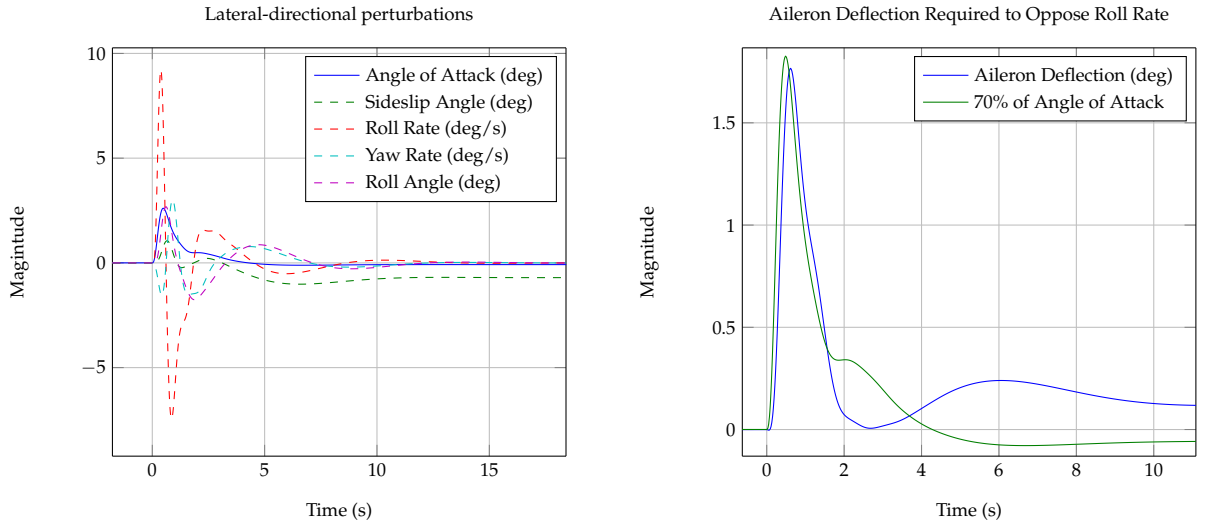

(a) Lateral-directional perturbations due to angle of attack perturbation for damaged aircraft

(b) Aileron deflection required to oppose roll rate for damaged aircraft

Figure 7.13: Coupling between longitudinal and lateral-directional dynamics

deflection that the flight control system commands to counter the roll rate due to the angle of attack perturbation. Note that it is approximately 70% of the angle of attack perturbation.

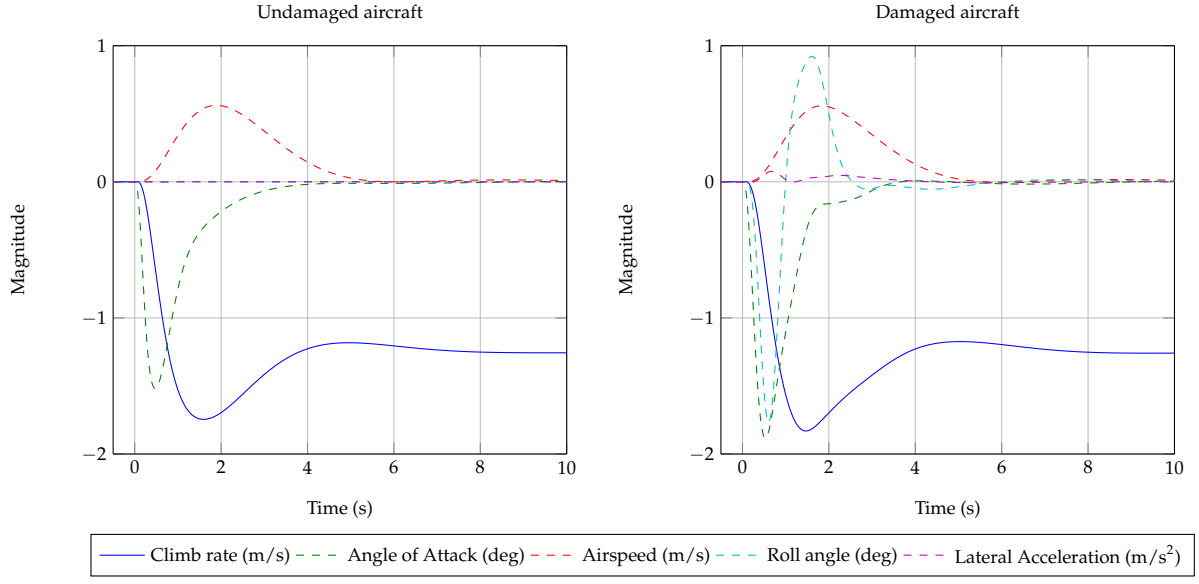

Figure 7.14: Longitudinal perturbation coupling into lateral-directional and axial dynamics: A climb rate step due to glide slope tracking results in an angle of attack perturbation, which couples into the lateral-directional and airspeed dynamics

The coupling of the longitudinal dynamics into the lateral-directional dynamics is not of great concern while navigating. However, it becomes significant when attempting to land the aircraft. When the flight control system adjusts the climb rate of the aircraft to track the glide slope, an angle of attack perturbation induces a rolling moment, resulting in the aircraft to deviate from its cross track trajectory. To ensure that the aircraft lands on the runway, the guidance controller must

steer the aircraft back onto its track. If the aircraft deviates too far, the guidance controller might not be able to steer the aircraft back onto track before touchdown. Figure 7.14 shows the climb rate commanded by the flight control system to enable the undamaged and damaged aircraft to track the glide slope. Note that for the undamaged aircraft, only a velocity disturbance is observed. The damaged aircraft, on the other hand, experiences velocity, roll angle, and lateral acceleration disturbances that must be rejected and corrected before the aircraft touches down.

7.2.10 Waypoint Navigation

The simulated step responses in the previous section verified the performance of the individual controllers in full coupled nonlinear simulation. The results showed that the nonlinear responses agreed sufficiently well with the linear responses and therefore validated the linearisation and decoupling approximations that were used to design the controllers. All the controllers were tested with noise and wind disturbances as well. The step responses are plotted in Chapter 8 where they are compared to the practical step responses. In this section, the full autonomous waypoint navigation and autonomous landing is simulated with sensor noise and wind disturbances included. Figure 7.15 shows the circuit flown by the aircraft while in the waypoint navigation state. Both the undamaged and the damaged aircraft perform equally well at waypoint navigation.

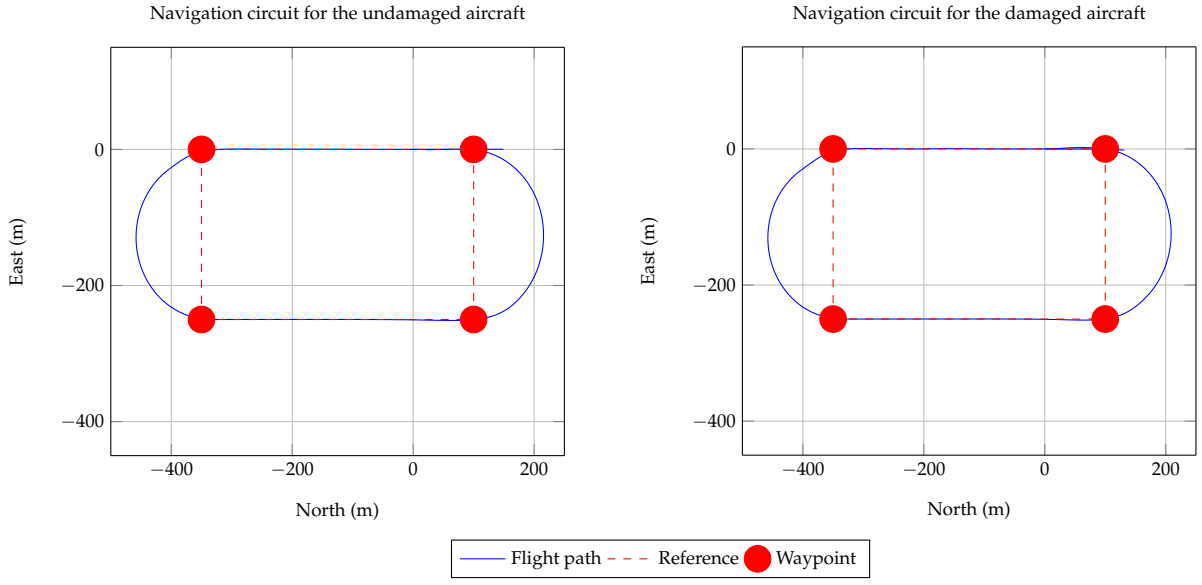

Figure 7.15: Waypoint navigation circuit simulated in HIL environment

The aircraft will continue to navigate around the circuit until the landing command is given. It will then continue on the circuit until it reaches the approach point. The autonomous landing state machine guides the aircraft onto the glide slope and through the glide slope phases until touchdown.

7.2.11 Autonomous Landing

Figure 7.16 shows the glide slope tracking for both the undamaged and the damaged aircraft. The flight control system manages to control both the undamaged and damaged aircraft to track the

glide slope before touchdown.

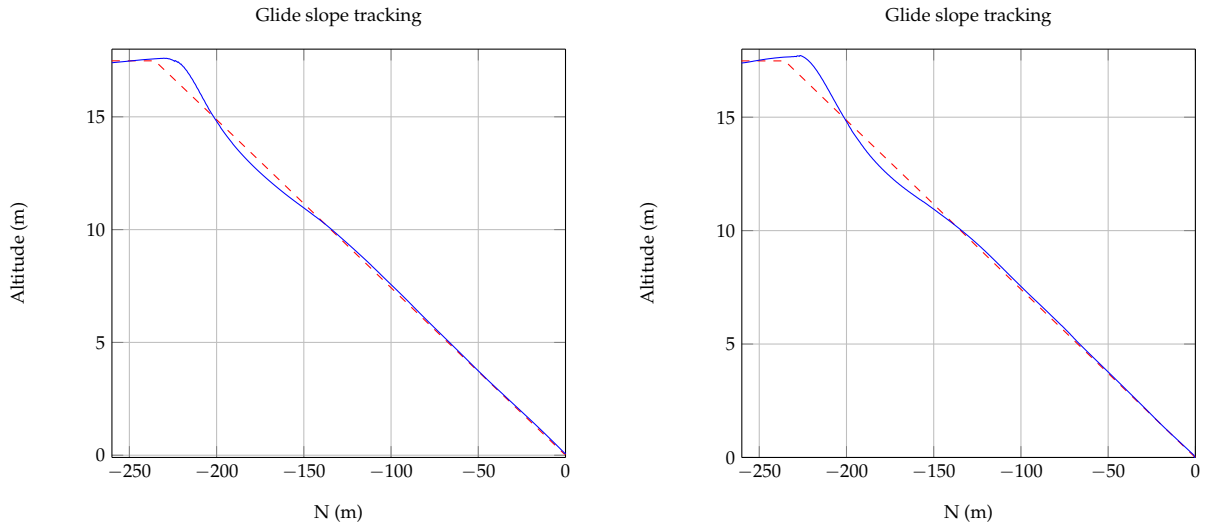

(a) Undamaged aircraft (b) Damaged aircraft

Figure 7.16: Glide slope tracking simulated in HIL environment

Note that a small altitude error results in a large in-track overshoot or undershoot from the desired touchdown position. The overshoot or undershoot can be written as a function of the glide slope angle and altitude error:

$$\text{OS/US} = \frac{e_h}{\tan\gamma} \tag{7.2.1}$$

where e_h is the altitude error and γ the glide slope angle. Tight glide slope tracking is therefore require for accurate landings.

Figure 7.17 shows the touchdown positions, marked with a plus, where the undamaged and damaged aircraft touched down. In both cases, the aircraft overshoots its initial touchdown point by approximately 1 m. Note that the undamaged aircraft accomplishes a more accurate cross track touchdown point. Unlike the undamaged aircraft, the damaged aircraft is disturbed from its cross track path when it starts the glide slope. The flight control system now has to work harder to align the aircraft with the runway. Due to the limited amount of time from when the aircraft starts the glide slope, which is where the disturbance originates, to when it touches down (approximately 14 s later), the guidance controller does not have enough time to completely regulate the cross track position error to zero. Nevertheless, the flight control system still manages to autonomously land the damaged aircraft with sufficient performance and accuracy. Note that after touchdown, runway controllers are activated to guide the aircraft down the centre line of the runway. The runway controllers are activated when a large normal acceleration spike is detected. A pitch rate and pitch angle controller then keeps the nose of the aircraft down; a roll rate and roll angle controller keeps the aircraft wings-level; and a guidance controller, which makes use of the rudder and the steering wheel, guides the aircraft down the runway. The aircraft used in this project does not have any form of braking mechanism, thus upon touchdown the throttle is turned off and the aircraft runs freely until it rolls to a standstill.

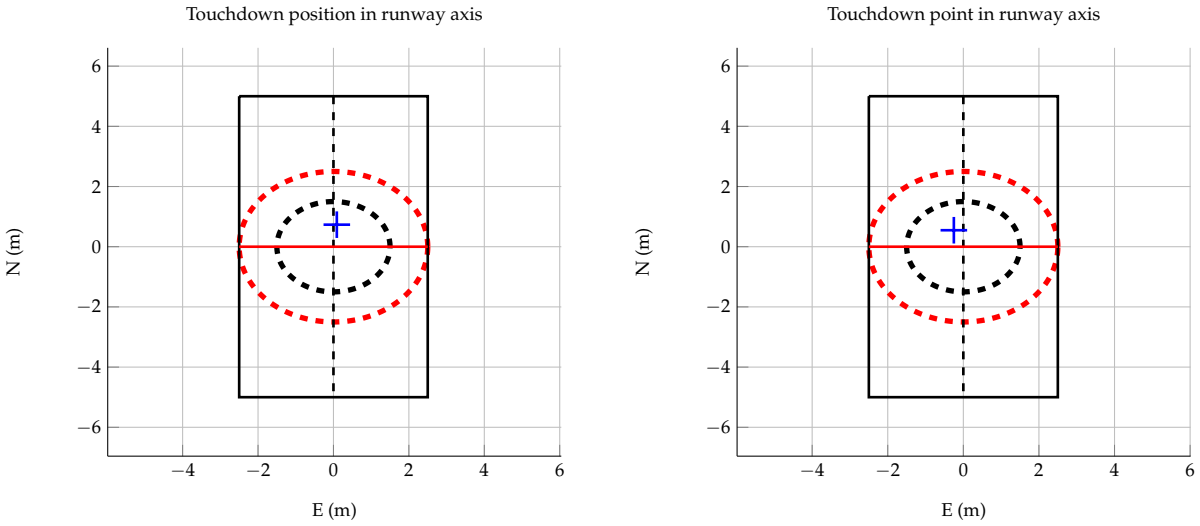

(a) Undamaged aircraft (b) Damaged aircraft

Figure 7.17: Touchdown point: The black dotted line circle represents a 1.5 m radius circle and the red dotted line circle a 2.5 m radius circle

7.3 Summary

A high-fidelity simulation environment that combines software and hardware was described in this chapter. This simulation environment was used to verify the performance and robustness of the flight control system developed in Chapter 5 and to test the autonomous navigation and landing strategies described in Chapter 6. The hardware and software that would be used for the practical flight tests were successfully tested. It was found that the flight control system performed sufficiently and achieved the level of robustness it was designed for. Furthermore, the flight control system and the autonomous waypoint navigation and landing strategies were able to autonomously navigate and land the undamaged aircraft as well as the aircraft that has suffered 20% wing loss, 70% horizontal stabiliser loss, and 20% vertical stabiliser loss. In both cases the landing accuracy was acceptable and within the desired specifications.

Now that the flight control system has been successfully verified in simulation and it has been demonstrated that the aircraft, both undamaged and damaged, is able to perform waypoint navigation and autonomous landing, the system can be verified with practical flight tests.

This chapter describes the practical flight tests that were performed to verify the flight control system and autonomous landing system on the real test aircraft. The flight tests were performed using the test aircraft described in Chapter 1 in both its undamaged and damaged airframe configurations. A nominal damage configuration with 20% partial wing loss, 70% partial horizontal stabiliser loss, and 20% vertical stabiliser loss was used for the real aircraft.

An overview of the flight test campaign is provided, followed by a description of the detailed flight test plan that was executed to systematically test the flight controllers and landing system. First, doublets were performed to validate the flight dynamics models developed in Chapter 3 for both the undamaged and damaged airframe configurations. Next, incremental flight tests were performed to successively build up and test the longitudinal and lateral flight control laws in both the undamaged and damaged configurations. The flight tests culminated in full autonomous waypoint navigation and landing of the aircraft. A successful autonomous landing was demonstrated for the undamaged aircraft, and mock landings were attempted with the damaged aircraft. Unfortunately, the aircraft was lost due to a remote control malfunction before a successful landing with the damaged aircraft could be achieved.

8.1 Overview of Flight Test Campaign

The primary objective of the practical flight test campaign is to practically validate the performance and robustness of the flight control system and its ability to land both the damaged and the undamaged aircraft A test aircraft equipped with all the required avionics and additional hardware is used for the practical validation. A flight test plan is followed whereby all the flight controllers are systematically tested. The flight plan is composed in such a manner that the tests are performed in a sequence that ensures that the functionality of preceding components are in working order before the next components are tested.

Practical flight testing a new (as yet untested) flight control system is not a simple task. The task is even more complicated due to the degraded handling qualities of a damaged aircraft. Thorough preparation is required to ensure that the flight tests proceed successfully and without any disruptions. Although the system was thoroughly tested in HIL simulations, undetected implementation errors may still be present. Therefore a flight test plan is set up and strictly followed to ensure the safety of the aircraft by minimising the risk involved with the practical flight testing. The flight test plan is set up so that the low-risk tests are done before the high-risk tests. This allows one to obtain the most practical data out of the flight test campaign in case of an incident. The flight tests were executed in the following order:

- Maiden test flight
- Doublet tests for model validation
- Longitudinal controller tests
- Lateral controller tests
- Waypoint navigation
- Autonomous landing

The flight test setup and aircraft configuration as described in Chapter 1 were used during all the practical flight tests. Due to flight battery time constraints, the flight test plan was carried out over several days, hence atmospheric conditions such as air density and wind conditions may differ between results. Flight tests were, however, planned for days when light wind conditions were predicted in order to obtain uncontaminated results. Unfortunately, none of the days were completely windless. Each practical step response was compared to its related HIL simulated response for visual validation purposes. In this chapter, the "undamaged" aircraft refers to the aircraft with no damage, and the "damaged" aircraft refers to the aircraft that has suffered 20% wing loss, 70% horizontal stabiliser loss, and 20% vertical stabiliser loss.

During the aircraft's maiden flight, the safety pilot flew the undamaged aircraft to verify that the system as a whole functions correctly. The safety pilot recommended the cruise airspeed that he was comfortable with. Also, all the aircraft states were recorded and analysed after the flight. The recorded aircraft states were analysed to ensure that all the sensors on the aircraft and the state estimator are functioning correctly. The safety pilot then flew the aircraft with partial wing loss, partial horizontal stabiliser loss, and partial vertical stabiliser loss respectively. After successful flights, the damaged aircraft was flown (20% wing loss, 70% horizontal stabiliser loss, and 20% vertical stabiliser loss). A strict requirement is that the safety pilot must be able to fly the aircraft in its damaged configuration using manual control only. If an incident occurs and the safety pilot must take control of the aircraft, he must feel confident flying the damaged aircraft. When the safety pilot was comfortable with the aircraft, and all the systems functioned correctly, the next tests began.

By following a flight test plan, all the required tests to practically validate the performance and robustness of the flight control system can be performed with minimum risk of an incident occurring in the early stages of the flight test campaign. In the upcoming sections, the flight test results and the flight test plans that were followed are discussed.

8.2 Model Verification

8.2.1 Flight Test Description

The model of the aircraft developed in Chapter 3 relied mostly on software packages to model the various forces and moments acting on the aircraft, which together govern the behaviour of the aircraft. The aerodynamic model was obtained with the AVL software package. Limitations in this package prohibited the modelling of certain aspects like the forces and moments due to the

fuselage and drag. Therefore, the aircraft model that was obtained is only an approximation of the practical aircraft and contains parameter uncertainties.

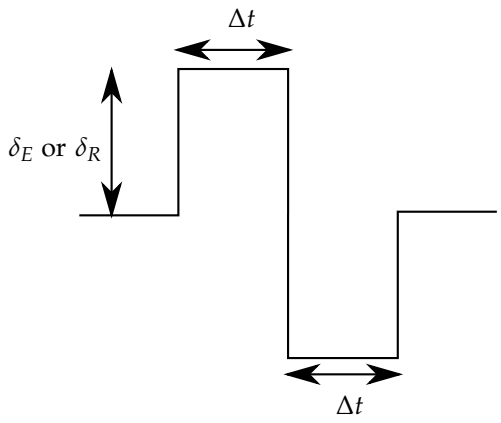

Figure 8.1: Specific input type: doublet with Δt step width in seconds

Through specific control input types, the natural modes of motion of the aircraft can be excited. By exciting the natural modes of motion, one can determine the frequencies and damping ratios of a particular mode. Based on the flight test data, adjustments can be made to the aircraft model. In this project the doublet, shown in Figure 8.1, was used as a control input to excite the short period and Dutch roll modes respectively.

If the natural modes of motion are not adequately excited, the identification will be ill-conditioned and the natural modes of motion will not become apparent in the time responses. The excitement must be relatively small for the aircraft states to remain small, so that the assumptions of linearity are maintained. Due to noisy sensors, the inputs should not be too small, otherwise the modes will not be recognisable within the data. Therefore the signal to noise ratio consideration is important for small state manoeuvres. If the natural frequency ω_n of the mode to be excited is approximately known, then the duration of the time unit Δt for a doublet should be chosen as [32]:

$$\Delta t = 1.5/\omega_n \tag{8.2.1}$$

A number of doublet tests were done to validate the aircraft model. Essentially we want to determine if the short period mode and Dutch roll mode of the aircraft model are a good approximation of the actual aircraft's short period mode and Dutch roll mode dynamics. Doublet tests were done on: the undamaged aircraft, the aircraft with 70% horizontal stabiliser loss, and the aircraft with 20% vertical stabiliser loss. The tests proceeded as follows:

- The autopilot regulated the airspeed of the aircraft to the cruise airspeed (20 m/s).
- The elevator, ailerons and rudder remained under safety pilot control.
- An elevator doublet was superimposed onto the safety pilot elevator command and the safety pilot was instructed not to disturb the short period dynamics (fix stick doublet).
- A rudder doublet was superimposed onto the safety pilot rudder command and the safety pilot was instructed not to disturb the Dutch roll mode dynamics (fix stick doublet).

This test procedure was followed for all the damage cases listed above. Both elevator and rudder doublets were performed on the undamaged aircraft, followed by an elevator doublet for the aircraft with 70% horizontal stabiliser loss, and lastly a rudder doublet for the aircraft with 20% vertical stabiliser loss. By using the expected short period mode and Dutch roll mode natural frequencies, the Δt of the doublets were chosen.

8.2.2 Short Period Mode Validation

Figure 8.2 shows the pitch rate response to an elevator doublet for the undamaged and damaged aircraft respectively. From Figure 8.2, by looking at the response inside the green shaded area,

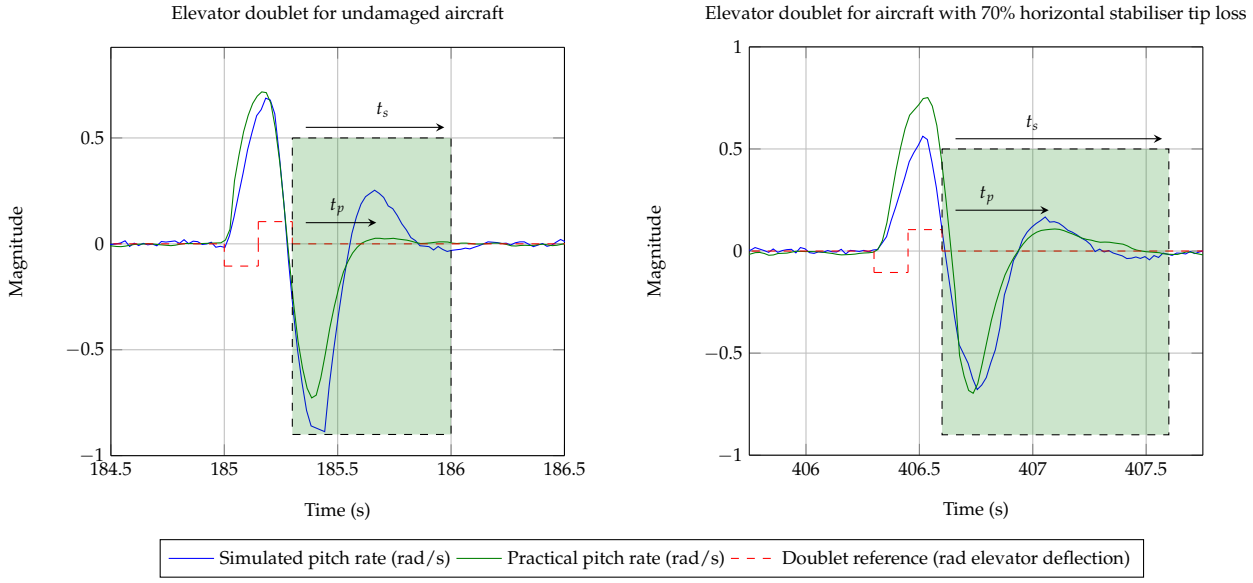

Figure 8.2: Pitch rate time response for an elevator doublet input

it is clear that the short period mode of the undamaged aircraft is more damped than initially modelled.

Table 8.1: Damping ratio of the pitch rate response to an elevator doublet

Parameter	Modelled	Practical
ζ	≈ 0.53	≈ 0.787

The pitch damping derivative C_{m_Q}, obtained from AVL, is therefore too small. A number of factors play a role in this derivative. The centre of mass of the practical aircraft might not be at the modelled location. Assuming that the centre of mass is at the modelled location, the pitch damping derivative C_{m_Q} can be increased in order to increase the damping of the short period mode of the aircraft model. Note that as the model predicted, the natural frequency of the short period mode decreases with partial horizontal stabiliser loss (see Table 8.2).

Table 8.2: Frequencies of the pitch rate response to an elevator doublet

Parameter	Undamaged	Damaged
ω_n (rad/s)	≈ 11.33	≈ 9.018

The short period damping for the damaged aircraft agrees well with the modelled damping (by looking at the response inside the green shaded area). Figure 8.3 shows the normal acceleration response to an elevator doublet for the undamaged and damaged aircraft respectively. Again, by

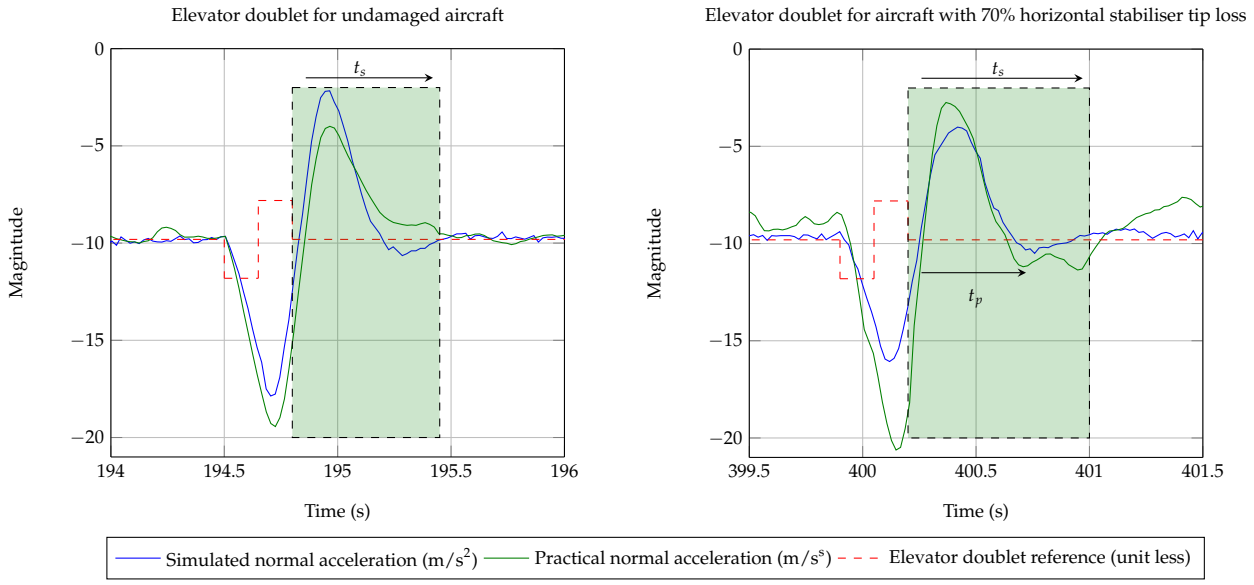

Figure 8.3: Normal acceleration time response for an elevator doublet input

looking at the response inside the green shaded area, it is clear that the short period mode of the undamaged aircraft is more damped than initially modelled. Due to the highly damped nature of the practical response, it is difficult to establish if the damping frequency ω_d is modelled correctly. The natural frequency, however, seems to be of a similar magnitude as the model; slightly slower in fact. The pitching stiffness derivative C_{m_α} can be adapted to slightly slow down the short period natural frequency of the aircraft model. But, again, this derivative is a function of the centre of mass of the aircraft, which might not be at the modelled location. By making small adjustments to the derivatives, a more representative model of the short period mode dynamics is obtained.

8.2.3 Dutch Roll Mode Validation

Figure 8.4 shows the yaw rate response to a rudder doublet for the undamaged and damaged aircraft respectively. Due to the slow nature of the Dutch roll mode, it is difficult to obtain a response that is not contaminated by the safety pilot's inputs. The damping and natural frequency of the Dutch roll mode can be calculated from the first two peaks after the rudder doublet is completed. First, the damping frequency can be obtained,

$$\omega_d = \frac{2\pi}{T_{p-p}} \tag{8.2.2}$$

where T_{p-p} is the peak to peak time of the response. The inverse of the time constant σ can be obtained from the envelope of the response

$$r(t) = Ae^{-\sigma t} \tag{8.2.3}$$

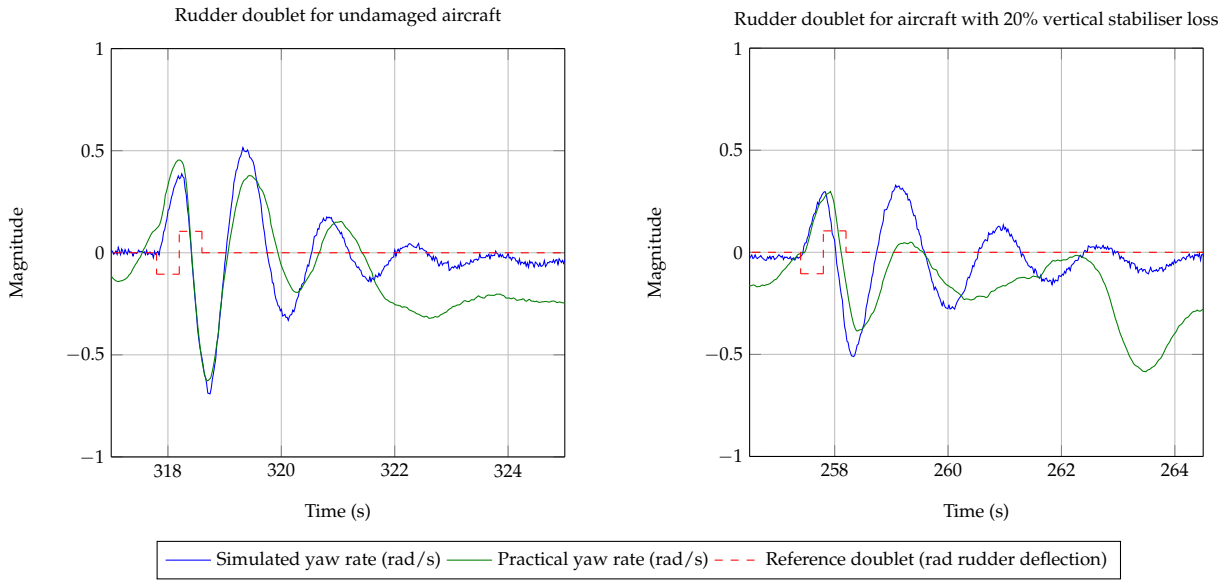

Figure 8.4: Yaw rate time response for a rudder doublet input

where A is calculated at $t = 0$ and $r(t)$ is the magnitude of the response at time t. From the simulated response of the undamaged aircraft, the complex pole pair is calculated to be

$$s = -0.726 \pm 4.304i \tag{8.2.4}$$

and from the practical response the complex pole pair is calculated to be

$$s = -0.564 \pm 3.92i \tag{8.2.5}$$

Note that both the damping ratio and the natural frequency of the model are very close to those of the practical aircraft (see Table 8.3).

Table 8.3: Damping ratio and the natural frequency of the Dutch roll model

Parameter	Modelled	Practical
Damping ratio	0.1663	0.1424
Natural frequency	4.36	3.96

The natural frequency of the Dutch roll mode can be slightly decreased by decreasing the weathercock or directional static stability derivative C_{n_β}, and the damping of the Dutch roll mode can be slightly increased by increasing C_{n_R}. Figure 8.5 shows the lateral acceleration response to a rudder doublet for the undamaged and damaged aircraft respectively. The same behaviour as mentioned above is observed. The damping ratios of both the damaged and undamaged aircraft coincide with that of the aircraft model, although the natural frequencies differ slightly.

8.2.4 Trim Condition

Table 8.4 shows the straight and level flight trim values at which the flight control system trimmed the aircraft during the practical the flight tests.

Table 8.4: Practical flight equilibrium control surface values.

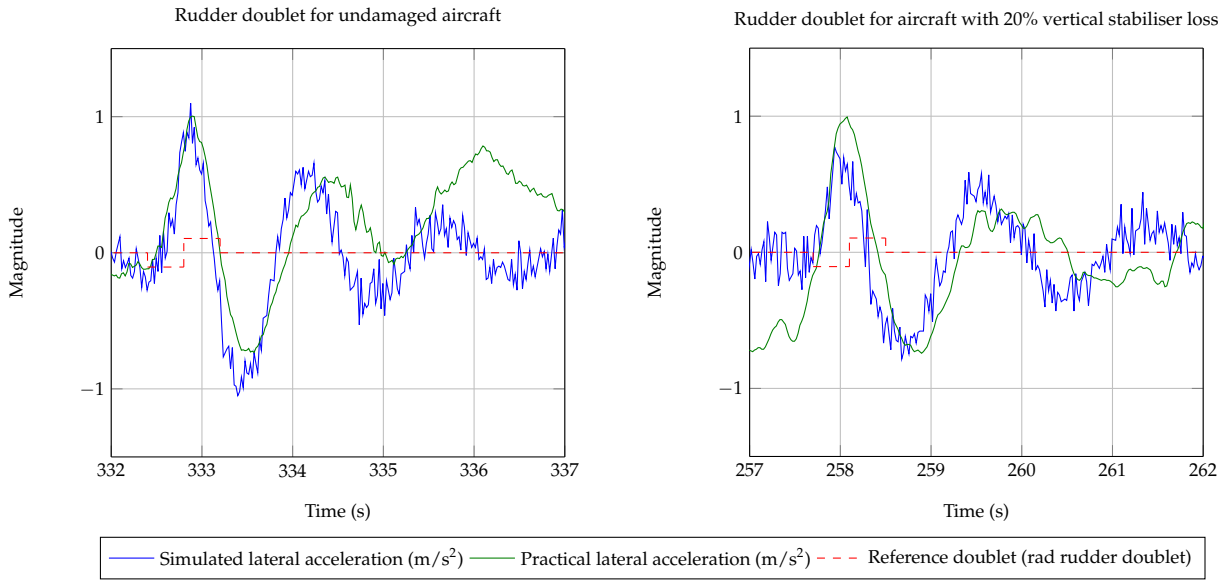

Figure 8.5: Lateral acceleration time response for a rudder doublet input

Control surface	Undamaged	Damaged
Trim elevator deflection	$-1.3°$	$-4.1°$
Trim aileron deflection	$0°$	$3.6°$
Trim rudder deflection	$0.3°$	$2.4°$

The aileron and rudder trim values are very similar to the trim values calculated in Chapter 4. However, the elevator trim values are significantly smaller than expected. The calculated trim values were $-3.8°$ and $-8.3°$ for the undamaged and damaged aircraft respectively, whereas during the practical flight tests the flight control system trimmed the aircraft's elevator at $-1.3°$ and $-4.1°$ for the undamaged and damaged aircraft respectively. This could be due to the centre of mass not being at the modelled position, the elevator being more effective than modelled, or a combination of the two.

The derivatives mentioned above were adjusted to obtain an aircraft model that better represents the dynamics of the practical aircraft. Note that one must be careful when changing derivatives because of coupling that might exist, especially in the case of the damaged aircraft (asymmetrical damage). After very slight adjustments, one can conclude that the aircraft model developed in Chapter 3 is a sufficient representation of the practical aircraft.

8.3 Longitudinal Controller Tests

In this section the practical results of the longitudinal controllers are discussed. The longitudinal controller to be discussed includes the climb rate controller, the altitude controller, and the airspeed controller. Each response is plotted together with a HIL response for visual comparison purposes. A flight test description of how the practical flight test was approached is first presented.

8.3.1 Flight Test Description

For all the longitudinal controller tests, the autopilot regulated the airspeed of the aircraft to the cruise airspeed (20 m/s). The longitudinal controller tests proceeded as follows:

- The autopilot regulated the climb rate of the aircraft to 0 m/s.
- The ailerons and rudder remained under safety pilot control.
- The safety pilot was instructed to keep the aircraft's roll angle zero while climb rate steps were commanded.
- After the success of the climb rate steps, the altitude controller was armed and the altitude was regulated at the current armed altitude.
- The safety pilot was instructed to keep the aircraft's roll angle zero while altitude steps were commanded.
- Lastly, the safety pilot was instructed to keep the aircraft's roll angle zero while airspeed steps were commanded.

This test procedure was followed for both the damaged and undamaged aircraft. Note that the NSA controller was not included in the practical flight testing. The inner-loop controllers are difficult to practically test due to the unstable nature of the aircraft when not under at least climb rate and roll angle control. The NSA, LSA and roll rate controllers were therefore not directly practically tested, but indirectly through the outer-loop controllers.

8.3.2 Climb Rate Response

Figure 8.6 shows a 2 m/s climb rate step response for both the undamaged and damaged aircraft. Also indicated on the plots are the airspeed and partial roll angle perturbations. Note that the undamaged and damaged aircraft were tested on two different days under different wind conditions. Stronger wind conditions were present for the undamaged aircraft tests. The climb rate step response for both the undamaged and damaged aircraft had a slightly faster rise time but, in general the responses were as expected. It was concluded that the designed climb rate controller is robust to partial horizontal stabiliser loss. As expected due to the partial wing loss, a large roll angle perturbation was present when the damaged aircraft was commanded a climb rate. Furthermore, airspeed perturbations were present in both cases, as seen in Figure 8.6, due to the coupling of the longitudinal dynamics into airspeed through gravity and drag.

8.3.3 Altitude Response

Figure 8.7 shows a 10 m altitude step response for both the undamaged and damaged aircraft. Note that the altitude response now had additional overshoot that was not designed for. The additional overshoot is due to the limited integrator that was added to allow for zero steady state error, even when climb rate biases (up to 0.6 m/s) are present. Figure 8.7 focuses more on the transient response of the altitude controller to illustrate the robustness of the controller. Observe that the rise time and overshoot in both cases correspond well to the simulated rise time and overshoot.

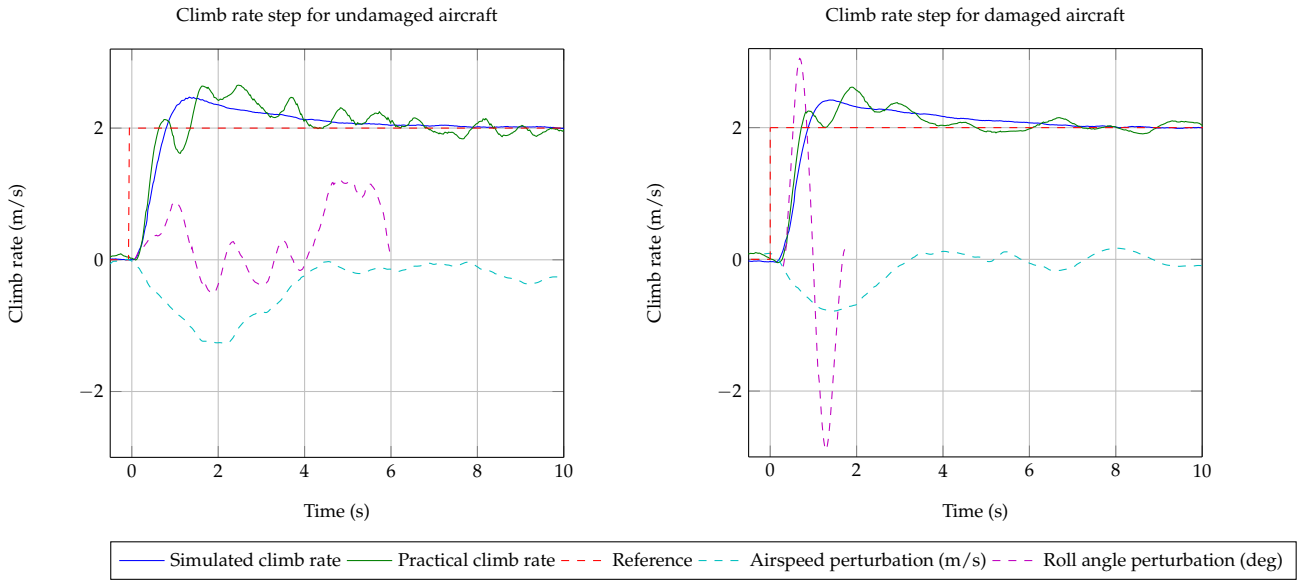

Figure 8.6: Climb rate step response (+2 m/s) for the undamaged aircraft on the left and the damaged aircraft on the right

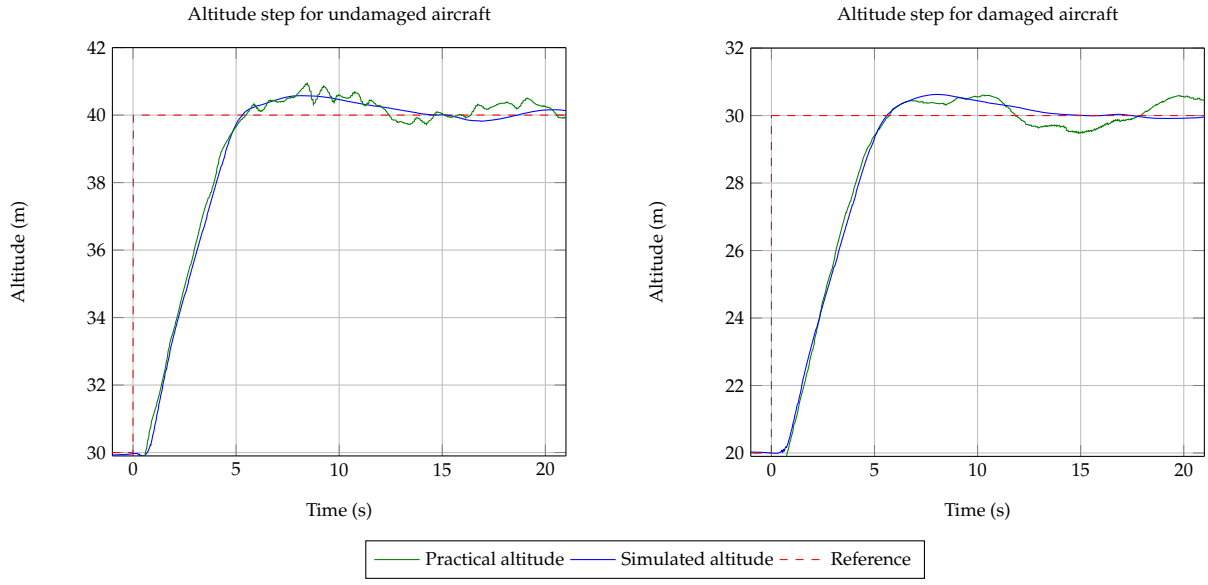

Figure 8.7: Altitude step response (+10 m) for the undamaged aircraft on the left and the damaged aircraft on the right

In steady state, the altitude controller regulates the altitude around the reference altitude with a deviation of ±0.15 m, depending on the wind conditions. This steady state tracking was achieved for both the undamaged and damaged aircraft. Altogether, the altitude controller performed well and achieved the level of robustness that was required of it.

8.3.4 Airspeed Response

Figure 8.7 shows a −2 m/s airspeed step response for both the undamaged and damaged aircraft. A negative airspeed step is shown due to its significant importance for autonomous landing. Upon approach, the aircraft has to decrease its airspeed from cruise to approach. The aircraft relies only

on its drag to slow down its airspeed due to the lack of active drag control surfaces such as air brakes. When the aircraft reduces its airspeed, the angle of attack increases, causing an increase in the induced drag. As mentioned in Chapter 3, AVL fails to estimate the aircraft drag accurately. Furthermore, the drag from the fuselage is also neglected in the modelling process. The airspeed step response of the damaged aircraft has more overshoot than the airspeed step response of the undamaged aircraft.

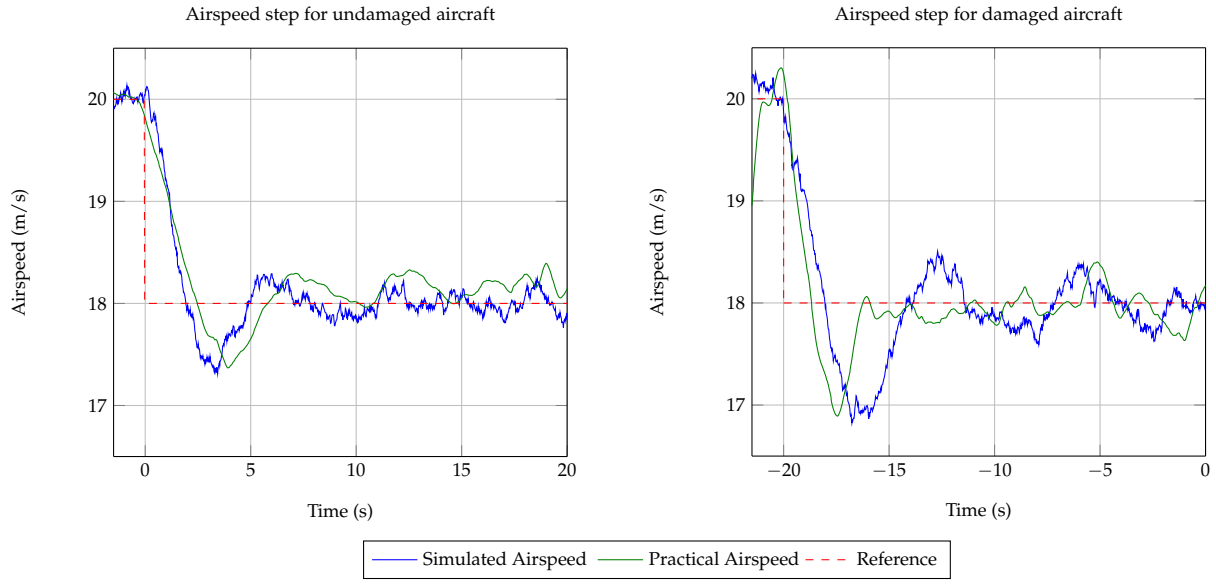

Figure 8.8: Airspeed step response (-2 m/s) for the undamaged aircraft on the left and the damaged aircraft on the right

From Figures 8.6 to 8.8 it can be concluded that the longitudinal controllers achieved the desired robustness against partial wing loss and stabiliser losses while retaining their performance.

8.4 Lateral Controller Tests

In this section the practical results of the lateral controllers are discussed. The lateral controller to be discussed includes the roll angle controller and the LSA controller. Each response is plotted together with a HIL response for visual comparison purposes. A flight test description of how the practical flight test was approached is first presented.

8.4.1 Flight Test Description

After the longitudinal controllers functioned correctly, the lateral controllers were tested. The tests for the lateral controllers and waypoint navigation proceeded as follows:

- The autopilot regulated the altitude at the current armed altitude.
- The autopilot regulated the roll angle of the aircraft to 0° and the lateral acceleration to 0 m/s^2.
- At this point the safety pilot does not have any control over the aircraft.

- Roll angle steps were commanded.
- Lateral control was given back to the safety pilot and he was instructed to fly over the runway.
- When the aircraft was over the runway, the waypoint navigation was enabled.
- The aircraft is then in full autopilot, flying a predetermined set of waypoints.

This test procedure was followed for both the damaged and undamaged aircraft. Note that the guidance controller was not explicitly tested. The guidance controller is indirectly tested through the waypoint navigation.

8.4.2 Roll Angle Response

During all the lateral controller tests, all the longitudinal controllers were active to regulate the altitude and airspeed of the aircraft. The flight control system therefore had control of all the aircraft control inputs (throttle, elevator, ailerons, and rudder). Figure 8.9 shows a 20° positive roll angle step response for both the damaged and undamaged aircraft. In Figure 8.9, it can be

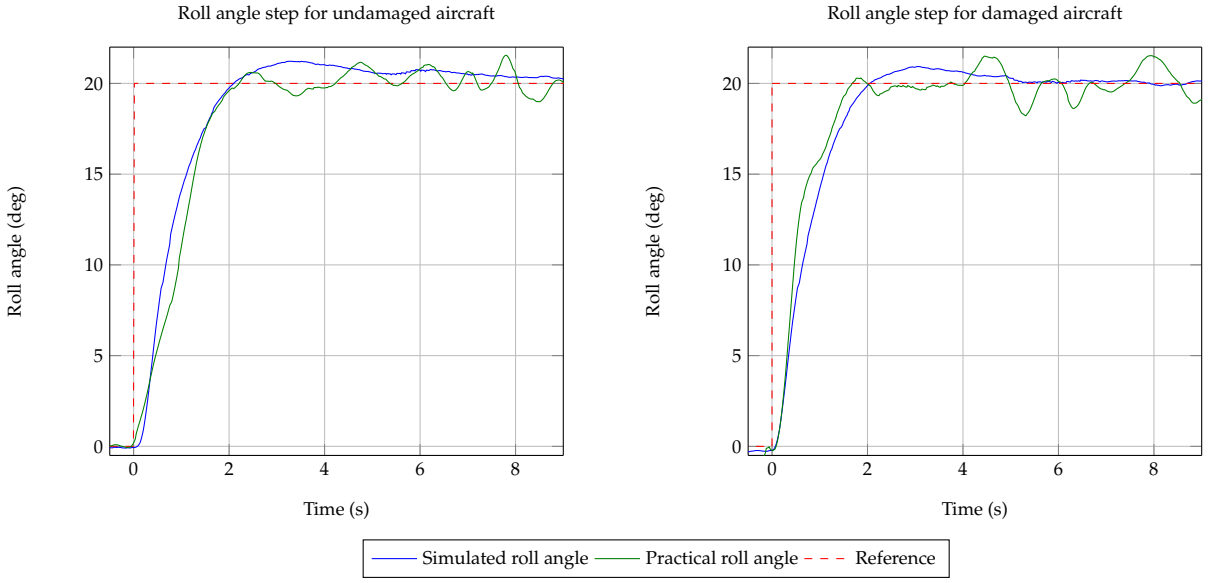

Figure 8.9: Roll angle step response (+20°) for the undamaged aircraft on the left and the damaged aircraft on the right

observed that the roll angle controller achieved the desired robustness against partial wing loss. In both the undamaged and damaged cases, the practical roll angle step responses closely followed the simulated roll angle step responses.

8.4.3 Lateral Specific Acceleration Doublet Response

Figure 8.10 shows the lateral acceleration response to a rudder doublet. To illustrate the functionality and robustness of the LSA controller, a rudder doublet was commanded to disturb the

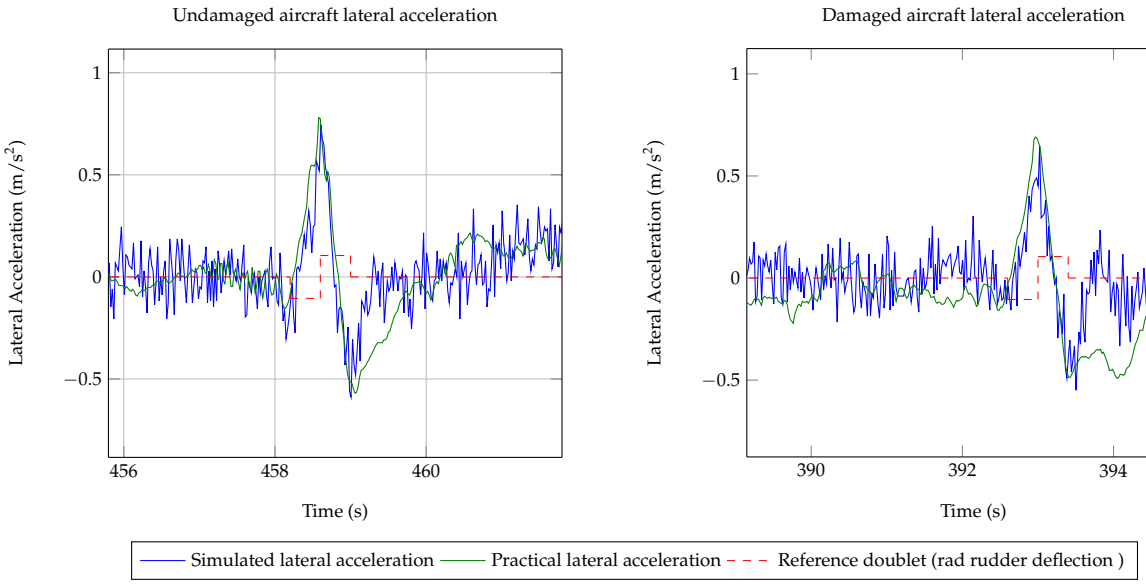

Figure 8.10: LSA regulation and damping for the undamaged aircraft on the left and the damaged aircraft on the right

directional dynamics, while the LSA controller was commanded to regulate the lateral acceleration to zero. By comparing the results in Figure 8.10 to those of the open-loop doublet in Figure 8.3, one will note that the LSA controller damped the response significantly. The LSA controller also managed to regulate both the undamaged and damaged aircraft's lateral acceleration to zero.

8.5 Waypoint Navigation

The performance of the guidance controller is validated by how well it controls the cross track position error while performing waypoint navigation. Figure 8.11 shows the waypoint navigation flight path performed by the undamaged and damaged aircraft in real flight tests. In both cases, pseudo-landings were commanded to determine how much the aircraft would deviate from the track when entering the glide slope, and if the aircraft would fix the cross track position error before touchdown. Note that when the damaged aircraft enters the glide slope at (-250 m North, 0 m East), it deviates from the track. The deviation at its maximum is approximately 4 m. Note that the guidance controller was capable of correcting the cross track position error deviation before the aircraft reached the touchdown point (0 m North, 0 m East). Also note that the undamaged aircraft did not experience a significant cross track position error deviation upon entering the glide slope. At the first circular turn, between (100 m North, 0 m East) and (100 m North, -250 m East), the aircraft had a slower turn rate than required to perfectly perform the circular turn. In both cases, this was due to head wind conditions resulting in the aircraft having lower ground speeds. From (6.1.3) one will note that when travelling at a lower ground speed, a lower roll angle is commanded to perform the turn. The aircraft therefore turns slightly slower than required, thus overshooting the destination waypoint. This phenomenon was, however, not present in the HIL simulations with similar atmospheric conditions. Nevertheless, the navigation strategy achieved good results and was able to guide the aircraft to within the desired 1.5 m cross track position error accuracy before the touchdown point was reached for both the damaged and undamaged

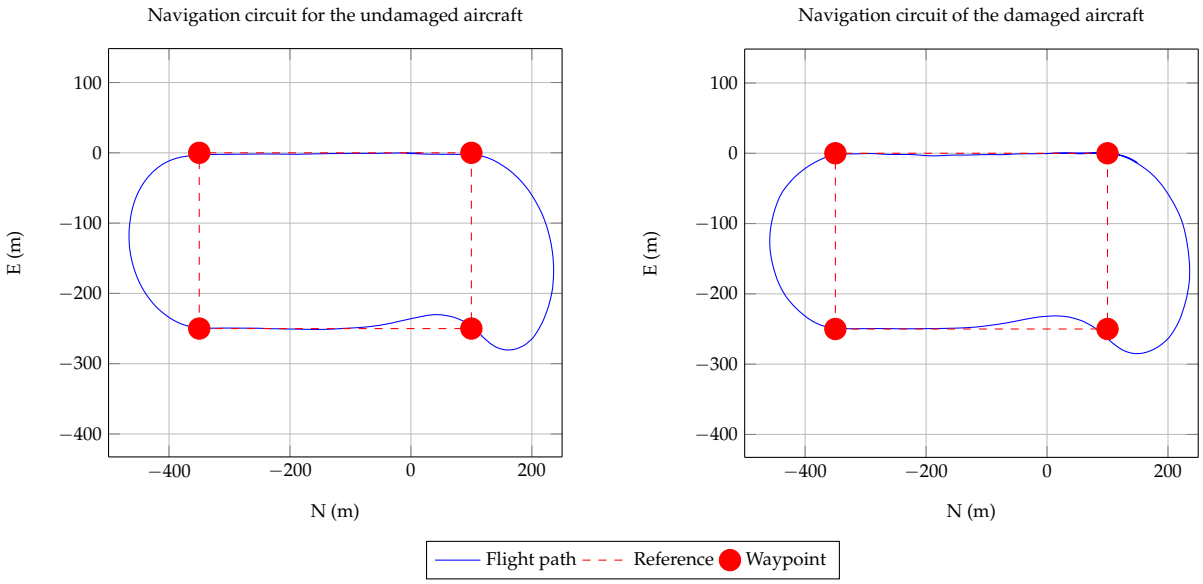

Figure 8.11: Autonomous navigation track executed in actual flight tests for the undamaged aircraft on the left and the damaged aircraft on the right

aircraft.

From Figures 8.9 to 8.11, it can be concluded that the lateral controllers and the waypoint navigation achieved the desired robustness against partial wing loss and stabiliser losses while retaining their performance.

8.6 Coupling of Longitudinal Dynamics into Lateral Dynamics

To verify how the longitudinal dynamics couple into the lateral dynamics, the aircraft was disturbed with an angle of attack perturbation by commanding an elevator doublet while performing waypoint navigation. The resultant angular rates are shown in Figure 8.12. Note that when the undamaged aircraft is disturbed, only the longitudinal dynamics were affected. However, when the damaged aircraft is disturbed, the longitudinal, lateral and directional dynamics were affected. Due to the partial wing loss, a large roll rate is observed when the angle of attack is perturbed. Excessive longitudinal manoeuvres on the glide slope or close to the ground should therefore be avoided when the aircraft has suffered partial wing loss.

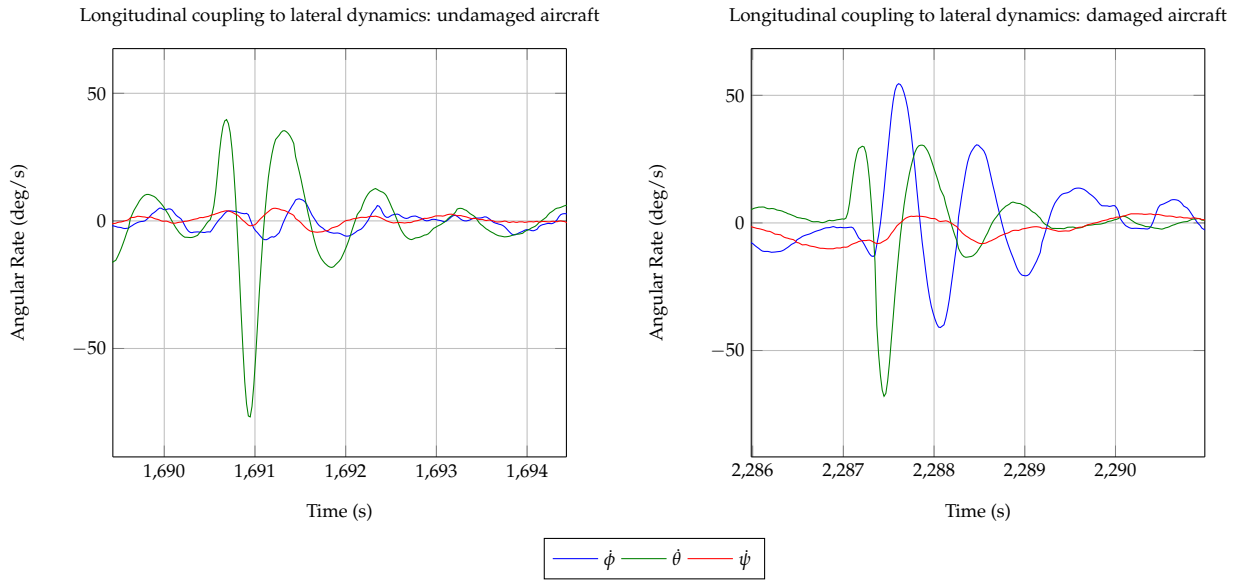

Figure 8.12: Longitudinal coupling into lateral dynamics: Practical flight data

8.7 Autonomous Landing

8.7.1 Flight Test Description

The final tests are the autonomous landing tests, first for the undamaged aircraft and then for the damaged aircraft. Before the autonomous landing tests can commence, it must first be verified that the aircraft is capable of flying at the desired approach airspeed. While the aircraft is under full autopilot control performing waypoint navigation, the airspeed of the aircraft is reduced incrementally until the desired approach airspeed is obtained. If the desired approach airspeed is not obtainable, the landing strategy must be adapted. The autonomous landing test proceeded as follows:

- The autopilot regulated the altitude at the current armed altitude.
- The ailerons and rudder remained under safety pilot control.
- The safety pilot was instructed to fly over the runway.
- While the aircraft was over the runway, the waypoint navigation was enabled.
- The aircraft is then in full autopilot, flying a predetermined set of waypoints.
- The aircraft is given a pseudo-landing command, whereby the aircraft changes and regulates its altitude to the approach altitude.
- The aircraft proceeds on the navigation track until it reaches the approach point and begins with the landing approach.
- At the end of the short final phase, the aircraft aborts and continue with waypoint navigation. The safety officer monitors the pseudo-landing and if everything looks good (cross

track and in-track), the safety officer contacts the GCS operator to command that the aircraft can land.

- The aircraft is then given the landing command, at which this point it regulates its altitude to the approach altitude.
- The aircraft proceeds on the navigation track until it reaches the approach point and begins with the landing approach.
- After touchdown, the safety pilot is instructed to take control and guide the aircraft to stand-still.

An identical procedure was followed for the autonomous landing of the damaged aircraft. If the damaged aircraft is not able to fly at the desired touchdown airspeed, the second landing technique described in Chapter 6 will be used to land the damaged aircraft. The autonomous landing test poses the biggest risk of all the tests. This is mainly due to the aircraft flying at low altitudes most of the time, making it very difficult for the safety pilot to recover the aircraft in case of an incident.

8.7.2 Autonomous Landing Results

With the longitudinal and lateral controllers achieving both the performance and desired robustness, autonomous landings could be attempted. First, an autonomous landing was done with the undamaged aircraft. Figure 8.13 shows the landing glide slope tracking and the touchdown point on the runway. Comparing the glide slope tracking in Figure 8.13 to that in Figure 7.16 (a),

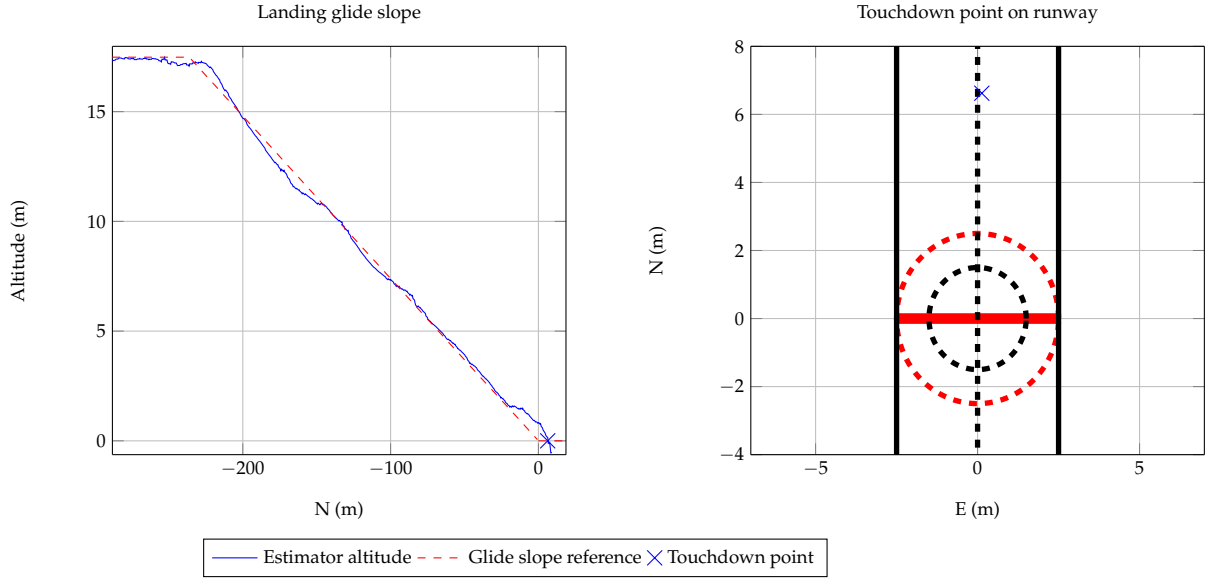

Figure 8.13: Autonomous landing of the undamaged aircraft

one can conclude that the aircraft is tracking the glide slope as expected. However, the aircraft was disturbed at about 1.6 m above the runway, which caused an altitude error of approximately 0.45 m above the glide slope. Due to the aircraft being disturbed so close to the touchdown point (18 m from touchdown point), the flight control system only had approximately 1 s to correct the

altitude error before touchdown. Furthermore, the aircraft was within one wing span from the ground and was therefore in ground effect, which made it harder for the flight control system to correct the altitude error. The aircraft touched down with a cross track position error of 0.131 m from the centre line, but with an in-track error of 6.56 m over the intended touchdown point.

After the autonomous landing of the undamaged aircraft was successfully demonstrated, further flight tests were performed to verify the autonomous landing of the damaged aircraft. Unfortunately, during the execution of these flight tests the aircraft was lost due to a remote control malfunction before a successful landing of the damaged aircraft was achieved. Due to time constraints, a new test aircraft could not be constructed in order to continue the flight testing. Nevertheless, the data obtained from the damaged aircraft flight tests proved invaluable and by analysing the data one can conclude that the flight control system designed is robust and will be capable of autonomously landing the damaged aircraft. In Figure 8.6 and 8.7, it can be seen that the flight control system is capable of sufficiently controlling the climb rate and altitude of the damaged aircraft, and therefore will be able to guide the aircraft to track the glide slope. From Figure 8.11, the flight control system is capable of sufficiently controlling the damaged aircraft's cross track position error and therefore will be able to guide the damaged aircraft within the desired 1.5 m cross track position error before touchdown. As mentioned, the guidance controller corrects the cross track position error deviation occurring upon glide slope entry before touchdown (see Figure 8.11). Furthermore, the model verification from the previous section indicated that the aircraft model developed is an accurate representation of the practical aircraft and therefore practical autonomous landing results for the damaged aircraft should correspond well with the simulated autonomous landing results obtained in the previous chapter.

8.8 Summary

Practical flight tests were conducted to verify the flight control system designed in Chapter 5. The standard Stellenbosch University test aircraft, modified to account for partial wing loss and stabiliser losses, was used to conduct the practical flight tests. All the tests were conducted according to a flight test plan that was created to minimise the risk associated with the loss of the aircraft during flight tests. The tests were therefore conducted in order of low risk to high risk to get the most data out of the flight test campaign.

By studying all the practical data as a whole, the flight control system achieved the level of robustness which it was designed for, and was able to successfully navigate both the undamaged and damaged aircraft to follow predetermined waypoints. By commanding specific control input types to the aircraft's actuators, the aircraft model developed in Chapter 3 was validated. Validating the aircraft model allowed one to have more confidence that the results obtained from the HIL simulations would be representative of the results that could be expected in actual flight tests. The flight control system successfully landed the undamaged aircraft with acceptable accuracy.

Unfortunately, the aircraft was lost due to a remote control malfunction before a successful landing with the damaged aircraft could be achieved. However, from studying the practical flight data of the damaged aircraft, the flight control system was robust to partial wing and stabiliser losses, and successfully controlled all the aircraft states necessary to perform an autonomous landing. Since the damaged aircraft model was validated, and since the flight control system could

control the damaged aircraft, and was able to land it successfully in the high-fidelity simulation environment, it is expected that the flight control would also be able to land the damaged aircraft in a practical flight test.

This thesis presented the design, implementation and verification of an autonomous landing system for a fixed-wing unmanned aerial vehicle that is able to land after suffering partial wing loss and partial losses of the horizontal and vertical stabilisers. This chapter presents a summary of the research performed for this thesis and highlights the important results that were obtained. The chapter finishes with the main conclusions and recommendations for future research.

9.1 Summary

The dynamic model for the damaged aircraft studied in this thesis was derived and based on an asymmetric, six-degrees-of-freedom equations of motion model. The effects of the partial wing and partial stabiliser losses on the aerodynamic coefficients, mass, centre of mass location, and moments of inertia were calculated as a function of percentage wing loss, percentage horizontal stabiliser loss, and percentage vertical stabiliser loss using Athena Vortex Lattice (AVL) aerodynamic modelling software and Autodesk Inventor mechanical design software respectively. The model also accounted for changes in the aileron, rudder, and elevator control authorities due to partial control surface losses. The model was developed using a number of defined reference frames and aircraft notations. The model described the behaviour of both a conventional symmetrical aircraft and an unconventional asymmetrical aircraft. It accomplished this by incorporating the full moment of inertia matrix and allowing for a shift of the centre of mass of the aircraft. For a conventional symmetrical aircraft, the former only consisted of the diagonal components, and the latter was zero shift. Furthermore, the forces and moments acting on the aircraft were described as a function of the percentage of wing loss, percentage of horizontal stabiliser loss, and percentage of vertical stabiliser loss respectively.

The static and dynamic stability of the aircraft was analysed as a function of the percentage of wing loss, percentage of horizontal stabiliser loss, and percentage of vertical stabiliser loss. The aircraft stability was investigated separately for wing loss and stabiliser losses to determine how each affects the dynamics of the aircraft. It was found that the aircraft remains longitudinally statically stable for all the partial horizontal stabiliser loss cases (up to 100% semi-span horizontal stabiliser tip loss) and also remains laterally statically stable for all the partial wing loss cases (up to 40% semi-span wing tip loss). It was found, however, that the aircraft becomes directionally statically unstable for partial vertical stabiliser losses of more than approximately 70% (span vertical stabiliser tip loss). The full nonlinear aircraft model was linearised about valid flight equilibrium trim conditions. Two lateral-directional trim configurations, namely wings-level and small bank angle, were investigated. The Newton-Raphson method was used to solve the nonlinear force and moment equations to obtain the straight and level flight trim values as a function of the percentage

of wing loss and percentage of stabiliser losses respectively. The feasibility of maintaining flight was evaluated for all damage cases by checking whether the required equilibrium actuator deflections are within the range of physically realisable actuator deflections for the aircraft. From the linearised aircraft model, the aircraft's natural modes of motion were investigated as a function of percentage wing loss and stabiliser losses respectively. It was found that partial horizontal stabiliser loss mostly affects the short period mode of the aircraft, partial wing loss mostly affects the roll mode and short period mode of the aircraft, and partial vertical stabiliser loss mostly affects the Dutch roll mode of the aircraft. Furthermore, the coupling of the longitudinal dynamics into the lateral-directional dynamics and vice versa were investigated. It was found for asymmetrical damage that the longitudinal dynamics do couple into the lateral-directional dynamics.

A fixed-gain fault-tolerant flight control system was designed that is able to land a fixed-wing aircraft after it has suffered partial wing loss and partial stabiliser losses. The design strategy for the flight control system was to ensure that the inner-loop controllers remain stable and within acceptable transient response specifications when the aircraft has suffered partial wing loss and stabiliser losses. A successive loop closure control structure was used to design the outer-loop controllers. This allowed the outer-loop controllers to benefit from the robustness of the inner-loop controllers, enabling the outer-loop controllers to also remain stable throughout all damage cases. The design approach was to find controller gains that provide the best performance for the undamaged aircraft while still providing at least the minimum acceptable performance over all damage cases. The flight control system was developed for autonomous landings, hence controller limitations and sensor biases were taken into account during the development phase. The longitudinal controllers achieved sufficient performance while remaining robust for horizontal stabiliser losses of up to 70% semi-span. The lateral controllers achieved sufficient performance while remaining robust for wing losses of up to 40% semi-span. The directional controllers achieved sufficient performance while remaining robust for vertical stabiliser losses of up to 20% span.

A suitable waypoint navigation and autonomous landing strategy required to achieve the research objectives was proposed. The navigation strategy was structured in such a way that the aircraft could optimally align itself with the runway with minimal cross track position error deviation to ensure an accurate landing. To accomplish this, an open-loop roll angle control circular turns strategy was adopted. This allowed the aircraft to align itself quickly with the runway without excessive roll angle manoeuvres. Two landing strategies were proposed: a single glide slope crabbed landing, and a single glide slope crabbed landing with a complementary sink rate control before touchdown. The former resulted in a more accurate landing, but with a higher sink rate, and the latter in a less accurate landing, but with the desired sink rate. Both the navigation strategy and the landing strategy adhered to aircraft limitations and constraints.

The flight control system was verified in a high-fidelity simulation environment that combined software and hardware, and also with practical flight tests. The simulation environment was used to verify the performance and robustness of the flight control system, and to test the autonomous navigation and landing strategies. It was found that in simulation the flight contol system was able to autonomously navigate and land both the undamaged and damaged aircraft successfully within a defined circle with a radius of 1.5 m. The standard Stellenbosch University test aircraft, modified to account for partial wing, horizontal and vertical stabiliser damage, was used to conduct the practical flight tests. All the tests were conducted according to a flight test plan that was

created to minimise the risk of an aircraft incident. The flight control system successfully landed the undamaged aircraft with acceptable accuracy (6.62 m in-track error and 0.13 m cross track error). Unfortunately, the aircraft was lost due to a remote control malfunction before a successful landing with the damaged aircraft could be achieved. However, it was concluded from studying the practical flight data of the damaged aircraft that the flight control system is robust to partial wing loss and partial stabiliser losses, and the flight control system successfully controlled all the aircraft states necessary to perform an autonomous landing. Since the damaged aircraft model was validated with practical flight test, and since it was concluded that because the flight control system can control the damaged aircraft, and was able to land it successfully in the high-fidelity simulation environment, it is expected that the flight control system would also be able to land the damaged aircraft in a practical flight test.

9.2 Conclusion

A fixed-gain passive fault-tolerant flight control system that is able to land a fixed-wing aircraft after it has suffered partial wing loss and partial stabiliser losses was designed. The flight control system was designed to be robust to 20% wing loss, 70% horizontal stabiliser loss, and 20% vertical stabiliser loss, while retaining the performance required to achieve autonomous landings. In a high-fidelity HIL simulation environment, an aircraft with 20% wing loss, 70% horizontal stabiliser loss, and 20% vertical stabiliser loss achieved successful autonomous landings within a 1.5 m radius circle (aiming for the centre). Furthermore, the flight control system successfully landed the undamaged aircraft with acceptable accuracy (6.62 m in-track error and 0.13 m cross track error) in a practical flight test. Unfortunately, the aircraft was lost due to a remote control malfunction before a successful landing with the damaged aircraft could be achieved. However, by studying the practical flight test data of the damaged aircraft, it was found that the proposed flight control system was robust to 20% wing loss, 70% horizontal stabiliser loss, and 20% vertical stabiliser loss. It was therefore concluded that successful autonomous landings are possible.

9.3 Recommendations

The following recommendations are made for future work that builds on the work presented in this thesis:

1. **Aircraft**

    - Due to all the modifications made to the aircraft to accommodate for partial wing loss and partial stabilisers losses, the aircraft's mass increased significantly. For various safety reasons, the safety pilot was not comfortable when the aircraft flew at too-low airspeeds. The airspeed at which the aircraft flew for the practical flight tests ended up being higher than initially desired. When flying at a higher airspeed, a higher sink rate is experienced, resulting in a harder landing. Furthermore, the controllers will have less time to settle before the aircraft reaches the touchdown point. Modifying the aircraft in an elegant way where the mass does not increase significantly would be beneficial.

2. **Aircraft modelling**

- It was found that even after adding the thin body in AVL to obtain a better estimate of the side force stability and control derivatives, these were still not correctly estimated. This was noticed during the rudder doublet tests. Using a combination of software packages (use each package's strong points) when obtaining the stability and control derivatives will lead to a better mathematical model.

3. **Aircraft stability analysis**

   - In this project, the stability analysis was only done for horizontal stabiliser damage of up to 100% semi-span. It was found that the aircraft remained longitudinally statically stable and that the aircraft could be trimmed with 100% semi-span horizontal stabiliser loss. A stability analysis can therefore be conducted on more than 100% semi-span horizontal stabiliser loss.

4. **Flight control system**

   - The NSA, LSA and roll rate inner-loop controllers were all designed on the reduced-order models developed by Peddle [7]. The reduced-order models were developed by making various assumptions which are typically true for symmetrical conventional aircraft. Due to the asymmetry of an aircraft with partial wing loss and partial horizontal stabiliser loss, the reduced-order models become less representative. The reduced-order models can be extended to account for some asymmetrical behaviour, for example centre of mass shift (in the Y_B-axis).

   - To achieve better performance, fault detection combined with gain scheduling can be implemented. A fault detection system can detect when the aircraft suffered damage, after which a robust set of gains can be scheduled. To maintain reliability, the scheduled gains must be robust as, described in this thesis.

   - In this project, the cruise airspeed was very close to the approach airspeed, and therefore the controller gains were not scheduled based on airspeed. The flight control system can be extended to schedule gains based on the aircraft's airspeed.

5. **Navigation and landing**

   - The turn radius based strategy adopted for circular turns did not perform as well as intended in the practical flight tests. Alternative strategies can be investigated and implemented to improve the cross track position error out of the turns.

   - The flaps of the aircraft were not used in this project. By using the flaps, lower landing airspeeds can be achieved and therefore lower sink rates. The flaps can also be used as flaperons to increase the roll authority of the aircraft. This will in turn increase the amount of wing loss that can be maintained for straight and level flight. However, if more wing is lost, the next limiting factor for landing the aircraft will become airspeeds that are too high.

- A de-crab controller was never designed in this thesis on the assumption that when the aircraft is trimmed in wings-level configuration, the sideslip angle (in windless conditions) would remain small and thus a safe landing would be possible. A de-crab controller can be designed to reduce the sideslip angle upon touchdown.

Appendices

A.1 Vector Operations

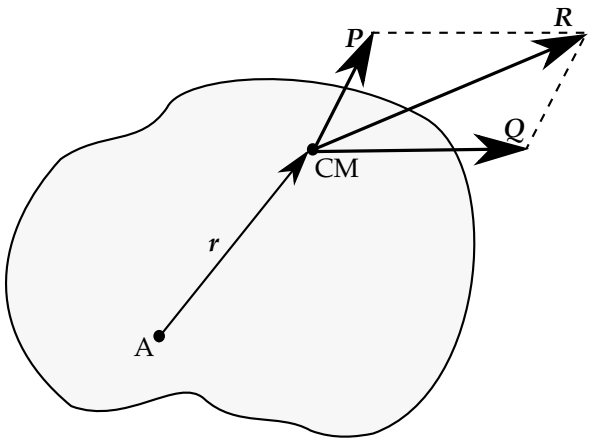

Figure A.1: Free body diagram with vector notations.

A.1.1 Vector notation

Vector quantities are printed in capital or lower case boldface type, for example $\boldsymbol{P}$ or $\mathbf{r}$. Matrices are capital non math boldface type, for example $\mathbf{P}$.

A.1.2 Unit vectors

The unit vectors are given as

$$\boldsymbol{i},\ \boldsymbol{j},\ \boldsymbol{k} \tag{A.1.1}$$

so that

$$\boldsymbol{P} = P_x\boldsymbol{i} + P_y\boldsymbol{j} + P_z\boldsymbol{k} \tag{A.1.2}$$

where

$$|\boldsymbol{P}| = \sqrt{P_x^2 + P_y^2 + P_z^2} \tag{A.1.3}$$

A.1.3 Differentiation of a vector

$$\frac{d\boldsymbol{P}}{dt} = \dot{\boldsymbol{P}} = \dot{P}\boldsymbol{i} + \dot{P}_y\boldsymbol{j} + \dot{P}_z\boldsymbol{k} \tag{A.1.4}$$

$$\frac{d(\boldsymbol{P}\times\boldsymbol{Q})}{dt} = \boldsymbol{P}\times\dot{\boldsymbol{Q}} + \dot{\boldsymbol{P}}\times\boldsymbol{Q} \tag{A.1.5}$$

A.1.4 The time derivative of a vector measured from a translating-rotating system

The time derivative of any vector $\boldsymbol{P}$ as observed from the fixed X, Y, Z reference frame is equal to the time rate of change of $\boldsymbol{P}$ as observed from the x, y, z translating-rotating reference frame [27]

$$\dot{\boldsymbol{P}}_{XYZ} = \dot{\boldsymbol{P}}_{xyz} + \boldsymbol{\omega} \times \boldsymbol{P} \tag{A.1.6}$$

where $\boldsymbol{\omega}$ is the angular velocity of the x ,y ,z reference frame measured from the fixed X ,Y ,Z reference frame.

A.2 Kinematics

A.2.1 Relative general plane motion - Translating axis

$$\mathbf{v}_{CM} = \mathbf{v}_A + \boldsymbol{\omega} \times \mathbf{r} \tag{A.2.1}$$

where $\boldsymbol{\omega}$ is the angular velocity of the body.

A.2.2 Relative general plane motion - Translating and rotating axis

$$\mathbf{v}_{CM} = \mathbf{v}_A + \boldsymbol{\omega} \times \mathbf{r} + \dot{\mathbf{r}}_{xyz} \tag{A.2.2}$$

where $\boldsymbol{\omega}$ is the angular velocity of the x ,y ,z reference frame measured from the fixed X ,Y ,Z reference frame.

A.3 Varignon's Theorem

Varignon's Theorem states that the moment of a force about any point is equal to the algebraic sum of the moments of its components about that point.

$$\boldsymbol{M}_A = \mathbf{r}\boldsymbol{R} = \mathbf{r}\boldsymbol{P} + \mathbf{r}\boldsymbol{Q} \tag{A.3.1}$$

where

$$\boldsymbol{R} = \boldsymbol{P} + \boldsymbol{Q} \tag{A.3.2}$$

A.4 Small angle Approximation

The standard small angle approximations are given by

$$\cos A \approx 1 \tag{A.4.1}$$

$$\sin A \approx A \tag{A.4.2}$$

where A is a small angle.

B.1 Undamaged Aircraft

This section lists the physical parameters of the undamaged aircraft.

B.1.1 Airframe Specifications

B.1.1.1 Mass

The total aircraft mass is

$$m = 7.71kg \tag{B.1.1}$$

This includes the mass of the airframe (with all the modifications), the avionics, the actuators and the batteries.

B.1.1.2 Moment of Inertia

The moment of inertia of the aircraft was determined by Smit [5] by means of the double pendulum method, which is summarised by [2]. In short the method involves suspending the aircraft by two equally long strings such that the strings are parallel to the moment of inertia axis being calculated. The aircraft is rotated slightly about this axis and released. It will begin to oscillate and this period is timed and the moment of inertia is then calculated as[10]

$$I = \frac{mgd^2}{4\pi^2 l} T^2 \tag{B.1.2}$$

where m is the mass of the aircraft, d the distance between each string, l is the length of the string and T is the period of oscillation. This method only obtains the principal components. As determined by Smit:

$$\boldsymbol{I} = \begin{bmatrix} 0.7212 & 0 & 0 \\ 0 & 0.5139 & 0 \\ 0 & 0 & 0.9239 \end{bmatrix} \tag{B.1.3}$$

B.1.1.3 Airframe Geometric Properties

Table B.1: Test aircraft specifications

Parameter	Symbol	Value	Unit
Root chord	c_r	0.373	m
Tip chord	c_t	0.333	m
Mean cord	$\bar{c}$	0.363	m
Wing Span	b	1.918	m
Wing Area	S	0.6975	m^2
Aspect ratio	A	5.28	ND
Oswald efficiency factor	e	0.858	ND

The Oswald efficiency factor is estimated as according to Nita et al. [30]. An empirical diagram is given which was obtained from flight testing data. Nita proposed to estimate the Oswald efficiency factor as

$$e = \frac{1}{Q + P\pi A} \tag{B.1.4}$$

where Q and P are constant experimental based values 1.05 and 0.007 respectively and A is the reference aspect ratio.

B.1.1.4 Non-dimensional Stability and Control Derivatives

The non-dimensional stability and control derivatives of the aircraft are obtained the Athena Vortex Lattice (AVL). The aircraft geometry is constructed in AVL by measuring the dimensions of the Phoenix Trainer 60. Figure B.1 shows the geometry of the airframe constructed in an AVL editor. Note that a flat fuselage is added in order to obtain a better estimate of the side forces acting on the fuselage of the aircraft. Alternatively the fuselage will be ignored completely. The stability

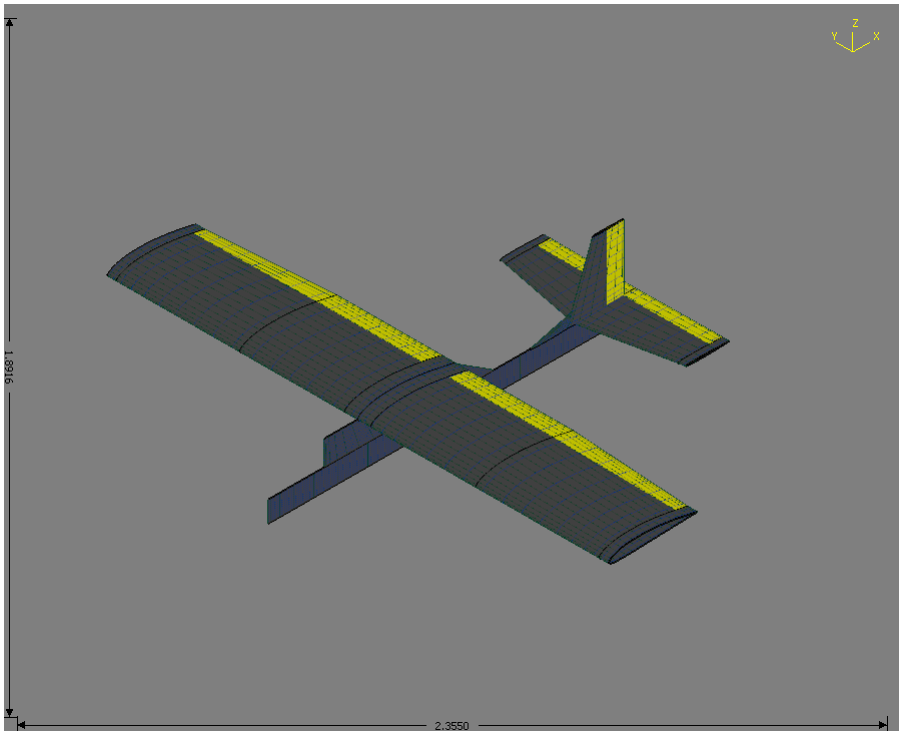

Figure B.1: Aircraft geometry in AVL using dimensions for the Phoenix Trainer 60

and control derivatives calculated by AVL is presented in Tables B.2 and B.3 respectively.

Table B.2: Force Derivatives as obtained from AVL

Lift force	Value	Side force	Value	Drag force	Value
C_{L_0}	0.243900	C_{y_0}	0.000000	C_{D_0}	0.0344000
C_{L_α}	4.229354	C_{y_α}	-0.000002		
C_{L_β}	0.000000	C_{y_β}	-0.216357		
C_{L_P}	0.000000	C_{y_P}	0.118043		
C_{L_Q}	7.204948	C_{y_Q}	-0.000003		
C_{L_R}	-0.000001	C_{y_R}	0.152937		
$C_{L_{\delta_A}}$	0.000008	$C_{y_{\delta_A}}$	0.000136		
$C_{L_{\delta_E}}$	0.418443	$C_{y_{\delta_E}}$	0.000000		
$C_{L_{\delta_R}}$	0.000000	$C_{y_{\delta_R}}$	0.115706		

Table B.3: Moment Derivatives as obtained from AVL

Roll moment	Value	Pitch moment	Value	Yaw moment	Value
C_{l_0}	0.000000	C_{m_0}	-0.0311000	C_{n_0}	0.000000
C_{l_α}	0.000001	C_{m_α}	-0.864255	C_{n_α}	0.000009
C_{l_β}	-0.060435	C_{m_β}	0.000001	C_{n_β}	0.040747
C_{l_P}	-0.414460	C_{m_P}	0.000002	C_{n_P}	-0.034068
C_{l_Q}	0.000000	C_{m_Q}	-7.387185	C_{n_Q}	0.000004
C_{l_R}	0.136337	C_{m_R}	-0.000001	C_{n_R}	-0.070245
$C_{l_{\delta_A}}$	-0.257158	$C_{m_{\delta_A}}$	0.000002	$C_{n_{\delta_A}}$	0.007271
$C_{l_{\delta_E}}$	0.000000	$C_{m_{\delta_E}}$	-0.928991	$C_{n_{\delta_E}}$	-0.000000
$C_{l_{\delta_R}}$	0.000736	$C_{m_{\delta_R}}$	0.000000	$C_{n_{\delta_R}}$	-0.050348

B.1.2 Engine Thrust

A static thrust test was used to determine the maximum aircraft engine thrust and time constant:

$$T_{max} \approx 48N \tag{B.1.5}$$

$$\tau_T \approx 0.2s \tag{B.1.6}$$

B.2 Damaged Aircraft

This section lists the physical parameters of the aircraft with 20% wing loss, 70% horizontal stabiliser loss and 20% vertical stabiliser loss.

B.2.1 Airframe Specifications

B.2.1.1 Mass

The total aircraft mass is

$$m = 7.430kg \tag{B.2.1}$$

This includes the mass of the airframe (with all the modifications), the avionics, the actuators and the batteries.

B.2.1.2 Moment of Inertia

The moment of inertia of the undamaged aircraft was determined by Smit [5] and was stated the subsection B.1.1.2. A replica of the Phoenix Trainer 60 aircraft was constructed in Autodesk Inventor which was used to determine the centre of mass shift and the moment for inertia of the damaged aircraft. The moment of inertia of the damaged aircraft is given by,

$$\boldsymbol{I} = \begin{bmatrix} 0.61060 & -0.00034 & -0.01925 \\ -0.00034 & 0.49320 & 0.00012 \\ -0.01925 & 0.00012 & 0.77330 \end{bmatrix} \tag{B.2.2}$$

The centre of mass shift is given by,

$$\bar{\boldsymbol{\rho}} = \begin{bmatrix} 0.01457 & -0.03100 & 0.00303 \end{bmatrix} \tag{B.2.3}$$

B.2.1.3 Airframe Geometric Properties

Table B.4: Damaged test aircraft specifications

Parameter	Symbol	Value	Unit
Root chord	c_r	0.373	m
Tip chord	c_t	0.333	m
Mean cord	$\bar{c}$	0.363	m
Wing Span	b	1.918	m
Wing Area	S	0.6975	m^2
Aspect ratio	A	5.28	ND
Oswald efficiency factor	e	0.858	ND

The reference standard mean chord $\bar{c}$, the reference wing span b and the wing reference area S are all kept constant throughout the modelling process. All the effects due to damage are therefore encapsulated within the non-dimensional stability and control derivatives. The Oswald efficiency factor is calculated as stated in section B.1.1.3.

B.2.1.4 Non-dimensional Stability and Control Derivatives

The non-dimensional stability and control derivatives of the aircraft are obtained the Athena Vortex Lattice (AVL). The aircraft geometry is constructed in AVL by measuring the dimensions of the Phoenix Trainer 60. Figure B.1 shows the geometry of the airframe constructed in an AVL editor. Note that a flat fuselage is added in order to obtain a better estimate of the side forces acting on the fuselage of the aircraft. Alternatively the fuselage will be ignored completely. The stability and control derivatives calculated by AVL are presented in Tables B.5 and B.6 respectively.

Table B.5: Force Derivatives as obtained from AVL

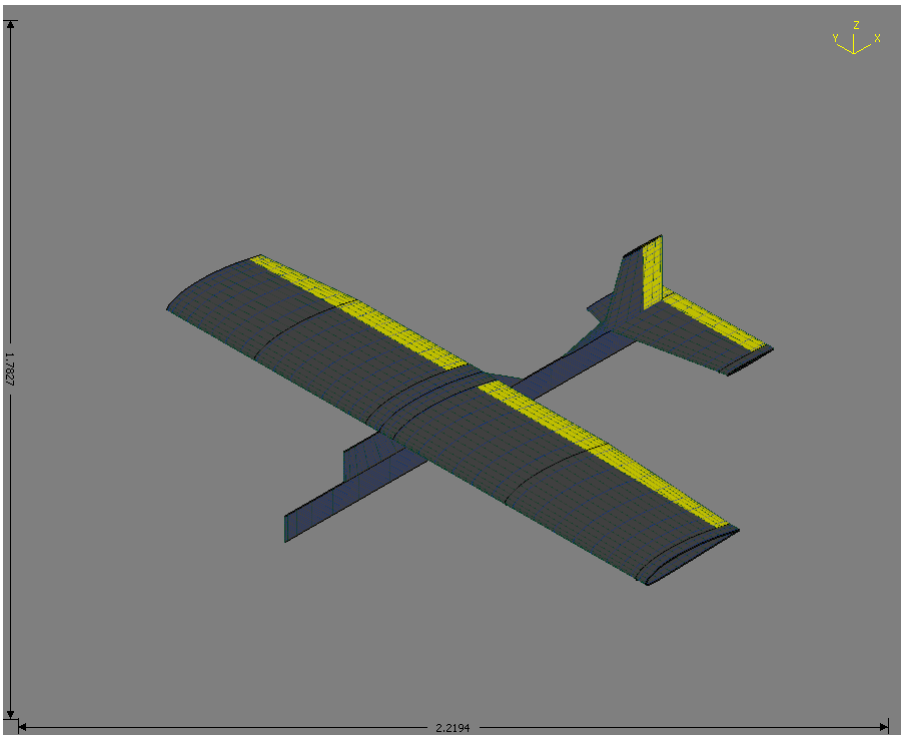

Figure B.2: Aircraft geometry in AVL using dimensions for the Phoenix Trainer 60

Lift force	Value	Side force	Value	Drag force	Value
C_{L_0}	0.215900	C_{y_0}	0.0002695	C_{D_0}	0.036200
C_{L_α}	3.445177	C_{y_α}	-0.001713		
C_{L_β}	0.045337	C_{y_β}	-0.173667		
C_{L_P}	-0.368927	C_{y_P}	0.086587		
C_{L_Q}	5.000596	C_{y_Q}	-0.040054		
C_{L_R}	0.078268	C_{y_R}	0.086186		
$C_{L_{\delta_A}}$	-0.206779	$C_{y_{\delta_A}}$	-0.003575		
$C_{L_{\delta_E}}$	0.217614	$C_{y_{\delta_E}}$	-0.005366		
$C_{L_{\delta_R}}$	-0.018219	$C_{y_{\delta_R}}$	0.072020		

Table B.6: Moment Derivatives as obtained from AVL

Roll moment	Value	Pitch moment	Value	Yaw moment	Value
C_{l_0}	0.011200	C_{m_0}	-0.040400	C_{n_0}	-0.000360
C_{l_α}	0.187239	C_{m_α}	-0.378381	C_{n_α}	-0.015173
C_{l_β}	-0.052910	C_{m_β}	-0.092696	C_{n_β}	0.022947
C_{l_P}	-0.299601	C_{m_P}	0.023437	C_{n_P}	-0.020587
C_{l_Q}	0.284106	C_{m_Q}	-3.912634	C_{n_Q}	0.002774
C_{l_R}	0.101521	C_{m_R}	0.027705	C_{n_R}	-0.039160
$C_{l_{\delta_A}}$	-0.189341	$C_{m_{\delta_A}}$	0.053021	$C_{n_{\delta_A}}$	0.007238
$C_{l_{\delta_E}}$	0.014549	$C_{m_{\delta_E}}$	-0.491848	$C_{n_{\delta_E}}$	0.002479
$C_{l_{\delta_R}}$	0.000429	$C_{m_{\delta_R}}$	0.038561	$C_{n_{\delta_R}}$	-0.031659

B.2.2 Engine Thrust

A static thrust test was used to determine the maximum aircraft engine thrust and time constant:

$$T_{max} \approx 48N \tag{B.2.4}$$

$$\tau_T \approx 0.2s \tag{B.2.5}$$

The maximum thrust and thrust time constant is not affected by the structural damage.

The aerodynamic forces and moments are shown here as a function of partial wing loss, partial horizontal stabiliser loss, and partial vertical stabiliser loss respectively.

C.1 Aerodynamic Forces and Moments with Partial Wing Tip Loss

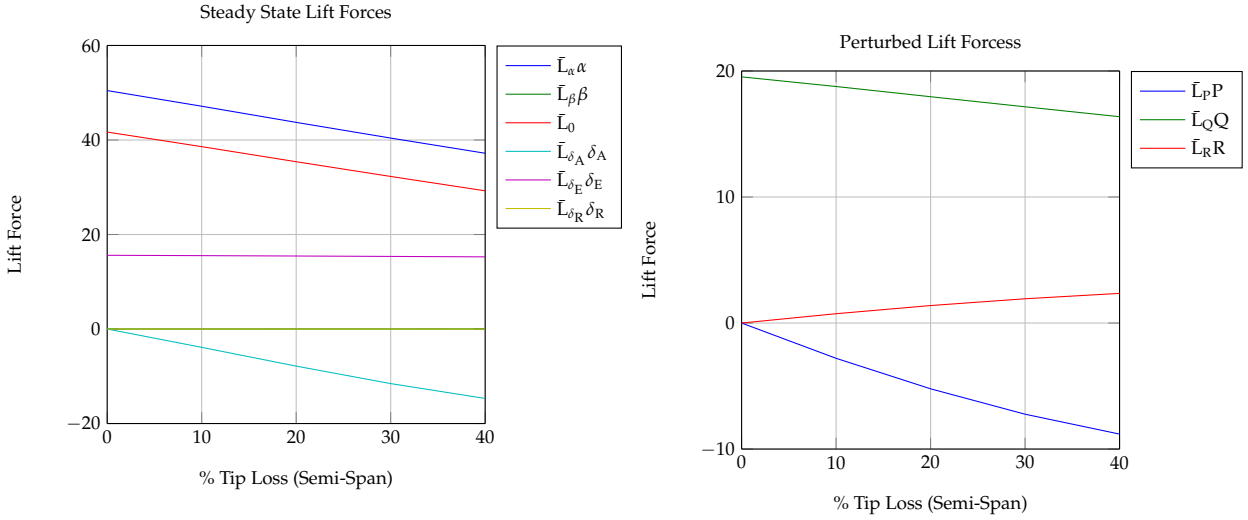

(a) Steady state lift forces

(b) Perturbed lift forces

Figure C.1: Aerodynamic lift forces with wing loss

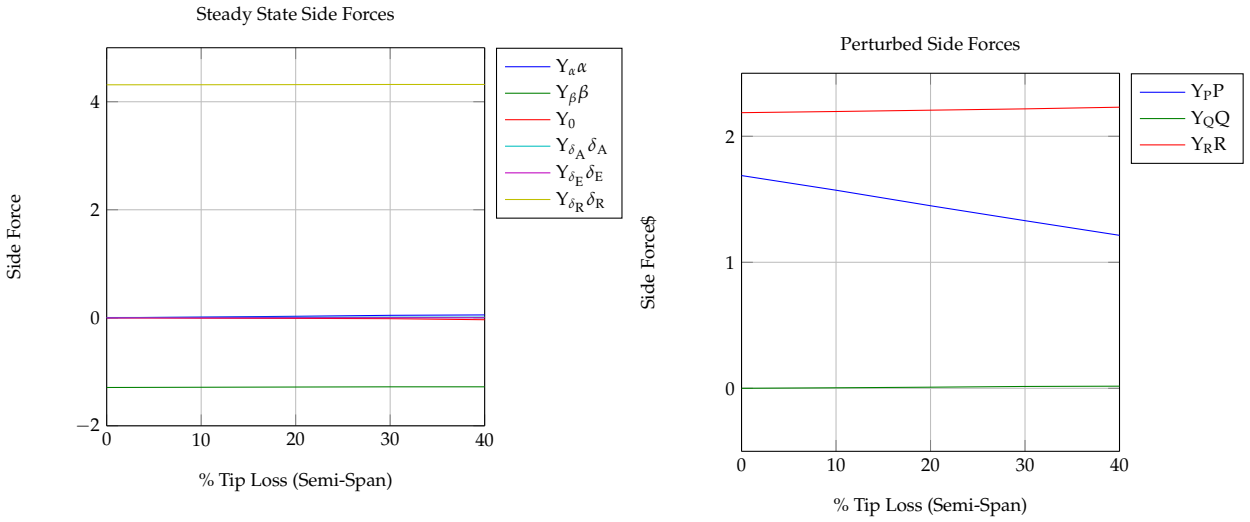

(a) Steady state lift forces (b) Perturbed lift forces

Figure C.2: Aerodynamic side forces with wing loss

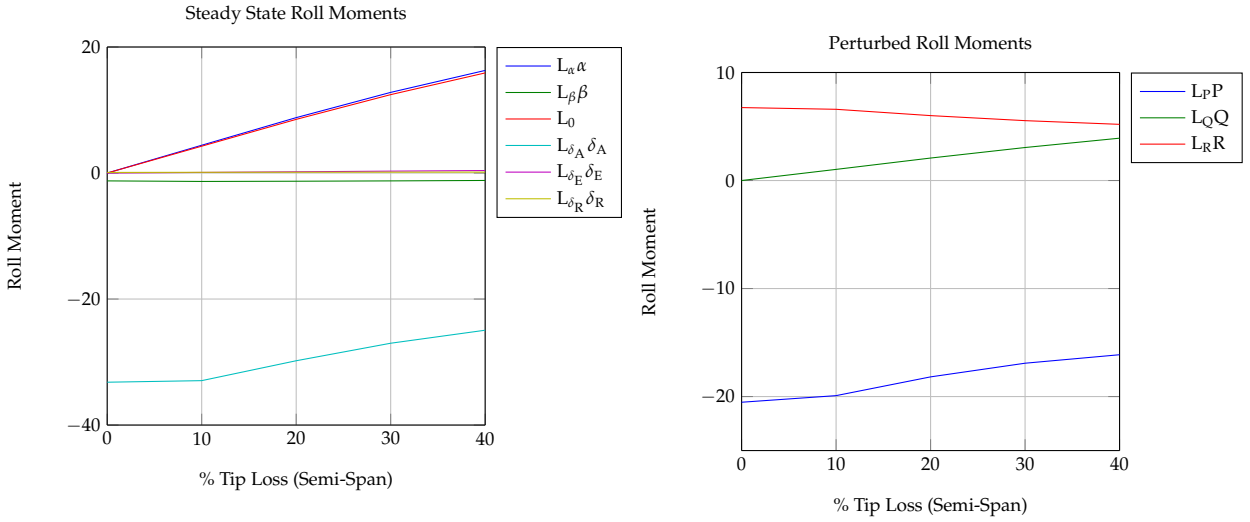

(a) Steady state lift forces (b) Perturbed lift forces

Figure C.3: Aerodynamic rolling moments with wing loss

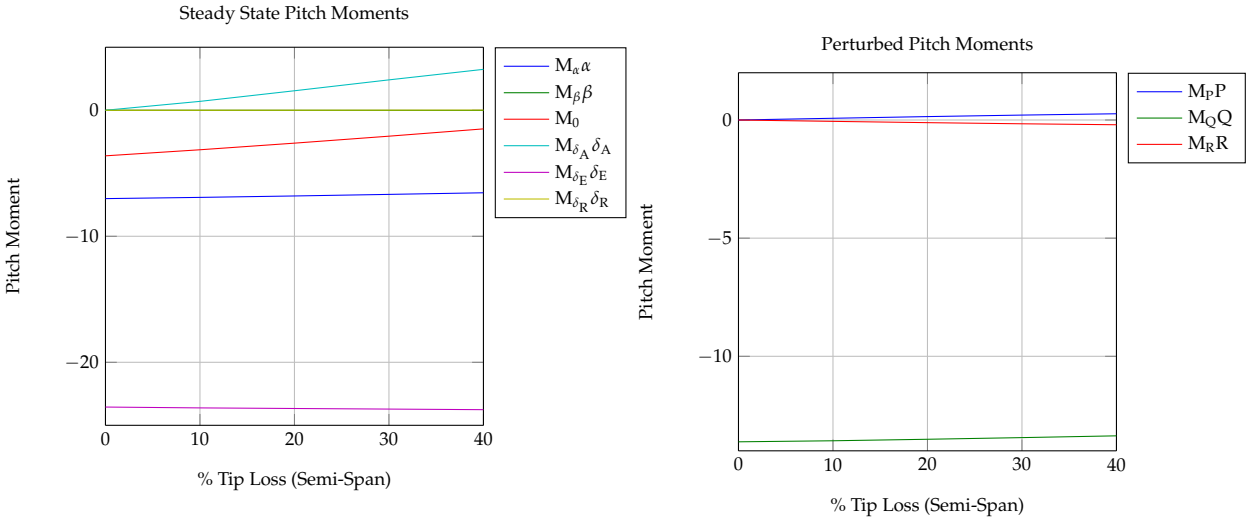

(a) Steady state lift forces (b) Perturbed lift forces

Figure C.4: Aerodynamic pitching moments with wing loss

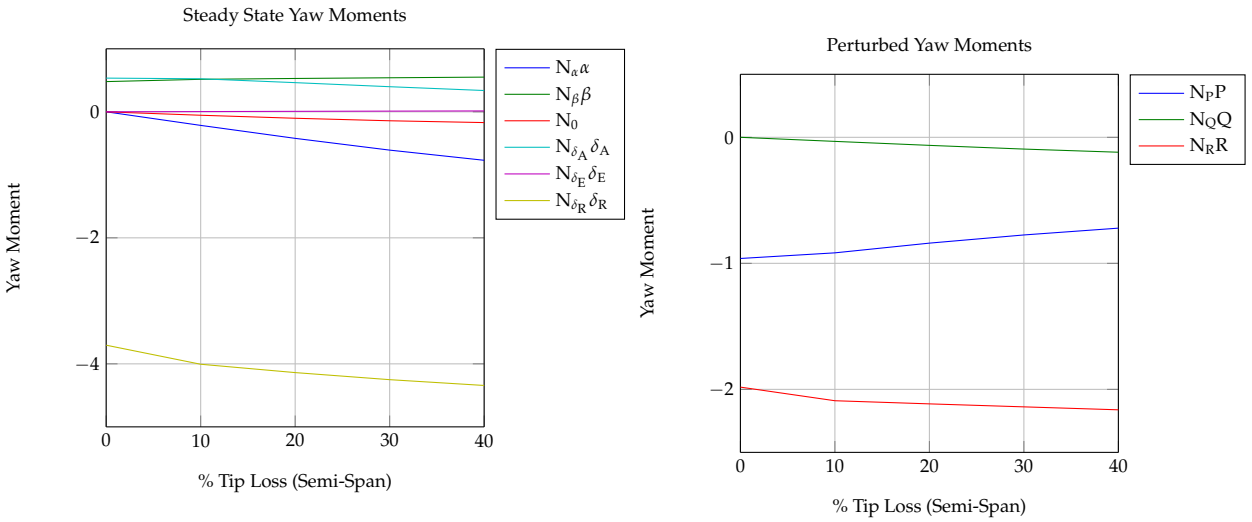

(a) Steady state lift forces (b) Perturbed lift forces

Figure C.5: Aerodynamic yawing moments with wing loss

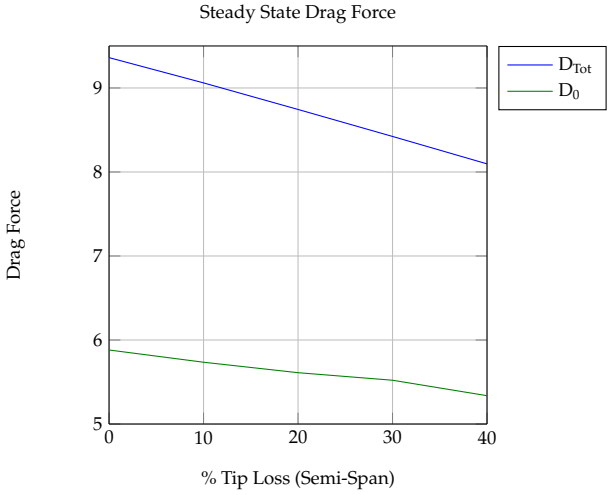

Figure C.6: Aerodynamic drag forces with wing loss

C.2 Aerodynamic Forces and Moments with Partial Horizontal Stabiliser Tip Loss

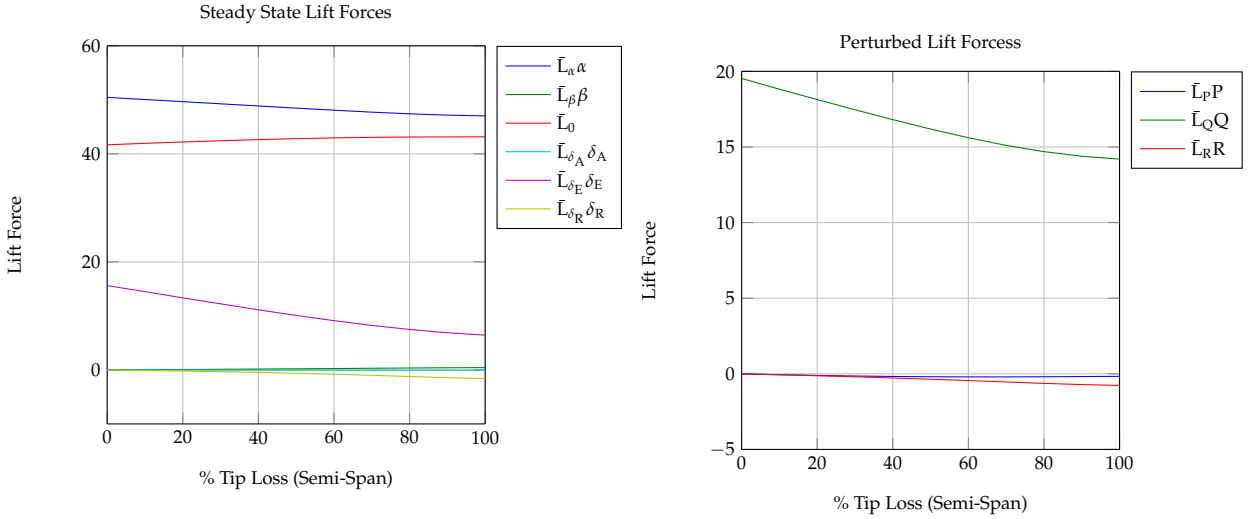

(a) Steady state lift forces (b) Perturbed lift forces

Figure C.7: Aerodynamic lift forces with horizontal stabiliser loss

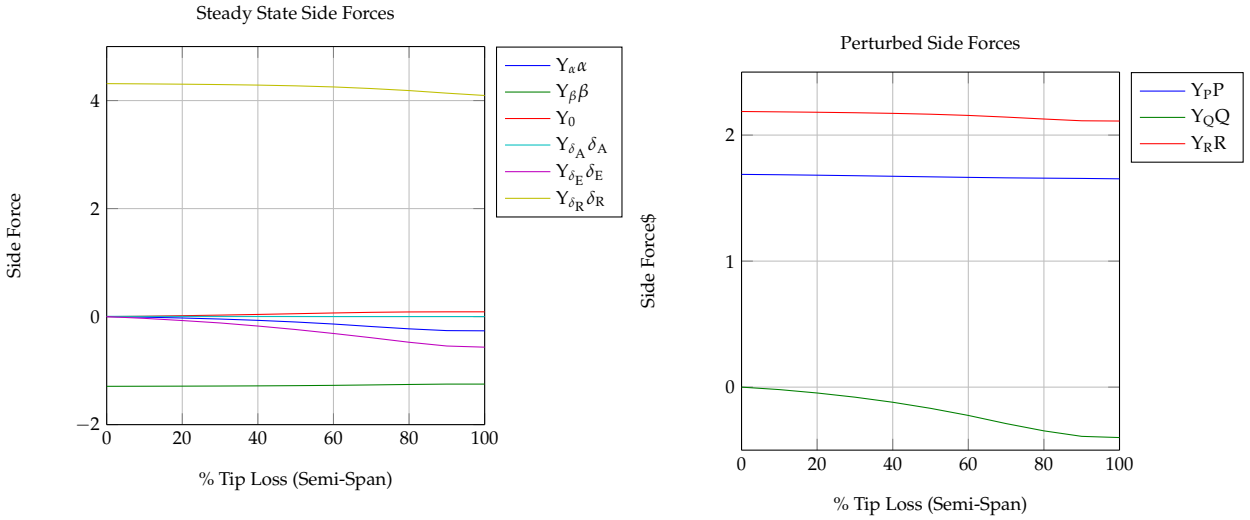

(a) Steady state lift forces (b) Perturbed lift forces

Figure C.8: Aerodynamic side forces with horizontal stabiliser loss

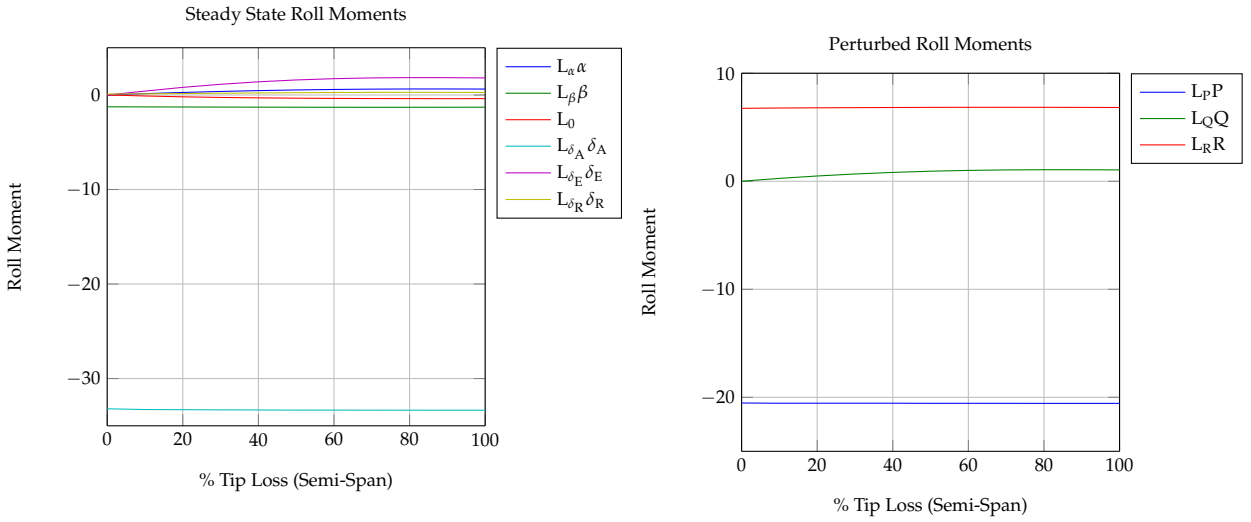

(a) Steady state lift forces (b) Perturbed lift forces

Figure C.9: Aerodynamic rolling moments with horizontal stabiliser loss

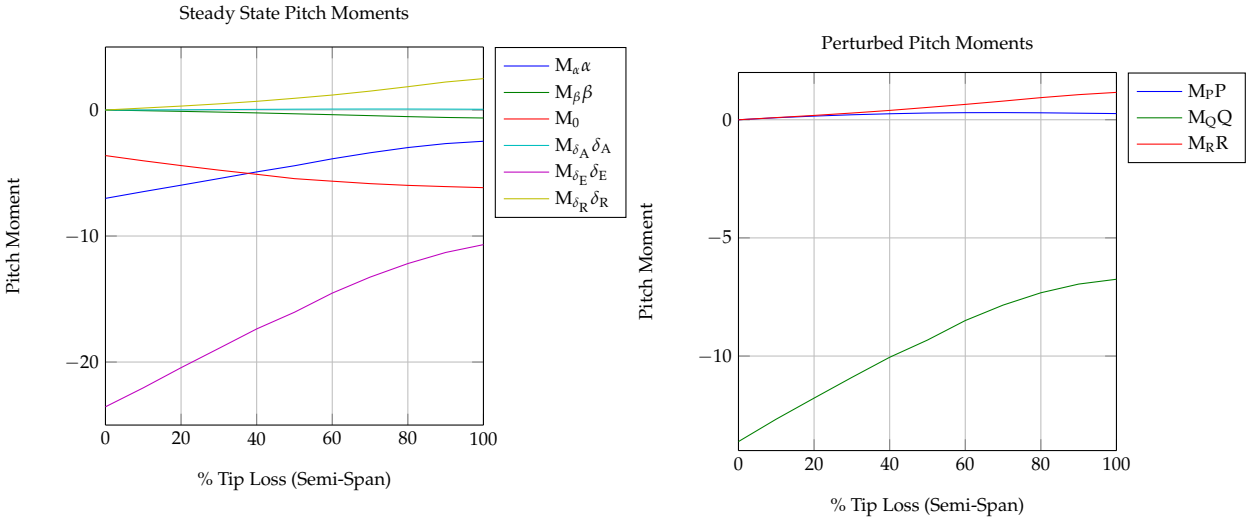

(a) Steady state lift forces (b) Perturbed lift forces

Figure C.10: Aerodynamic pitching moments with horizontal stabiliser loss

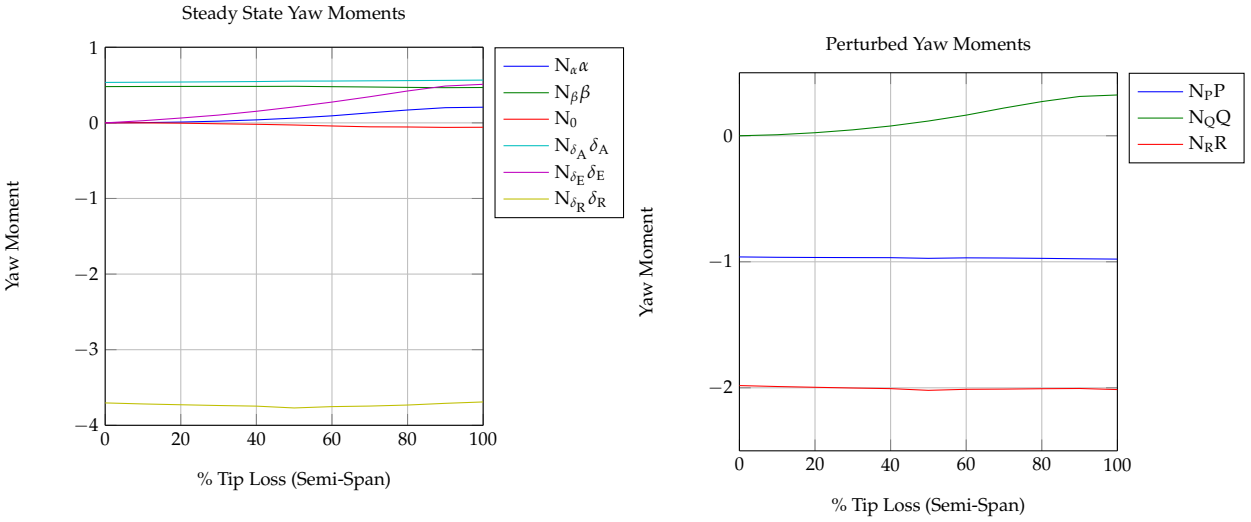

(a) Steady state lift forces (b) Perturbed lift forces

Figure C.11: Aerodynamic yawing moments with horizontal stabiliser loss

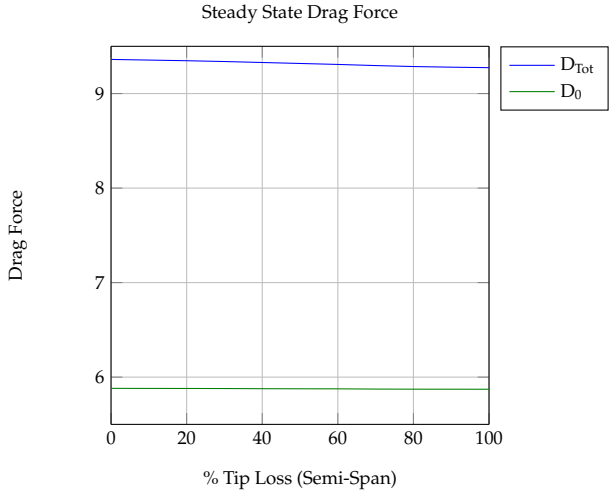

Figure C.12: Aerodynamic drag forces with horizontal stabiliser loss

C.3 Aerodynamic Forces and Moments with Partial Vertical Stabiliser Tip Loss

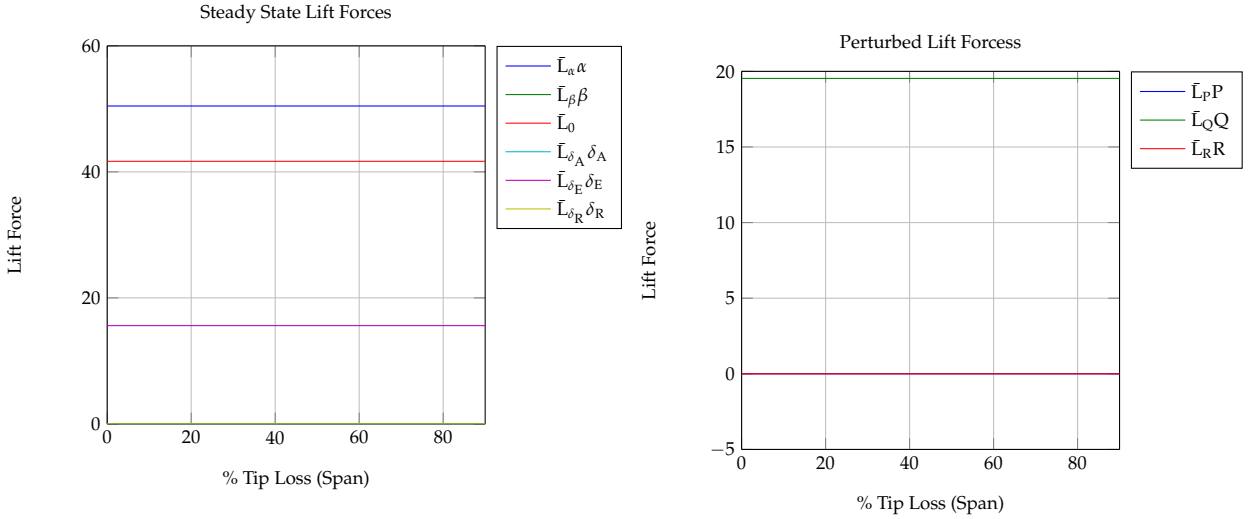

(a) Steady state lift forces (b) Perturbed lift forces

Figure C.13: Aerodynamic lift forces with vertical stabiliser loss

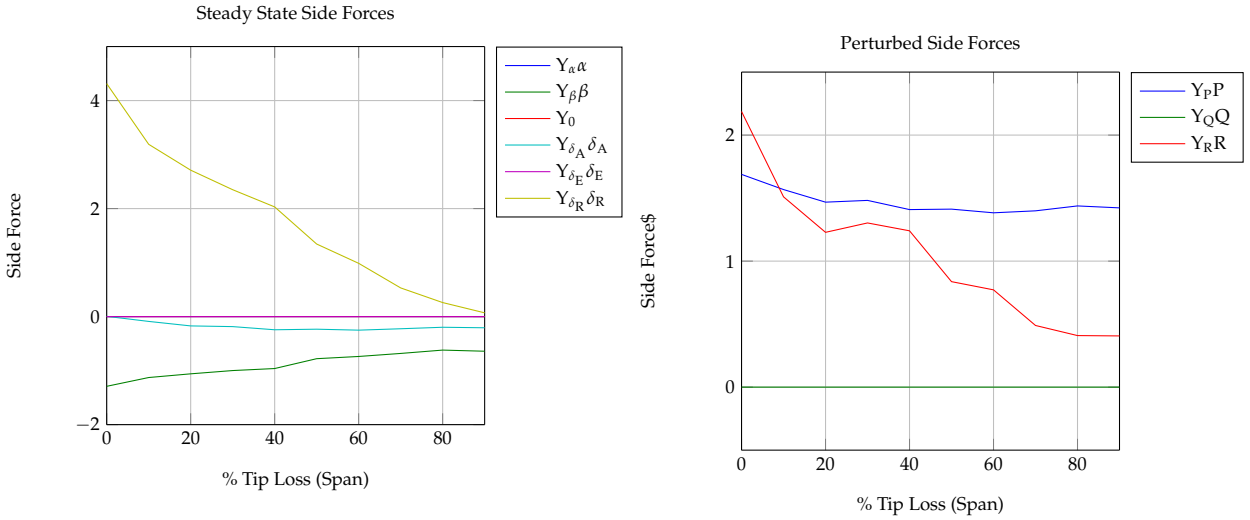

(a) Steady state lift forces (b) Perturbed lift forces

Figure C.14: Aerodynamic side forces with vertical stabiliser loss

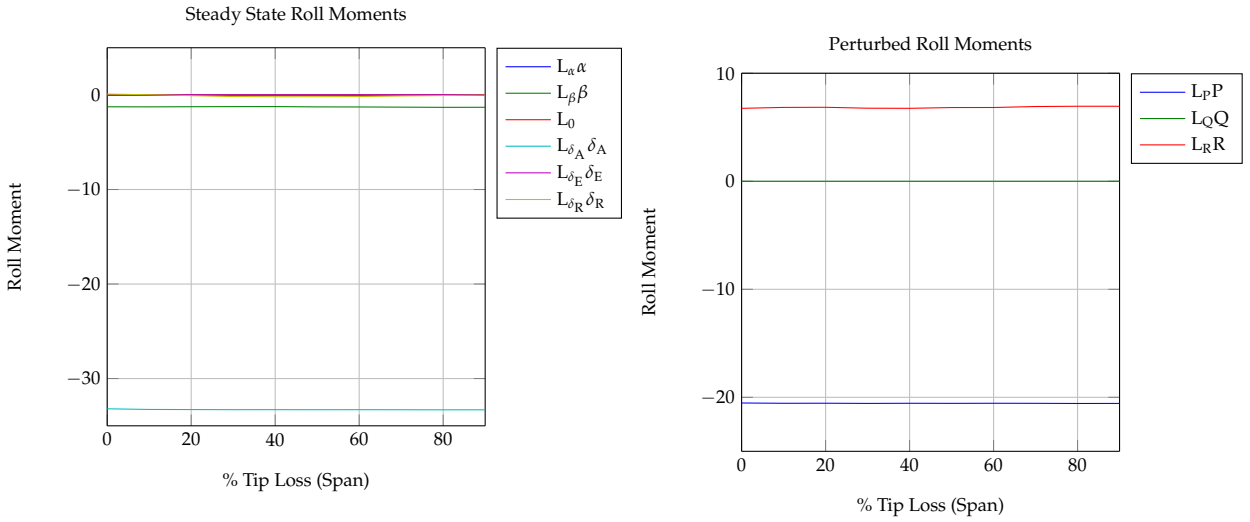

(a) Steady state lift forces (b) Perturbed lift forces

Figure C.15: Aerodynamic rolling moments with vertical stabiliser loss

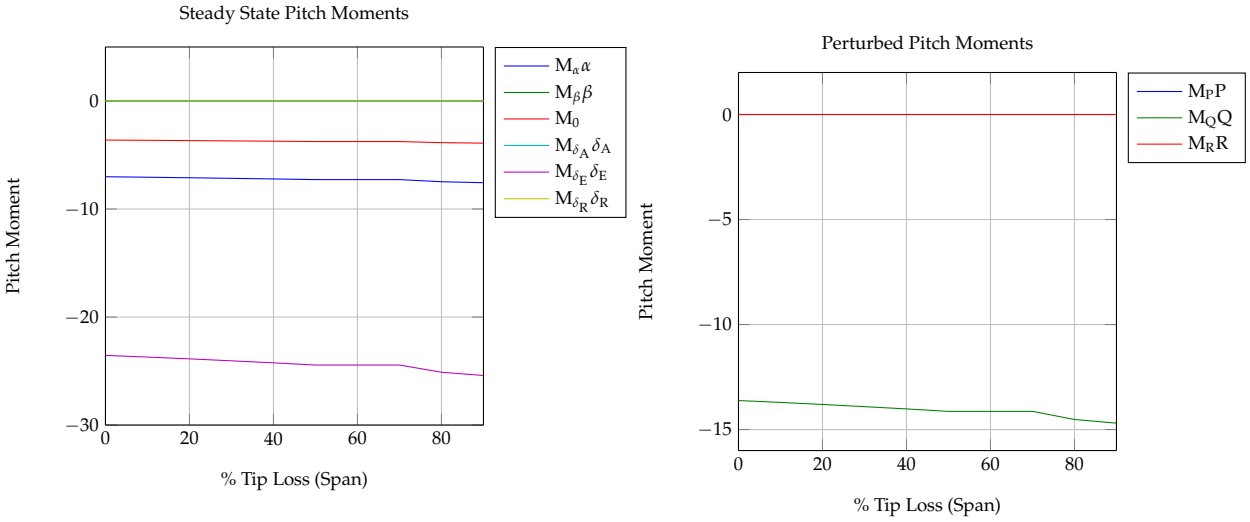

(a) Steady state lift forces (b) Perturbed lift forces

Figure C.16: Aerodynamic pitching moments with vertical stabiliser loss

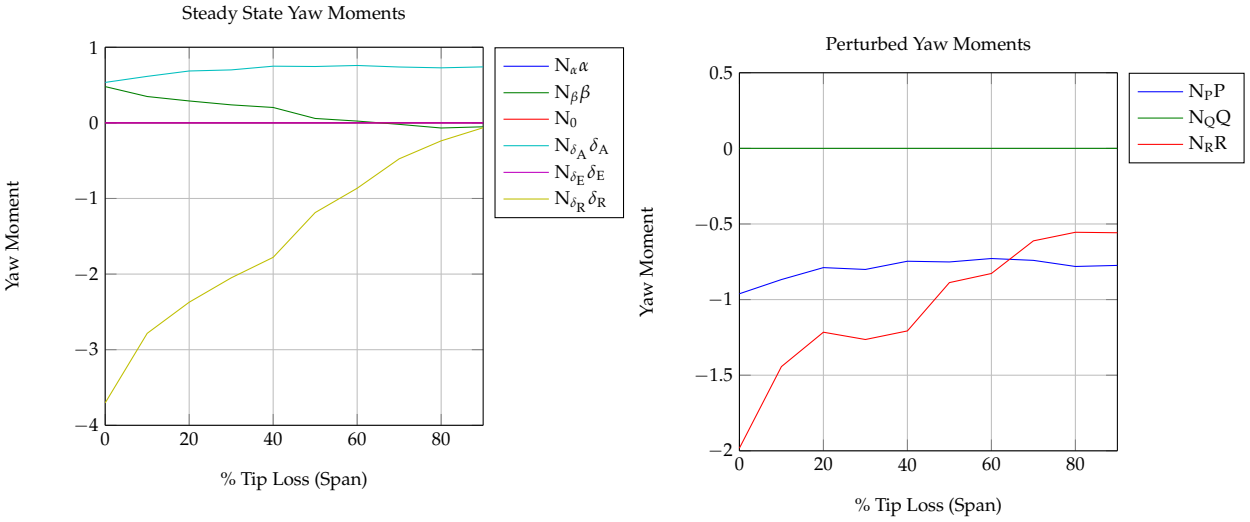

(a) Steady state lift forces (b) Perturbed lift forces

Figure C.17: Aerodynamic yawing moments with vertical stabiliser loss

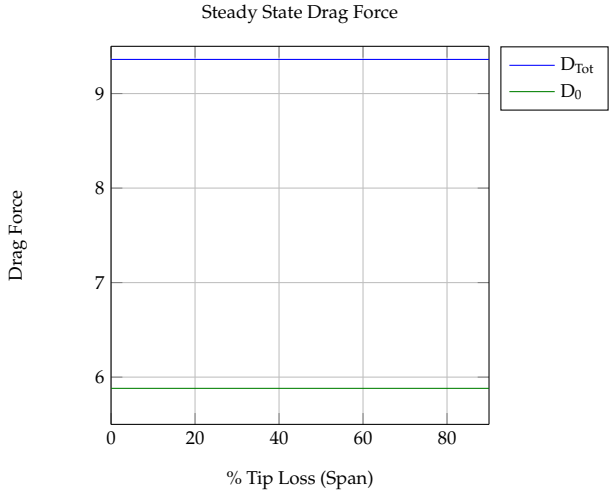

Figure C.18: Aerodynamic drag forces with vertical stabiliser loss

Appendix D includes all the trim value for:

- Partial wing tip loss (0% up to 40% semi-span)
- Partial horizontal stabiliser tip loss(0% up to 100% semi-span)
- Partial vertical stabiliser tip loss(0% up to 50% span)

D.1 Wing Tip Loss

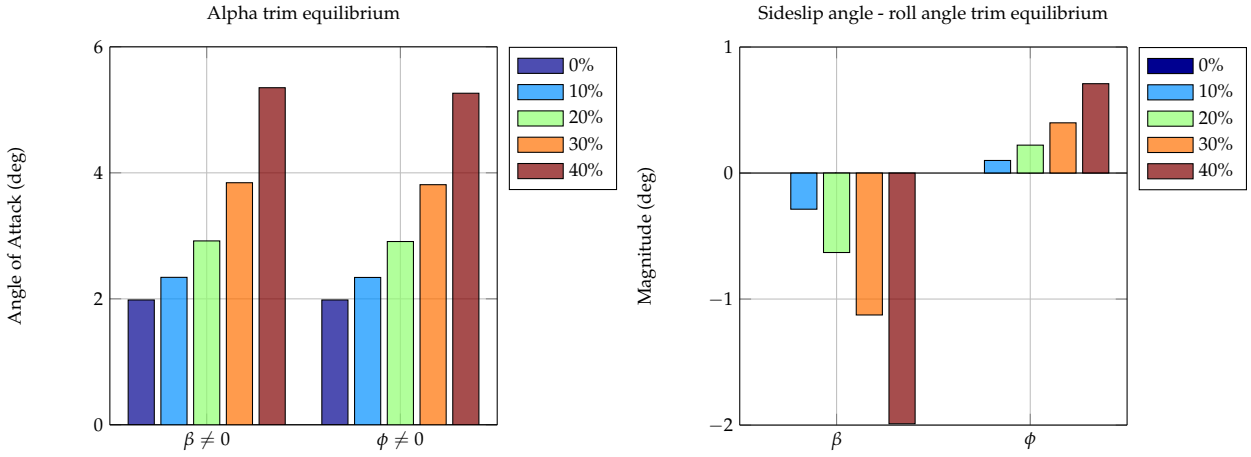

(a) Trim angle of attack

(b) Trim sideslip angle and roll angle

Figure D.1: Trim angle of attack and trim sideslip angle and roll angle for wing damage cases

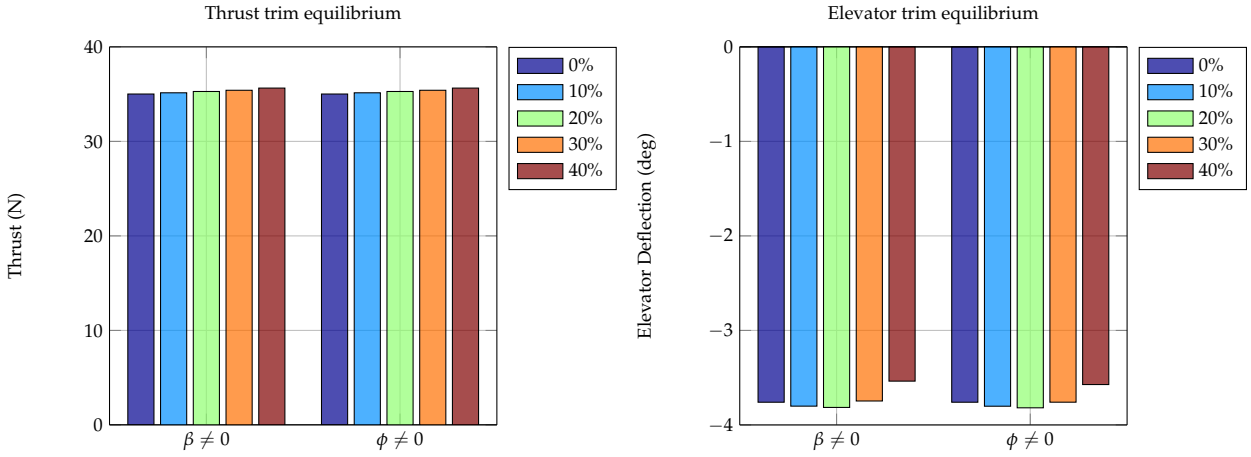

(a) Trim thrust (b) Trim elevator deflection

Figure D.2: Trim thrust and trim elevator deflection for wing damage cases

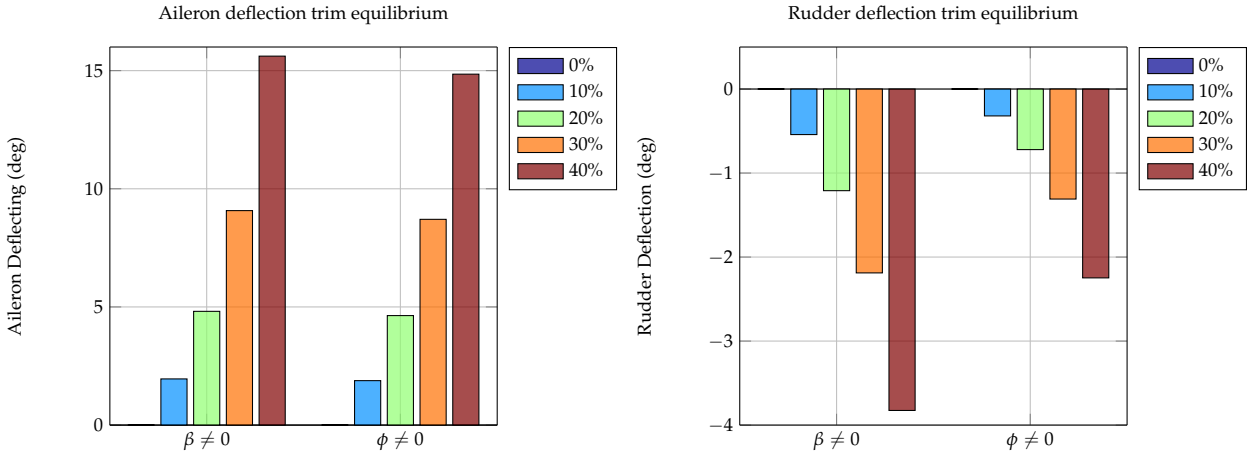

(a) Trim aileron deflection (b) Trim rudder deflection

Figure D.3: Trim aileron and rudder deflections for wing damage cases

D.2 Horizontal Stabiliser Tip Loss

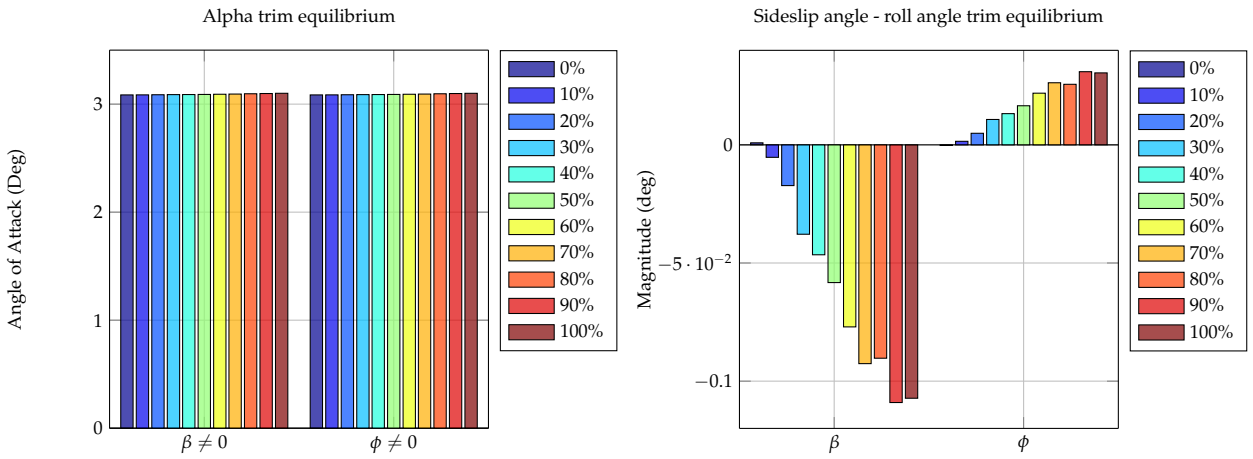

(a) Trim angle of attack (b) Trim sideslip angle and roll angle

Figure D.4: Trim angle of attack and trim sideslip angle and roll angle for horizontal stabiliser damage cases

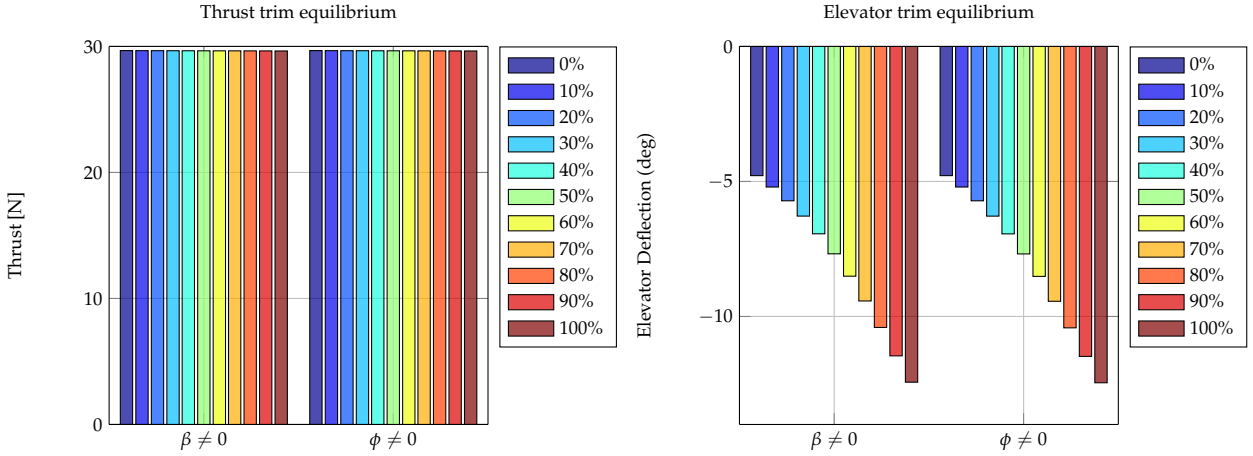

(a) Trim thrust (b) Trim elevator deflection

Figure D.5: Trim thrust and trim elevator deflection for horizontal stabiliser damage cases

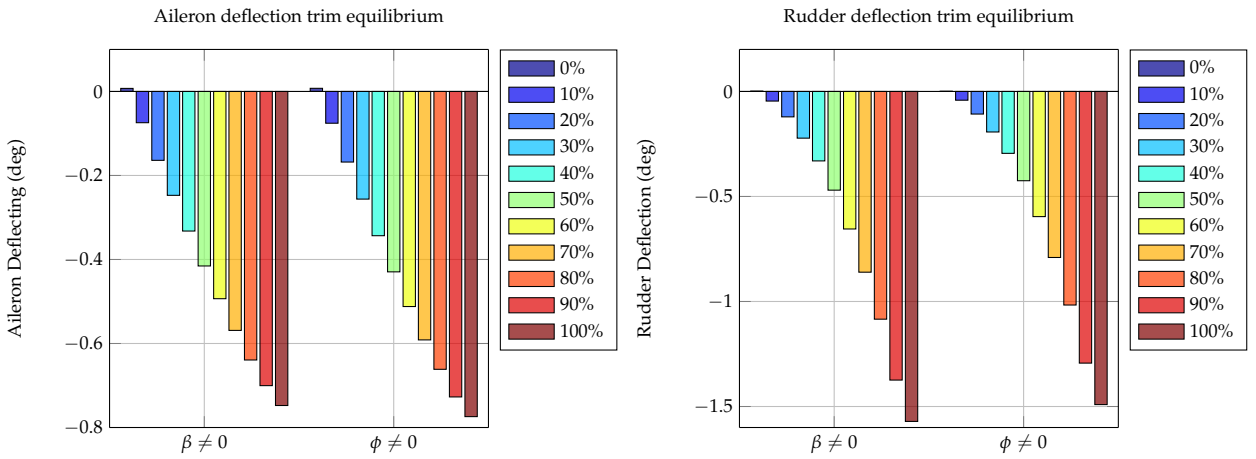

(a) Trim aileron deflection

(b) Trim rudder deflection

Figure D.6: Trim aileron and rudder deflections for horizontal stabiliser damage cases

D.3 Vertical Stabiliser Tip Loss

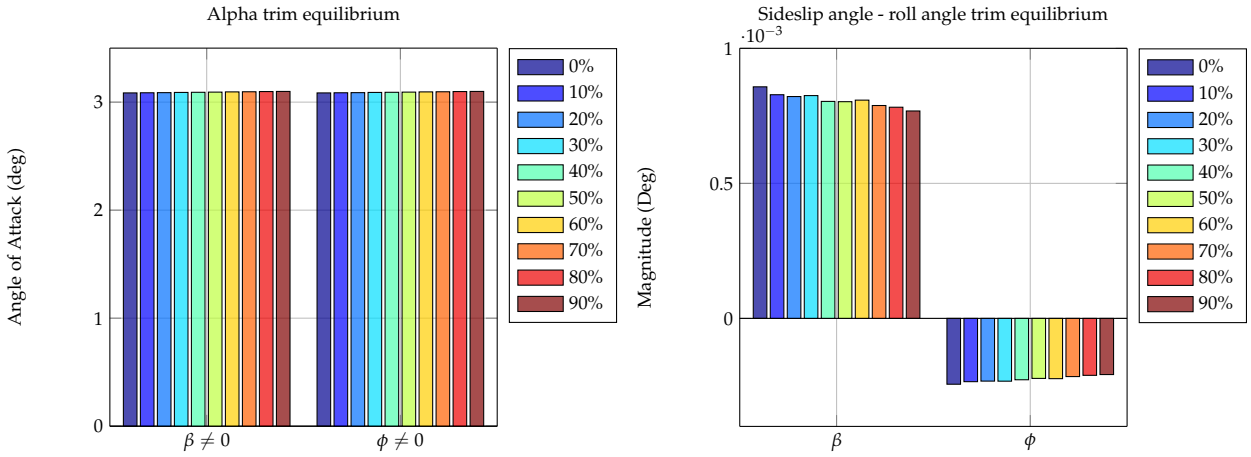

(a) Trim angle of attack (b) Trim sideslip angle and roll angle

Figure D.7: Trim angle of attack and trim sideslip angle and roll angle for vertical stabiliser damage cases

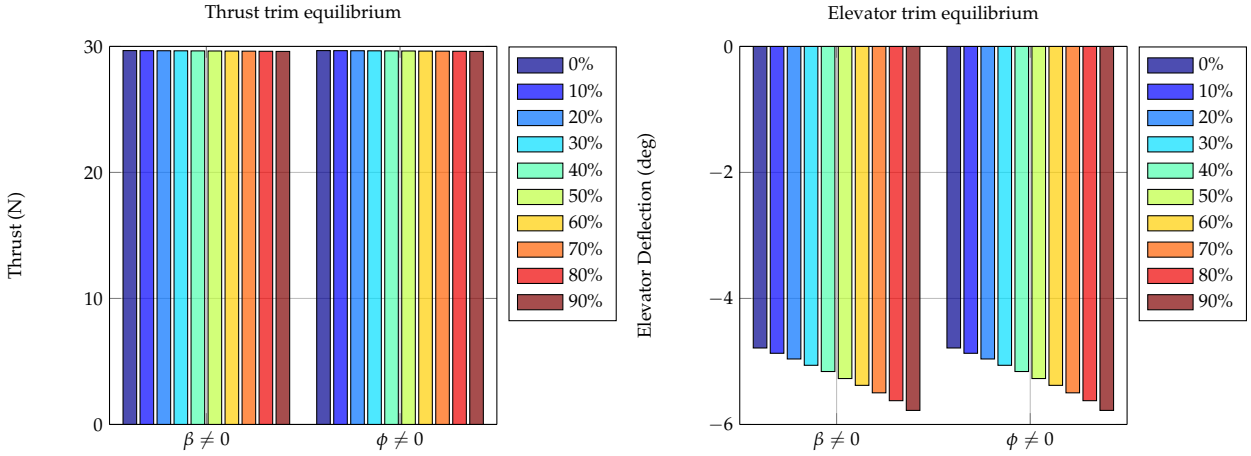

(a) Trim thrust (b) Trim elevator deflection

Figure D.8: Trim thrust and trim elevator deflection for vertical stabiliser damage cases

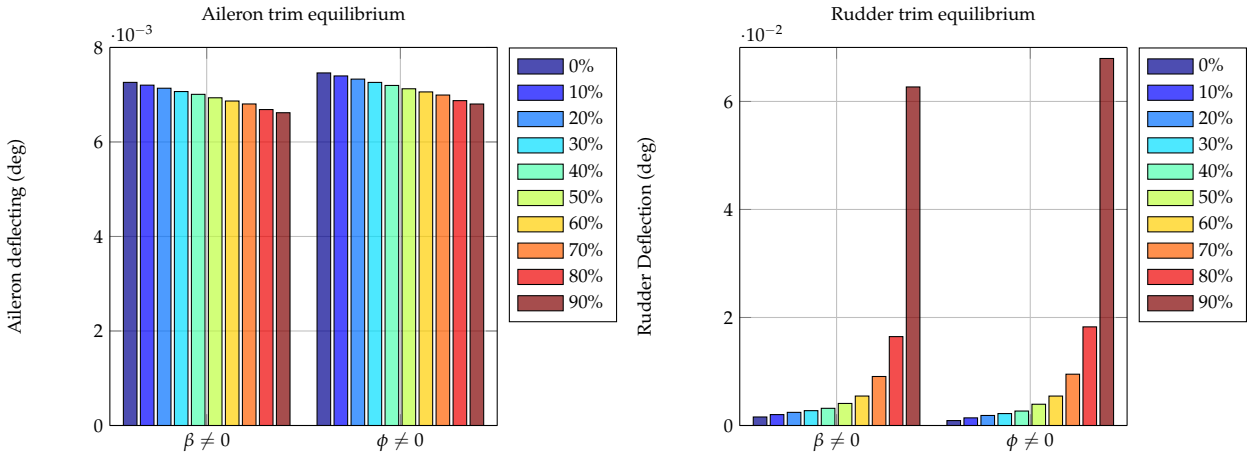

(a) Trim aileron deflection

(b) Trim rudder deflection

Figure D.9: Trim aileron and rudder deflections for vertical stabiliser damage cases

E.1 Design Approach

The gains of a control system is said to be robust when the gains yield closed-loop poles that fall within the required admissible region. From Figure E.1 an admissible pole region is defined as the region where the poles have a natural frequency between $\omega_{n_{max}}$ and $\omega_{n_{min}}$ and a damping ratio between ζ_{max} and ζ_{min}. Figure E.1 illustrates the case of a system which only consists of a complex pole pair but the algorithm can easily be adapted to include real poles (e.g $\zeta_{max} = 1$) or to have multiple admissible pole region.

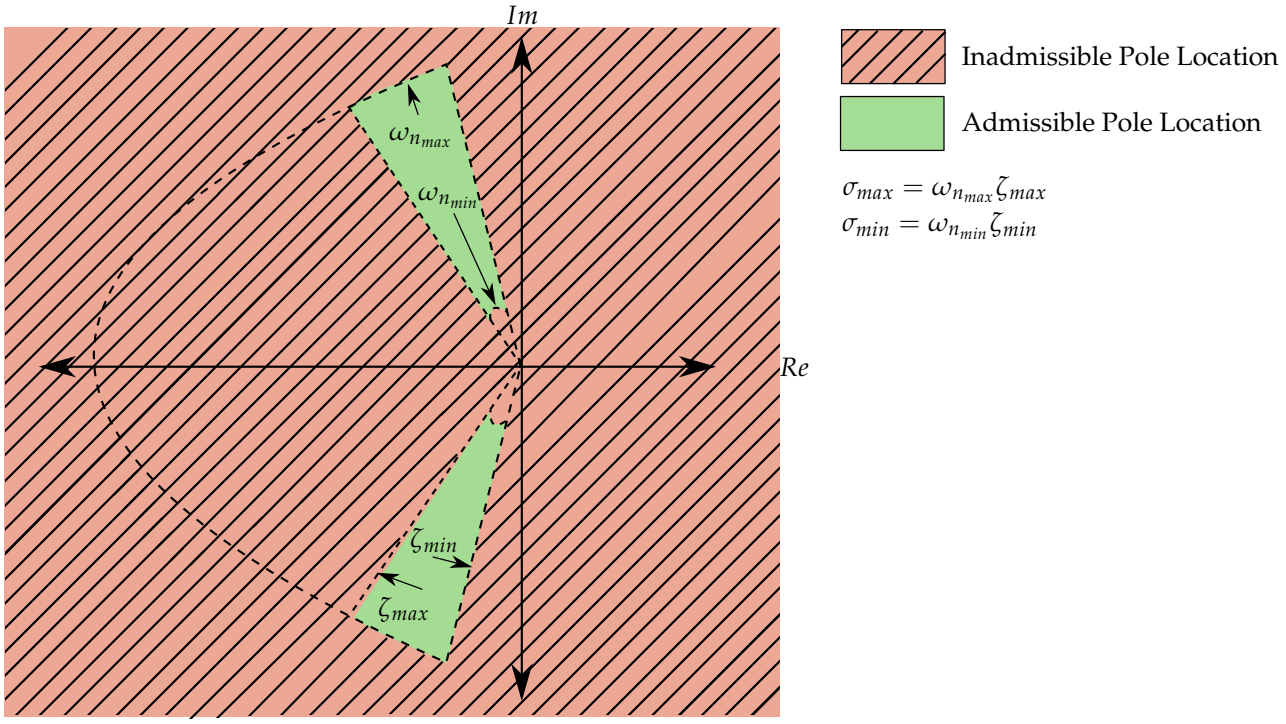

Figure E.1: Admissible closed-loop pole region required for robustness

The robust gains are iteratively obtained by means of the algorithm seen in Figure E.2.

E.2 Algorithm To Find Robust Gains

```
1:  for range of natural frequencies do
2:    for range of damping ratios do
3:      Design gains on undamaged aircraft
4:      if closed-loop poles in admissible region then
5:        if performance > previous best performance then
6:          for all horizontal stabiliser damage cases do
7:            if closed-loop poles in admissible region then
8:              Gains robust for particular damage case
9:            end if
10:         end for
11:         if gains robust for all damages cases then
12:           Store gains
13:           best performance = performance
14:         end if
15:       end if
16:     end if
17:   end for
18: end for
```

Figure E.2: Algorithm used to obtain robust gains

Appendix F includes all the pole-zero and unit step response plots to verify the robustness of the flight control system. The performance and robustness of all the controllers are included. Appendix F is divided into three sections:

- Robustness to partial wing tip loss (0% up to 40% semi-span)
- Robustness to partial horizontal stabiliser tip loss(0% up to 100% semi-span)
- Robustness to partial vertical stabiliser tip loss(0% up to 50% span)

F.1 Robustness to Wing Tip Loss

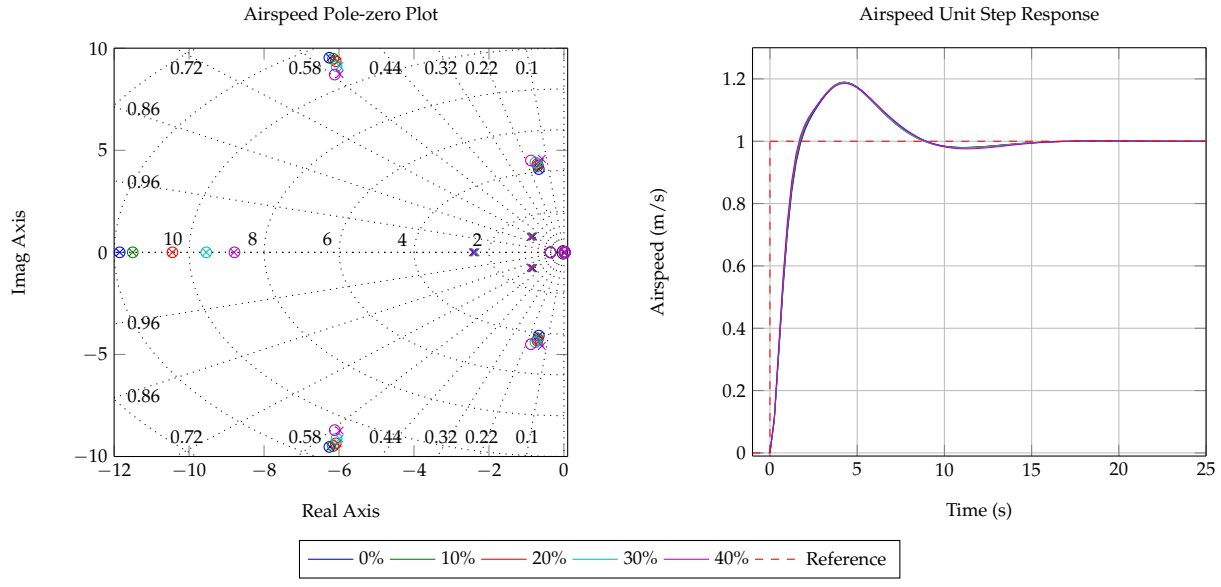

Figure F.1: Airspeed unit step and pole-zero plot for wing loss

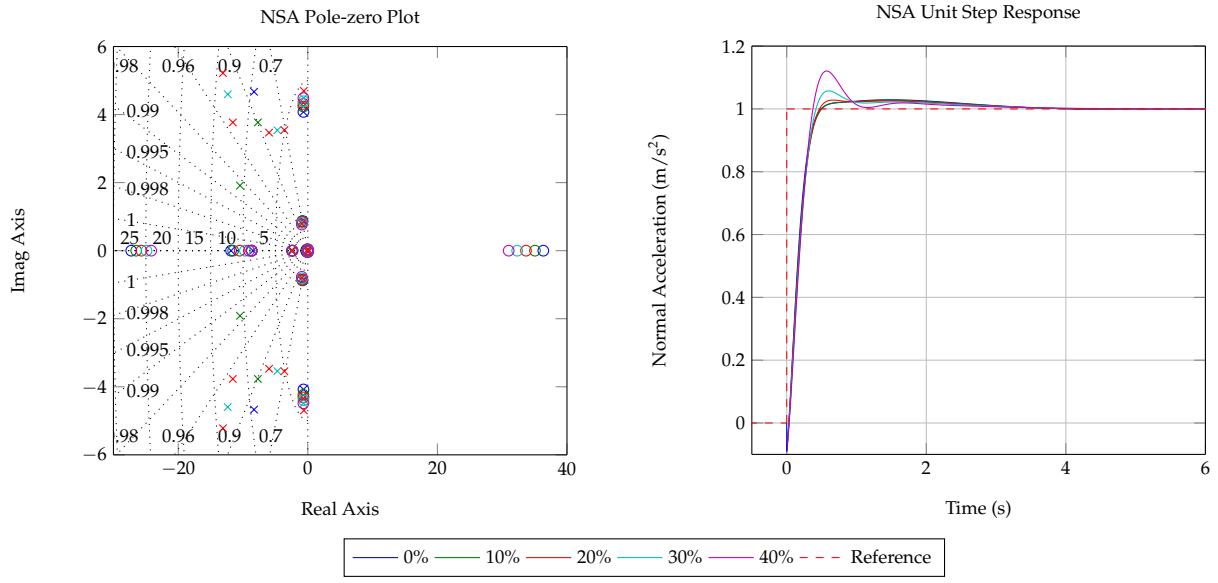

Figure F.2: NSA unit step and pole-zero plot for wing loss

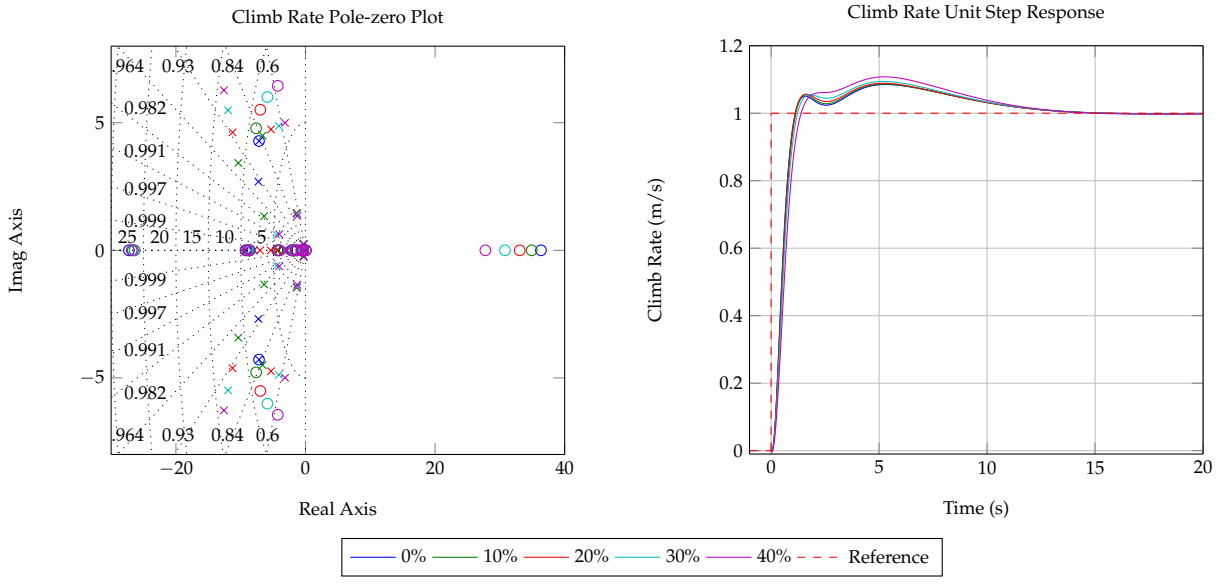

Figure F.3: Climb rate unit step and pole-zero plot for wing loss

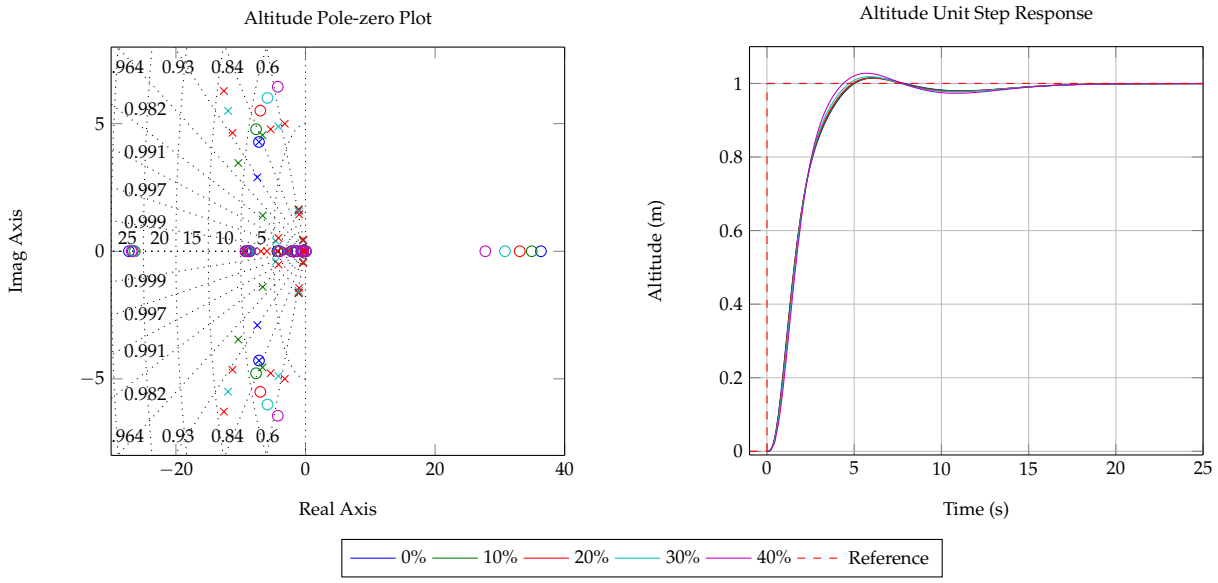

Figure F.4: Altitude unit step and pole-zero plot for wing loss

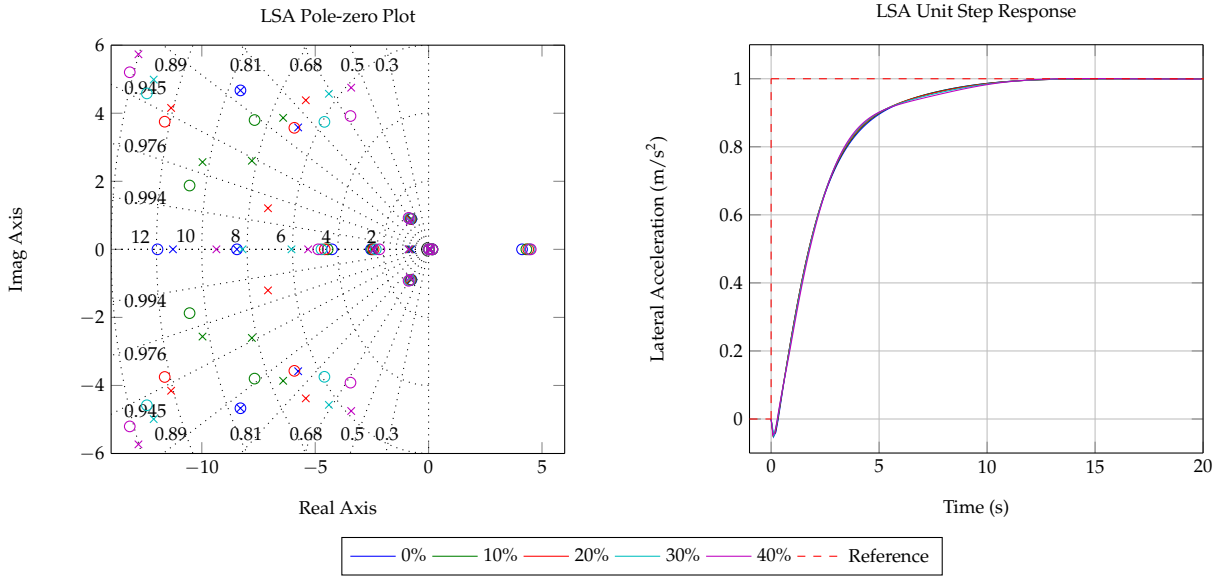

Figure F.5: LSA unit step and pole-zero plot for wing loss

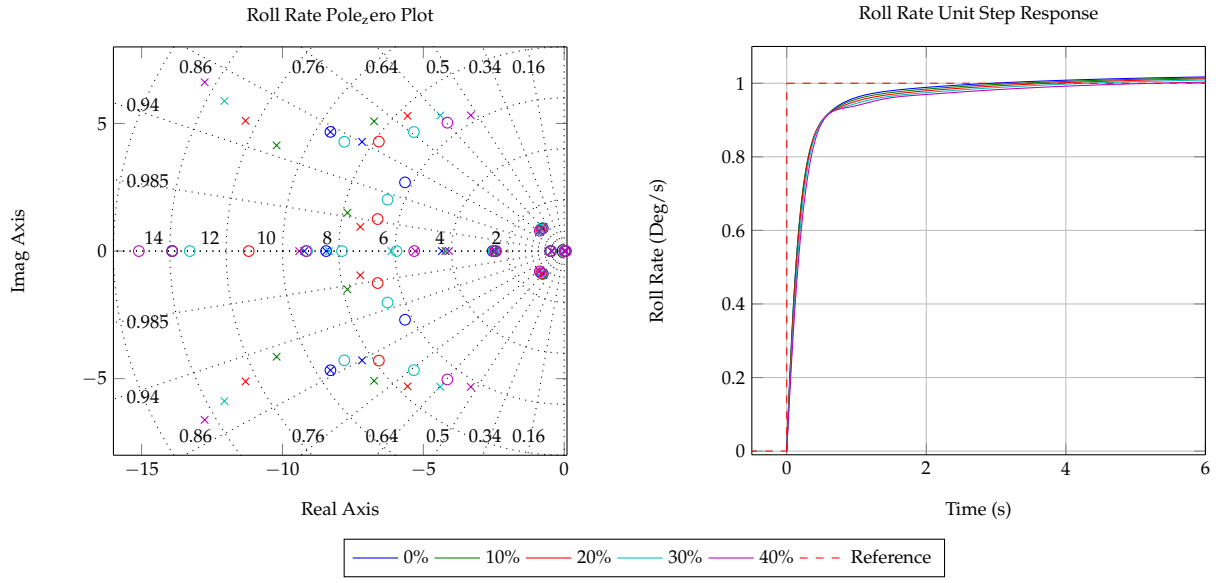

Figure F.6: Roll rate unit step and pole-zero plot for wing loss

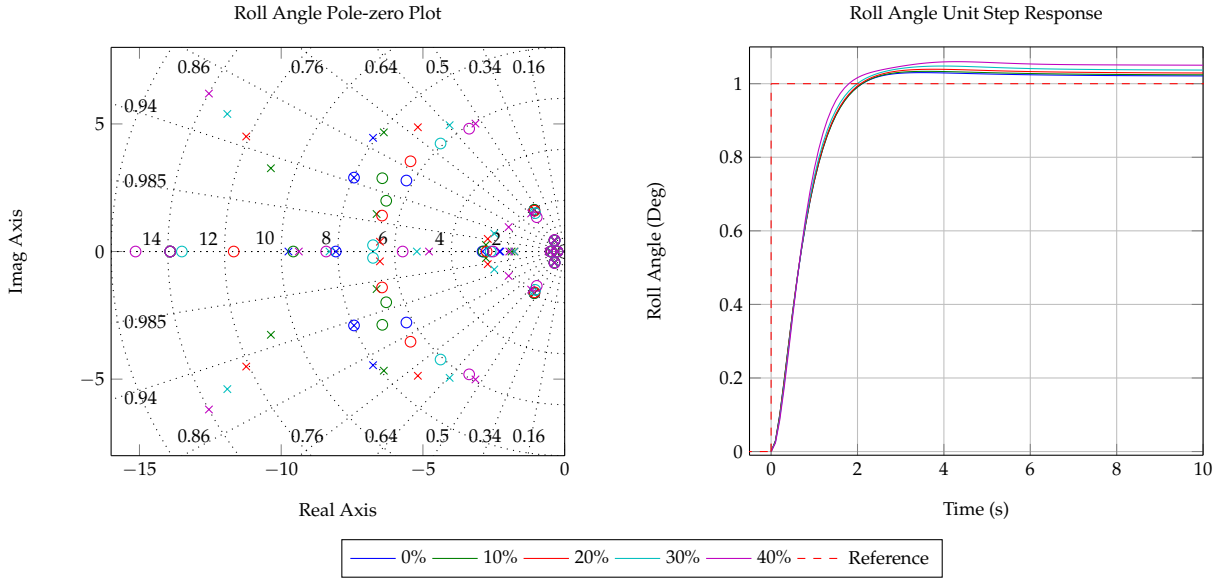

Figure F.7: Roll angle unit step and pole-zero plot for wing loss

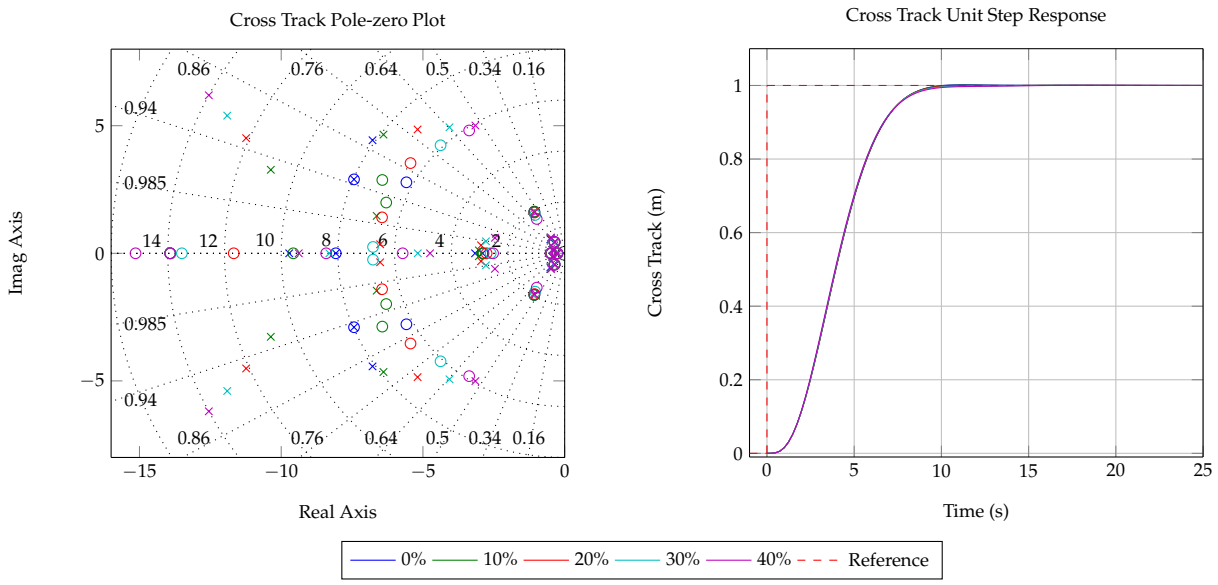

Figure F.8: Cross track position error unit step and pole-zero plot for wing loss

F.2 Robustness to Horizontal Stabiliser Tip Loss

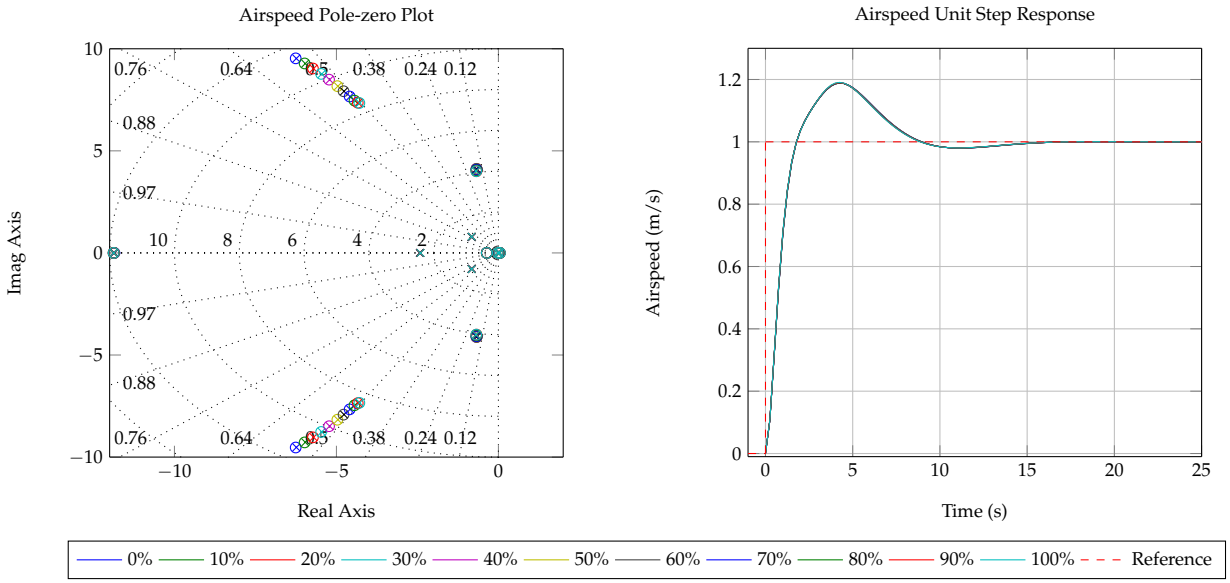

Figure F.9: Airspeed unit step and pole-zero plot for horizontal stabiliser loss

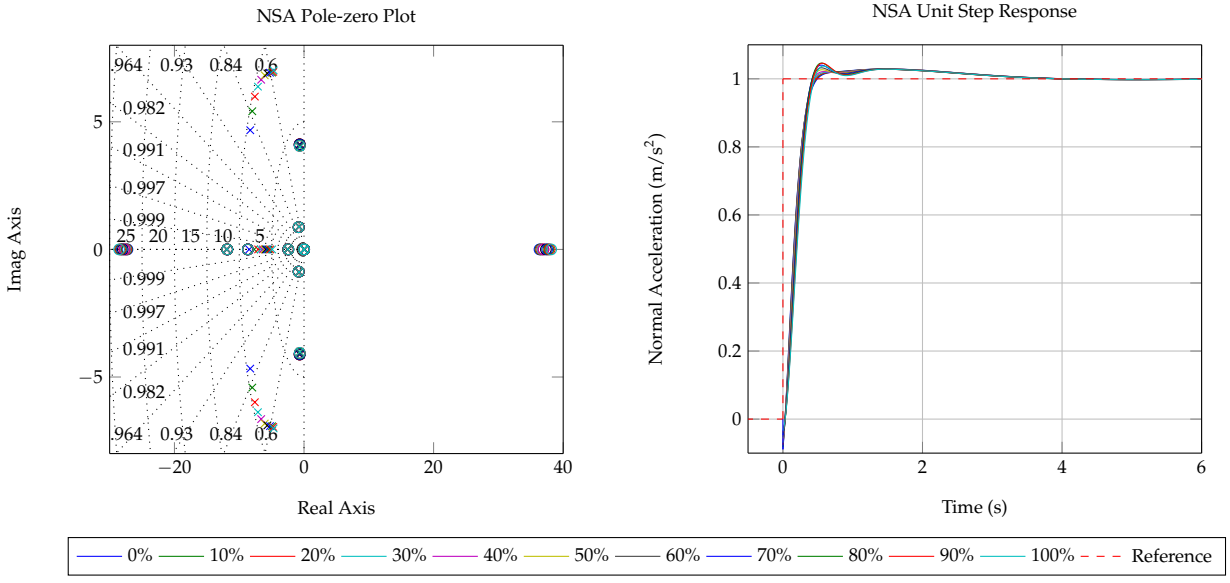

Figure F.10: NSA unit step and pole-zero plot for horizontal stabiliser loss

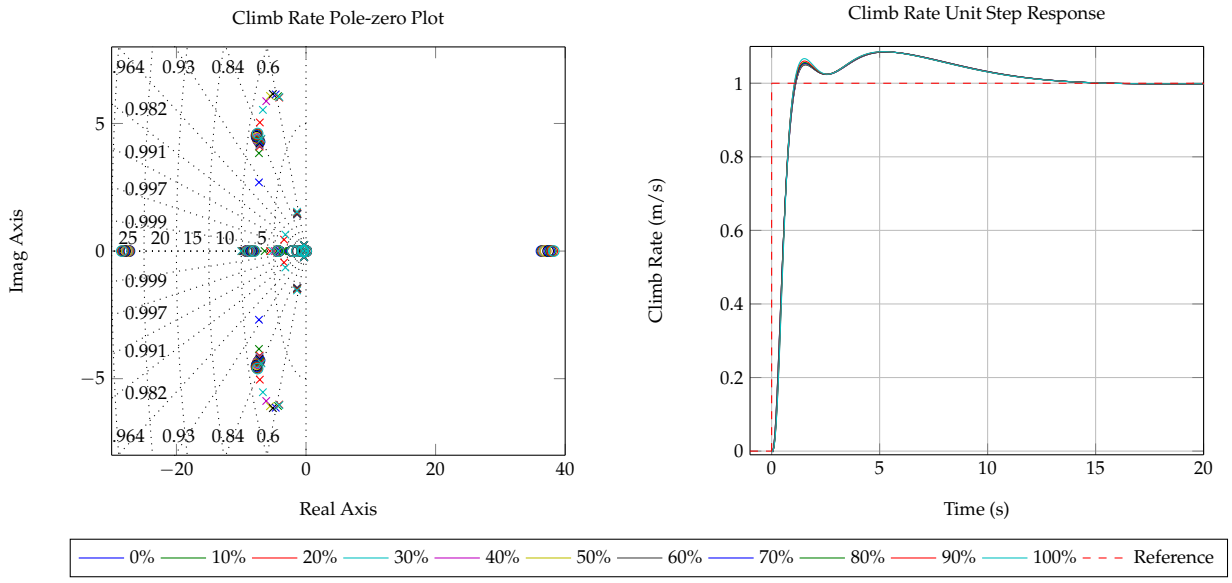

Figure F.11: Climb rate unit step and pole-zero plot for horizontal stabiliser loss

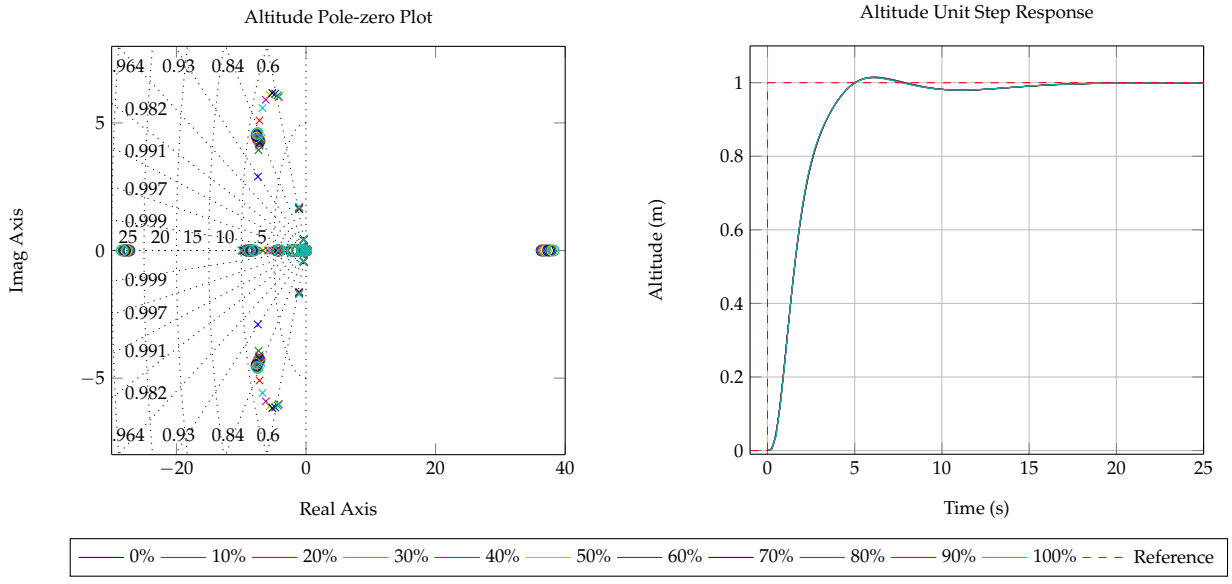

Figure F.12: Altitude unit step and pole-zero plot for horizontal stabiliser loss

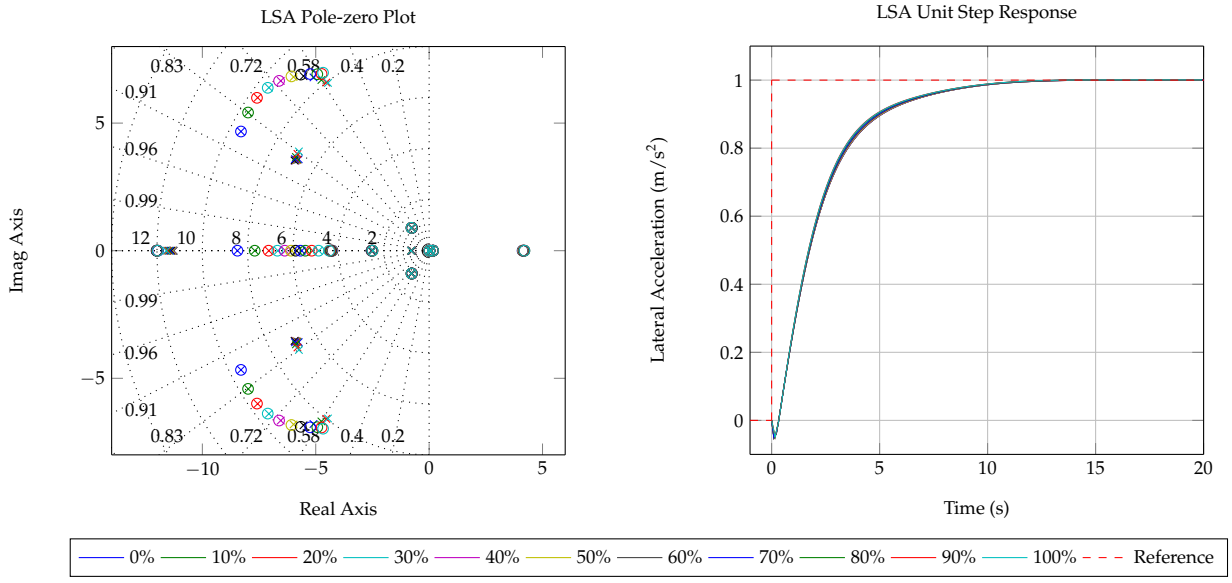

Figure F.13: LSA unit step and pole-zero plot for horizontal stabiliser loss

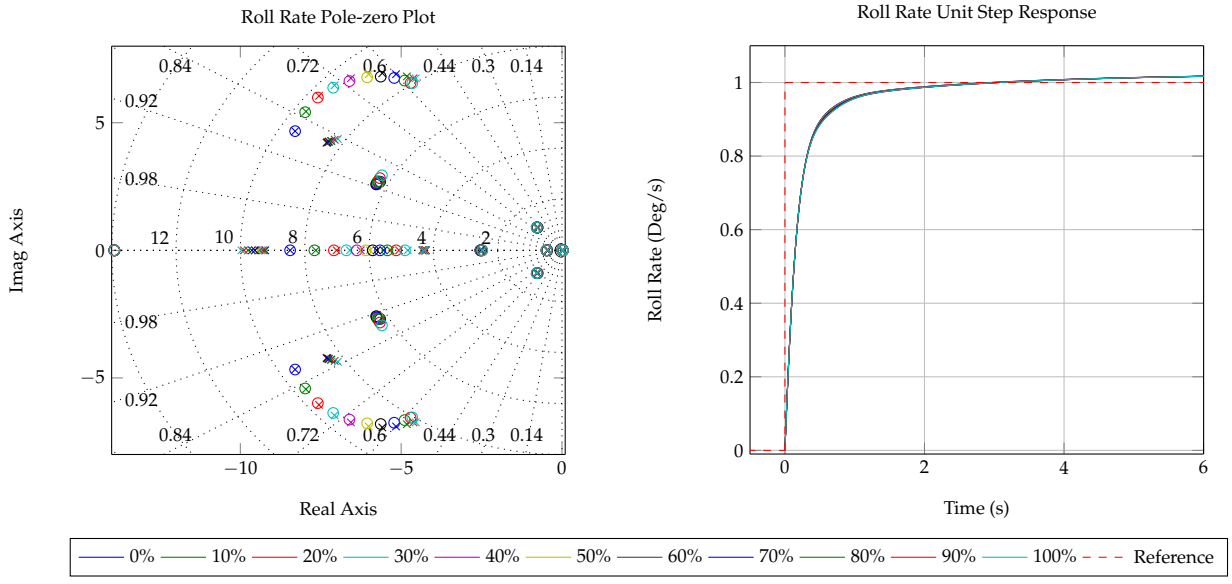

Figure F.14: Roll rate unit step and pole-zero plot for horizontal stabiliser loss

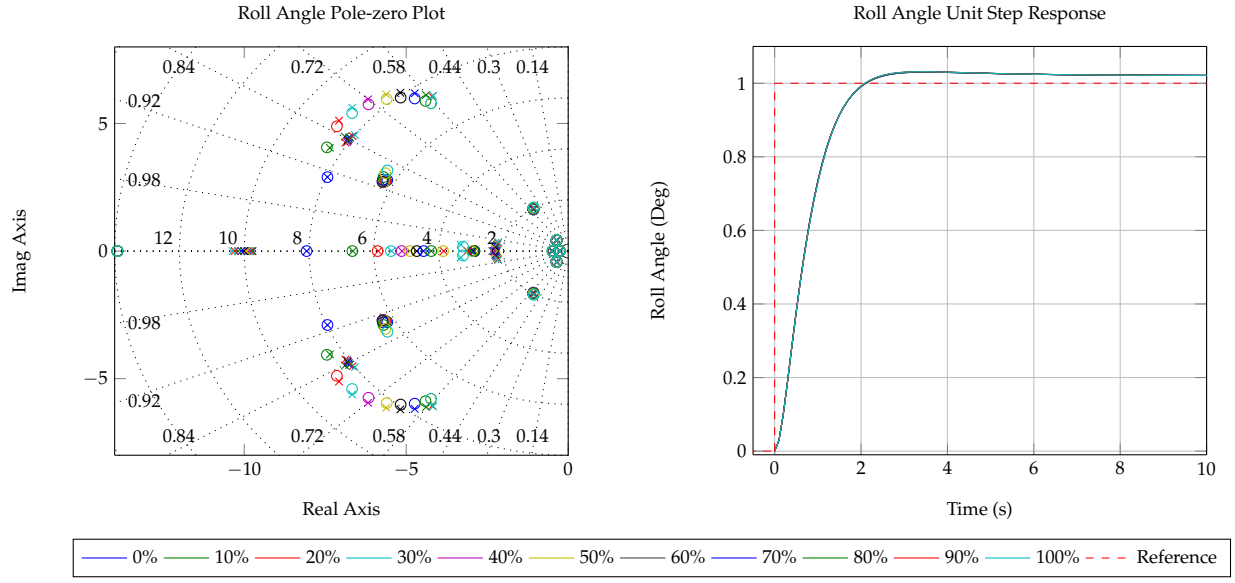

Figure F.15: Roll angle unit step and pole-zero plot for horizontal stabiliser loss

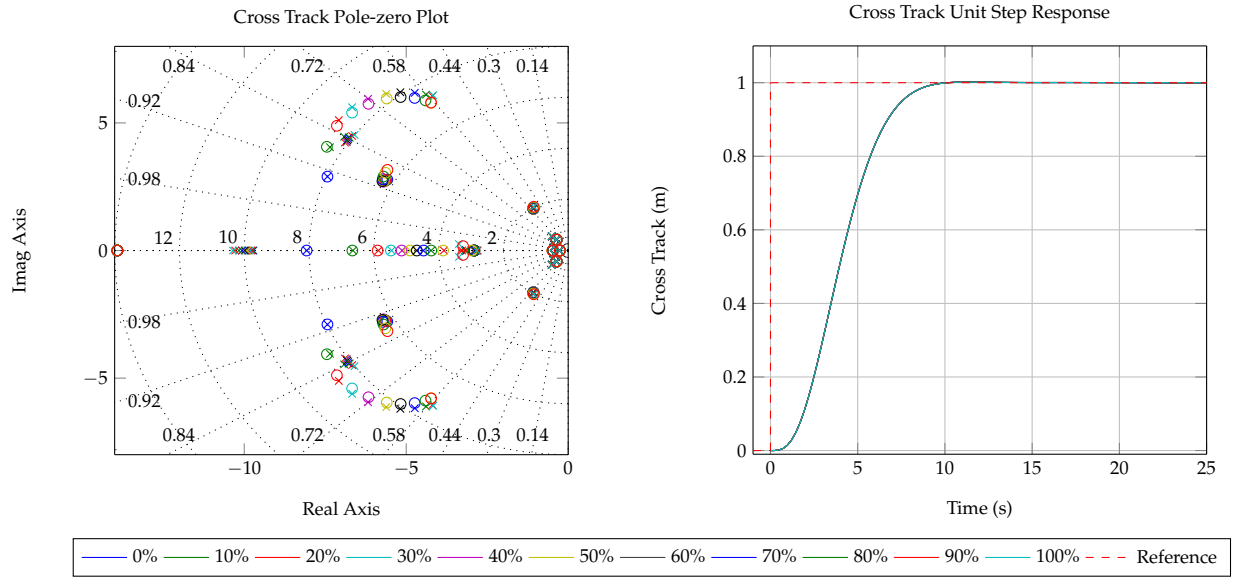

Figure F.16: Cross track position error unit step and pole-zero plot for horizontal stabiliser loss

F.3 Robustness to Vertical Stabiliser Tip Loss

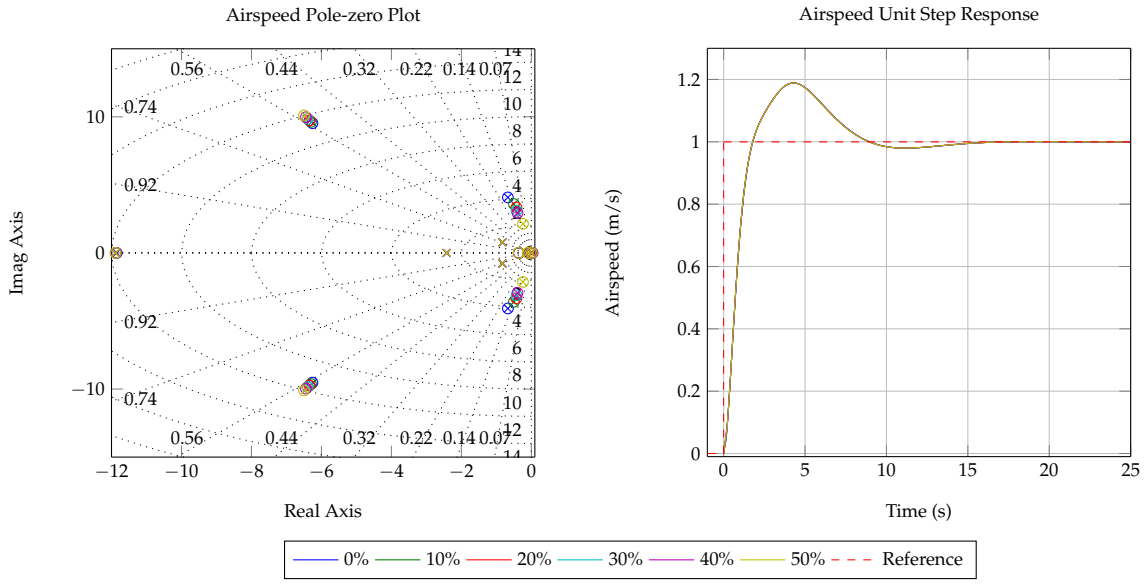

Figure F.17: Airspeed unit step and pole-zero plot for vertical stabiliser loss

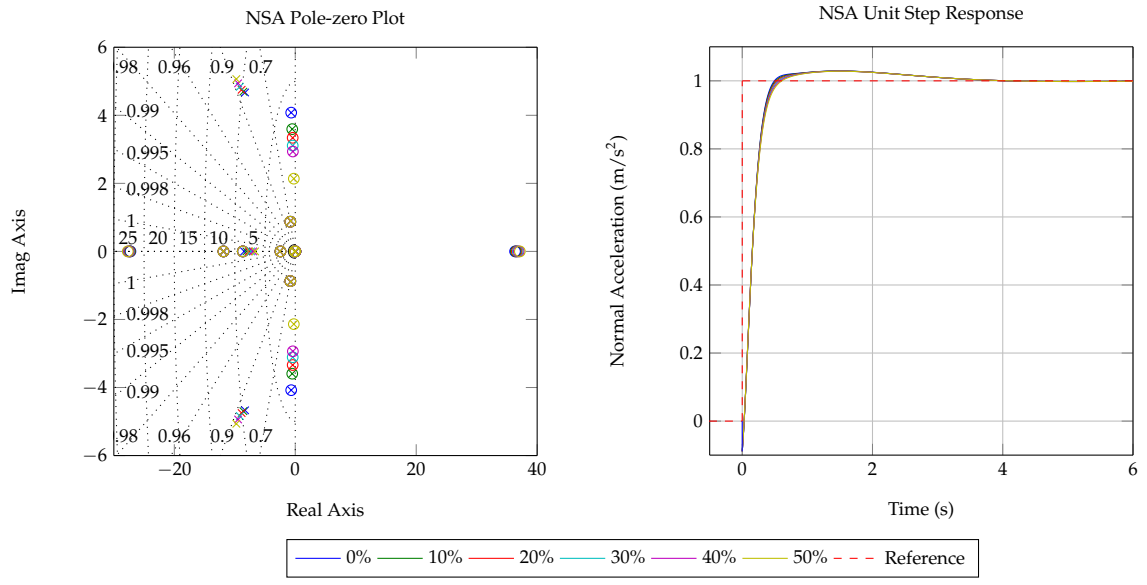

Figure F.18: NSA unit step and pole-zero plot for vertical stabiliser loss

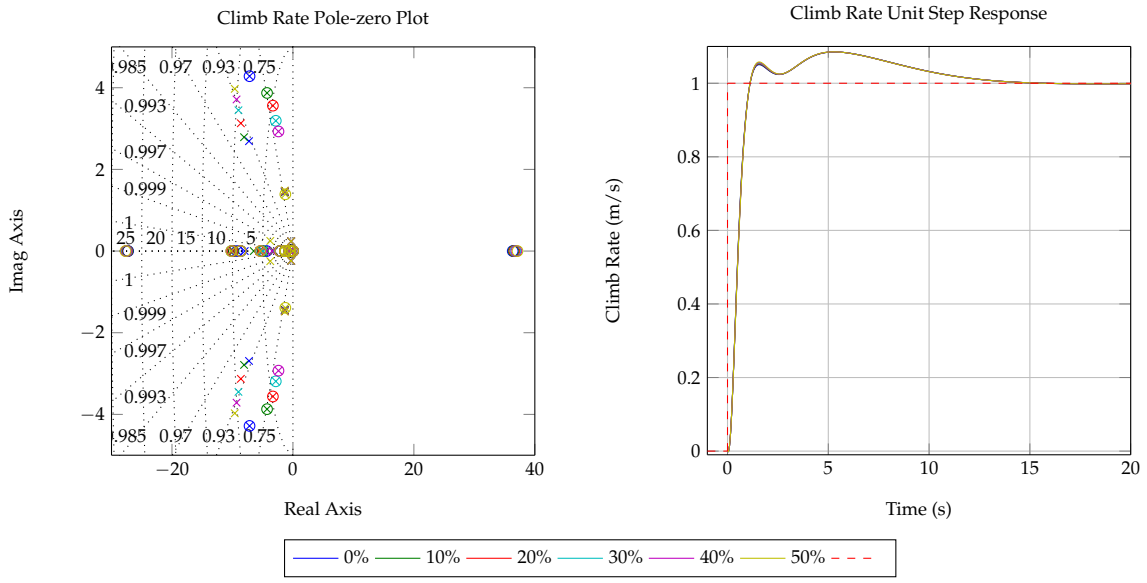

Figure F.19: Climb rate unit step and pole-zero plot for vertical stabiliser loss

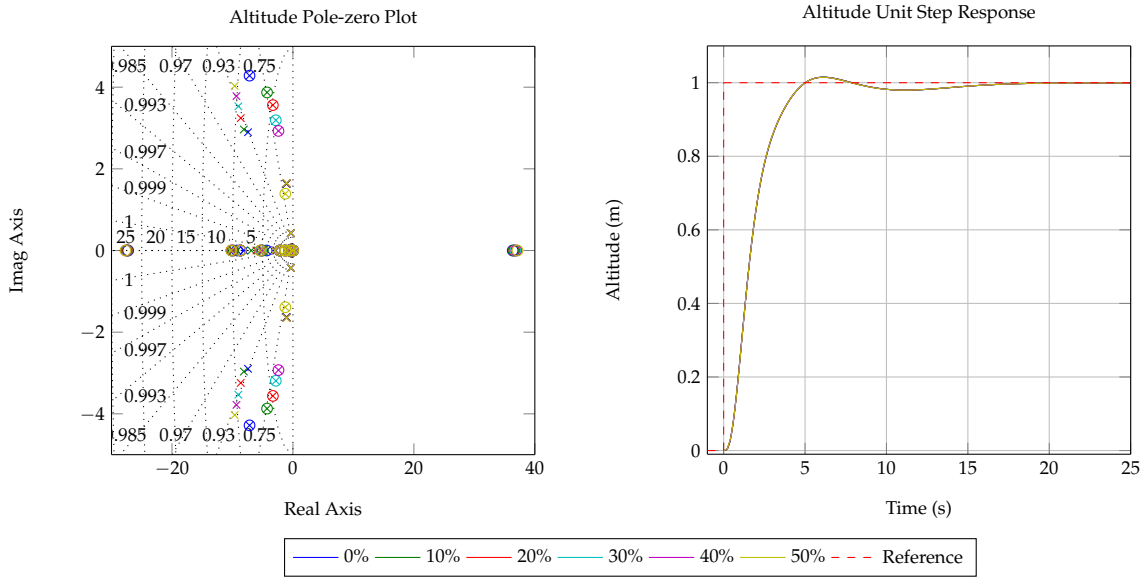

Figure F.20: Altitude unit step and pole-zero plot for vertical stabiliser loss

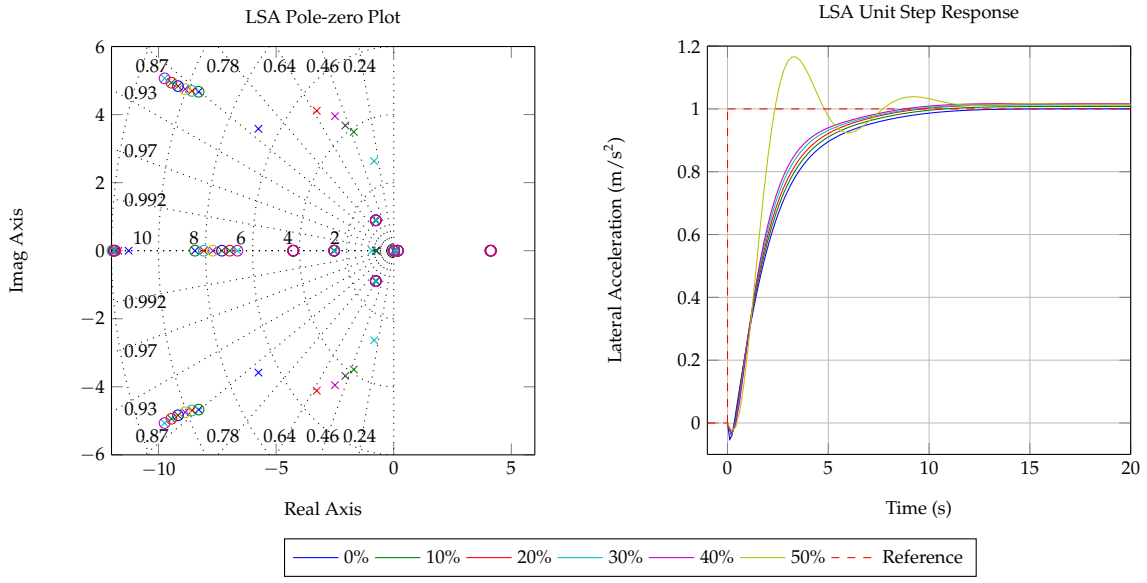

Figure F.21: LSA unit step and pole-zero plot for vertical stabiliser loss

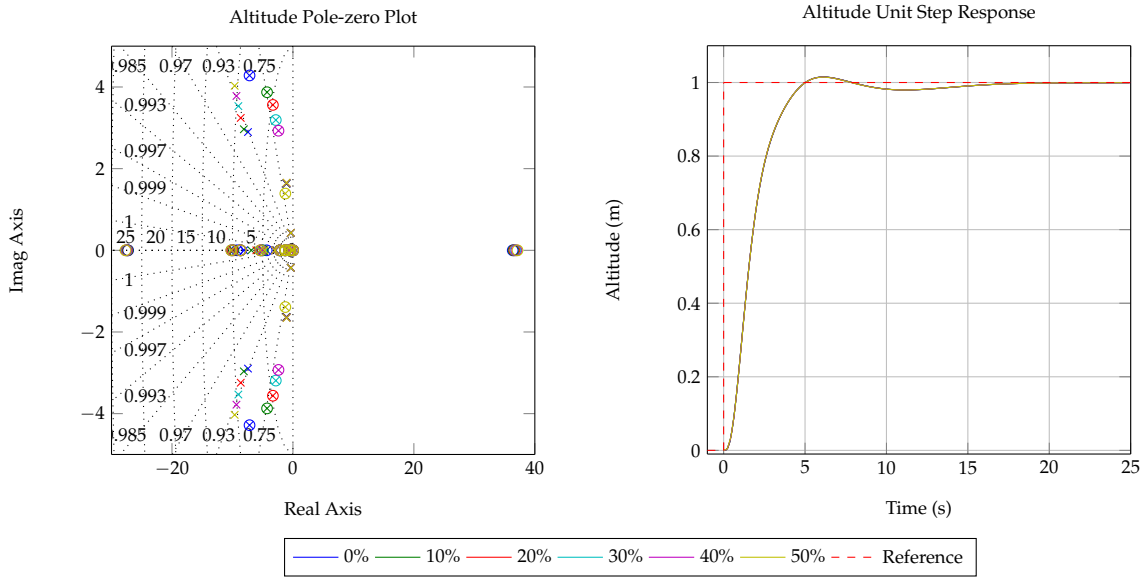

Figure F.22: Altitude unit step and pole-zero plot for vertical stabiliser loss

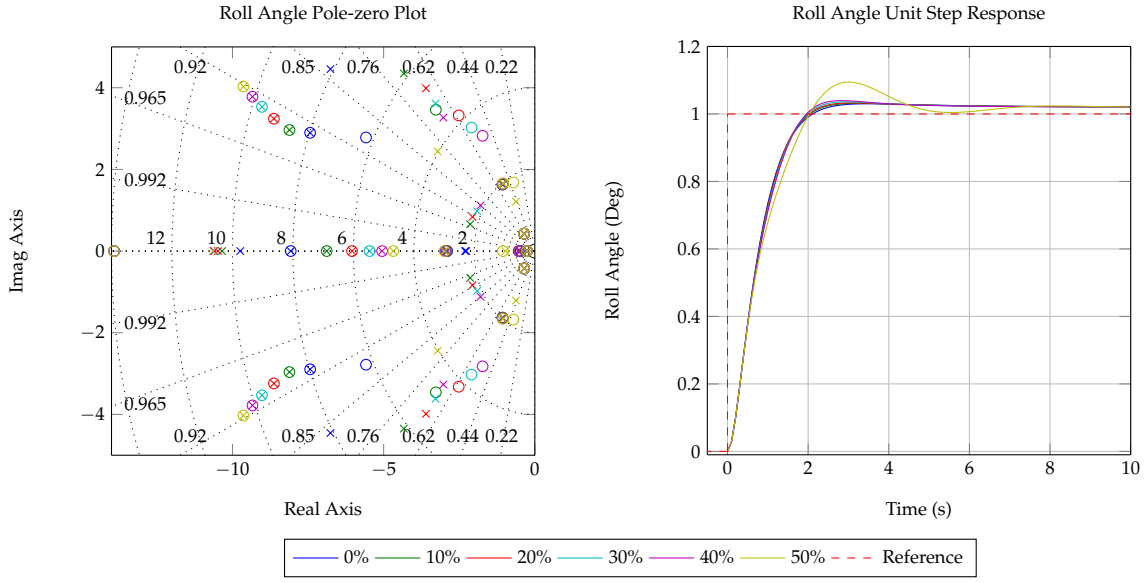

Figure F.23: Roll angle unit step and pole-zero plot for vertical stabiliser loss

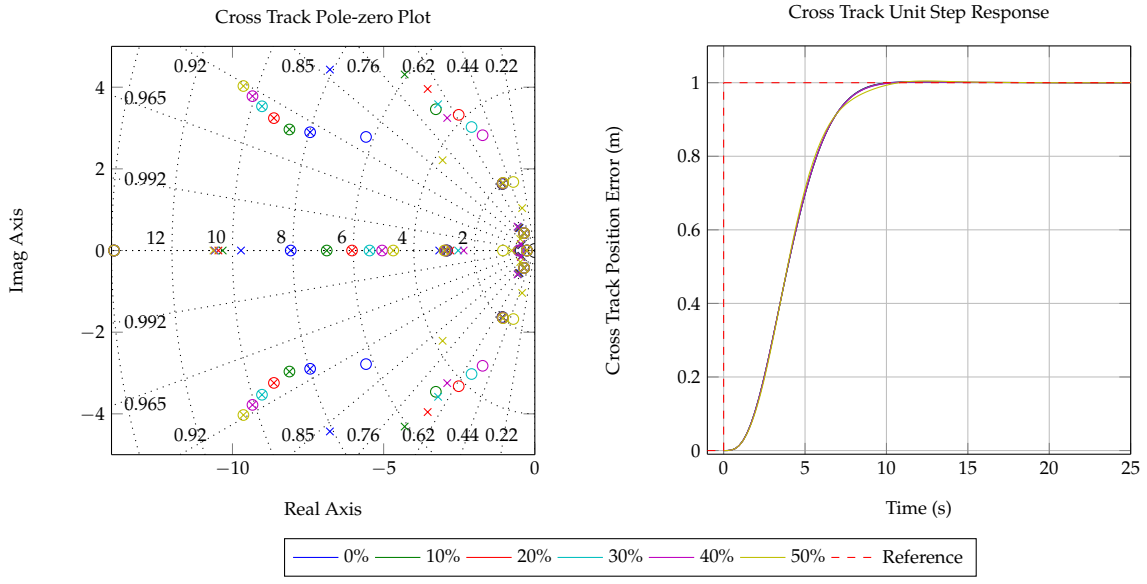

Figure F.24: Cross track position error unit step and pole-zero plot for vertical stabiliser loss

List of References

[1] Ducard, G.J.J.: *Fault-Tolerant Flight Control and Guidance Systems for a Small Unmanned Aerial Vehicle*. PhD, Swiss Federal Institute of Technology, 2007. 2, 11

[2] Peddle, I.K.: *Autonomous Flight of a Model Aircraft*. MEng, Stellenbosch University, 2005. 2, 166

[3] Roos, J.: *Autonomous Take-Off and Landing of a Fixed Wing Unmanned Aerial Vehicle6*. MEng, Stellenbosch University, 2006. 3, 128

[4] Visser, B.J.: *Presisie Landing van 'n Onbemande Vliegtuig*. MEng, Stellenbosch University, 2008. 3, 8, 9

[5] Smit, S.J.A.: *Autonomous Landing of a Fixed-Wing Unmanned Aerial Vehicle using Differential GPS*. MEng, Stellenbosch University, 2013. 3, 6, 7, 9, 78, 166, 169

[6] Blaaw, D.: *Flight Control System for a Variable Stability Blended-Wing-Body Unmanned Aerial Vehicle*. MEng, Stellenbosch University, 2009. 3

[7] Peddle, I.K.: *Acceleration Based Manoeuvre Flight Control System for Unmanned Aerial Vehicles*. PhD, Stellenbosch University, 2008. 3, 76, 80, 81, 95, 96, 97, 98, 100, 104, 161

[8] Basson, W.A.: *Fault Tolerant Adaptive Control of an Unmanned Aerial Vehicle*. MEng, Stellenbosch University, 2011. 3, 9

[9] Beeton, W.: *Fault Tolerant Flight Control of a UAV with Asymmetric Damage to its Primary Lifting Surface*. MEng, Stellenbosch University, 2013. 4, 6, 8, 9, 32, 35

[10] Alberts, F.N.: *Accurate Autonomous Landing of a Fixed-Wing Unmanned Aerial Vehicle*. MEng, Stellenbosch University, 2012. 6, 9, 15, 78, 166

[11] Maggot, R.N.: *Fault-Tolerant Control for a Fixed Wing Unmanned Aerial Vehicle with Partial Horizontal and Vertical Stabiliser Loss*. MEng, Stellenbosch University, 2016. 8

[12] Chowdhary, G., Johnson, E.N., Chandramohan, R., Kimbrell, M.S. and Calise, A.: *Autonomous Guidance and Control of Airplanes under Actuator Failures and Severe Structural Damage*. Journal of Guidance, Control, and Dynamics, pp. 1–25, 2011. 11

[13] Arruda, M.: *Dynamic Inverse Resiliant Control for Damaged Asymmetric Aircraft: Modeling and Simulation*. Msc, Wichita State University, 2009. 11

[14] Nguyen, N., Krishnakumar, K., Kaneshige, J. and Nespeca, P.: *Dynamics and Adaptive Control for Stability Recovery of Damaged Asymmetric Aircraft*. AIAA Guidance, Navigation, and Control Conference and Exhibit, pp. 1–24, 2006. 12

[15] Zhao, J., Jiang, B., Shi, P. and He, Z.: *Fault Tolerant Control for Damaged Aircraft Based on Sliding Mode Control Scheme*. pp. 293–302, 2014. 12

[16] Hitachi, Y.: *Damage-Tolerant Flight Control System Design for Propulsion-Controlled Aircraft*. 2009. 12

[17] Kada, B. and Ghazzawi, Y.: *Robust PID Controller Design for an UAV Flight Control System*. Proceedings of the World Congress on Engineering and Computer Science, pp. 1–6, 2011. 12

[18] Sadraey, M. and Colgren, R.D.: *Robust Nonlinear Controller Design for a Complete UAV Mission*. Proceedings of the AIAA Guidance, Navigation, and Control Conference and Exhibit, 2006. 12

[19] Prach, A.: *Robust Controller Design for a Fixed Wing Uav*. Msc, Middle East Technical University, 2009. 12

[20] Bacon, B.J. and Gregory, I.M.: *General Equations of Motion for a Damaged Asymmetric aircraft*. AIAA Atmospheric Flight Mechanics Conference and Exhibit, 20-23 August 2007, Hilton Head, SC, , no. August, pp. 1–13, 2007. 13, 16, 20, 25

[21] Shah, G.H.: *Aerodynamic Effects and Modeling of Damage to Transport Aircraft*. AIAA Atmospheric Flight Mechanics Conference and Exhibit, pp. 1–13, 2008. 13, 14

[22] Ouellette, J., Raghavan, B., Patil, M. and Kapania, R.: *Flight Dynamics and Structural Load Distribution for a Damaged Aircraft*. AIAA Atmospheric Flight Mechanics Conference, pp. 1–20, 2009. 14

[23] Cheng, P., Wu, C., Duan, X., Guo, Y., Pengfei Cheng, Chengfu Wu, Xiaojun Duan and Yue Guo: *An Approach of Flight Trim for Wing-damaged Asymmetric Aircraft*. Control Conference (CCC), 2013. 14

[24] Kargin, V.: *Design of an Autonomous Landing Control Algorithm for a Fixed Wing UAV*. MEng, Middle East Technical University, 2007. 15

[25] Kurnaz, S. and Cetin, O.: *Autonomous Navigation and Landing Tasks for Fixed-Wing Small Unmanned Aerial Vehicles*. Acta Polytechnica Hungarica, pp. 87–102, 2010. 15

[26] Li, Y., Sundarajan, N., Saratchandran, P. and Wang, Z.: *Robust Neuro-H Controller Design for Aircraft Auto-Landing*. IEEE Transactions on aerospace and electronic systems, 2004. 15

[27] Hibbler, R.C.: *Engineering Mechanics Dynamics*. 12th edn. Prentile Hall, 2010. ISBN 9810681372. 23, 165

[28] Cook, M.V.: *Flight Dynamics Principles, Second Edition: A Linear Systems Approach to Aircraft Stability and Control*. 2nd edn. Elsevier Ltd., 2007. ISBN 9788578110796. 30, 31, 32, 53, 66, 67, 68, 69

[29] Koen, M.C.: *Modelling and Simulation of an RPV for Flight Control System Design Purposes*. 2006. 30, 31

[30] Nita, M. and Scholz, D.: *Estimating the Oswald Factor from Basic Aircraft Geometrical Parameters*. Deutscher Luft- und Raumfahrtkongress, pp. 1–19, 2012. 31, 167

[31] Hull, D.G.: *Fundamentals of Airplane Flight Mechanics*. 2007. ISBN 3540465715. 33, 34, 53, 118, 120

[32] Raol, J.R. and Singh, J.: *Flight Mechanics Modelling and Analysis*. Taylor & Francis Group, LLC, 2009. ISBN 9781420067552. 34, 143

[33] Roskam, J.: *Airplane Flight Dynamics and Automatic Flight Controls*. Part 1 edn. DARcorporation, 2001. ISBN 1884885179. 34, 38, 39, 40, 42, 43, 44, 47, 48, 51, 52

[34] Anderson, J.D.: *Introduction to Flight*. Seventh edn. McGraw-Hill, 2005. ISBN 0072825693. 40

[35] Airbus: *Landing Techniques: Crosswind landings*. pp. 1–8, 2004. 123

[36] United States Department of Defense: *Flying Qualities of Piloted Aircraft*. Tech. Rep. MIL-F-8785C, 1980. 128, 129

[37] United States Department of Defense: *Flying Qualities of Piloted Aircraft*. Tech. Rep. MIL-HDBK, 1997. 128